WARSAW UNIVESITY OF TECHNOLOGY

DOCTORAL THESIS

Beam-induced Backgrounds at the Compact Linear Collider

Author:
Dominik AROMINSKI

Supervisor:
Dr Andre SAILER
Prof. Adam KISIEL

*A thesis submitted in fulfillment of the requirements
for the degree of Doctor of Philosophy*

in the

Faculty of Physics

14.01.2020

Abstract

The Compact Linear Collider (CLIC) is a concept for a future linear e^+e^- collider, able to reach multi-TeV centre-of-mass energies. High intensities and nanometre-sized beams are needed to meet the required luminosity performance. These lead to many challenges in the design of the accelerator and detector. This study concentrates on the performance of the Beam Delivery System (BDS) and the CLIC detector (CLICdet) at the 380 GeV and 3 TeV energy stages, taking into account the resistive wall wakefields, synchrotron radiation emission and reflection, and beam-beam backgrounds.

The beam pipe apertures in the BDS are estimated taking into account the lower limits coming from the resistive wall wakefields. The wakefield impact on the beams is simulated using PyHEADTAIL, and the impact on the luminosity with Guinea-Pig. At both energy stages, the apertures need to be enlarged in the Final Focus System to reach the desired luminosity performance and stability.

The synchrotron radiation (SR) emission and the transverse distribution of the photons in the detector region are studied with PLACET and Synrad+. Significant amounts of power are emitted, 16 W at 380 GeV and 2.2 kW at 3 TeV. The power deposited in the beam pipe leads to heating and outgassing. The outgassing rate and the radiation levels in the BDS tunnel are not challenging in comparison with circular e^+e^- colliders. The number of photons that can interact with the detector due to reflections from the vacuum chamber walls is substantial for both iron and copper beam pipe walls and average surface roughness between 10 nm and 1 µm. In the full detector simulations done in GEANT4, the large number of photons leads to significant hit densities in the tracking detectors, reaching 100% in the first layer of the vertex detector at 380 GeV, and 40% at the inner radius of the vertex disks at 3 TeV. Therefore, a mitigation method has to be implemented. The most promising is a high-roughness surface used in a winglet beam pipe shape. Complete removal of photons that can interact with the detector is predicted when such a high-roughness surface is implemented in the final 30 m of the BDS.

The beam-induced backgrounds are created in e^+e^- collisions simulated with Guinea-Pig. The input beams are transported through the BDS using six-dimensional tracking in PLACET, taking into account the beam conditions at the end of the Main Linac. The background particles are simulated in the CLICdet model using GEANT4. The occupancy levels calculated from hit densities reach the 3% acceptable limit in the inner layers of the vertex barrel and inner radii of the vertex endcaps at 3 TeV. The occupancies in the tracking detectors are at least a factor of three lower at 380 GeV, than at 3 TeV. High occupancies, reaching 100%, are found in the endcaps of the Hadronic Calorimeter (HCal) and the Muon Identification System. For the HCal endcap, the occupancies are addressed by a combination of shielding, consisting of lead and polyethylene, and increased granularity. For the muon system, the granularity does not need to change but additional shielding to the HCal shielding is needed. In this way, the occupancies are lowered to acceptable levels, below 10% in both subdetectors.

beam-induced backgrounds, resistive wall wakefields, synchrotron radiation, linear collider, CLIC

Streszczenie

Compact Linear Collider (CLIC) jest projektem przyszłego liniowego zderzacza elektron-pozyton, który może osiągać energię zderzeń w zakresie TeV. Wysokie intensywności i nanometrowe rozmiary wiązek są konieczne aby uzyskać wymaganą przez przyszły eksperyment świetlność. Restrykcyjne wymagania prowadzą do licznych wyzwań w projekcie przyszłego akceleratora i detektora. Niniejsza rozprawa koncentruje się na badaniu sprawności systemu dostarczania wiązki (BDS) i detektora dla CLIC dla dwóch energii zderzeń, 380 GeV i 3 TeV. Wzięto pod uwagę wpływy impedancji ścian jonowodu, emisji i odbić promieniowania synchrotronowego oraz efekty tła pochodzącego z oddziaływań wiązek.

Promienie wewnętrzne jonowodu w BDS zostały oszacowane biorąc pod uwagę ograniczenia wynikające z rozmiarów wiązek i wpływu impedancji ścian jonowodu. Symulacje wpływu impedancji na stabilność wiązek wykonano w programie PyHEADTAIL, a wpływ na świetlność symulowano w Guinea-Pig. Dla obu energii zderzenia, promienie jonowodu musiały zostać powiększone w Final Focus System (FFS) w celu uzyskania wymaganej stabilności wiązek i świetlności.

Emisję promieniowania synchrotronowego (SR) symulowano przy pomocy programów PLACET i Synrad+. Odkryto, iż znaczna moc jest emitowana przez wiązki w BDS w postaci SR: 16 W dla 380 GeV i 2.2 kW dla 3 TeV. Energia zdeponowana przez fotony w jonowodzie prowadzi do fotoemisji elektronów i rozgrzewania się materiału. Emisja fotoelektronów jest na znacznie niższym poziomie niż w przypadku kołowych zderzaczy elektron–pozyton i nie stanowi ograniczenia sprawności akceleratora, natomiast rozgrzewanie się jonowodu stanowi istotny problem, który musi zostać rozwiązany dla energii zderzeń 3 TeV. Liczba fotonów, która na skutek odbić od jonowodu może oddziaływać z detektorem jest znacząca gdy jonowód zbudowany jest z żelaza lub miedzi i ma średnią chropowatość powierzchni w zakresie od 10 nm do 1 µm. W symulacjach w GEANT4, duża liczba fotonów skutkuje wysoką liczbą zderzeń z czułym materiałem detektorów śledzących. Czas martwy w pierwszej podwójnej warstwie detektora wierzchołkowego osiąga 100%, znacznie powyżej akceptowalnego poziomu 3%. Z powodu wysokiej gęstości niechcianych interakcji, rozważono różne metody zmniejszenia wpływu fotonów SR na detektor. Najlepszym rozwiązaniem jest zmniejszenie prawdopodobieństwa odbicia fotonu poprzez zwiększenie chropowatości ścian jonowodu. Całkowite usunięcie fotonów SR z akceptancji detektora jest możliwe gdy taka powierzchnia jest wykorzystana w ostatnich 30 m BDS.

Tło pochodzące z interakcji elektron–pozyton było symulowane przy użyciu Guinea-Pig wykorzystując wiązki elektronów i pozytonów które zostały przetransportowane przez BDS przy użyciu programu PLACET z uwzględnieniem efektów dynamiki nieliniowej. Interakcje cząstek tła z detektorem były symulowane w GEANT4. Czas martwy obliczony z gęstości zderzeń cząstek tła z detektorem wierzchołkowym osiągnął maksymalny akceptowalny poziom 3% w części detektora położonej najbliżej punktu interakcji dla energii 3 TeV. Czas martwy dla energii 380 GeV jest niższy niż dla energii 3 TeV, przynajmniej o czynnik równy trzy w detektorach śledzących. Wysokie czasy martwe, osiągające 100%, znalezione zostały w przednich częściach kalorymetru hadronowego (HCal) oraz systemu identyfikacji mionów (MuonID).

Mogą one zostać zredukowane przy wykorzystaniu kombinacji ekranowania kompozytową tarczą złożoną z warstw ołowiu i polietylenu, oraz zwiększeniu granularności detektorów. MuonID nie wymaga zwiększenia granularności, natomiast konieczne jest wykorzystanie dodatkowej tarczy w dodatku do tarczy ekranującej HCal. Wykorzystując powyższe metody, czas martwy w HCal i MuonID jest zmniejszony do akceptowalnego poziomu poniżej 10%.

tło wiązka-wiązka, impedancja jonowodu, promieniowanie synchrotronowe, zderzacz liniowy, CLIC

In dedication to my loving parents

Contents

Chapter 1

Introduction

The Standard Model (SM) of particle physics is one of the most successful theories developed in the 20th century. The theory describes the electroweak interactions that unify the weak and electromagnetic forces, the strong nuclear force, and classifies the elementary particles. The theoretical predictions have been tested over the decades using generations of particle accelerators, with precise parameters measurements done using the Large Electron–Positron Collider (LEP) at CERN between 1990 and 2000, leading to the conclusion that there are precisely three generations of leptons and quarks. Notable discoveries include the top quark in 1995 using the Tevatron at Fermilab, and the famous discovery of the Higgs boson announced in 2012, using the Large Hadron Collider at CERN.

There are many phenomena and issues that are not described in the framework of the SM, such as dark matter, neutrino oscillations, and the unification of the known forces. The particle physics theories going beyond the description given by the SM are called Beyond Standard Model (BSM) physics. Some of the answers to the outstanding questions about nature can be addressed by precise measurement of the SM parameters, for example, the interaction and production cross-sections, or top quark and Higgs boson masses, with a conviction that if discrepancies are found BSM models can explain them. The second approach is to reach to higher centre-of-mass energies that could lead to the production of currently unknown particles, such as supersymmetric partners of the known bosons and leptons. These two approaches can be pursued in the next generation of particle accelerators.

A future collider may accelerate either hadrons (protons, heavy-ions) or leptons (electrons, positrons, muons). A hadron collider has an advantage of the possibility of reaching high centre-of-mass energies in a circular machine that is not constrained by the emission of synchrotron radiation. However, the physics measurements suffer from high rates of background events, thus requiring complex triggering systems. A lepton collider, for example an electron–positron one, offers a significantly cleaner experimental environment, wherein principle the initial state after the collision can be precisely known, and gives access to processes that are not possible to measure in a hadron collider.

There are several possible layouts for the future collider, with the main distinction between a linear and circular accelerator. A circular electron–positron collider allows one to achieve high beam currents and high repetition rates in the order of kHz, where the beams can be continuously used over a period of time. This leads to high achievable event rates, which is favourable for physics studies. However, there is a significant limitation of the circular electron–positron accelerators coming from the emission of synchrotron radiation (SR). The total emitted SR power in the necessary bending magnets is proportional to the fourth power of the beam energy and inversely proportional to the bending radius. Therefore, for a given accelerator radius, the achievable centre-of-mass energy is limited to a few hundred GeV to limit the power loss, as it is the case for both the Future Circular Collider (FCC-ee) [1] and Circular Electron–Positron Collider (CEPC) [2]. The power loss also limits the average beam current, which is detrimental to the physics event rate. The intense SR emission made it impossible for LEP to increase the beam energy beyond 110 GeV and denied the LEP experiments the discovery of the Higgs boson, that was discovered years later in the LHC experiments with a mass of about 125 GeV [3, 4].

Linear accelerators, such as CLIC or International Linear Collider (ILC) [5], are mostly free from synchrotron radiation, and thus are the best choice for the high-energy (above about 200 GeV per beam) electron–positron colliders. There are some disadvantages of linear accelerators, such as the low collision frequency because the beams cannot be recirculated and are used only once. Ultra-relativistic beams with possibly large bunch charges in the order of at least 10^9 and nanometre transverse bunch sizes are required in a future linear collider to increase the event rates.

The Compact Linear Collider (CLIC) is a concept for a future linear electron–positron collider. CLIC is the only proposed project that allows exploration of both the precision frontier with precise measurements of the Standard Model processes and the energy frontier with the possibility to be extended into multi-TeV centre-of-mass energies.

From the time of the first-ever built linear electron–positron collider, the Stanford Linear Collider (SLC) in 1987, it became apparent that the intensity-related issues and beam-induced backgrounds cannot be neglected for such a machine. The two-mile accelerator that was repurposed for the SLC suffered from single-beam break-up, which significantly limited the maximal intensity of the beams [6]. This issue has been solved by the time of the SLC. However, numerous new challenges have arisen, ranging from betatron oscillations to the emission of hard synchrotron radiation during beam crossing and their impact on detector backgrounds [7]. The knowledge and experience gained with the SLC make the future linear electron–positron colliders more reliable and allow these future machines to achieve their maximal performance. The nanometre-sized beams and large beam intensities required for the luminosity performance at CLIC and the high collision energies make the intensity-related issues and beam-induced backgrounds more relevant than ever before.

Another issue to be addressed is the reflection of the synchrotron radiation (SR) photons in a linear machine. In a linear accelerator, the emission of the radiation is significantly smaller in comparison with storage rings due to the lack of strong bending magnets. However, there are strong quadrupole magnets, and weak bending magnets aiming to produce dispersion that is necessary for the chromatic aberration correction in sextupole magnets. Synchrotron radiation is produced in those magnets, and due to the almost perfectly straight layout of the machine and low grazing angles, the reflection probability is not negligible for the SR photon energies below 30 keV. The SR photons can travel long distances along the accelerator, and leave significant energy deposits in the detector region. Therefore, this work studies the power lost to the synchrotron radiation and its distribution in the detector region to ensure the safety and performance of the future machine.

The aperture of the beam pipe needs to be known to study the synchrotron radiation reflections. The very minimum beam pipe aperture needs to provide enough space for the transported beam, thus is in the order of the beam size multiplied by a safety factor. The other significant limitation comes from the beam stability concerns and considers the impact of the resistive wall wakefields. The impact of wakefields has been studied previously for the 500 GeV and 3 TeV CLIC Beam Delivery Systems [8]. The aperture design at 380 GeV taking into account the resistive wall wakefields has not been studied before and is addressed in this work, and the 3 TeV energy stage is revisited.

In principle, the initial state of an electron–positron collision can be known precisely due to the fundamental nature of the interacting particles. However, during a collision, electrons and positrons are strongly focused in the electromagnetic field of the oncoming beam and emit high-energy SR photons called beamstrahlung that reduce the collision energy. The reduction of the energy due to emission of radiation leads to particles colliding below the nominal centre-of-mass energy and gives rise to the luminosity spectrum.

The beamstrahlung photons can interact with each other, with the particles of the oncoming beam, or with the macroscopic field leading to the production of unwanted background particles. These beam-induced background particles impose constraints on the detector design. The large energy carried by the beamstrahlung photons and coherent pairs needs to be safely removed from the detector. The background particles that are impinging on the tracking detectors can lead to high hit rates and thus lower the performance of the reconstruction and tracking algorithms. The hit densities caused by them in the vertex and tracker give the limit on the minimal radius of the vertex detector, and the maximal sensor cell size, driving the requirements for the silicon sensors R&D programme.

In the case where high occupancies are found in one of the subdetectors, mitigation methods based on changing the inner radius, granularity or introducing shielding can be proposed to be implemented for the best performance of the future experiment.

The conceptual design reports (CDR) of the CLIC accelerator [9], of the two detectors – CLIC_ILD [10] and CLIC_SiD [11] – and of the physics programme and reach [12] were published in 2012. Since then, a number of studies on the accelerator and detector have been performed. The staging scenario has been modified, with the first stage now at 380 GeV instead of 500 GeV, including a short run at 350 GeV [13]. The detector development has been focused on a single detector model, leading to the CLIC detector (CLICdet) model published in 2017 [14]. The new detector model takes into account the removal of the last quadrupole of the Final Focus System (FFS) from the detector region. This change has lead to a redesign of the forward detector region and impacts also the Beam Delivery System (BDS) at both 380 GeV and 3 TeV.

Due to the significant changes since the CDR, their impact on the performance of the BDS and the new detector is assessed in this study. In addition, the 380 GeV energy stage backgrounds have not been studied before. Precise estimates of the luminosity, beam-induced backgrounds and the beam quality are required for the optimal design of this energy stage, as well as a crucial input for the physics studies.

In Chapter 2, the general introduction to the landscape of the future colliders and the advantages of a linear electron–positron collider are discussed. The CLIC project with its physics programme, the planned accelerator complex and the detector model are described.

In Chapter 3, the simulation software and its application are described. The definitions of a hit and occupancy calculation in tracking detectors and calorimeters are described.

The phenomena taking place during an electron–positron collision, including the processes that lead to the production of the background particles are described in Chapter 4. In addition, the backgrounds and their possible impact in the CLIC detector at two energy stages: 380 GeV and 3 TeV are discussed. The luminosity spectra of four initial states: e^+e^-, $e^+\gamma$, $e^-\gamma$ and $\gamma\gamma$ are given.

In Chapter 5 of this thesis, the Beam Delivery System apertures for the 380 GeV and 3 TeV energy stages are optimised. The calculation takes into account the limitations of the maximal magnet strength and the stability of the beams disturbed by the resistive wall wakefields, as well as the luminosity performance.

In Chapter 6, the study of the synchrotron radiation impact on the CLIC Final Focus System and detector are presented. The basic properties of the radiation and the probability of reflection are given. The impact of the SR both in the BDS and the detector region is discussed, as well as the mitigation methods.

Chapter 7 considers the impact of the background particles produced in the electron–positron collision on the CLIC detector model using full detector simulations in GEANT4. The tracking detectors, electromagnetic and hadronic calorimeters, and the muon identification system are studied.

In Chapter 8, modifications of the geometry of the CLIC detector are described. The changes aim to mitigate the impact of the unwanted particles on the detector performance. Particular focus is given to the HCal endcap optimisation.

Chapter 9 contains a summary of the presented results and suggestions for future studies.

Chapter 2

Compact Linear Collider

The Compact Linear Collider is a concept for a future multi-TeV linear electron–positron collider currently developed by the CLIC collaboration at CERN. This chapter gives a short overview of the CLIC project, including the physics programme and the accelerator. An introduction to the future energy-frontier particle colliders currently being considered is given in section 2.1 The general parameters and physics potential of the CLIC project with precise top-quark and Higgs boson measurements are described in section 2.2. The information regarding the CLIC accelerator complex, including the novel accelerating scheme to be adopted in the Main Linac is provided along with a description of the Beam Delivery System in section 2.3. A description of the CLIC detector concept is given in section 2.4.

2.1 Future particle colliders

There are several large-scale future colliders currently considered by the physics community that have different accelerator geometries and collided particle types. A decision needs to be made whether to pursue the energy frontier with a high centre-of-mass energy hadron collider, or the precision frontier with an electron–positron collider. A geometry of the future electron–positron collider, whether it is going to be a circular or a linear machine also needs to be established.

A lepton collider provides more favourable experimental conditions with lower background levels than are present at hadron colliders. The initial state of the collision of the point-like particles can in principle be precisely known, in comparison to the uncertain initial state of collisions of composite particles, such as protons or heavy-ions. The event rates in proton-proton collisions are very high, too large to store and analyse all events taking place in collisions. The total cross-section for proton-proton collision is orders of magnitude above any other process, for example W-boson production, as can be observed in Figure 2.1. Therefore, hadron colliders require advanced and sophisticated triggering systems to be able to record and measure the interesting physics processes. The total cross-section for an electron–positron collision, shown in Figure 2.2, is smaller than in proton-proton collisions, and the event rates are also significantly lower. There is no need for a triggering system in a linear electron–positron collider, and all events can be measured and recorded. In addition, lepton colliders have access to processes that cannot be measured at a hadron machine, such as a direct and model independent

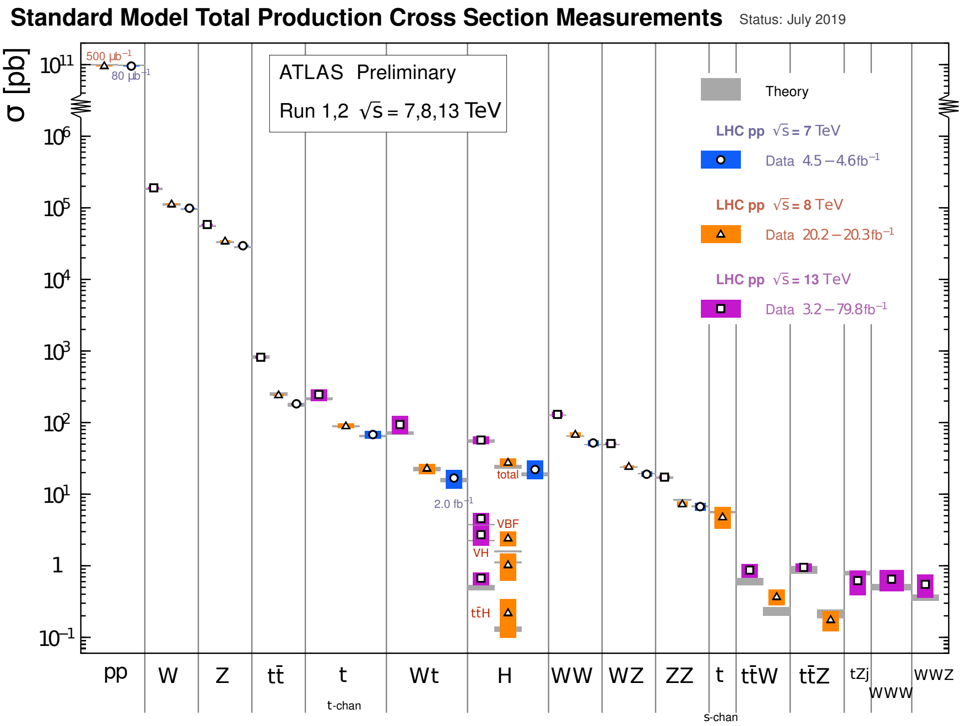

Figure 2.1: Standard Model total production cross-section measurements, corrected for branching fractions, compared to the corresponding theoretical expectations from proton-proton collisions at $\sqrt{s} = 7,\ 8,\ 13$ TeV measured by ATLAS [16].

measurement of the Higgs boson coupling to the Z boson, obtained from the recoil mass distribution [15].

In the case of a circular lepton collider, for example Future Circular Collider (FCC-ee) [18] or the Circular Electron–Positron Collider (CEPC) [2], one of the limiting factors is the emission of synchrotron radiation (SR). The energy loss per turn due to SR scales with the fourth power of the particle energy and is inversely proportional to the particle mass and the bending radius of the trajectory: $U_0 \propto \frac{E^4}{m^4 \rho}$. For example, electrons and positrons in the planned FCC-ee, with a beam energy of 182.5 GeV and bending radius of 10.8 km lose 9.2 GeV per turn to SR, a substantial fraction of their energy. This energy needs to be replenished by the RF system. The FCC-ee accelerator design assumes an acceptable amount of power that is lost to SR at the level of 100 MW per beam. This assumption drives the other accelerator parameters, such as the average current. As a result of rapidly increasing intensity of the SR emission with increasing beam energy, the beam current needs to be proportionally decreased, that leads to a decrease of luminosity. [18]. In comparison, protons circulating in the Large Hadron Collider (LHC) with a beam energy of 7 TeV and a bending radius of 2.8 km lose on average 10 keV per turn to SR. CLIC or ILC [5], as linear accelerators, are mostly free from synchrotron radiation. The limitations of linear accelerators are linked to the length required by the Main Linac to achieve the desired centre-of-mass energy and the power consumption, rather than the emission of SR.

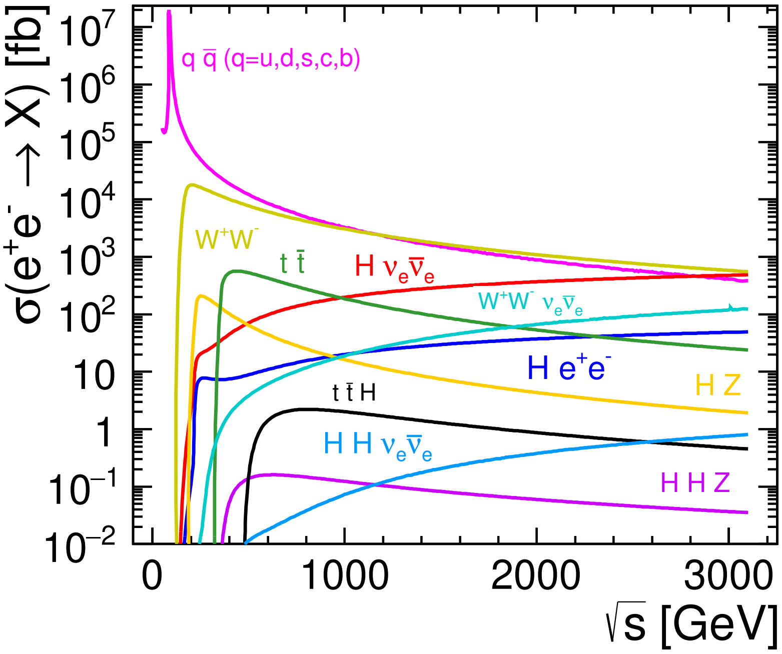

Figure 2.2: Leading-order cross-sections for Standard Model processes in electron–positron collisions at CLIC energies [17].

2.2 CLIC overview

The CLIC accelerator and physics programme is planned to be undertaken in three sequential energy stages: the first at the centre-of-mass energy of 380 GeV, the second at 1.5 TeV, and the third at 3 TeV. The staged approach allows for an optimised utilisation of the potential for the physics programme and flexibility of the design in the case of discoveries at the LHC. Each energy stage is foreseen to take seven or eight years, with two-year separations between the stages needed for the assembly of components and commissioning. The total time span of the CLIC programme is thus in the range of 25–30 years [19]. The main parameters of CLIC at all energy stages are summarised in Table 2.1. The current parameters are a result of an optimisation of the cost, luminosity and its quality required by the physics programme [13]. The 1.5 TeV and 3 TeV stages are used as a benchmark and can be modified to fit best the needs of the future physics programme, for example, if a new particle is discovered [9, 19]. If a particle is discovered at LHC or CLIC, CLIC has the ability to measure its mass and couplings at the per cent level or better [12, 19].

The CLIC beams are accelerated in normal-conducting copper RF cavities operating at a frequency of 12 GHz and with a gradient of 72 MV/m at 380 GeV and 100 MV/m for higher energy stages. These accelerating gradients are larger than what is possible to achieve with superconducting RF cavities, where state-of-the-art cavities designed for the ILC reach the gradients of about 35 MV/m [20]. The frequency and gradient choices are a result of the cost-optimisation process [21]. CLIC employs a novel approach to the power generation for its accelerating cavities, called two-beam acceleration. In this scheme, a second beam, called drive beam, is decelerated in Power Extraction and Transfer Structure (PETS) and the RF power is fed to the accelerating cavities of the main beam. This approach to the powering of accelerating cavities is significantly more efficient in comparison with the industry standard of using klystrons, as there are no klystrons available that work at 12 GHz, thus lossy signal compression would need to be used [21].

The first energy stage requires a 11.4 km long main tunnel and a single drive-beam complex [19]. The physics programme at 380 GeV focuses on precise measurements of the Standard Model Higgs boson and top quark physics. CLIC also has a direct and indirect sensitivity to BSM processes at this energy stage. A short run at 350 GeV around the top quark pair production threshold dedicated to the measurement of top quark mass is foreseen, where a mass measurement with a precision as low as 50 MeV is possible [22]. At this energy stage, the dominant Higgs boson production mechanism is the Higgsstrahlung process. The analysis of the Higgsstrahlung events enables a model-independent measurement of the total production cross-section and Higgs branching ratios and width. The second most relevant production mechanism is WW-fusion, which improves the precision of the Higgs boson width and couplings measurement when analysed together with Higgsstrahlung. The initial CLIC energy stage provides measurements that are in many cases more precise than in the High Luminosity LHC [19].

The second energy stage at 1.5 TeV requires a tunnel of 29 km and is the maximal energy stage that can be accelerated using a single drive-beam complex. While the centre-of-mass energy increases by a factor of four, the main linac length is increased only by a factor of three due to the use of accelerating cavities with a higher gradient of 100 MV/m alongside the 72 MV/m reused from the first stage. The 1.5 TeV energy stage differentiates CLIC from the other proposed future electron–positron colliders as it is the only machine that can reach such high centre-of-mass energies.

The physics programme at 1.5 TeV opens the energy frontier and allows for wider searches for Beyond Standard Model (BSM) phenomena. At this energy stage, the programme aims to improve the insight into the top quark and Higgs boson properties, such as Higgs self-coupling and rare decays potentially leading to the discovery of the new physics processes [17]. The double Higgsstrahlung process $\mathrm{e}^+\mathrm{e}^- \to \mathrm{ZHH}$ can be observeds with a $5\,\sigma$ significance. The top Yukawa coupling can be extracted with a statistical precision of less than 3% [22].

The third energy stage at 3 TeV requires a 50.4 km long main linac tunnel and a second drive-beam complex. The physics programme continues precision top quark and Higgs boson measurements, with the inclusion of vector-boson fusion processes. Searches are possible for new BSM phenomena, new electro-weak particles and dark matter candidates. The kinematic limit of the direct discovery of new particles is about: $mc^2 \approx 1.5\,\mathrm{TeV}$ for particles produced in pairs, yet indirect discoveries are possible up to tens of TeV [17].

Table 2.1: CLIC parameters at the major energy stages including with the two parameter options of the top-quark mass measurement treshold scan at 350 GeV [9, 21].

Parameter	Symbol	Units	$\sqrt{s} = 350\,\text{GeV}$		$\sqrt{s} = 380\,\text{GeV}$	$\sqrt{s} = 1.5\,\text{TeV}$	$\sqrt{s} = 3\,\text{TeV}$
			Option 1	Option 2			
Repetition rate	f_{rep}	Hz	50	50	50	50	50
Number of bunches per train	n_{b}		352	352	352	312	312
Number of particles per bunch	N		$5.2 \cdot 10^9$	$4.68 \cdot 10^9$	$5.2 \cdot 10^9$	$3.7 \cdot 10^9$	$3.7 \cdot 10^9$
Bunch separation	Δt	ns	0.5	0.5	0.5	0.5	0.5
Transverse beam size (IP)	σ_x/σ_y	nm	149/2.9	149/2.9	149/2.9	60/1.5	40/1
Bunch length	σ_z	µm	70	77	70	44	44
Normalised emittance (end of linac)	$\varepsilon_x/\varepsilon_y$	nm	900/20	900/20	900/20	660/20	660/20
Distance of the last quadrupole	L^*	m	6	6	6	6	6
Total luminosity	$\mathcal{L}$	$10^{34}\text{cm}^{-2}\text{s}^{-1}$	1.47	1.12	1.5	3.7	5.9
Luminosity above 99% of $\sqrt{s}$	$\mathcal{L}_{0.01}$	$10^{34}\text{cm}^{-2}\text{s}^{-1}$	0.9	0.75	0.9	1.4	2.0
Energy spread	$\Delta E/E$	%	0.21	0.31	0.35	0.35	0.35
Crossing angle (IP)	θ_{c}	mrad	16.5	16.5	16.5	20	20

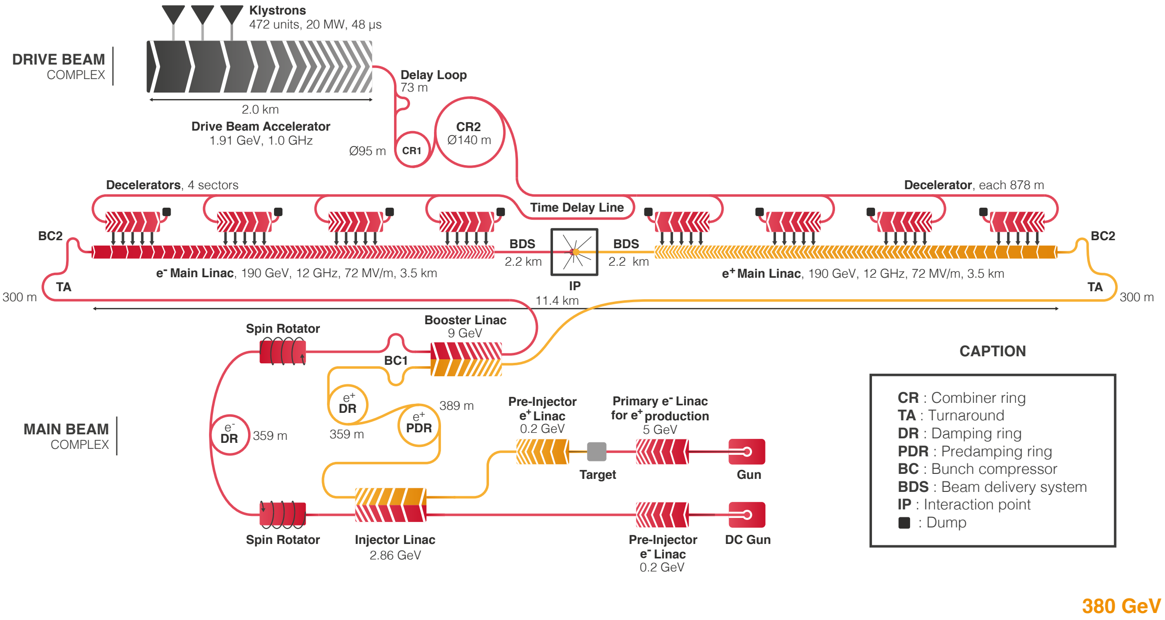

Figure 2.3: Layout of the CLIC accelerator complex at 380 GeV. At 1.5 TeV, the layout is similar, albeit with a longer Main Linac with a total length of 22.8 km and 13 decelerator sectors [13, 23].

2.3 CLIC accelerator

The layout of the CLIC accelerator complex is shown in Figure 2.3 for 380 GeV and 1.5 TeV and in Figure 2.4 for 3 TeV. The addition of the second drive beam complex is necessary to reach beam energies above 750 GeV [21].

The main electron beam is produced polarised in a DC gun and pre-accelerated to 200 MeV. A separately created electron beam accelerated to 5 GeV is collided with a tungsten hybrid target to create the positrons that are captured and pre-accelerated to 200 MeV. Both beams are accelerated to 2.86 GeV in a common injector linac. The electron beam is sent to a Damping Ring (DR) to reduce the emittance through synchrotron radiation emission in superconducting wigglers. The positron beam has a significantly worse initial emittance due to the production mechanism, thus an extra Pre-Damping Ring (PDR) is required to lower the emittance before the beam is injected into the DR [9, 21].

From the DR to the Main Linac (ML), the beams are accelerated to 9 GeV in the Booster Linac, and their length is compressed in the Ring to Main Linac transfer line. The Main Linac accelerates the beams to the nominal energy. Finally, the Beam Delivery System (BDS) collimates the beams and focuses them to nanometre transverse sizes at the Interaction Point (IP).

2.3.1 Main Linac

There are two Main Linacs in the CLIC accelerator complex. One is accelerating the electron beam and the other the positron beam from 9 GeV to the nominal energy at each energy stage.

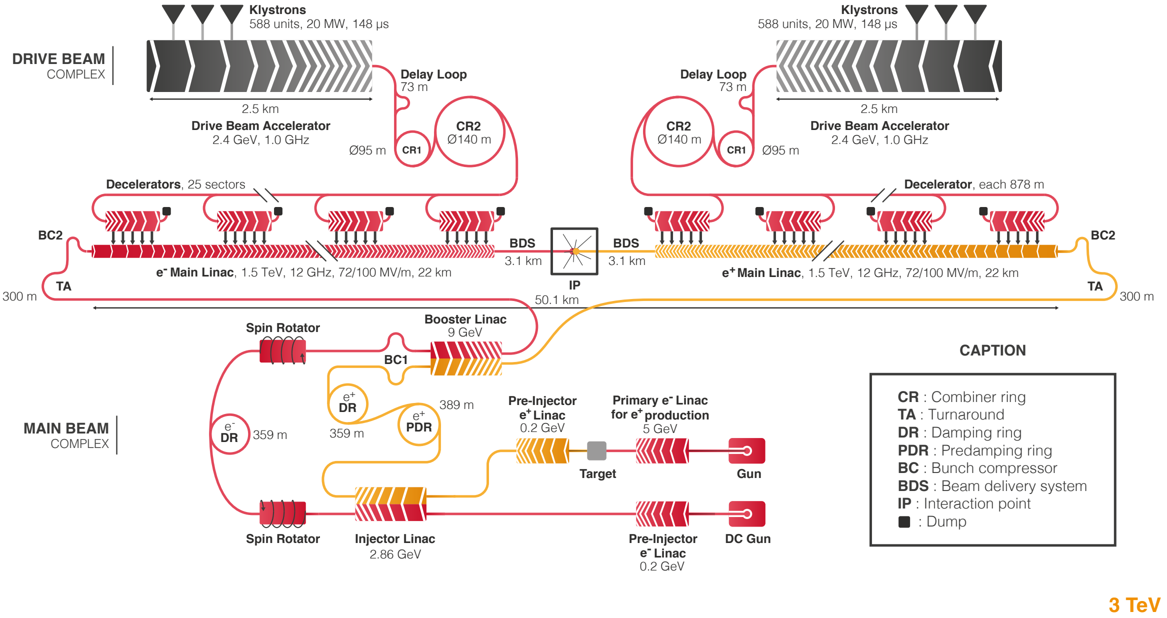

Figure 2.4: Layout of the CLIC accelerator complex at 3 TeV [13, 23]. The main difference in comparison with the layout at lower energy stages (Figure 2.3) is an additional Drive Beam complex.

The accelerating normal-conducting RF cavities operate at a frequency of 12 GHz and have a maximal accelerating gradient of 100 MV/m, with a lower gradient of 72 MV/m foreseen to be used at the initial energy stage. The design of the linacs is identical for both the electron and positron line. The length of each linac ranges from 3.5 km at the 380 GeV energy stage to 22 km at 3 TeV. The tunnel is laser-straight over the entire length. An accelerator that follows the curvature of the Earth would make preserving of the emittance more challenging [24]. The ML is the longest component of the accelerator complex as well as the primary cost driver [9, 21].

The CLIC main linacs can efficiently accelerate the beams to the desired energy due to the use of the two-beam acceleration scheme. The use of klystrons, especially at the energy stage above 380 GeV, would be unfeasible in terms of cost and maintenance. [9]. A low-energy high-intensity beam provides power to the RF cavities accelerating the low-intensity high-energy main beam. The drive beam is decelerated in Power Extraction and Transfer Structures (PETSs) and the extracted energy is transported using waveguides to power the main cavities. A visualisation of the two-beam module is shown in Figure 2.5. The feasibility of the two-beam acceleration concept was confirmed experimentally in the CLIC Test Facility (CTF3) [25].

The main challenge of the ML is the preservation of ultra-low transverse emittances, which is achieved by high-precision pre-alignment, stabilisation against dynamic imperfections, and a beam-based feedback system.

The transverse wakefields present in the ML can distort bunches leading to single-bunch break-up instability [9]. If the wakefields are not mitigated, the amplitude of the oscillations

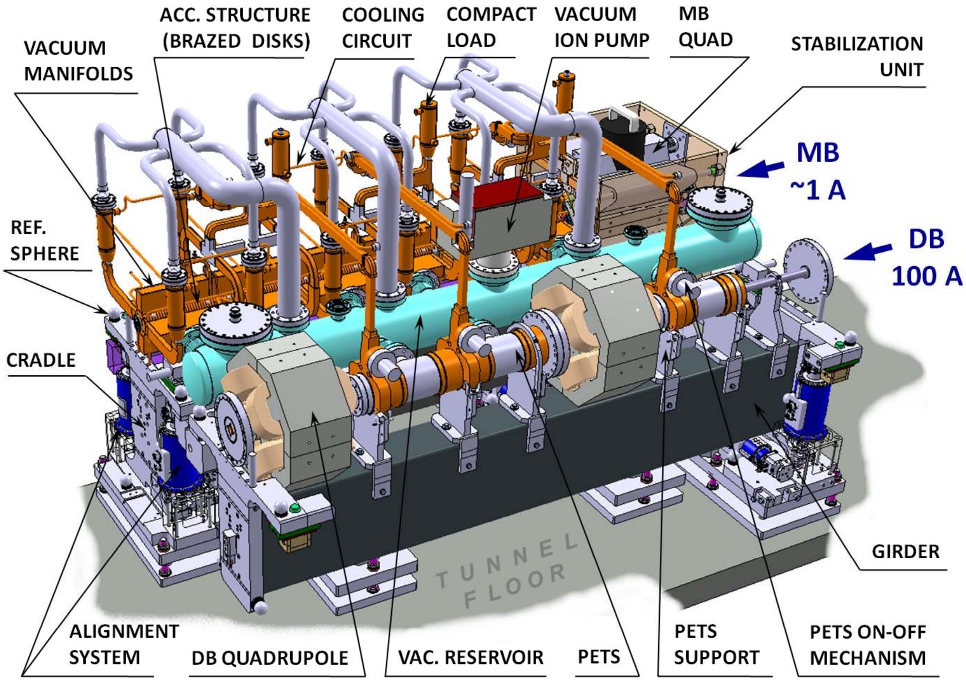

Figure 2.5: A visualisation of the CLIC two-beam accelerating system with the drive beam line and the Power Extraction and Transfer Structure in the front and the main beam line and accelerating cavities behind [9].

in the bunch tail increases to arbitrarily large value. Then, the bunch is lost and the luminosity decreases. This instability can be prevented by the use of Balakin, Novokhatsky, and Smirnov (BNS) damping [26], where a correlation between the energy of particles and their position in a bunch is required. The energy has to be higher in the bunch head than in the tail to ensure the damping. Such a distribution of energy can be achieved with short-range longitudinal wakefields.

The introduction of the position-dependent energy requires the beams to be accelerated with different RF phases Φ_1[1] along the ML. At the beginning of the ML, the beams are accelerated with a small RF phase, which results in a substantial energy spread due to low suppression of the longitudinal wake. In the final part of the linac, the RF phase is increased to limit the energy spread. The length of the region with a higher Φ_1 is optimised for the desired energy spread. For example, in the low-energy spread option of acceleration to a centre-of-mass energy of 350 GeV, three-fourths of the linac accelerate the beams close to the crest with $\Phi_1 = 6^\circ$, and in the final one-fourth the phase is increased to 30° that results in an RMS energy spread of 0.21% [27]. The baseline energy spread for CLIC is 0.35% RMS at 380 GeV and 3 TeV, although options exist to lower this number to 0.21% for the short run at 350 GeV. There, longer bunches and a lower bunch charge, as well as an optimised RF phase acceleration scheme, are needed to achieve the low energy spread.

---

[1] $\Phi_1 = 0^\circ$ provides maximal acceleration.

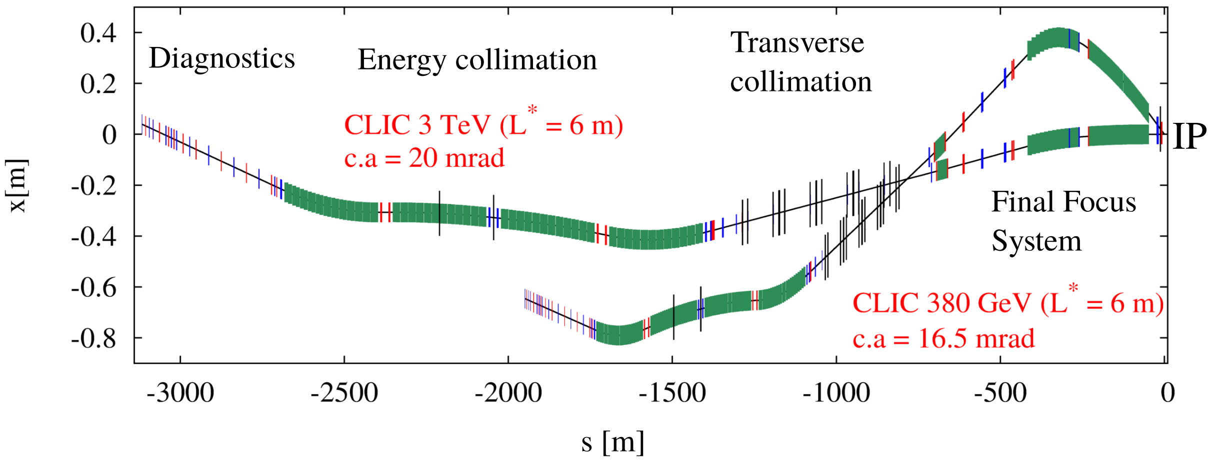

Figure 2.6: Layout of the CLIC Beam Delivery System at 380 GeV and 3 TeV [21].

2.3.2 Beam Delivery System

The CLIC Beam Delivery System transports the electron and positron beams from the end of the Main Linac to the Interaction Point. The BDS can be split into four sections, each performing a different function to achieve the CLIC luminosity goal while ensuring the safety of the machine and the detector. The layout of the BDS and the position of each section are shown in Figure 2.6. There is a significant difference in length between the energy stages, with 2200 m (including drifts) at 380 GeV and 3100 m at 3 TeV [9, 21]. The difference is due to more challenging beam conditions in the energy collimation section at the higher energy.

The experimental tests of the accelerator physics challenges relevant to the CLIC BDS were performed in the Accelerator Test Facility (ATF2) at KEK [28]. ATF2 is a scaled-down model of a Final Focus System of a linear electron–positron collider. There are three main issues linked with collisions of nanometre-sized beams studied at ATF2, namely the creation and the preservation of the ultra-low emittances, and the focusing of the beams to nanometre sizes at the IP. The two main goals are obtaining beam sizes of 37 nm and controlling the beam position with nanometre precision using intra-train beam feedback. The beam sizes of 41 nm have been achieved [29]. The beam stabilisation of the vertical beam position was achieved at the level of 67 nm using a local IP feedback system [30].

The first part of the BDS performs beam diagnostics, where the properties of the beams are measured and corrected if necessary. The beam emittance, energy, and polarisation are measured. The emittance diagnostic section consists of laser wires capable of measuring the transverse beam sizes with 1% resolution. The wire scanners with a 45 ° betatron separation allow a complete two-dimensional scan of the beam phase space and the determination of the emittances. The energy measurement is designed to provide energy resolution better than 0.04% [9].

The next section is the energy collimation. This section protects the systems located downstream from mis-steered beams or beams with incorrect energy. The most common source of incorrect energy is a failure of one of the accelerating elements in the ML. A beam with an energy error above 1.3% needs to be intercepted in the collimators. The collimation is designed as a spoiler-absorber system, where the spoiler increases the angular divergence of the errant beam. As a result, the transverse beam size is increased, which reduces the risk of damaging the absorber by reducing the energy density. The energy spoiler is optimised to survive the impact of the full bunch train at the 3 TeV [9].

The transverse betatron collimators are placed downstream from the energy collimators. The goal of the transverse collimators is to remove the beam halo to ensure the safety of the machine and the detector region. The halo particles can be lost in the final several hundred meters of the BDS or emit synchrotron radiation in the final doublet quadrupole magnets at large transverse position and with polar angles sufficient for these SR photons to interact with the sensitive material of the detector. The depth of the transverse collimation (the collimation depth) is therefore optimised to remove the particles that could lead to the effects described above.

The last section of the BDS directly leading to the IP is the 770 m long Final Focus System (FFS). The main goal of the FFS is to deliver to the IP nanometre-sized beams free from high-order aberrations needed for the high luminosity performance. The design of the system is concentrated on cancelling the chromaticity created by two strong quadrupole magnets located directly upstream from the IP, labelled QF1 and QD0. The chromatic effects, if unmitigated, lead to significant growth of the transverse beam sizes and subsequently to luminosity loss. The local chromaticity correction scheme is employed, with sextupoles located next to the final doublet quadrupoles, where the chromaticity is produced. The dispersion needed by the sextupole magnets to cancel the chromaticity is created upstream by bending magnets. The dispersion at the IP is kept at zero [9]. Otherwise, the dispersion effect would also contribute to increasing the transverse beam sizes and luminosity performance loss.

The crossing angle between the opposing beamlines at the IP is 16.5 mrad at 380 GeV and 20 mrad at 3 TeV [9, 21]. The difference is due to the necessity of keeping the BDS aligned with the axis of the Main Linac at all energy stages. Collisions at such crossing angles would lead to significant luminosity losses [31], and therefore need to be counteracted by the use of crab cavities [32]. Crab cavities rotate the bunches before the collision by providing a longitudinal position-dependent kick which does not impact the centre of the bunch.

After the collision, the beams are extracted from the detector region in the post-collision line, and are transported, along with the beam-induced backgrounds, to the beam dumps.

2.4 Detector model

Following the Conceptual Design Report (CDR) [12], a number of studies have been completed to optimise the performance of the CLIC detectors. The result was a change in the paradigm from using two detectors: CLIC_ILD [10] and CLIC_SiD [11] to a single detector model, CLICdet [14]. The benefits include budget savings and the possibility to use the full available integrated luminosity, rather than splitting it between two separate detectors. The additional gain can be achieved in the utilisation of the running time, as the time necessary to move the detectors in position can be used to collect data [14].

The main change in comparison with the CLIC_SiD and CLIC_ILD detector models is the consequence of the removal of the QD0 magnet from the detector region. The distance between

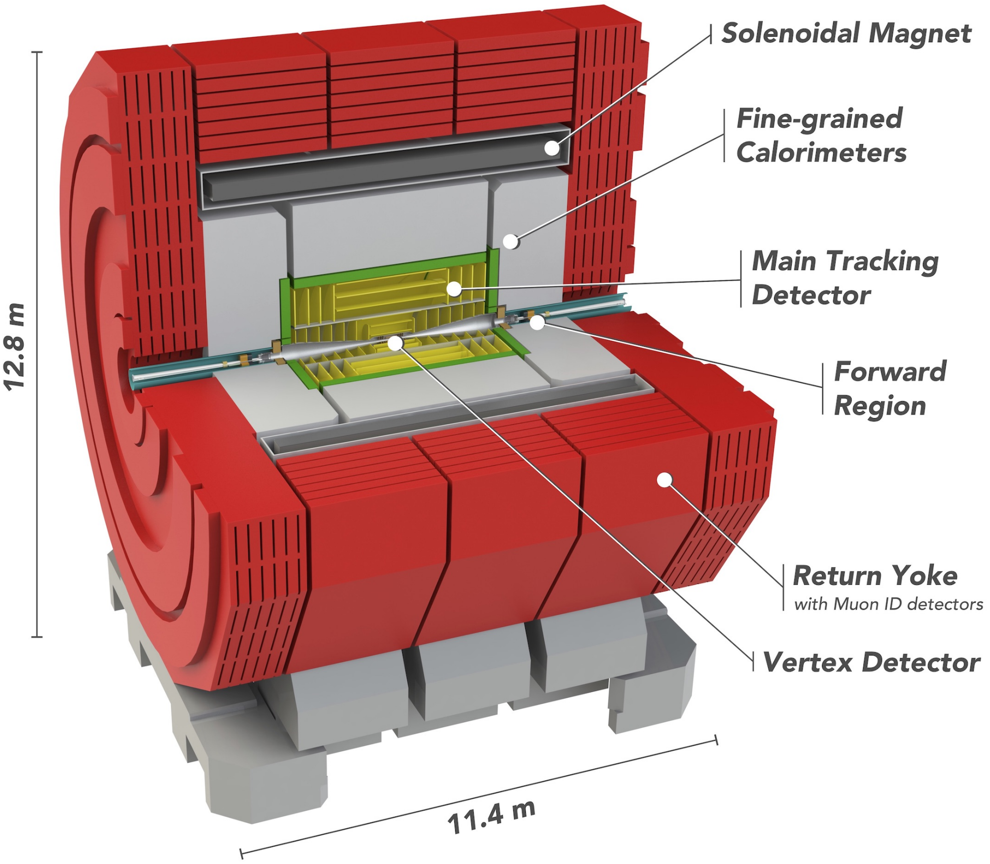

Figure 2.7: Layout of the CLIC detector with major systems and subdetectors.

the final quadrupole and the IP, L^*, was changed from 3.5 m to 6 m at 3 TeV and from 4.3 m to 6 m at 380 GeV. The removal of the QD0 also included the support tube and the anti-solenoid magnet from the forward detector region. The change provided additional space that was used to extend the hadronic calorimeter endcap and muon identification system endcap angular coverage towards lower polar angles.

The layout of the CLICdet model is shown in Figure 2.7 and the overall dimensions and parameters are summarised in Table 2.2. The layout of the CLIC detector follows the typical multi-purpose high-energy physics collider detector design, similar to the Compact Muon Solenoid (CMS) detector [33] at the LHC. The design of the detector is optimised for high precision measurements using Particle Flow Algorithm (PFA) reconstruction. The PFA approach combines information from high-precision silicon trackers with energy measurement in high-granularity calorimeters for optimal jet reconstruction [34].

The innermost subdetector is a vertex detector surrounding a beryllium beam pipe. The layout of the vertex detector is presented in Figure 2.8, and its position in the tracker in Figure 2.9. The subdetector consists of a cylindrical barrel, split into three double layers with the cylinder radii between 32 mm and 60 mm and a half-length of 130 mm. On each side of the barrel, there are three double-layered disks of the endcap each made of eight petals. The petals are located at a 5.5 mm longitudinal distance from each other, and the overlap between the petals in the

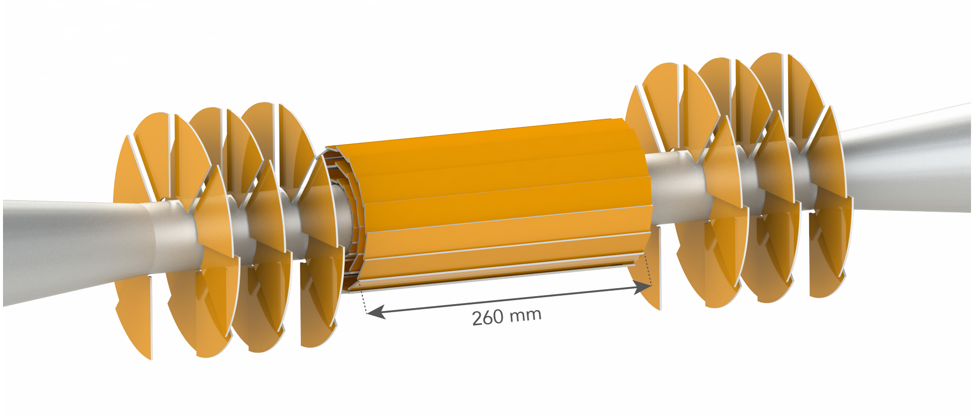

Figure 2.8: Layout of the Vertex detector.

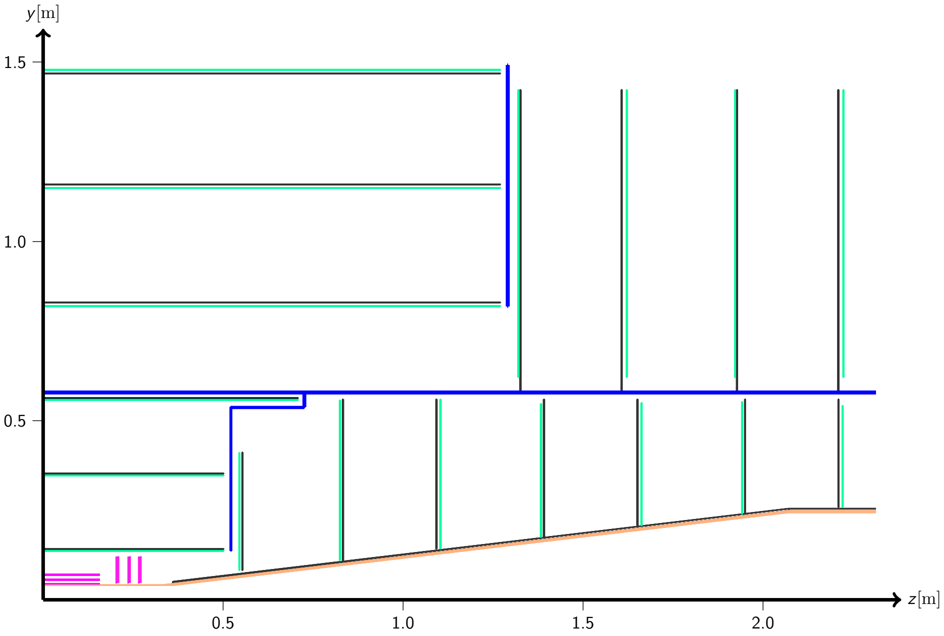

Figure 2.9: A cross-section view of the tracker implemented in the CLICdet simulation model. The black lines signify the tracker support structures, including cooling and cables, the green lines represent the tracker sensor layers. The blue lines show the main support tube and the interlink structures, the orange one indicates the vacuum chamber wall. The vertex detector layers are shown in the centre as red lines. Cables going outwards from the vertex detector are represented in magenta [14].

$r\phi$ direction is 2 mm. The layout of the vertex endcap disks with overlapping petals is shown in Figure 2.10(left). The result is a spiral-like shape necessary for air cooling. The vertex detector is a silicon detector with a sensor pitch of $25 \times 25\,\mu\text{m}^2$ and a sensitive material thickness of 50 µm.

Outside of the vertex is a silicon-sensor tracker. The layout of the tracker and positions of the layers and disks are shown in Figure 2.9. The radius of the tracker is 1.5 m and the half-length is 2.2 m. The tracker provides a full azimuthal coverage and a polar angle acceptance down to 8°. The coverage is limited by the conical beam pipe, as visible in Figure 2.9. The main support tube, located between the radial position of 0.575 m and 0.6 m, splits the tracker into

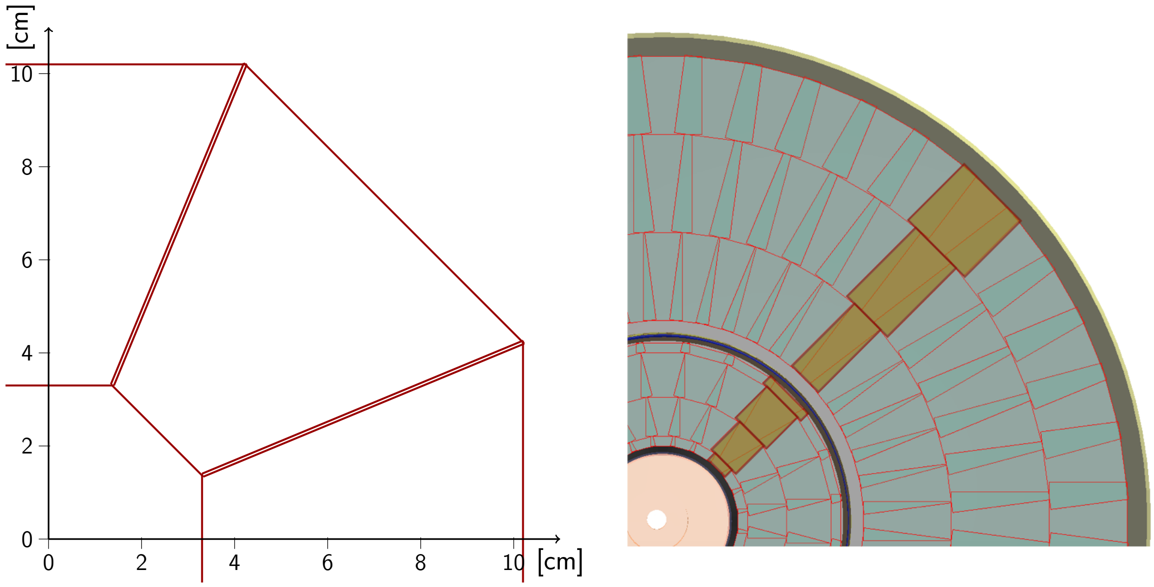

Figure 2.10: Schematic XY-plane view of the Vertex endcap disks with petals overlapping by 2 mm (left) and XY-plane view of the implementation of the tracker disk in the CLICdet simulation model (right). The darker rectangular elements are the tracker sensor pads, and the overlap between the sensor petals in the tracker is visible as wedges [14].

two regions: Inner Tracker and Outer Tracker. There are three layers in both the Inner (ITB 1-3) and Outer (OTB 1-3) tracker barrel. An overlap of 2 mm in the $r\phi$ direction between sensors in each layer is foreseen [14]. The tracker barrel is enclosed with endcap disks. There are seven disks in the Inner Tracker (ITD 1-7) endcap, and four in the Outer Tracker (OTD 1-4). A considerable ovelap between sensors is foreseen in all tracker disks, as shown in Figure 2.10(right).

Two granularity options are considered for the tracker, and the parameters are summarised in Table 2.3. The first disk of the Inner Tracker uses the same pixel pitch as the vertex detector. In the 'pixel sensor' option the sensor pitch is $30 \times 300\,\mu\text{m}^2$, based on the CLICTD sensor design [35]. In the 'strixel' option, the sensitive material is split into elongated pixels, or 'strixels', with one dimension significantly larger than the other and increasing in the layers located further away from the IP.

Two calorimeters are surrounding the tracking detectors: electromagnetic (ECal) and hadronic (HCal), have a dodecagon symmetry. The calorimeter endcaps aim to provide maximum coverage in the transition region between the calorimeter barrel and endcaps and down to small polar angles. The polar angles are limited by the conical beampipe and Forward Calorimeters. Together with the tracker, calorimeters provide the jet reconstruction with a 3.5-5% energy resolution using Pandora PFA [36].

The ECal is a highly granular silicon-tungsten calorimeter. The detector is split into forty layers in both the barrel and endcaps. Each layer consists of 1.9 mm of tungsten and 500 μm of silicon sensitive material, resulting in the radiation length of 22 X_0. The sensitive material is segmented into $5 \times 5\,\text{mm}^2$ cells.

The HCal is a steel-scintillator calorimeter, split into sixty layers in both the barrel and endcaps. Each layer consists of 19 mm stainless steel absorber, 3 mm of plastic scintillator, and 2.7 mm of air, adding to a total of 6.5 λ_I. The scintillator and read-out electronics are placed

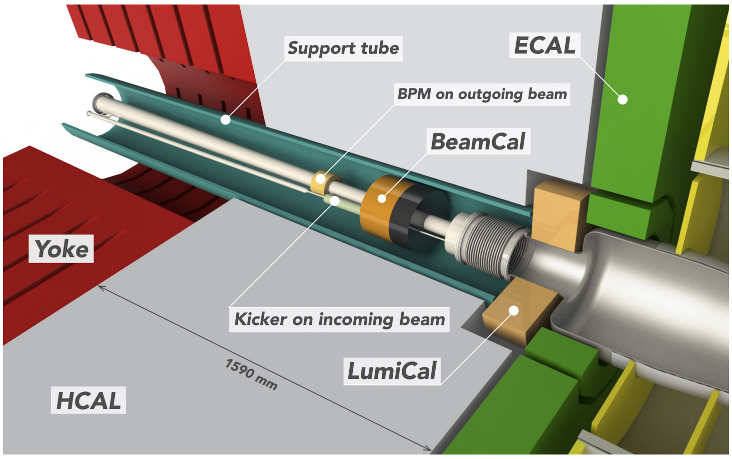

Figure 2.11: Layout of the CLICdet forward region [35].

in cassettes with a cell size of $30 \times 30\,\mathrm{mm}^2$. Analogue readout with Silicon Photo-Multipliers is envisaged. The inner radius of the HCal endcap in the CLICdet model has been reduced to 250 mm following the removal of the QD0 to increase the angular acceptance.

A superconducting solenoid magnet surrounds the HCal barrel. The solenoid provides a field of 4 T in the centre of the detector. The magnet is encompassed by an iron return yoke to close the magnetic flux.

The Muon Identification System (MuonID) is located in the return yoke. The MuonID is made of six layers in the endcaps and seven in the barrel, where the first layer close to the solenoid magnet can be used to reduce the energy leakage from the HCal barrel. Each layer consists of resistive plate chamber (RPC) sensitive elements interleaved with iron. The RPCs are split into $30 \times 30\,\mathrm{mm}^2$ cells [14].

The layout of the forward detector region is shown in Figure 2.11. There are two electromagnetic calorimeters in the forward region: the Luminosity Calorimeter (LumiCal) and the Beam Calorimeter (BeamCal). Both calorimeters are split into forty layers, each with a 3.5 mm tungsten absorber. The LumiCal covers a polar angle range from 39 mrad to 134 mrad. The sensitive element is 300 μm thick silicon. The LumiCal is optimised for high-precision luminosity measurement using Bhabha events. The BeamCal extends the angular acceptance of the detector down to 10 mrad. Since the BeamCal is closer to the beamline and receives high-doses of ionising radiation from the background particles, the sensor needs to be radiation-resistant, although in the CLICdet simulation model silicon is temporarily used as the sensitive material [14].

Table 2.2: CLICdet model main parameters. The r_{min} and r_{max} values are given for a circle inscribed in a dodecagon [36].

Parameter	Units	CLICdet
Vertex inner radius	mm	31
Vertex outer radius	mm	60
Vertex barrel half length	mm	130
Tracker inner radius	mm	127
Tracker outer radius	mm	1486
Tracker barrel half length	mm	2200
Tracker sensitive material		Silicon
ECal absorber		W
ECal X_0		22
ECal sensitive material		Silicon
ECal barrel r_{min}	mm	1500
ECal barrel r_{max}	mm	1702
ECal endcap r_{min}	mm	260
ECal endcap r_{max}	mm	1700
ECal endcap z_{min}	mm	2310
ECal endcap Δz	mm	202
HCal absorber		Fe
HCal λ_{I}		7.5
HCal sensitive material		Scintillator
HCal barrel r_{min}	mm	1740
HCal barrel r_{max}	mm	3330
HCal barrel z_{max}	mm	4129
HCal endcap r_{min}	mm	250
HCal endcap r_{max}	mm	3246
HCal endcap z_{min}	mm	2539
HCal endcap Δz	mm	1590
Solenoid field	T	4
Solenoid bore radius	mm	3500
Solenoid half length	mm	4150
Overall height	m	12.9
Overall length	m	11.4
Overall weight	t	8100

Table 2.3: CLIC vertex and tracker sensor pitch, with two granularity options in the tracker, one with elongated pixels (strixels) and the other with pixels [36].

	Strixels	Pixels
Vertex barrel and disks	$25 \times 25\,\mu\text{m}^2$	$25 \times 25\,\mu\text{m}^2$
Inner Tracker barrel 1–2	$50\,\mu\text{m} \times 1\,\text{mm}$	$30 \times 300\,\mu\text{m}^2$
Inner Tracker barrel 3	$50\,\mu\text{m} \times 5\,\text{mm}$	$30 \times 300\,\mu\text{m}^2$
Outer Tracker barrel 1–3	$50\,\mu\text{m} \times 10\,\text{mm}$	$30 \times 300\,\mu\text{m}^2$
Inner Tracker disk 1	$25 \times 25\,\mu\text{m}^2$	$25 \times 25\,\mu\text{m}^2$
Inner Tracker disks 2–7	$50\,\mu\text{m} \times 1\,\text{mm}$	$30 \times 300\,\mu\text{m}^2$
Outer Tracker disks 1–4	$50\,\mu\text{m} \times 10\,\text{mm}$	$30 \times 300\,\mu\text{m}^2$

Chapter 3

Simulation software and analysis methods

The issues of the beam transport in the Beam Delivery System, including the impact of the wakefields on the beam quality, the emission and interactions of the synchrotron radiation with the material of the beam pipe and the production of the unwanted background particles in beam-beam interactions are complex and non-analytical. Therefore, to provide precise descriptions and estimates, numerical calculations are performed with dedicated software packages.

In section 3.1, the software packages used in this study are described, along with the simulation chains that required interfacing between different codes. In sections 3.2.1 and 3.2.2, the definitions are provided for the hits in the tracking detector and calorimeters. It is followed by a description of the method used to take into account the safety factors and combine the occupancies coming from different sources in section 3.2.3. Finally, in section 3.2.4, the normalisation of the occupancy distributions is described for all studied subdetectors.

3.1 Simulation software

Simulations of the impact of the resistive wall wakefields and beam-induced backgrounds on the CLIC Beam Delivery System and the detector require a sequence of separate codes, each responsible for a different task.

Simulations of the resistive wall wakefields start with beams created at the beginning of the Beam Delivery System and a distribution of apertures along the simulated accelerator. The beams are transported through the BDS using PyHEADTAIL [37]. At the IP, the beams are stored and analysed offline. Then, they are used as input in Guinea-Pig [38] simulations to quantify the wakefields impact on the luminosity.

The synchrotron radiation emission is studied using PLACET [39] and Synrad+ [40]. The total emitted power and the emission distribution along the BDS are recorded. The reflections from the beam pipe walls are simulated in Synrad+, using different possible materials, such as iron and copper, and with varying surface roughnesses. The photons that go through the QD0 aperture and have sufficiently large polar angles to interact with the sensitive material of the detector are stored. They are later simulated in the full detector simulations using GEANT4. The energy depositions in the tracking detectors are stored and related occupancies calculated offline.

For the beam-induced backgrounds produced at the IP the simulation starts with bunches that are created at the exit of the Main Linac, with parameters obtained from linac-focused simulations, in particular, the longitudinal energy spread distribution. These bunches are transported to the IP using PLACET. The electron and positron bunches are used directly as input in beam collision simulations, without additional assumptions or approximations. The beam collisions are simulated in Guinea-Pig, which provides the luminosity spectra and produces the background particles. The output particles are saved in the LCIO file format and are used in GEANT4 simulations. Particle transport and interactions with the DD4hep/lcgeo [41] model is run on the Grid, split into so-called jobs to take advantage of the parallelization. The job submission and monitoring is done using iLCDirac [42]. All of the offline processing and data analysis is performed in ROOT [43].

The job submission and running computations in parallel were greatly aided by the GNU Parallel tool [44].

3.1.1 PyHEADTAIL

PyHEADTAIL is a numerical many-body simulation framework used for studying beam dynamics with collective effects. The code has been designed for coherent beam stability studies in synchrotrons, although in this study it is adapted to simulate the beam dynamics in a linear accelerator. The code is modular, where each individual simulation is built from provided tools. The tracking implemented in PyHEADTAIL is a linear betatron tracking. However, the impact of the dispersion and chromaticity can also be taken into account [37]. The impact of dispersion on the beams is enabled in the following PyHEADTAIL simulations, but the chromaticity is not.

Most relevant for this study is the ability of PyHEADTAIL to simulate the beam interactions with beam-coupling impedances through wakefields. The wakefield can be pre-calculated or computed from an analytical model during simulation. In addition, PyHEADTAIL has an aperture model that is used to study the beam sensitivity to the resistive wall wakefield.

A PyHEADTAIL simulation starts with user-defined transverse dynamics parameters containing the information of the transverse emittances $\varepsilon_{x,y}$, Courant-Snyder β and α functions and a phase advance per revolution. PyHEADTAIL tracks beams in six-dimensional phase-space, where macroparticles represent the charges. In addition, the bunches in a bunch train are split into a selected number of longitudinal slices. A drift-kick approach models the beam dynamics by alternatively applying a single-particle dynamics and multi-particle effects. The transverse beam dynamics consists of transporting the beam through all accelerator lattice elements using the provided transverse map. After each step of the transverse dynamics is applied, the wakefield effects are imposed on the beam [37].

The linear tracking is equivalent to multiplying the beam parameters by a matrix, called transfer matrix, to calculate the beam response to the accelerator lattice elements, such as drifts or bending magnets. Linear tracking between point s_1 and s_2 can be represented by the following equation:

$$\begin{pmatrix} \vec{x} \\ \vec{x}' \end{pmatrix}_{s_2} = M_{s_1 \to s_2} \begin{pmatrix} \vec{x} \\ \vec{x}' \end{pmatrix}_{s_1}, \tag{3.1}$$

where: $\vec{x}$ - macroparticle position, $\vec{x}'$ - macroparticle angle coordinate, $M_{s_1 \to s_2}$ - transfer matrix.

Dispersion is introduced to the beam by expanding the transverse beam sizes:

$$\begin{aligned} x &= x_0 + D_x\delta, \\ y &= y_0 + D_y\delta, \end{aligned} \tag{3.2}$$

where: $D_{x,y}$ - horizontal or vertical dispersion, $D_y \approx 0$ for linear accelerators, $\delta = \frac{\Delta P}{P}$ - normalised momentum spread.

When tracking through the prepared geometry is finished, the beams are stored and are analysed offline.

3.1.2 Synrad+

Synrad+ is a Monte Carlo software designed for simulations of emission and interactions with vacuum chamber walls of synchrotron radiation photons. The code has been designed to run simulations efficiently on commercially available desktops [40] and does not require large-scale shared resources, such as the WLCG [45]. In this study, this is a disadvantage, as the user cannot benefit from parallel computing to obtain significant statistics needed for the precise study of the interactions of the SR photons with the detector material.

The simulated geometry can be read from CAD files or from MAD-X [46] output containing lattice parameters and aperture radii. In addition, the code has a custom geometry builder that can be used to create simple test geometries. Circular, elliptical, and race-track vacuum chamber cross-sections are available in the software, and more complex shapes can be created by the user. The 3D geometry is represented by polygons, which also contains information about physical properties of the surface, such as the material, reflectivity, sticking factor, and number of received hits.

User input defines the beam parameters, including the initial position and energy spread. The virtual photons, each representing specific flux of the SR, are created along the beam trajectory in the magnetic regions. The photons can be emitted in the provided magnetic regions: bending and quadrupole magnets, or in periodic structures, such as wigglers. The photons are propagated through the geometry until they interact with a vacuum chamber polygon. When a hit is recorded, the photon can be absorbed, reflected, backscattered or transmitted, depending on the photon's energy, incident angle, and the properties of the material used [40].

The material data is stored in CSV files and can be easily modified. Synrad+ contains reflectivity tables for common vacuum chamber materials, such as copper or iron, but also the properties of complex elements such as saw-tooth beam pipe shapes. The reflectivity tables in Synrad+ are based on the measured reflectivity tables for X-rays in the energy range from 50 eV to 30 keV [47]. User can change the average roughness of the material that is currently used from the simulation GUI without the need to modify the reflectivity tables.

Synrad+ allows storing of all parameters of virtual photons interacting with a chosen polygon, including the position, momentum, energy, and represented flux. The stored photons are used in the offline analysis in ROOT and embedded in the GEANT4 detector simulations.

Table 3.1: Beam parameters at the IP at two energy stages: 380 GeV and 3 TeV obtained with tracking simulations in the CLIC Beam Delivery System using PLACET.

Energy stage	x [nm]	y [nm]	z [µm]	σ_E [%]
380 GeV	149.4	3.1	70	0.35
3 TeV	48.2	1.3	44	0.35

3.1.3 PLACET

The PLACET (Program for Linear Accelerator Correction and Efficiency Tests) software simulates beam dynamics and transport in linear electron–positron colliders in ultra-relativistic regimes using a macroparticle representation of the beams. PLACET is a modular software package parallelized in an Open Source High Performance Computing message passing interface (OpenMPI) [48], and is executed using the Tcl/Tk interface. Some notable functionalities implemented are normal accelerating RF cavities, non-linear elements, such as multipole magnets, synchrotron radiation, and orbit correction tools. The code allows one to study single- and multi-bunch effects, bunch compression, and ground motion impact on the beams [39].

PLACET takes as input a description of the accelerator to transport a beam through, and an initial beam distribution with the user-defined number of macroparticles. The code is executed from a custom wrapper where the user has to describe the relevant beam parameters at the beginning of the simulation, such as values of Courant-Snyder α and β functions, emittances, bunch charge and bunch length.

In this study, PLACET is used to transport the beams through the CLIC BDS up to the IP using six-dimensional tracking. A perfectly aligned beam line without any magnetic field errors is assumed. The beams tracked with PLACET were created with a realistic energy spread coming from the Main Linac, such as shown in Figure 3.1. The transported beams are stored, and used as input in the Guinea-Pig software. In this analysis the PLACET code has been modified to allow for the extraction of synchrotron radiation photons to study their properties and possible impact on the detector.

The beam parameters at the IP obtained from the PLACET tracking simulations can be found in Table 3.1, and are presented in Figure 3.2. The beam sizes are obtained from a Gaussian fit to the transverse beam distributions, as is shown in Figure 3.3. The beam sizes, shown in Table 3.1, are slightly larger than the nominal beam sizes at each respective energy stage (see Table 2.1). This is mostly due to the emission of the synchrotron radiation in the Beam Delivery System. The beams have long tails in the vertical direction, especially at 3 TeV. This beam quality loss impacts the luminosity performance negatively.

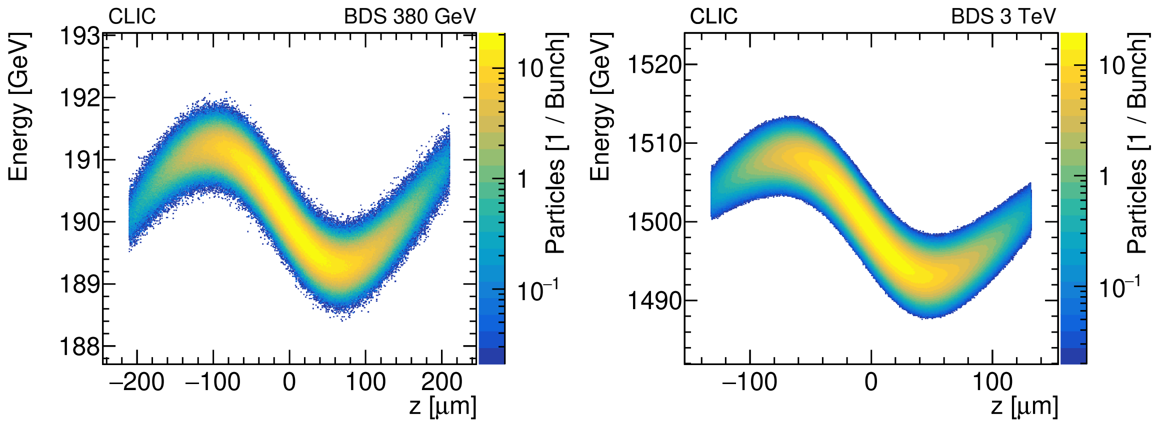

Figure 3.1: Energy spread of the beams in the CLIC Beam Delivery System used in simulations in PLACET at 380 GeV(left) and 3 TeV(right).

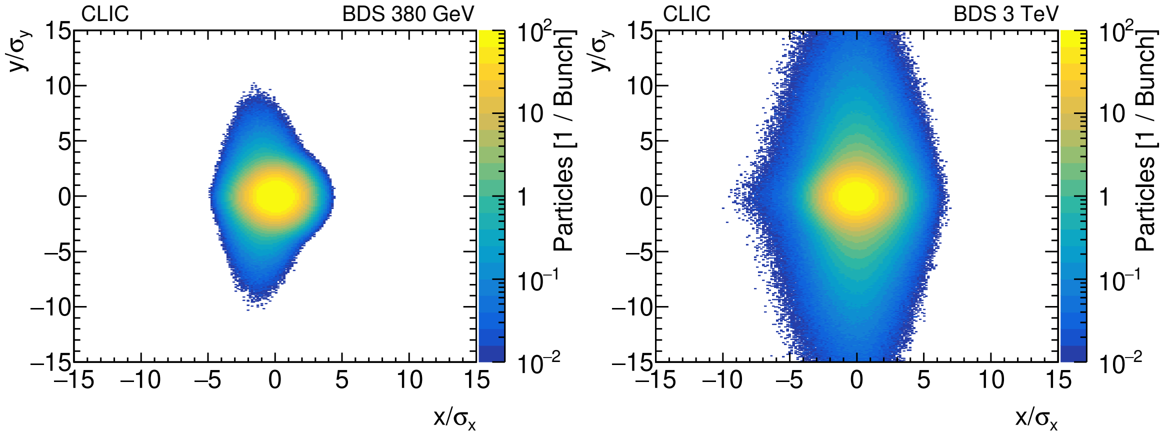

Figure 3.2: Transverse position distributions of the beams at the IP coming from PLACET before bunch crossing at 380 GeV(left) and 3 TeV(right).

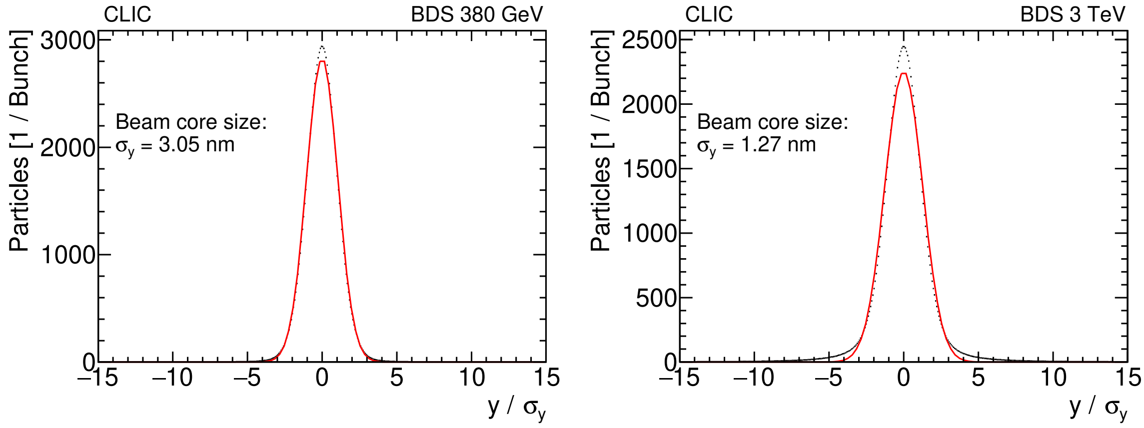

Figure 3.3: Vertical position distributions of the beams at the IP with a Gaussian distribution fitted coming from PLACET at 380 GeV(left) and 3 TeV(right).

3.1.4 Guinea-Pig

Guinea-Pig (Generator of Unwanted Interactions for Numerical Experiment Analysis - Program Interfaced to GEANT) is a program used to simulate electron–positron collisions of nanometer-scale beams [38]. It provides information about luminosity and the luminosity spectrum. It also creates background particles and provides information about their yields and momentum distributions.

Guinea-Pig requires at least one input beam of electrons or positrons to be provided, or a configuration file containing all the relevant information about the beams (energy, sizes or emittance and beta functions at IP), and parameters of the simulation to be run (grid sizes, processes to simulate).

The simulation starts with two beams opposing each other. The particles in the beams are replaced by macroparticles and are allocated into longitudinal slices. The longitudinal slices are moved in their respective direction, and the electromagnetic fields are calculated on a transverse grid. The particles are ultra-relativistic, thus all dynamics can be reduced to a two-dimensional problem. The transverse plane is also split into a given number of cells, and the charges in the cells are calculated according to the macroparticle distributions. When the longitudinal slices overlap after they are moved, cells that face each other are assumed to collide. The potential of the electromagnetic field is computed using Fast Fourier Transformation. The field potentials interact with the charges, changing their trajectories. The impact of the EM field is used to compute the emission of the synchrotron radiation. The luminosity is calculated from the distribution of colliding cells, and production of the background particles is computed using the relevant process cross-section [38].

In this study, Guinea-Pig is used after the beams are transported through the BDS with PLACET or PyHEADTAIL. The bunch collisions along the bunch trains are independent and are simulated independently. This approach offers a significant time-saving in comparison to sequential computations. The simulations with the code version GP++.1.2.1 are run on the Grid using iLCDirac. For each simulated collision incoherent electron–positron and muon pairs, coherent pairs, trident cascades, beamstrahlung photons and initial states of $\gamma\gamma \to$ hadron events are saved. The luminosity spectra for e^+e^-, $e^+\gamma$, $e^-\gamma$, and $\gamma\gamma$ initial states are also collected. The results obtained for each bunch crossing are analyzed offline using ROOT. The initial states of $\gamma\gamma \to$ hadron events are hadronized in PYTHIA6.4 [49] to obtain the final states particles which can be used in the full detector simulations.

In Guinea-Pig, the transverse electromagnetic field is computed numerically on a grid at each time step, and charge-in-cell approach is used to distribute the macroparticle charges on the mesh. To ensure obtaining the reliable results, the parameter selection of the grid granularity in the Guinea-Pig simulations has been studied with the 380 GeV beam conditions.

A dependence of luminosity on the grid granularity is found, as well as the dependence on the use of the same beam to collide with its mirrored self (one-beam mode), or two independent beams (two-beam mode). In the case where the one beam mode was used, as in Figure 3.4(left), there is a strong correlation between the grid granularity and luminosity. The luminosity does not converge, and in principle arbitrarily large luminosities can be obtained. In comparison, when two independent beams are used, as shown in Figure 3.4(right), the luminosity increase

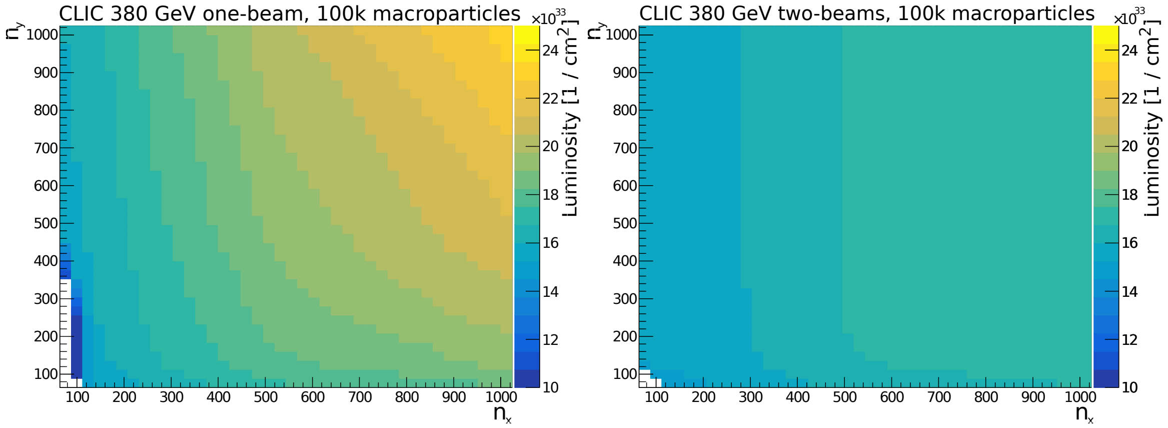

Figure 3.4: Luminosity dependence on the grid granularity when one-beam mode is used (left), and with the two-beam mode (right). In both cases 10^5 macroparticles per bunch and 380 GeV CLIC beam parameters have been used.

with the grid granularity is significantly slower than in the one-beam case. The luminosity stabilises for $n_x > 500$, and $n_y > 200$.

The dependence on the grid selection persists in the one-beam mode if the number of macroparticles is doubled in comparison with a default simulation, from 10^5 to $2 \cdot 10^5$, as shown in Figure 3.5(left). The convergence of luminosity is not reached, but the increase as a function of the number of cells is slower.

When a small offset, for example of half a beam size in the transverse direction, is introduced in the one-beam collision simulations, the dependence of luminosity on the grid granularity is diluted and becomes negligible, as shown in Figure 3.5(right).

The correlation between the grid granularity and obtained luminosity is due to saturation of the charges-in-cell and collisions between the exact same cells in the one-beam mode. The weights given to each collision scale inversely with the cell size, thus an increase in granularity in the one-beam mode without offsets results in larger luminosity.

In conclusion, the one-beam mode without offsets should be avoided as it leads to the luminosity values that depend strongly on the grid parameters, and not only on the beam properties. The two-beam mode is preferred and recommended for the Guinea-Pig simulations.

The simulations done for this study are either one-beam with an offset or two-beam simulations. The configuration script containing the parameter choice is available in Appendix A.

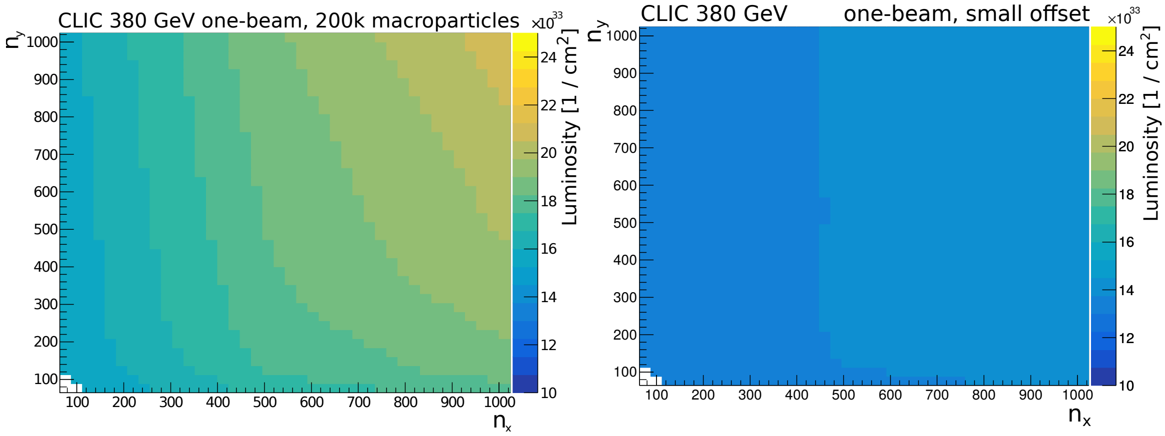

Figure 3.5: Luminosity dependence on the grid granularity when one-beam mode is used and a small offset of half a beam size is applied (right), and when the number of maroparticles per bunch is doubled (left). In both cases the 380 GeV CLIC beam parameters have been used.

3.1.5 Geant4

GEANT4 is a Monte Carlo toolkit that allows one to simulate particle interactions with matter. The implemented physics includes electromagnetic, hadronic, and optical processes in the energy range from hundreds of eV to multi-TeV. The toolkit consists of a wide range of components from building geometry, selecting physics processes, to tracking of the created particles in the prepared three-dimensional space, and recording hits in the sensitive material [50].

In this study, GEANT4 is used predominantly to estimate the impact of the unwanted background particles: photons, electron–positron pairs, and hadrons on the sensitive elements of the CLIC detector. These particles are simulated in the detector model, and the energy deposits in each subdetector are collected and analysed offline using ROOT.

Aside from the CLICdet background impact study, GEANT4 was also used for two small-scale simulations. One was an optimisation of the shield composition and thickness for the HCal endcap, described in further detail in section 8.3.3. The other was a study of the limits of the currently available GEANT4 physics models concerning the low-energy photons, with energies below 30 keV.

GEANT4 has two different particle types that are photons: a *gamma* and an *optical* photon. The *gamma* photon contains all relevant physics processes linked with photon interactions with matter at high energies, such as photoelectric effect, Compton scattering, and pair production. The *optical* photon does not have these processes implemented but instead interacts with matter through low-energy processes, such as reflection, Rayleigh scattering, and Cerenkov effect.

The GEANT4 low-energy electromagnetic physics description of *gamma* photons has been checked by preparing a small-scale simulation, which is schematically described in Figure 3.6. A metallic element, either copper or iron, with a thickness of 1 mm was impinged by photons at various angles and energies. The energy range for the photons was from 1 eV to 1 MeV, and the angular range from 1 mrad to 200 mrad.

Two low-energy physics lists, Penelope [51] and Livermore [52] was used as well as the standard physics list QGSP_BERT with electromagnetic option 4 [53, 54]. GEANT4 performs

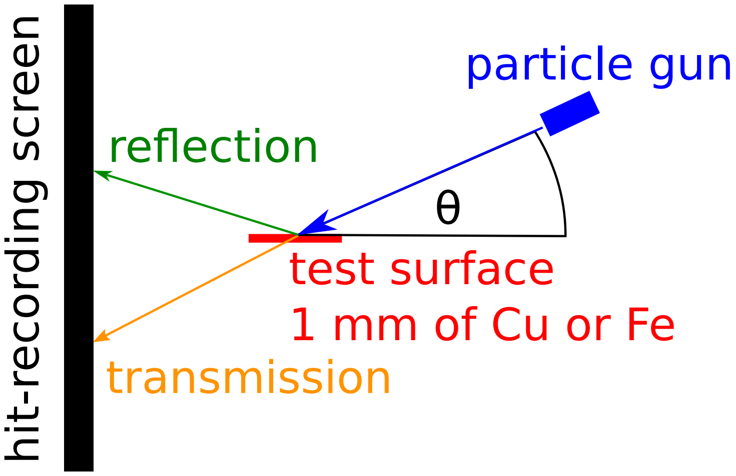

Figure 3.6: Schematic view of a Geant4 simulation model used to test the low-energy photon interactions with a thin metallic surface.

well when compared with experimental data for the electromagnetic processes [55]. However, in the simulations the only observed phenomena were either absorption or transmission, without significant changes in the photon direction of motion. The reflections are not included in these physics lists, and the implemented processes do not reproduce the expected angular distributions of photons. The interactions of photons with metallic surfaces at low angles and energies ($E < 30\,\mathrm{keV}$) should lead to reflections, according to experimental data [47].

The photon reflections from metallic surfaces are included in the Optical Photon physics list. The processes implemented in the optical physics list act upon a particular particle type: an *optical* photon. The *optical* photon is defined as a photon with a wavelength much larger than the atomic distances, or equivalently, with energies below 100 eV. This pre-defined energy limit is lower than the energy range of photons that can undergo reflections and the energy spectrum of photons at CLIC, therefere renders this physics list not useful for the photon reflections study.

Even if it was possible to extend the description of the reflection phenomena for higher energy photons by providing GEANT4 with relevant reflectivities and refractive indexes for the desired energy range another issue arises. In this case, the simulated particle type remains to be an *optical* photon. The *optical* photons implementation does not have the same high-energy interactions with material as *gamma* photons. Therefore, the optical physics photons cannot be used to study the interactions of photons with the material of the beam pipe and sensitive elements of the CLIC detector.

In summary, GEANT4 should be used with caution when the low energy photon interactions with material may be relevant to the experiment or simulation outcome.

3.1.6 iLCSoft and iLCDirac

Linear Collider Software (iLCSoft) is a package providing detector geometry description and reconstruction tools used by the Linear Collider (LC) community. The detector description lcgeo is based on the Detector Description for high energy physics (DD4hep) toolkit. DD4hep is a set of tools that reuses the existing software solutions, such as the ROOT geometry package and Geant4 simulation toolkit. ROOT provides geometry building functionalities, while

Geant4 simulates the particle interactions with the detector material. The compact detector description is used to define and parametrize a detector model. The parameters are provided in minimalistic form using XML files, which allows one to introduce new elements or modify the geometry with ease [56]. The full detector simulations benefit from parallelization and are run on the Grid, which is monitored using iLCDirac.

iLCDirac is a Grid solution used by the Linear Collider community, and it is an extension of the DIRAC software [57]. iLCDirac provides an interface to the distributed computing resources and the applications used by the LC community with its simplified API. The software is used for application handling during job execution and monitoring, as well as file access to the Grid [42].

In this study, the DD4hep/lcgeo simulations take as input a CLICdet model description and background particles translated to Linear Collider I/O (LCIO) [58] format. The iLCSoft built from November 1, 2018, is used for all simulations involving the toolkit. The detector model version used to obtain all results on the background impact is CLIC_o3_v13, and it also serves as a base for any modifications of the geometry.

3.2 Occupancy estimate

The definition of the occupancy depends on the subdetector considered because it is directly linked with the way a hit is recorded. In the simulations performed for this study, a hit in the tracking detectors is stored if its energy surpasses the relevant threshold for that subdetector. In the case of calorimeters, all hits in a specific time frame are integrated and based on their collective impact a hit is recorded if their total deposited energy is over the threshold.

3.2.1 Occupancy in tracking detectors

The definition of occupancy used in silicon trackers follows the example used in [59] and is based on the background hit density per bunch train, which is scaled up by assumed clustering effects and safety factors. First, the hit density is calculated taking into account the relevant energy threshold of the sensitive surface and the area of the sensitive element:

$$\rho_{\text{Hits}} = \frac{1}{A_{\text{sens}}} \sum_{i=1}^{N_{\text{hits}}} \mathrm{H}(E^{i}_{\text{dep}} - E_{\text{threshold}}), \tag{3.3}$$

where: A_{sens} - area of the sensitive surface, N_{hits} - number of hits recorded by Geant4, H - Heaviside step function, E^{i}_{dep} - energy deposition connected with i-th hit, $E_{\text{threshold}}$ - relevant energy threshold of the sensitive element.

Then, the hit density can be used to calculate the occupancy level. The following definition allows for hits originating from different types of backgrounds to be added as a simple sum:

$$O_{\text{train}} = \sum_{\text{background}} \rho_{\text{Hits/BX}} \cdot n_{\text{bunches/train}} \cdot p \cdot c \cdot sf_{\text{background}}, \tag{3.4}$$

where:

- $Hits_{\text{density/BX}}$ - density per mm^2 of hits above the threshold of 3.2 keV for 50 µm thick silicon sensors, and 6.4 keV 100 µm sensors [60];
- p - sensor pitch, e.g. $300 \times 30\,\mu\text{m}^2$ in the tracker;
- c - clustering factor, 5 for pixel sensors, 3 for other;
- sf - safety factor, 5 for incoherent electron–positron pairs and 2 for $\gamma\gamma \to$ hadrons [59].

The energy deposited by background particles will lead to the releasing of free charges in the silicon volume. As these charges migrate towards the minimum of electric potential at a readout, they are spreading laterally and charge sharing occurs, leading to the formation of clusters of one or more hit pixels. The exact cluster size depends on the sensor geometry, angular and momentum distribution of the incident particle and the design of the readout system. In this study, an approximate value of five for the pixel sensors and of three for the sensors in the trackers are assumed, in line with the values used in the previous study [60].

A safety factor of two is applied to $\gamma\gamma \to$ hadron events. It takes into account the uncertainty of the $\gamma - -\gamma$ luminosity spectrum, production cross-section and the hadronisation model. For the incoherent pairs, a larger factor of five is applied. The value is chosen to accommodate the uncertainty of electron and positron interactions with the material of the detector, especially in the forward region. The incoherent pairs interactions lead to scattering and production of a significant number of secondary particles, that cause hits in the sensitive detector elements [60].

3.2.2 Occupancy in calorimeters

A different approach has to be used in the case of calorimeters, where the integration time of hits and their energy depositions have to be taken into account. The integration time has been chosen to be 200 ns to exceed the bunch train lengths of 156 ns and 176 ns at 3 TeV and 380 GeV, respectively, to allow for the recording of all events in a bunch train, taking into account the time for particle showers to develop. To better understand the time structure of the occupancy, the integration time has been split into eight equal time windows of 25 ns. When data rates have been studied, only one time window has been used with a length equal to the total integration time. A time window is considered to be occupied if the energy deposition during that time surpasses the threshold. The occupancy for the calorimeters is defined as the number of occupied time windows. This occupancy estimation is summarized in Equation (3.5).

$$O_{\text{time slice}} = \frac{1}{N_{\text{slices}}} \sum_{i=1}^{N_{\text{slices}}} \mathrm{H}\left(\int_{t_1^i}^{t_2^i} \mathrm{d}E_{\text{deposit}} - E_{\text{threshold}} \right) \tag{3.5}$$

where:

- N_{slices} - number of time slices of the total integration time, equal to 8 or 1, depending on the analysis,
- H - Heaviside step function,
- t_1^i, t_2^i - integration time boundaries of i-th time slice,
- $E_{\text{threshold}}$ depends on the calorimeter sensitive material: 40 keV (half of the expected energy deposit of a minimally ionising particle (MIP)) for silicon in the ECal and 300 keV (0.3 MIP) for scintillator in the HCal [60]

Occupancies coming from two different sources, e.g. $\gamma\gamma \rightarrow$ hadrons and incoherent electron–positron pairs cannot be added as a simple sum, instead a special approach needs to be applied. In addition, no safety factors are taken into account in the calculation described above, the proper safety factor treatment in given in section 3.2.3.

3.2.3 Safety factors and combining of occupancy sources

The occupancy definitions described by Equations (3.4) and (3.5) can be also understood in terms of probabilities. An occupancy of a sensitive element can be described as a probability of being hit in a bunch train, e.g. an occupancy of 50% is equivalent of a 50% chance of that element being hit.

Applying a safety factor to the occupancy is equivalent to combining two independent probabilities, with the same probability used each time:

$$O = 1 - (1 - O_{\mathrm{i}})^{SF}, \tag{3.6}$$

where:

- O_{i} - occupancy without safety factor applied,
- SF - safety factor, five for incoherent pairs or two for $\gamma\gamma \rightarrow$ events.

In the limit of low O_{i} and after a Taylor expansion it can be simplified to:

$$O = SF \cdot O_{\mathrm{i}} \tag{3.7}$$

Combining two (or more) sources of occupancy is equivalent to combining two independent probabilities:

$$O_{\mathrm{combined}} = 1 - (1 - O_{\mathrm{pairs}}) \cdot (1 - O_{\mathrm{hadrons}}), \tag{3.8}$$

which can be simplified in a low occupancy regime to:

$$O_{\mathrm{combined}} = O_{\mathrm{pairs}} + O_{\mathrm{hadrons}} \tag{3.9}$$

3.2.4 Normalisation of the hit densities

The hit densities need to be correctly normalised for a reliable estimate of the occupancy level. The hit definitions differ between the tracking detectors and the calorimeters. Therefore, the simulation data collection and analysis need to take it into account.

The hit densities and occupancy normalisation for the tracking detectors are described in section 3.2.4.1. The analogue description for the calorimeters, that also applies to the Muon Identification System, is given in section 3.2.4.2.

3.2.4.1 Normalisation in the tracking detectors

The first step of the occupancy calculation is a Geant4 simulation of background particles in the detector model. The hits with energy deposition above the relevant threshold are stored, and their three-dimensional position saved. At this point, the method of calculating the occupancies in the vertex barrel and disks diverges.

In the case of the vertex barrel, the hits are stored as two-dimensional histograms with longitudinal vs $r\phi$ cylindrical coordinates for each of the vertex ladders. The radii for the cylinders on which the hits are projected for each of the six layers are as following: 31.3 mm, 33.3 mm, 44.3 mm, 46.3 mm, 58.3 mm, and 60.3 mm. These are chosen as they represent the vertex barrel geometry on a cylinder in the least distorted way, and with the minimal amount of overlaps. The histograms representing the ladders of one vertex layer are merged together to create the hit distribution over the full azimuthal angle. The overlaps are removed by taking the larger number of hits from two overlapping surfaces. The resulting two-dimensional histograms are

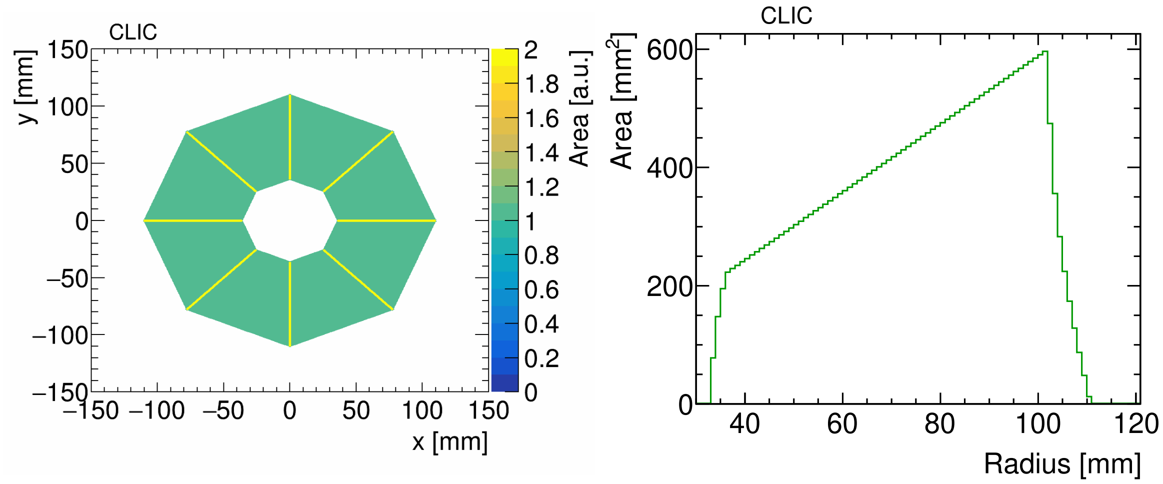

Figure 3.7: Transverse projection of the vertex disk layout (left) and the radial area distribution of such disk (right).

normalised to one bunch crossing and to the surface area to obtain the hit density per bunch bin per bunch crossing. An example hit density distributions projected on the $r\phi$ axis for the $\gamma\gamma \rightarrow$ hadron events at 3 TeV are shown in Figure 3.8. There are some fluctuations in the hit density, which are caused by binning effects and are remnants of projecting the overlapping ladders on a cylindrical surface. The hit density distributions are generally flat along the $r\phi$ dimension, thus averaging over this axis does not introduce a systematic error or cause information loss. The longitudinal hit density distributions are obtained by projecting the two-dimensional histograms on the longitudinal axis and dividing them by the number of $r\phi$ bins. From the longitudinal hit density distribution the longitudinal distribution of the occupancy can be calculated using Equation (3.4), where the safety factors are also applied. The occupancies coming from different sources can be combined using the Equation (3.8) or its simplified version in Equation (3.9).

The vertex disk occupancy calculation requires a different approach, due to a more complicated geometry. The transverse x and y positions of the hits are stored on two-dimensional histograms representing each vertex disk. The hits are averaged over ϕ. The histograms are normalised with a distribution of area as a function of the radius that takes into account the 2 mm overlap between each petal. The overlap is represented by the yellow area in Figure 3.7(left). The radial area distribution has a step-like shape at inner and outer edge of the disk. This effect is a result of finite resolution of the binning in the transition region from the inner region to the sensitive surface of the trapezoids building the vertex disks. The radial hit density is obtained by dividing the distribution of radial hits by the distribution of the radial area. Finally, the occupancy can be calculated using Equation (3.4), where the safety factors are applied. The occupancies from different background sources can be similarly combined using the Equation (3.8) or its simplified version in Equation (3.9).

The occupancy calculation in the tracker is done in the same way as for the vertex detector. The disks have a similarly complicated geometry to the vertex disks, with significant overlaps between the sensitive elements. Two-dimensional area distributions are prepared and used to

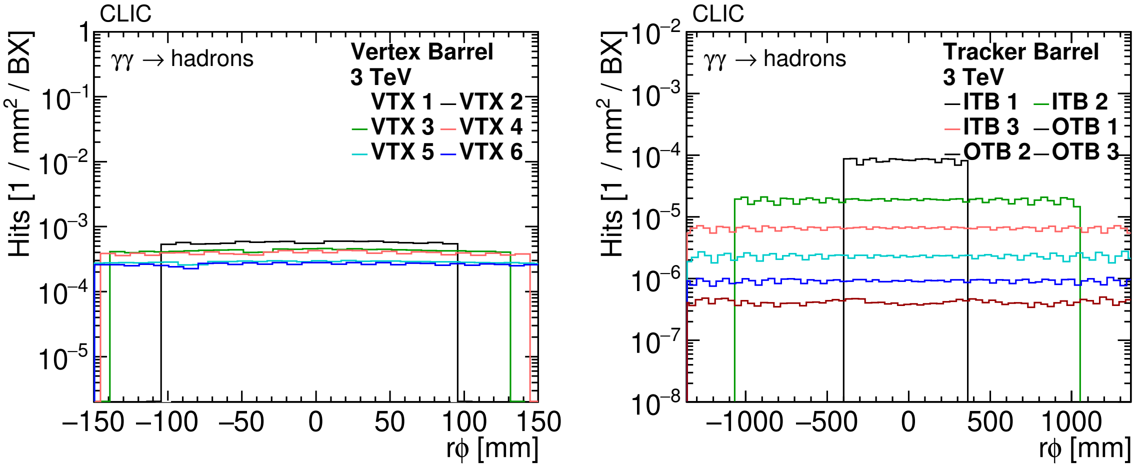

Figure 3.8: Distribution of the hit density per bunch train in the vertex barrel (left) and in the tracker barrel (right) at 3 TeV from $\gamma\gamma \to$ hadron events. Safety factors are not included.

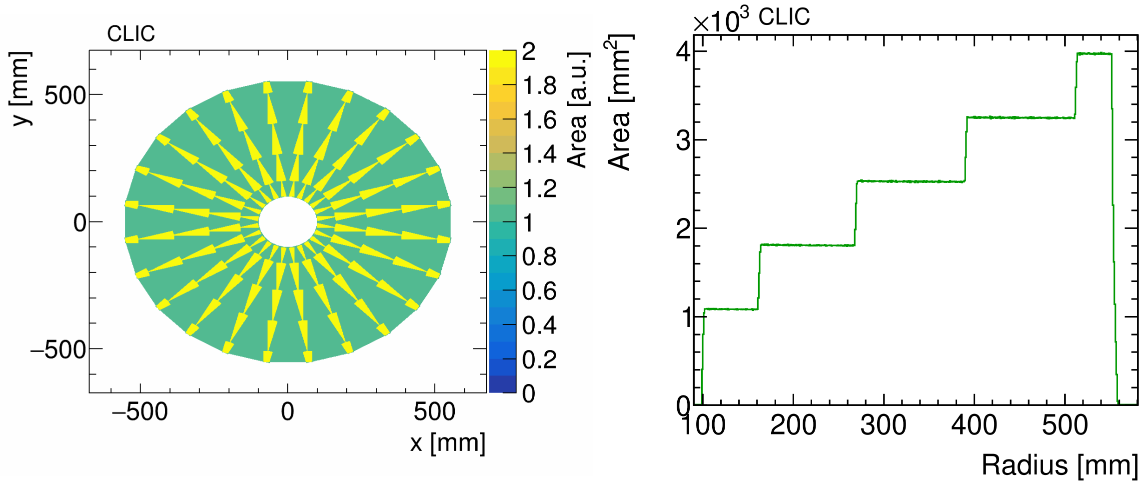

Figure 3.9: Transverse projection of the tracker disk layout (left) and the radial area distribution of such disk (right).

create radial area histograms, necessary for proper normalisation of the radial hit distributions. An example area distribution of the Inner Tracker 1 and related radial area plot are shown in Figure 3.9. The yellow area in the Figure 3.9(left) represents the overlapping sensors in the tracker disk. The radial area distribution in Figure 3.9(right) has a step-like shape with surface increasing each time a new rectangular petal is reached and flat along the petal.

3.2.4.2 Normalisation in the calorimeters

The occupancy estimation for the ECal and HCal barrel starts with transportation of background particles through the CLICdet detector model using DD4hep. In each calorimeter cell the energy depositions are added in the time window corresponding to the time of the hit. Equation (3.5) is utilised to calculate the occupancy per train of each cell. The distribution of occupied cells and time windows is stored as a function of the radius. These histograms are integrated over the full range to obtain the number of occupied cells and time windows per layer, and are divided by the total number of cells of the relevant layer multiplied by the number of time windows, either eight for 25 ns slicing or one for 200 ns slicing. The former allows one to study the impact of backgrounds with possible multiple hits per bunch train providing the information on how many hits need to be deconvoluted by the future readout, while the latter is used to establish the data rates with various readout scenarios. The resulting numbers are scaled by the safety factors, as expressed in Equation (3.6). Finally, the occupancy distributions coming from different sources are combined using Equation (3.8).

The occupancy estimation for the ECal and HCal endcaps consists of several steps. It starts with transportation of background particles through the CLICdet detector model using DD4hep. The energy depositions in each calorimeter layer are integrated and the cells occupancy per train is calculated with Equation (3.5). The distribution of occupied cells and time windows is stored as a function of radius. These radial distributions of occupied cells are normalised by dividing them by a radial distribution of all cells of the relevant calorimeter endcap, in analogy to the radial surface distributions described in section 3.2.4.1. The resulting numbers are scaled by the respective safety factors, as expressed in Equation (3.6). Finally, the occupancy distributions coming from different sources can be combined using Equation (3.8).

Chapter 4

Beam-induced backgrounds at CLIC

At CLIC, beam-induced backgrounds are produced in large quantities in the electron–positron collisions due to the high concentration of charges in nanometre-sized beams. The beams are deflected and focused by the strong macroscopic electromagnetic field of the oncoming beam of the opposite charge. As a result, the beams emit intense and high-energy synchrotron radiation, called beamstrahlung. The radiation of the beamstrahlung introduces the luminosity spectrum. Interactions of the beamstrahlung photons with the EM field, electrons, positrons and photons of the oncoming beam produce the unwanted particles: coherent and incoherent pairs, and $\gamma\gamma \rightarrow$ hadron events.

In section 4.1, the simplified beam dynamics is described. The luminosity spectra of CLIC for four initial states: e^+e^-, $e^+\gamma$, $e^-\gamma$ and $\gamma\gamma$ are shown in section 4.2. In section 4.3, the emission and properties of the beamstrahlung radiation is discussed. Section 4.4 concerns the creation of the coherent and incoherent pairs and their distributions. In section 4.5, the $\gamma\gamma \rightarrow$ hadron events are described. Finally, in section 4.6, the beam-induced backgrounds for two CLIC energies: 380 GeV and 3 TeV are summarised.

4.1 Simplified beam-beam interaction

Charged particles in electron–positron collisions are under a strong influence of the attractive electromagnetic force of the oncoming beam. Their trajectories are bent inwards, as the beams are focusing, leading to an enhancement of luminosity, an effect called pinching. The acceleration of the beams leads to emission of intense synchrotron radiation, called beamstrahlung, further described in section 4.3.

In this simplified description of the dynamics of the electron–positron beams collision assumed are ultra-relativistic conditions and symmetric collisions. The ultra-relativistic assumption greatly simplifies the calculations, as only the static transverse electric field needs to be considered, due to significant Lorentz contraction of the fields.

The radial electric field E_r of a long bunch of length σ_z with a transverse Gaussian charge distribution, constant longitudinal charge distribution, and a total number of particles N can be obtained using the Gauss law, and the transverse magnetic field B_θ can be obtained from

Ampere's law [61]:

$$E_r = \frac{Ne}{2\pi\varepsilon_0\sigma_z}\frac{1}{r}\left[1 - \mathrm{e}^{-\frac{1}{2}\left(\frac{r}{\sigma_\mathrm{T}}\right)^2}\right], \tag{4.1a}$$

$$B_\theta = \frac{Ne\mu_0}{2\pi\varepsilon_0\sigma_z}\frac{v}{r}\left[1 - \mathrm{e}^{-\frac{1}{2}\left(\frac{r}{\sigma_\mathrm{T}}\right)^2}\right] = \frac{v}{c^2}E_r, \tag{4.1b}$$

where: σ_T - transverse beam size, r - distance from the centre (impact factor), μ_0 - magnetic constant.
Lorentz force seen by a test particle is:

$$\vec{F} = e(\vec{E} + \vec{v} \times \vec{B}). \tag{4.2}$$

For a co-moving test particle, the force is:

$$F = e(E_\mathrm{r} - vB_\theta) = eE_\mathrm{r}\left(1 - \frac{v^2}{c^2}\right) = \frac{1}{\gamma^2}eE_\mathrm{r}, \tag{4.3}$$

where: $\gamma = \frac{1}{\sqrt{1-v^2/c^2}}$, the Lorentz factor. The force diminishes with increasing γ.

For a particle belonging to the oncoming beam, with the opposite velocity direction and with the opposite charge, the force becomes:

$$F = -e(E_r + vB_\theta) = -eE_r\left(1 + \frac{v^2}{c^2}\right) \approx 2eE_r = -\frac{Ne^2}{2\pi\varepsilon_0\sigma_z}\frac{1}{r}\left[1 - \mathrm{e}^{-\frac{1}{2}\left(\frac{r}{\sigma_T}\right)^2}\right]. \tag{4.4}$$

Near the beam centre, when $r \to 0$, the force is linearly proportional to the impact factor:

$$F(r)|_{r\to 0} = -\frac{Ne^2}{\pi\varepsilon_0\sigma_z}\frac{r}{\sigma_T^2}. \tag{4.5}$$

The force changes the transverse momentum of the test particle according to:

$$\Delta p_\mathrm{T} = \int_{-\infty}^{+\infty} F\mathrm{d}t = -2e\int E_\mathrm{r}\mathrm{d}t. \tag{4.6}$$

The change of the polar angle of the particles can be calculated using:

$$\tan\Delta\theta = \frac{\Delta p_\mathrm{T}}{p} \approx -\frac{2e}{\gamma mc}\int_{-\infty}^{+\infty} E_\mathrm{r}\mathrm{d}t = -\frac{2e}{\gamma mc}E_\mathrm{r}\Delta t, \tag{4.7}$$

where: $\Delta t = \frac{\sigma_z}{2c}$ - bunch crossing time.

At CLIC, the beams are flat, with $\sigma_x \ll \sigma_y$. In the case of the Gaussian flat beams, the kick can be described separately for each direction:

$$\Delta x' = -\frac{2Nr_\mathrm{e}}{\gamma\sigma_x(\sigma_x + \sigma_y)}, \tag{4.8a}$$

$$\Delta y' = -\frac{2Nr_\mathrm{e}}{\gamma\sigma_y(\sigma_x + \sigma_y)}, \tag{4.8b}$$

where: r_e - classical electron radius.

The force in Equation (4.5) is a focusing force, which can be described equivalently as a lens acting upon the particle with a focusing length $f_{x,y}$ equal to:

$$\frac{1}{f_{x,y}} = \frac{2Nr_\mathrm{e}}{\gamma\sigma_{x,y}(\sigma_x + \sigma_y)}. \tag{4.9}$$

The relative change of the impact parameter is called disruption and can be defined as:

$$D_{x,y} = \frac{\Delta r}{r} = -\frac{\sigma_z}{f_{x,y}}. \tag{4.10}$$

Disruption is equal to one when the focal length due to the beam-beam force is similar to the bunch length.

4.2 Luminosity

Luminosity $\mathcal{L}$ is a proportionality parameter between the rate of an event R in the case of instantaneous luminosity or the total number of recorded events for the integrated luminosity, and the cross-section of the process σ:

$$R = \mathcal{L}\sigma. \tag{4.11}$$

In the first order, and neglecting beam-beam interactions, a head-on electron–positron collision of Gaussian beams has a luminosity that is expressed by:

$$\mathcal{L}_0 = \frac{fN_1N_2}{4\pi\sigma_x\sigma_y}, \tag{4.12}$$

where: f - frequency of collisions, $N_{1,2}$ - number of particles in beam 1 and 2, $\sigma_{x,y}$ - horizontal and vertical r.m.s. beam sizes.

The transverse beam sizes at the IP are reduced due to the pinching effect, and in result, the luminosity is enhanced:

$$\mathcal{L}_1 = H_D\mathcal{L}_0, \tag{4.13}$$

where: H_D - luminosity enhancement factor, and $\mathcal{L}_0$ has the same form as in Equation (4.12).

The luminosity enhancement is defined by Equation (4.13), and can be expressed as:

$$H_D = \frac{\mathcal{L}_1}{\mathcal{L}_0} = \frac{\sigma_x\sigma_y}{\sigma_x^*\sigma_y^*}, \tag{4.14}$$

where the $\sigma_{x,y}^*$ are the reduced transverse r.m.s. beam sizes.

The analytical derivation of the enhancement factor exists only for a limited number of cases and where the disruption is small: $D \ll 1$. At CLIC, the disruption is more significant with $D \geq 1$, hence numerical simulations are needed to establish the value of the luminosity enhancement.

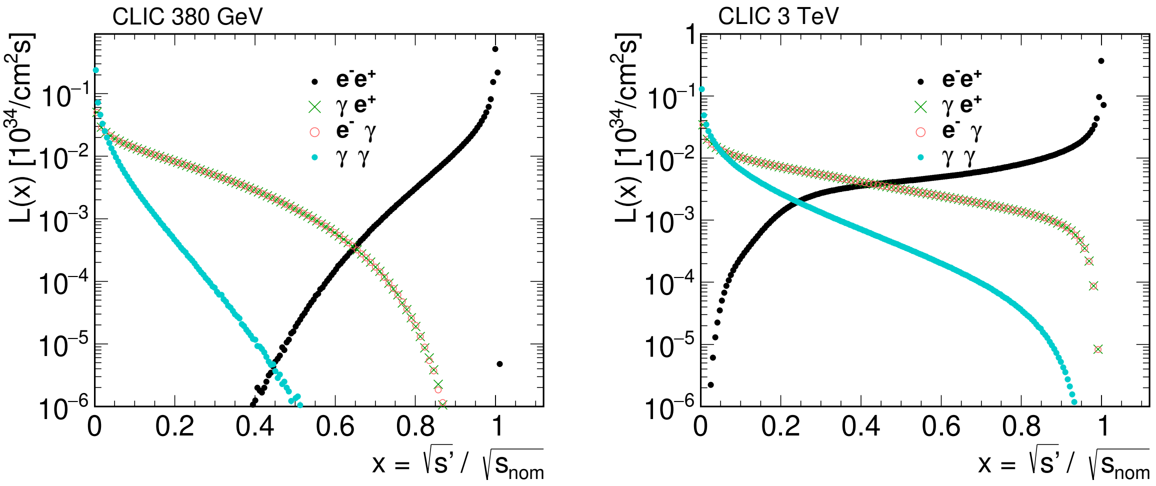

Figure 4.1: Luminosity spectra for 380 GeV(left) and 3 TeV(right) CLIC.

The luminosity spectra simulated with Guinea-Pig using 380 GeV and 3 TeV CLIC parameters are shown in Figure 4.1. The luminosity has a broad distribution that is diluted by the emission of beamstrahlung photons immediately before the collision.

The electron–positron luminosity spectrum is peaked around the nominal energy. At 3 TeV, the luminosity has a broad region of slight luminosity decrease, located between 30% and 90% of the nominal centre-of-mass energy. At 380 GeV, the electron–positron luminosity has a steeper slope, and there are more interactions near the nominal energy than at 3 TeV, due to less intense emission of beamstrahlung photons.

Beamstrahlung photons colliding with particles of the oncoming beam give rise to $e^+\gamma$ and $e^-\gamma$ initial states. The maximal energy of these collisions is limited to below 90% of the nominal centre-of-mass energy. Beamstrahlung photons are also interacting with the photons of the oncoming beam, and create the $\gamma\gamma$ initial state. All three luminosity spectra have a maximum at the lowest energies.

The instantaneous luminosity for four initial states is summarised in Table 4.1. The geometrical luminosity, calculated using Equation (4.12) and with beam parameters coming from Table 3.1, yields significantly lower luminosity than the number coming from Guinea-Pig. This is connected with a strong pinching effect present in collisions at both energy stages. The ratio between the geometrical and simulated luminosity can be used to calculate the luminosity enhancement factor. The H_D is 1.8 at 380 GeV and 2.3 at 3 TeV. The stronger pinching at 3 TeV is explained by stronger focusing force during a collision and beamstrahlung emission, as discussed in section 4.3.

The peak luminosity is the luminosity coming from collisions within 1% from the nominal centre-of-mass energy at each respective stage. It constitutes a more significant proportion of the total instantaneous luminosity at the lower energy stage, which is also consistent with weaker focusing and less intense emission of the beamstrahlung radiation than at 3 TeV.

At both energy stages, the $e^+\gamma$ and $e^-\gamma$ initial states have equal contributions to the luminosity, as the beams are symmetrical. These collisions have a lower rate than the e^+e^-. The $\gamma\gamma$

Table 4.1: Instantanoeus luminosity for four initial states: e^+e^-, $e^+\gamma$, $e^-\gamma$, and $\gamma\gamma$ simulated with Guinea-Pig with 380 GeV and 3 TeV CLIC beam parameters. The e^+e^- geometrical luminosity is calculated using Equation (4.12) and beam parameters coming from PLACET simulations, shown in Table 3.1. The e^+e^- peak luminosity denotes the luminosity that comes from collisions with energies within 1% of the nominal centre-of-mass energy.

	380 GeV $\left[\times 10^{34}\frac{1}{\mathrm{scm}^2}\right]$	3 TeV $\left[\times 10^{34}\frac{1}{\mathrm{scm}^2}\right]$
e^+e^- geometrical	0.82	2.3
e^+e^-	1.5	6.4
e^+e^- peak	0.9	2.3
$e^+\gamma$	0.8	5.1
$e^-\gamma$	0.8	5.1
$\gamma\gamma$	0.6	4.5

Table 4.2: Share of luminosity coming from collision above certain centre-of-mass energies is simulated with Guinea-Pig with 380 GeV and 3 TeV beam parameters.

	380 GeV	3 TeV
over 99% of $\sqrt{s}_{\mathrm{nominal}}$	60	36.3
over 90%	90.3	57.1
over 80%	97.6	68.6
over 70%	99.5	76.7
over 50%	100	88.5

initial state is the least probable interaction and leads to the lowest number of collisions.

The share of the luminosity coming from electron–positron taking place above certain energy thresholds are summarised in Table 4.2. As shown in Table 4.1, the luminosity at 380 GeV is more concentrated around the nominal centre-of-mass energy with the share of collisions in the peak is a factor of about two larger than at 3 TeV. All of the electron–positron collisions are above half of the nominal $\sqrt{s}_{\mathrm{nominal}}$ at 380 GeV, while at 3 TeV this share is only 88.5%.

The luminosity is significantly more spread out among the possible energies at 3 TeV. This is an issue for the physics programme because it limits the rate of events at the highest energies reachable by the machine.

4.3 Beamstrahlung emission

The emission of the synchrotron radiation during an electron–positron collision is coupled to the disruption parameter described by Equation (4.10). The beamstrahlung radiation is characterised by the critical frequency, classically defined as [62]:

$$\omega_\mathrm{c} = \frac{3}{2}\gamma\omega_\rho, \tag{4.15}$$

where $\omega_\rho = \frac{c}{\rho}$ is the orbital frequency on the curved trajectory, and ρ is the bending radius, typically [63] in the order of 10^{-6} and smaller than the bunch length. The description of the emission of the synchrotron radiation that is not quantum-mechanically rigorous is given in section 6.1.

The radiation and related phenomena of coherent pair production can be described in term of a dimensionless and Lorentz-invariant beamstrahlung parameter Υ, defined as [64]:

$$\Upsilon = \frac{2}{3}\frac{\hbar\omega_\mathrm{c}}{\mathcal{E}} = \gamma\frac{< B >}{B_\mathrm{c}} \tag{4.16}$$

where: $\mathcal{E}$ - electron energy before the beamstrahlung emission, γ - Lorentz factor, $< B >$ - average magnetic field experienced by a test particle during beam crossing, $B_\mathrm{c} = 4.4 \cdot 10^9\,\mathrm{T}$ - Schwinger critical field.

The beamstrahlung parameter changes during the collision. For the Gaussian beams the average and maximal values during an electron–positron collision can be estimated as [64]:

$$< \Upsilon > = \frac{5}{6}\frac{N r_\mathrm{e}^2\gamma}{\alpha\sigma_z(\sigma_x + \sigma_y)}, \tag{4.17a}$$

$$\Upsilon_\mathrm{max} = \frac{2N r_\mathrm{e}^2\gamma}{\alpha\sigma_z(\sigma_x + 1.5\cdot\sigma_y)}, \tag{4.17b}$$

where: N - number of particles, r_e - classical electron radius, γ - Lorentz factor, α - fine structure constant, σ_z - longitudinal r.m.s. beam size, $\sigma_{x,y}$ - transverse r.m.s. beam sizes.

Using Equation (4.17), one can calculate the maximal value of the beamstrahlung parameter for the CLIC beam conditions. Υ_max is equal to 0.4 at 380 GeV, and 13 at 3 TeV. The maximum beamstrahlung parameter value recorded in Guinea-Pig simulations is around 0.6 at 380 GeV and around 14 at 3 TeV. In both cases, the beamstrahlung parameter in Guinea-Pig reaches higher values than calculated using Equation (4.17). In both the calculated Υ and value obtained from simulations, it is clear that the impact of the beamstrahlung emission on the beams and coherent particle production is more significant at the higher energy stage.

The energy distributions of the beamstrahlung photons at 380 GeV and 3 TeV simulated with Guinea-Pig are shown in Figure 4.2. The average photon energy is equal to 6% of the beam energy at 380 GeV, and 13% at 3 TeV. Therefore, the recoil of the electron due to the emission of the radiation cannot be neglected. A formulation taking into account Quantum Electro-Dynamics (QED) of the emission, such as the Sokolov–Ternov formula [65], is needed. Using the Sokolov–Ternov formula, the frequency spectrum of the beamstrahlung can be described

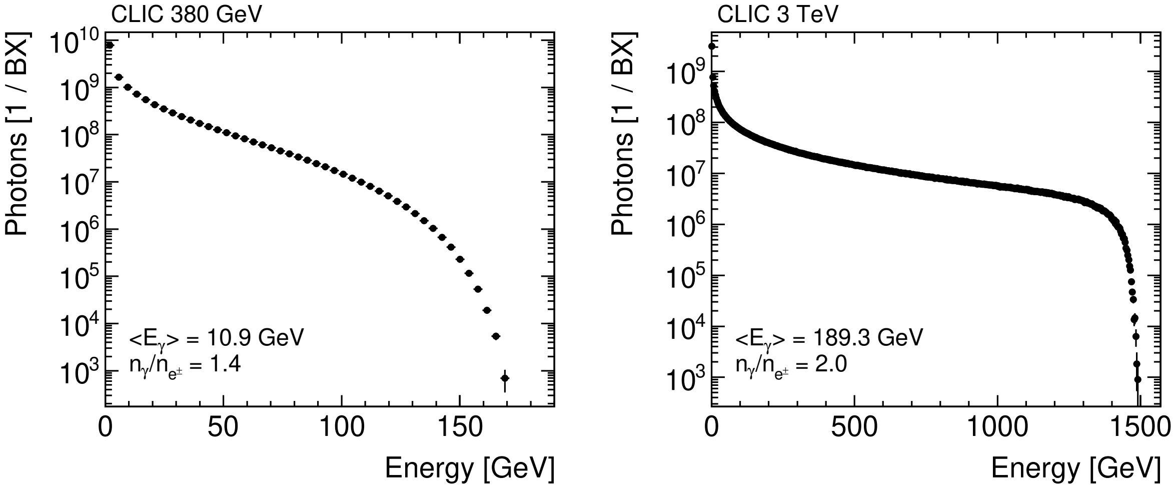

Figure 4.2: Energy distributions of beamstrahlung photons emitted in electron–positron collisions at 380 GeV (left) and 3 TeV (right).

as [63]:

$$P(\omega) = \frac{\alpha}{\sqrt{3}\pi\gamma^2}\left[\int_{\xi}^{+\infty} \mathrm{K}_{5/3}(\xi')\mathrm{d}\xi' + \frac{y^2}{1-y}\mathrm{K}_{2/3}(\xi)\right], \tag{4.18}$$

where: K - modified Bessel functions, $\xi = \frac{2\omega}{3\Upsilon(E-\omega)} = \frac{\omega}{\omega_c}\frac{1}{1-\omega/\mathcal{E}} = \frac{2}{3\Upsilon}\frac{y}{1-y}$, and $y = \frac{\omega}{E}$.

In the classical limit, where $\xi \to +\infty$ and $\mathrm{K}(\xi) \to 0$, the second term of Equation (4.18) can be neglected and the equation describes the classical spectrum of the synchrotron radiation.

For low frequencies ($y \approx 0$), the Sokolov–Ternov reproduces the behaviour of the classical description of the SR. The difference concentrates in the high-energy region. The classical formula extends to arbitrarily high frequencies and energies, while in the Sokolov–Ternov formula the frequencies are truncated at the energy of the emitting particle. This behaviour can be seen for the high energy stage of CLIC, as shown in Figure 4.2. The beamstrahlung distribution rapidly falls for photon energies close to the beam energy.

The way to reduce the impact of the beamstrahlung emission is through minimisation of the beamstrahlung parameter described in Equation (4.17). The minimisation of Υ while maintaining luminosity performance, as described by Equation (4.12), leads to the choice of flat beams for CLIC. Another example of the optimised design aiming to minimise the impact of the beamstrahlung and improve the luminosity quality is a beam parameter set for the run around the top-quark mass threshold at 350 GeV. There, an increase of the bunch length and the reduction of the charge reduces the energy loss per particle from 10.7 GeV to 8.5 GeV, and improves the luminosity quality needed for a precise top-quark mass measurement [27].

4.4 Creation of coherent and incoherent pairs

Virtual electron–positron pairs surround a photon travelling through a vacuum. These pairs cannot become real due to the four-momentum conservation. However, in a strong magnetic field, the field can provide momentum for the virtual particles to bring them on the shell. In the pair-rest frame, the electric field E to create an electron–positron pair is [64]:

$$E = \frac{\hbar\omega}{2m_\mathrm{e}c^2}B, \tag{4.19}$$

where ω is the photon frequency, B is the magnetic field induction in the laboratory frame and m_e is the electron mass. The magnetic field is $B = B_c\Upsilon$, where the B_c is the critical Schwinger field, equal to $4.4 \cdot 10^9$ T, and Υ_max is about 13 for 3 TeV CLIC.

At the production threshold, a particle with charge e should gain its rest mass within one Compton length λ_c to become real. The production threshold condition is thus:

$$eE\lambda_\mathrm{c} \approx m_\mathrm{e}c^2, \tag{4.20}$$

with λ_c of an electron equal to 2.4 m, leading to the necessary electric field being about $2.1 \cdot 10^{11}$ MV/m.

In the electron–positron collisions of the nanometre-sized beams the total number of created coherent pairs per beam particle is [63]:

$$n_\mathrm{c} = \left(\frac{\alpha\sigma_\mathrm{z}}{\gamma\lambda_\mathrm{c}}\Upsilon\right)^2 \Omega(\Upsilon), \tag{4.21}$$

where σ_z is the longitudinal beam size, and $\Omega(\Upsilon)$ is:

$$\Omega(\Upsilon) = \begin{cases} \frac{7}{128}\mathrm{e}^{-\frac{16}{3\Upsilon}} & \text{if} \quad \Upsilon \leq 1 \\ 0.295\Upsilon^{-\frac{2}{3}}\left(\ln\Upsilon - 2.488\right) & \text{if} \quad \Upsilon \gg 1 \end{cases}$$

The production of coherent pairs is exponentially suppressed for beamstrahlung parameter values below one. At 380 GeV, the maximal Υ is around 0.6, therefore the coherent pairs are not produced in significant quantities. The Guinea-Pig simulations result in no coherent pairs produced at this energy stage.

At 3 TeV, the beamstrahlung is more significant with the $\Upsilon \approx 14$. A large number of coherent pairs is being produced, in the order of 10^8 per bunch crossing. The coherent pairs thus constitute a significant proportion of the beam charge of the colliding bunches.

The energy production threshold scales inversely proportional to the beamstrahlung parameter [63], resulting in high energies of the produced pairs, with the average energy of 300 GeV. The large momenta translate to particles being strongly boosted in the beam direction. As a result, the coherent pairs have polar angles lower than 10 mrad, as shown in Figure 4.3. Due to the significant energy they carry, the coherent pairs constrain the acceptance of the detector to above 10 mrad, which needs to be provided for the outgoing beam pipe to safely remove these particles from the detector region.

Coherent electron–positron pairs can also be produced via a trident cascade ($\mathrm{e}^\pm \to \mathrm{e}^\pm\mathrm{e}^+\mathrm{e}^-$). The trident process involves a virtual photon carried by a beam particle in a strong electromagnetic field. The number of pairs created through in trident cascades scales differently than for the coherent pairs, linearly with the Υ rather than quadratically. The contribution from the trident cascades process is negligible when $\Upsilon \ll 1$.

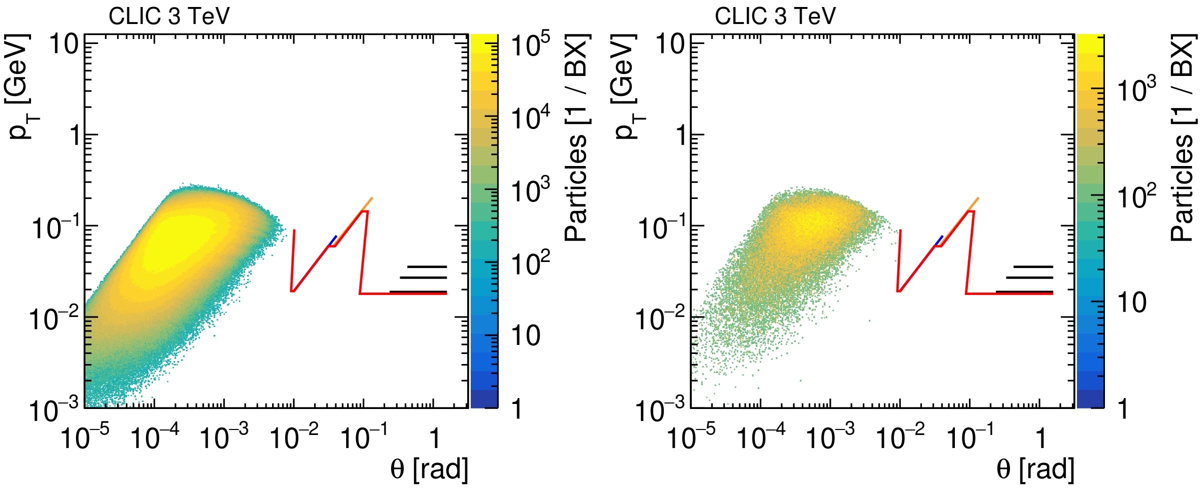

Figure 4.3: Polar angle and transverse momentum distributions for coherent pairs (left) and trident cascades (right) at 3 TeV.

The polar angle distributions of the trident cascades is shown in Figure 4.3(right). In the Guinea-Pig simulations, the trident process does not lead to pair production at the lower energy stage, but there is a large number of pairs produced at 3 TeV. On average, $6.7 \cdot 10^7$ trident particles are produced per bunch crossing, with an average energy of 250 GeV.

A significant number of the low energy e^+e^- pairs are produced by incoherent processes: Breit–Wheeler ($\gamma\gamma \rightarrow e^+e^-$), Bethe–Heitler ($e^\pm\gamma \rightarrow e^\pm e^+e^-$), and Landau–Lifshitz ($e^+e^- \rightarrow e^+e^-e^+e^-$) [66]. In total, there are $1.7 \cdot 10^7$ incoherent electrons and positrons produced per train at 380 GeV and $8.7 \cdot 10^7$ at 3 TeV. The average energy of incoherent electrons or positrons with a $p_T > 20$ MeV and $\theta > 10$ mrad is 1.7 GeV and 60 GeV respectively. The distribution of the incoherent pairs as a function of transverse momentum and polar angle is shown in Figure 4.4. Due to their low energy in comparison with coherent particles, the incoherent pairs are deflected by the electromagnetic fields during the collision and gain large polar angles. At 380 GeV, $1.3 \cdot 10^3$ particles per train can reach the first layer of the vertex barrel, and at 3 TeV there are $4.5 \cdot 10^3$ particles per train in the acceptance of the first vertex layer. Therefore, the incoherent pairs are a source of direct background and can significantly impact the occupancy levels of the detector.

The same processes that produce e^+e^- pairs can lead to the production of incoherent $\mu^+\mu^-$ pairs, although in much lower quantities. There are on average 920 incoherent muons produced per train at 380 GeV and $3.6 \cdot 10^3$ at 3 TeV, with an average energy of 5 GeV and 84 GeV respectively. The distributions of the incoherent muons as a function of polar angle and transverse momentum are shown in Figure 4.5. A large proportion of the produced $\mu^+\mu^-$ pairs can cause energy depositions in the vertex and tracker detectors and calorimeter endcaps.

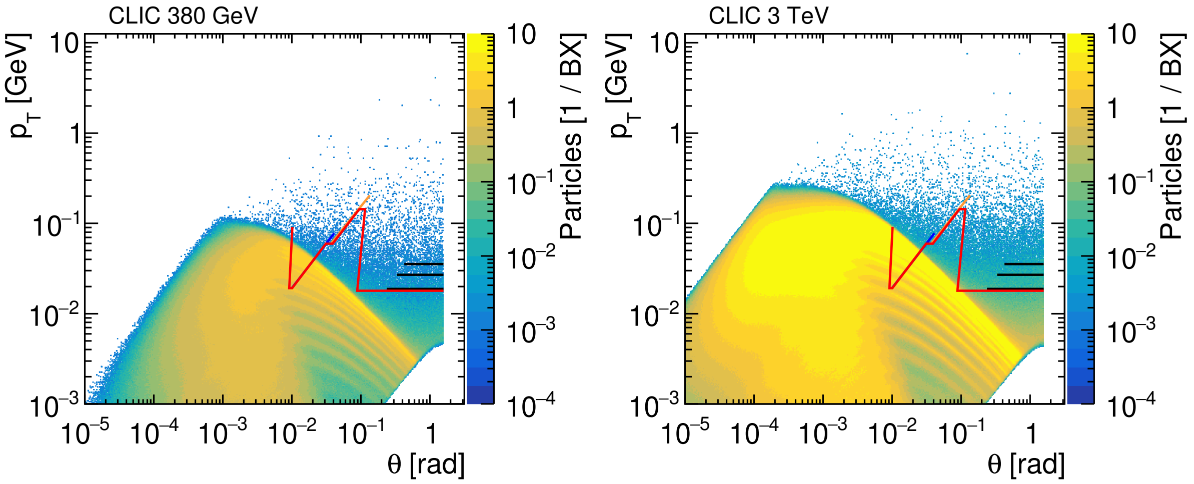

Figure 4.4: Polar angle and transverse momentum distributions of incoherent electron–positron pairs for 380 GeV (left) and 3 TeV (right). The red lines signify the beam pipe, the blue BeamCal, the orange LumiCal and the black lines the vertex barrel layers.

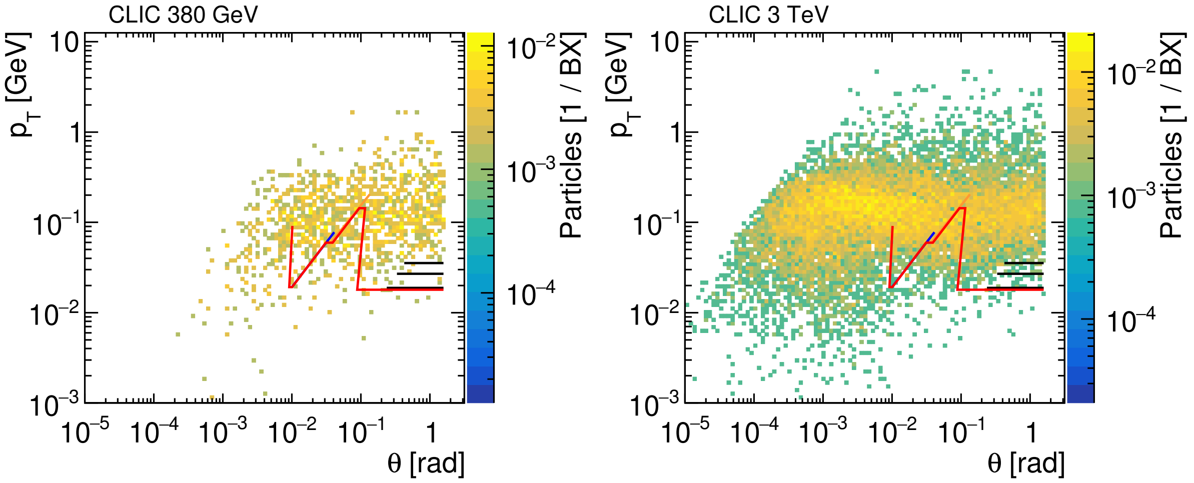

Figure 4.5: Polar angle and transverse momentum distributions of incoherent muon pairs for 380 GeV (left) and 3 TeV (right) CLIC. The red lines signify the beam pipe, the blue BeamCal, the orange LumiCal and the black lines the vertex barrel layers.

4.5 Creation of hadrons

In the e^+e^- collisions many high-energy beamstrahlung photons are produced. The $\gamma\gamma$ interactions lead predominantly to the production of coherent and incoherent pairs, but with a small probability hadronic states can also be created. Such final states of photon interactions are called $\gamma\gamma \to$ hadron events. The cross-sections of the $\gamma\gamma \to$ hadron events processes have been measured up to 110 GeV in experiments at LEP [67]. For the higher energies, only parametrisation of the cross-section are available.

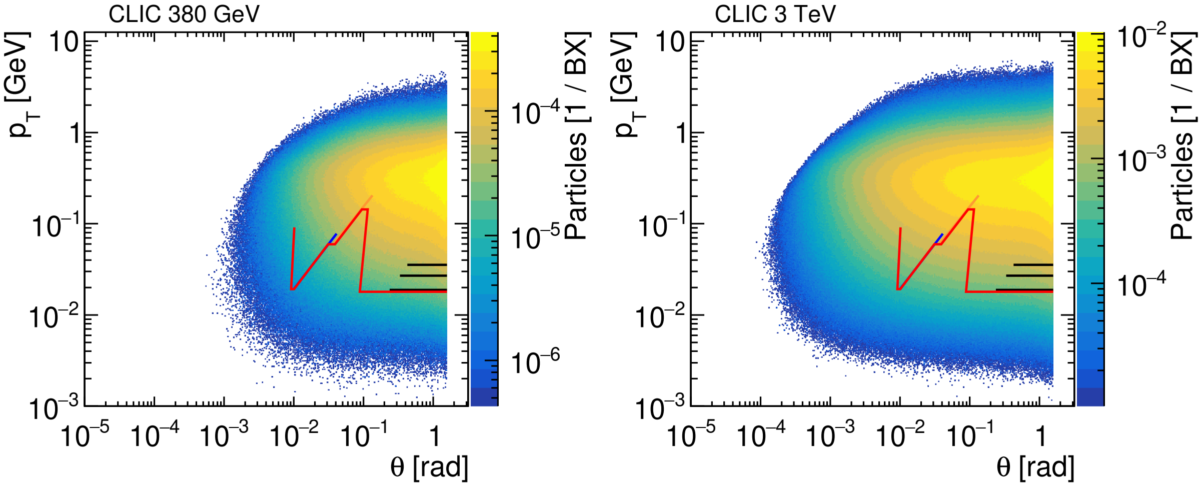

Figure 4.6: Polar angle and transverse momentum distributions of γγ → hadron eventsfor CLIC at 380 GeV(left) and 3 TeV(right). A 2 GeV centre-of-mass threshold for γγ → hadron production is applied.

The initial photon states for γγ → hadron events are created in the Guinea-Pig with the Schuler and Sjostrand parametrisation of the $\gamma\gamma$ cross-section:

$$\sigma_{\gamma\gamma}(E^2_{\text{cm}}[\text{GeV}]) = 211\,\text{nb}\,(E^2_{\text{cm}})^{0.0808} + 215\,\text{nb}\,(E^2_{\text{cm}})^{-0.4525}. \tag{4.22}$$

The resulting quark pairs are hadronized using Pythia 6.4 [49] with OPAL tunes [68]. Guinea-Pig imposes a lower energy limit of the initial states of $\sqrt{s_{\gamma\gamma}} = 2\,\text{GeV}$.

The transverse momentum against polar angle distributions of the γγ → hadron particles are shown in Figure 4.6. There are 17 times more γγ → hadron events per bunch crossing at 3 TeV than at 380 GeV, with 3.12 γγ → hadron events at 3 TeV and 0.18 at 380 GeV. A high percentage, 74% at 380 GeV and 53% at 3 TeV, of particles produced in γγ → hadron events is visible to the detector. A charged particle can interact with the sensitive material of the CLIC detector if its polar angle is above 10 mrad and the transverse momentum is larger than 20 MeV. The particles produced in the hadronic processes are particularly concentrated in the central region of the detector. Therefore, the γγ → hadron events are a direct source of background in the vertex and tracker detectors, as well as the calorimeters.

Table 4.3: The yield and average energy for each type of beam-induced background produced in the Guinea-Pig simulations at 380 GeV and 3 TeV. Safety factors not included.

			380 GeV	3 TeV
beamstrahlung photons	$< N >$	$[\gamma/e^{\pm}/BX]$	1.4	2.0
	$< E >$	[GeV]	11.0	$1.9 \cdot 10^2$
coherent e^+e^- pairs	$< N >$	[1/BX]	0	$6.1 \cdot 10^8$
	$< E >$	[GeV]	0	$3.1 \cdot 10^2$
trident e^+e^- pairs	$< N >$	[1/BX]	0	$6.7 \cdot 10^6$
	$< E >$	[GeV]	0	$2.1 \cdot 10^2$
incoherent e^+e^- pairs	$< N >$	[1/BX]	$4.9 \cdot 10^4$	$2.8 \cdot 10^5$
	$< E >$	[GeV]	4.6	75
incoherent $\mu^-\mu^+$ pairs	$< N >$	[1/BX]	2.6	11
	$< E >$	[GeV]	5.3	84
$\gamma\gamma \rightarrow$ hadron events	$< N >$	[events/BX]	0.18	3.2
	$< E >$	[GeV]	2.2	12

4.6 Background overview

The beam-induced background composition and yields vary significantly between the energy stages. At 380 GeV, the average beamstrahlung parameter is below 0.6, and the processes leading to coherent and trident pair production are strongly suppressed, and these processes are not observed. The relevant sources of direct background at 380 GeV include the incoherent pairs, $\gamma\gamma \rightarrow$ hadron events, and incoherent muons. The energy and polar angle distribution of background sources at 380 GeV are shown in Figure 4.7. The incoherent pairs are expected to be the dominating source of hits due to their high energy reach and polar angle distribution.

At the higher energy stage, the beamstrahlung parameter is significantly above 1, and the coherent processes are allowed. The distributions of the energy and polar angles of the produced background particles are shown in Figure 4.8. The coherent and trident pairs are numerically dominant over the other type of unwanted particles. Due to the high energy they carry the coherent particles pose a constraint on the design of the forward calorimeter region. No material should be placed at polar angles lower than 10 mrad to ensure a safe transport of the coherent and trident pairs from the detector region.

The main sources of hits in the detector at the 3 TeV energy stage are expected to be incoherent pairs and $\gamma\gamma \rightarrow$ hadron events, which have similar multiplicity in the mid-rapidity region. The incoherent muons are also present in the acceptance of the detector, although they are not as numerous as the other sources of background with a factor 100 fewer particles with polar angles larger than 100 mrad.

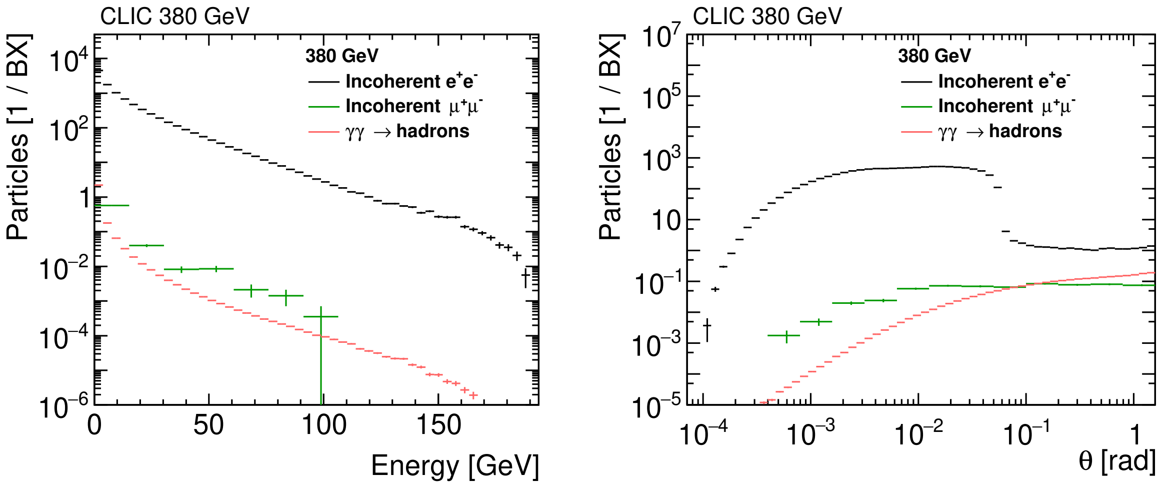

Figure 4.7: Energy distribution (left) and polar angle distribution (right) per bunch crossing of beam-induced backgrounds. Both figures are for CLIC at 380 GeV. A p_T cut of 20 MeV is applied to all shown particles and a 2 GeV centre-of-mass threshold for $\gamma\gamma \rightarrow$ hadrons production is used.

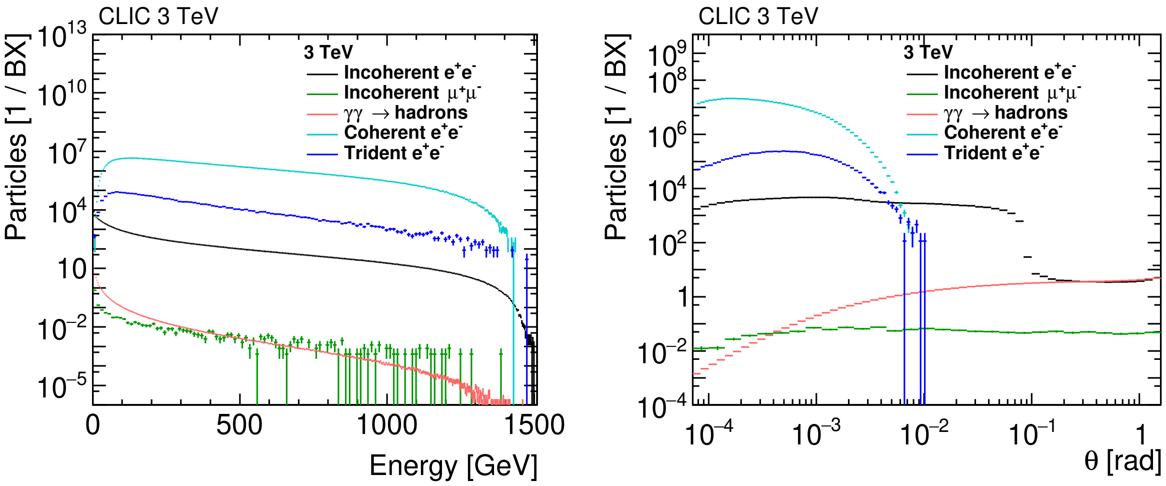

Figure 4.8: Energy distribution (left) and polar angle distribution (right) per bunch crossing of beam-induced backgrounds. Both figures are for CLIC at 3 TeV. A p_T cut of 20 MeV is applied to all shown particles and a 2 GeV centre-of-mass threshold for $\gamma\gamma \rightarrow$ hadrons production is used.

Chapter 5

Optimisation of the BDS apertures

This chapter contains the results of optimisation of the Beam Delivery System apertures. The knowledge of apertures provides important limits for the design of the CLIC Beam Delivery System. The apertures at 380 GeV and 3 TeV optimised in this chapter are used as input in the simulations of the synchrotron radiation, presented in Chapter 6.

In section 5.1 the aperture limitations are described and an initial aperture model is derived. In section 5.2 the resistive wall effect is derived and the results of the simulated impact of the wakefield on the CLIC beams in the BDS are presented. Finally, the apertures are optimised to limit the impact of the resistive wall effect in section 5.3.

The results presented in section 5.2.3 and section 5.3 were also published in [69].

5.1 Aperture limitations

The aperture calculation needs to take into account the lower limits coming from beam sizes and machine safety, and the emission of the synchrotron radiation and upper limits linked to the use of normal-conducting magnets in CLIC.

The very minimal estimate for the beam pipe aperture comes from the beam sizes. The beam sizes $\sigma_{x,y}$ can be calculated from the accelerator lattice parameters:

$$\sigma_{x,y} = \sqrt{\varepsilon_{x,y}\beta_{x,y} + (D_{x,y}\delta_E)^2}, \tag{5.1}$$

where: $\varepsilon_{x,y}$ - geometrical beam emittance, $\beta_{x,y}$ - betatron functions, $D_{x,y}$ - dispersion, δ_E - width of the normalised energy spread distribution.

This absolute limit of the lower aperture has to be multiplied by the collimation depth to ensure the safety of the final doublet magnets and the detector region. The collimation depth value comes from the collimation system optimisation to ensure removal of the particles located far from the beam centre that can be lost in the FFS or emit synchrotron radiation that can deposit energy in the sensitive material of the detector. The collimation depths of $15\sigma_x$ and $55\sigma_y$ are valid at 500 GeV and 3 TeV energy stages with $L^* = 3.5\,\text{m}$ of CLIC [70], and $L^* = 6\,\text{m}$ [71], and is used as the initial estimate for the 380 GeV BDS.

Given the limits described above the initial inner beam pipe apertures are calculated for each element along the BDS using the following formula:

$$R_{\text{min}}[\text{mm}] = \max\{r_{\text{wake}},\ 0.1\,\text{mm} + \max\{15\sigma_x, 55\sigma_y\}\}, \tag{5.2}$$

where: r_{min} - minimal radius coming from beam stability considerations, 0.1 mm - safety margin for alignment imperfections [21], and the beam sizes calculated using Equation (5.1).

The minimal radii r_{wake} are based on the previous study of the resistive wall wakefield at 500 GeV and 3 TeV with a shorter L^* [8]. The aperture of 6 mm can be used directly at 3 TeV, while the value for the 380 GeV BDS is not available. The impact of the wakefield kicks (Equation (5.19)) all other things being equal between the two designs scales inversely with energy. Therefore, one can scale the minimal radius found for the 500 GeV BDS of 12 mm to 15.5 mm at 380 GeV using the ratio of the energy.

The bending magnets present in the CLIC BDS do not need strong magnetic fields to perform their task, which is to create dispersion needed for chromaticity correction in sextupoles [21]. The bending magnets in the FFS have the bending radius in the order of 100 km, and the aperture requirements are not a limiting factor in comparison with the quadrupole magnets. The maximum pole magnetic induction in a quadrupole is set conservatively at 1.5 T, due to the magnetic field saturation in iron at around 2 T [72]. The upper limit of a quadrupole aperture can be estimated in convenient units using the following equation:

$$r_{\text{max}}[\text{mm}] = 0.3 \times \frac{B_{\text{max}}[\text{T}]L[\text{m}]}{E_{\text{beam}}[\text{GeV}]K_1[\text{m}^2]}, \tag{5.3}$$

where: B_{max} [T] - maximal induction of the magnetic field at the pole, L [m] - magnet length, E_{beam} [GeV] - beam energy, K_1 [m^2] - normalized strength of a quadrupole.

The apertures in the BDS at 380 GeV and 3 TeV are obtained by applying Equation (5.2) to each element of the lattice. The resulting aperture models are shown in Figure 5.1. There are a few points, for example at the beginning of the BDS, where the calculated aperture needs to be larger than allowed by the quadrupole magnets upper limitation coming from reaching the maximal pole field. The issue can be addressed by lowering the gradient of these quadrupoles and proportionally extending their lengths to achieve the same integrated magnetic effect.

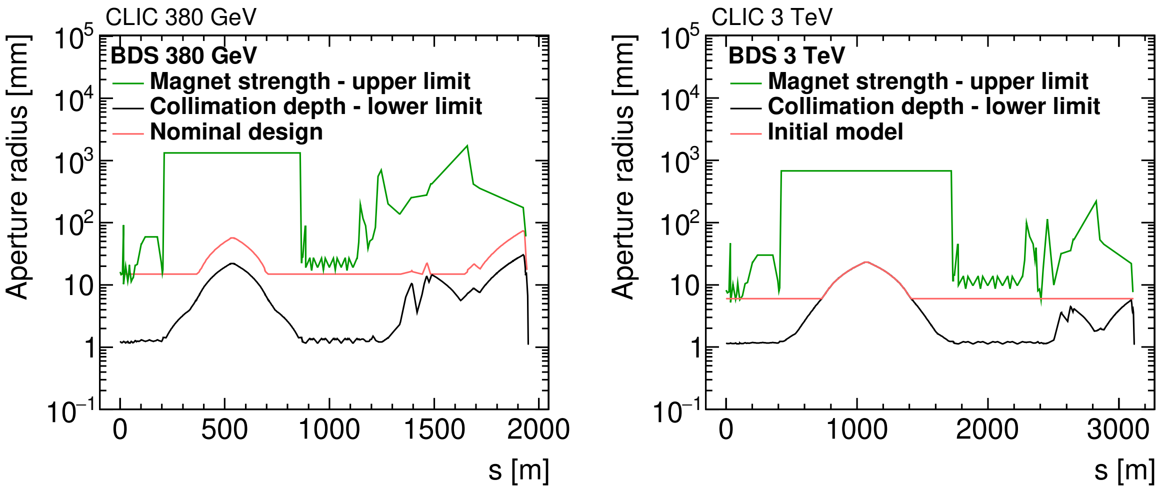

Figure 5.1: Initial aperture model along the BDS at 380 GeV (left) and 3 TeV (right), with limits imposed from the beam collimation depth and maximal allowable pole field strength in quadrupoles.

5.2 Resistive wall effect

Resistive wall wakefield originates from electromagnetic interaction between a beam and vacuum chamber walls that are not perfectly conductive. The resistance in the walls leads to an image-current travelling on the chamber surface that is delayed with regard to its source. The delayed charge interacts with bunches travelling behind the source and can lead to a collective instability. For a collective instability to occur, the beams need to be either non-relativistic or the walls rough and not perfectly conductive. The former is not the case in the CLIC BDS, as the beams are ultra-relativistic with the Lorentz factor larger than 10^5 at all energy stages. However, the second requirement is fulfilled and the resistive wall effect can impact the stability and quality of the beams.

First, the resistive wall wakefield formalism derivation is given in section 5.2.1. Then, the simulation methods are described in section 5.2.2 and the simulation results are presented in section 5.2.3.

5.2.1 Resistive wall wakefield formulation

In this section the most important steps of a derivation of the resistive wall wakefield formula are presented. The ultra-relativistic beams, infinitely thick vacuum chamber walls and axial symmetry of the chamber are assumed. All equations until up to the final formula of the wakefield are in cgs units. The derivation described in this section is based on the formalism developed in the literature [73].

First, let us explicitly write the Maxwell equations in cylindrical coordinates (r, θ, s):

$$\frac{1}{r}\frac{\partial(rE_r)}{\partial r}+\frac{1}{r}\frac{\partial E_\theta}{\partial \theta}+\frac{\partial E_s}{\partial s}=4\pi\rho \tag{5.4a}$$

$$\frac{1}{r}\frac{\partial B_s}{\partial \theta}-\frac{\partial B_\theta}{\partial s}+\frac{1}{c}\frac{\partial E_r}{\partial t}=\frac{4\pi}{c}j_r \tag{5.4b}$$

$$\frac{\partial B_r}{\partial s}-\frac{\partial B_s}{\partial r}-\frac{1}{c}\frac{\partial E_\theta}{\partial t}=\frac{4\pi}{c}j_\theta \tag{5.4c}$$

$$\frac{1}{r}\frac{\partial(rB_\theta)}{\partial r}-\frac{1}{r}\frac{\partial B_r}{\partial \theta}-\frac{1}{c}\frac{\partial E_s}{\partial t}=\frac{4\pi}{c}j_s \tag{5.4d}$$

$$\frac{1}{r}\frac{\partial(rB_r)}{\partial r}+\frac{1}{r}\frac{\partial B_\theta}{\partial \theta}+\frac{\partial B_s}{\partial s}=0 \tag{5.4e}$$

$$\frac{1}{r}\frac{\partial E_s}{\partial \theta}-\frac{\partial E_\theta}{\partial s}+\frac{1}{c}\frac{\partial B_r}{\partial t}=0 \tag{5.4f}$$

$$\frac{1}{r}\frac{\partial(rE_\theta)}{\partial r}-\frac{1}{r}\frac{\partial E_r}{\partial \theta}+\frac{1}{c}\frac{\partial B_s}{\partial t}=0 \tag{5.4g}$$

$$\frac{\partial E_r}{\partial s}-\frac{\partial E_s}{\partial r}+\frac{1}{c}\frac{\partial B_\theta}{\partial t}=0 \tag{5.4h}$$

The beam charge ρ and current $\vec{j}$ can be decomposed in terms of multipole moments, assuming the beam charge is distributed as an infinitesimally thin ring with a radius a:

$$\rho = \sum_{m=0}^{\infty} \rho_m = \sum_{m=0}^{\infty} \frac{I_m}{\pi a^{m+1}(1+\delta_{m0})} \delta(s-ct)\delta(r-a)\cos m\theta, \tag{5.5a}$$

$$\vec{j} = \sum_{m=0}^{\infty} \vec{j}_m = \sum_{m=0}^{\infty} c\rho_m \hat{s}, \tag{5.5b}$$

where: I_m - mth moment of the beam, e.g. the monopole moment I_0 is the net charge of the beam, r - aperture radius, m - moment number, and $\delta(s-ct)$ - Dirac delta.

The charge density and current are proportional to cos $m\theta$, therefore the angular dependence of the field components E_r, E_s and B_θ are also proportional to cos $m\theta$, while E_θ, B_r and B_s are proportional to sin $m\theta$. The field components described above can be written in terms of Fourier transformations:

$$(E_r, E_s, B_\theta) = \cos m\theta \int_{-\infty}^{\infty} \frac{dk}{2\pi} e^{ikz} (\tilde{E}_r, \tilde{E}_s, \tilde{B}_\theta), \tag{5.6a}$$

$$(E_\theta, B_r, B_s) = \sin m\theta \int_{-\infty}^{\infty} \frac{dk}{2\pi} e^{ikz} (\tilde{E}_\theta, \tilde{B}_r, \tilde{B}_s), \tag{5.6b}$$

where: $z = s - ct$, longitudinal displacement from the moving ring beam, $z < 0$ to maintain causality.

After applying Equation (5.6) to Equation (5.4), and assuming charge density $\rho = 0$ and current $\vec{j} = \sigma\vec{E}$ in the metal vacuum chamber wall, the Maxwell equations can be written as:

$$\frac{1}{r}\frac{\partial}{\partial r}\left(r\frac{\partial E_s}{\partial r}\right) + \left(\lambda^2 - \frac{m^2}{r^2}\right) E_s = 0 \tag{5.7a}$$

$$\frac{1}{r}\frac{\partial}{\partial r}\left(r\frac{\partial B_s}{\partial r}\right) + \left(\lambda^2 - \frac{m^2}{r^2}\right) B_s = 0 \tag{5.7b}$$

$$E_r = \frac{c}{4\pi\sigma}\left(\frac{m}{r}B_s + \frac{\partial E_s}{\partial r}\right) \tag{5.7c}$$

$$E_\theta = -\frac{c}{4\pi\sigma}\left(\frac{m}{r}E_s + \frac{\partial B_s}{\partial r}\right) \tag{5.7d}$$

$$B_r = \frac{c}{4\pi\sigma}\frac{\partial B_s}{\partial r} + \left(\frac{c}{4\pi\sigma} + \frac{i}{k}\right)\frac{m}{r}E_s \tag{5.7e}$$

$$B_\theta = \frac{c}{4\pi\sigma}B_s + \left(\frac{c}{4\pi\sigma} + \frac{i}{k}\right)\frac{\partial E_s}{\partial r}, \tag{5.7f}$$

where: k - wave number, $\lambda^2 = \frac{4\pi i\sigma k}{c}$, σ - wall material conductivity.

The λ parameter is related to the skin depth inside the conductor:

$$\delta_{skin} = \frac{1}{\mathrm{Im}\lambda} = \frac{c}{\sqrt{2\pi\sigma\omega}}, \tag{5.8}$$

where: ω - angular frequency of the current.

At CLIC the distance between bunches is 0.5 ns, which translates to a frequency of 2 GHz.

At such frequency the skin depth is minimal, for example, for copper it is 1.46 µm. Therefore, a copper coating in order of tens of micrometres should suffice to fulfil the requirement that the wall or coating thickness is significantly larger than the skin depth.

The calculation of the wakefield can be simplified if we limit ourselves to the low-frequency and long-range regime, applicable to distances between the bunches in a bunch train. The first condition assumes that λ is much larger than the inverse of the aperture or equivalently, the skin depth is much smaller than the aperture. The second condition limits the distance from the sources where the field is calculated, and is equivalent to a limit of allowed frequencies of the wakefield:

$$\lambda/|k| \gg |k|b. \tag{5.9}$$

The region where the derivation of the wakefield function applies is limited in space by the following conditions:

$$|z| \ll \frac{b}{\chi} \tag{5.10a}$$

$$|z| \gg b\chi^{1/3}, \tag{5.10b}$$

where: b - aperture radius, $\chi = \frac{c}{4\pi\sigma b}$.

The first limit is in order of 10^6 m assuming $b = 15\,\mathrm{mm}$ and a copper vacuum chamber wall, and is well fulfilled at CLIC. The second requirement yields that $|z| \gg 21.5\,\mu\mathrm{m}$ for the same beam pipe aperture. The bunch distance is 150 mm at both energy stages, thus in at CLIC both requirements are fulfilled on the bunch-to-bunch scale.

The Equations (5.7a) and (5.7b) are solved for E_s and B_s respectively, and the rest of the field components can be obtained from the remaining equations. The field behind the beam and in the metal pipe has the following components:

$$E_s = \frac{I_m}{\pi b^{2m+1}}\sqrt{\frac{c}{\sigma}}r^m\cos(m\theta)\frac{1}{|z|^{3/2}}, \tag{5.11a}$$

$$E_r = -\frac{3I_m}{4\pi b^{2m+1}}\sqrt{\frac{c}{\sigma}}\frac{1}{1+m}r^{m-1}\cos(m\theta)\left(r^2 + b^2\frac{1}{|z|^{5/2}}\right), \tag{5.11b}$$

$$E_\theta = -\frac{3I_m}{4\pi b^{2m+1}}\sqrt{\frac{c}{\sigma}}\frac{1}{1+m}r^{m-1}\sin(m\theta)\left(r^2 - b^2\frac{1}{|z|^{5/2}}\right), \tag{5.11c}$$

$$B_s = -\frac{I_m}{\pi b^{2m+1}}\sqrt{\frac{c}{\sigma}}r^m\sin(m\theta)\frac{1}{|z|^{3/2}}, \tag{5.11d}$$

$$B_r = -E_\theta - \frac{2I_m}{\pi b^{2m+1}}\sqrt{\frac{c}{\sigma}}mr^{m-1}\sin(m\theta)\frac{1}{|z|^{1/2}}, \tag{5.11e}$$

$$B_\theta = E_r - \frac{2I_m}{\pi b^{2m+1}}\sqrt{\frac{c}{\sigma}}mr^{m-1}\cos(m\theta)\frac{1}{|z|^{1/2}}. \tag{5.11f}$$

The Lorentz force experienced by a test charge has the following components in cylindrical coordinates:

$$F_s = eE_s \tag{5.12a}$$
$$F_\theta = e(E_\theta + B_r) \tag{5.12b}$$
$$F_r = e(E_r - B_\theta). \tag{5.12c}$$

Using the fields from Equation (5.11) we obtain the transverse and longitudinal force experienced by the beam:

$$\vec{F_\perp} = \frac{2eI_m}{\pi b^{2m+1}(1+\delta_{m0})}\sqrt{\frac{c}{\sigma}}mr^{m-1}\frac{1}{|z|^{1/2}}(\hat{r}\cos(m\theta) - \hat{\theta}\sin(m\theta)), \tag{5.13a}$$
$$\vec{F_\parallel} = \frac{eI_m}{\pi b^{2m+1}(1+\delta_{m0})}\sqrt{\frac{c}{\sigma}}r^m\frac{1}{|z|^{3/2}}\cos(m\theta)\hat{s}. \tag{5.13b}$$

The wake force impulses sensed by a test charge at the location of field creation (beam pipe wall) obtained by integrating the force over a distance longer than the wall structure are expressed by:

$$\int_{-L/2}^{L/2}\vec{F}_\perp ds = -eI_m W_m(z) m r^{m-1}(\hat{r}\cos m\theta - \hat{\theta}\sin m\theta) \tag{5.14a}$$
$$\int_{-L/2}^{L/2}\vec{F}_\parallel ds = -eI_m W_m'(z) r^m \cos m\theta, \tag{5.14b}$$

where: W_m - transverse wake functions, W_m' - longitudinal wake function, derivative of the transverse function with respect to z:

$$\nabla_\perp \int_{-L/2}^{L/2}\vec{F}_\parallel = \frac{\partial}{\partial z}\int_{-L/2}^{L/2}\vec{F}_\perp, \tag{5.15}$$

also known as the Panofsky-Wenzel theorem [74].

Using the integrated effect of the wake force on a test charge one can define the wake potential V:

$$\int_{-L/2}^{L/2} ds\vec{F} = -\nabla V \tag{5.16a}$$
$$V = eI_m W_m(z) r^m \cos(m\theta). \tag{5.16b}$$

Finally, for the special case of the resistive wall wakefield, the wake function over an accelerator element of length L in SI units is expressed as:

$$W_m(z) = -\frac{c}{\pi b^{2m+1}(1+\delta_{m0})}\sqrt{\frac{Z_0}{\sigma\pi}}\frac{L}{\sqrt{z}}, \tag{5.17}$$

where: Z_0 is the impedance of vacuum, b - aperture radius, δ_{m0} - Kronecker delta, σ - conductivity of the vacuum chamber material, L - element length, z - observation distance.

For the base longitudinal mode ($m = 0$) the wake function is inversely proportional to the beampipe aperture ($W_0(z) \propto \frac{1}{b}$), while for the base transverse mode ($m = 1$) the wake function is inversely proportional to the third power of the aperture ($W_1(z) \propto \frac{1}{b^3}$). Therefore, the transverse wakefield is significantly more sensitive to the aperture model and is the dominating source of instabilities.

5.2.2 Simulation methods

PyHEADTAIL is used to simulate the linear beam dynamics, including dispersion effects and resistive wall wakefields in the CLIC BDS at two energy stages of 380 GeV and 3 TeV. The collimators are not included in the simulated model, as the focus of this study is on the establishing the aperture model in the FFS. The aperture models described in section 5.1 and nominal beam parameters at the respective beam energy stage are used as initial parameters. The charge of each bunch is replaced with 10^5 macroparticles which are distributed over a 100 longitudinal slices. The main transverse mode $m = 1$ of the resistive wall wakefield is pre-calculated for each aperture. Using Equation (5.17) and substituting $m = 1$ we obtain:

$$W_1(z) = -L\frac{c}{\pi b^3}\sqrt{\frac{Z_0}{\sigma \pi z}} \tag{5.18}$$

The beams are created at the beginning of the BDS with a gaussian distribution of particle positions and with a 0.35% relative energy spread. All of the bunches have the same initial offset of a half beam size in both the horizontal and vertical directions, which is the worst case scenario leading to the largest impact of the wakefield. The beams are transported through the BDS with the wakefields impacting their quality, and are stored at the IP. A benchmark run for each energy stage is done where the wakefields do not impact the bunches. The conductivity used for copper is $5.9 \cdot 10^7 \frac{1}{\Omega \mathrm{m}}$ and $1.4 \cdot 10^6 \frac{1}{\Omega \mathrm{m}}$ for steel [75].

In PyHEADTAIL, the effects of the wakefield of the preceding slices are imposed on the slice k of the beam by modifying the momenta distributions of macroparticles by $\Delta x'$ calculated as:

$$\Delta x'_k(s) = \frac{e^2}{E_0}\sum_{j=1}^{k-1} N_j < x >_j W(|k-j| \cdot c\Delta t), \tag{5.19}$$

where: e - electron charge, E_0 - beam energy, N_j - number of charges, $< x >_j$ - centre of gravity of macroparticles in slice j, W - wakefield function, Δt - time between slices.

The cumulative effect of the wakefields, as shown in Equation (5.19), is proportional to the bunch charge and inversely proportional to the particle energy. Therefore, the impact of the wakefields at the 380 GeV is expected to be stronger than at the higher energy stage, due to smaller energy and larger bunch charges, all other things being equal.

The impact of the resistive wall wakefield on the beam quality is checked using two methods. The first method concentrates on the beam quality along the BDS using the radius of normalised phase-space to quantify the difference between the beginning of the bunch train and the end. This method simultaneously takes into account particle positions, momenta distributions, and accelerator lattice parameters.

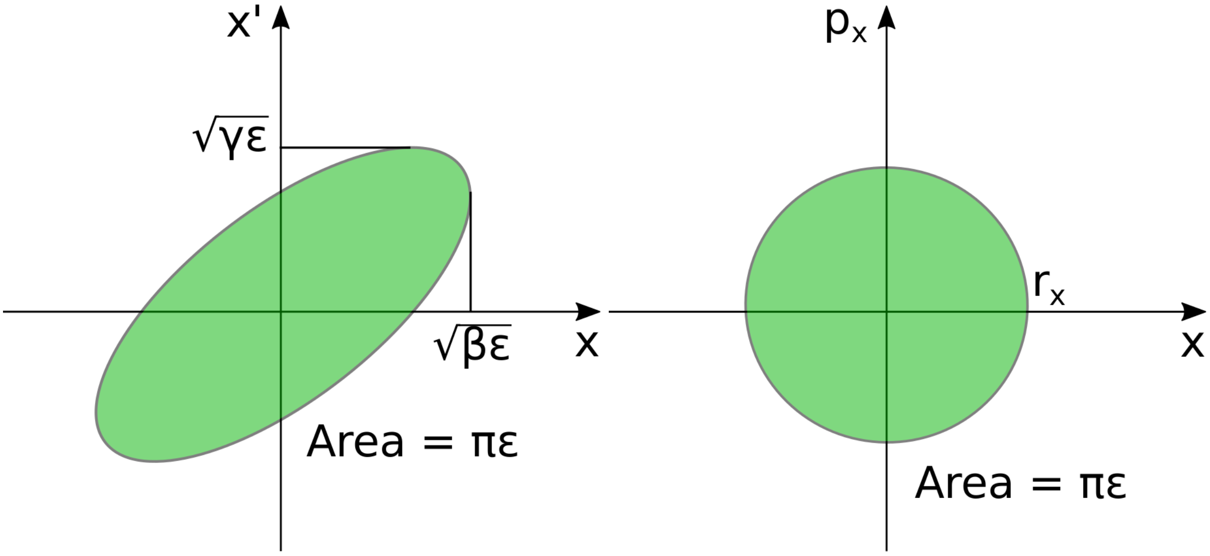

Figure 5.2: The betatron phase space ellipse before the coordinate normalisation (left), and in the normalised phase space (right). ε denotes beam emittance, and β and γ are Courant-Snyder parameters.

Using (x, x') conjugate phase-space coordinates, the particle motion in a periodic structure follows an ellipse defined by the beam and lattice parameters, as shown in Figure 5.2(left). The betatron ellipses change shape and slope during beam transport along the accelerator, but their area is invariant, provided the beam does not lose energy. It is possible [62] to normalise the conjugate phase space coordinates and transform the ellipse into a circle, as shown in Figure 5.2(right). Then, the particle motion can be described as a rotation in the normalised coordinates.

The normalised phase-space radius is defined as:

$$r_{x,y}(s)[\sqrt{\mathrm{m}}] = \sqrt{\left(\frac{x(s)}{\sqrt{\beta_s}}\right)^2 + \left(\frac{x(s)\alpha_s + x'(s)\beta_s}{\sqrt{\beta_s}}\right)^2}, \tag{5.20}$$

where: α_s, β_s - betatron functions at position s, x - bunch centre position, x' - average bunch angle connected with the bunch momentum through: $x' = \frac{p_x}{p}$.

For beams that are not impacted by the resistive wall wakefield, the normalised phase-space remains constant, and the difference between the beam head and tail is expected to be zero. This method allows one to find the location where the beams are most impacted by wakefields.

The second method uses luminosity to quantify the impact of the resistive wall wakefield on the beam quality at the IP. The beams transported with PyHEADTAIL through the BDS up to the IP are stored and duplicated. One of the duplicates can be used directly without any manipulations, while the other is centred at transverse position (0, 0) to remove the offsets. Beams prepared this way are used as input in Guinea-Pig simulations to obtain the luminosity along the bunch train. This way of preparing beams removes the issue with one-beam method self-correlations, as described in section 3.1.4, and the luminosity is sensitive only to the impact of the wakefield. The impact can be assumed to be negligible if the luminosity at the end of the bunch train is within 1% of the benchmark value. The benchmark luminosity comes from beams tracked through the BDS without offsets and resistive wall wakefields, and collided with their duplicated and centred selves in Guinea-Pig.

5.2.3 Impact in the CLIC BDS

In this section the impact of the resistive wall wakefield on the beams is presented. First, the normalised phase-space radii in both vertical and horizontal dimensions are analysed in section 5.2.3.1 and then the luminosity performance coming from these beams is discussed in section 5.2.3.2.

5.2.3.1 Normalised phase-space radii

The radii of the normalised phase-space in the horizontal and vertical direction at 380 GeV when copper is used as the material for the vacuum chamber walls are shown in Figure 5.3, and in Figure 5.5 when steel is used instead.

The benchmark case without wakefields included in the simulation is a straight line in both vertical and horizontal directions. It confirms the simulation stability, where without wakefields the head of the bunch train and its tail are indistinguishable.

The impact of the resistive wall effect scales well with the apertures when copper is used. The $r_{x,y}$ parameters are sensitive to the change of apertures. A 10% radius increase reduces the effect by 20% in the horizontal direction and 22% in the vertical one. A decrease in radius of 10% increases the impact by 34% and 33% in the horizontal and vertical directions, respectively. The impact of the changing apertures is thus symmetrical.

In the horizontal direction, as shown in Figure 5.3(left), a deviation from the benchmark distribution starts in all studied cases in the same point along the BDS: between a drift labelled D6 and a sextupole SF6 at $s \approx 1350\,\mathrm{m}$, at the beginnin of the FFS. The position difference between the first and last bunch continues growing quickly until around $s \approx 1600\,\mathrm{m}$, and then the rate of increase slows down up to the IP.

In the vertical direction, shown in Figure 5.3(right), the deviation from benchmark begins much earlier, already at $s \approx 250\,\mathrm{m}$, where weak bending magnets are located. A significant increase of the wakefield impact is located at $s \approx 1440\,\mathrm{m}$, around a sextupole SD5, and continues until around 1600 m, similar to the behaviour in the horizontal direction.

The resistive-wall wakefield is not a uniformly detrimental force to the beam quality measured by the offset at the IP, as can be seen in Figure 5.4. The impact on the beams tracked through a BDS with the initial aperture model with copper vacuum chamber walls is focusing in the horizontal direction and defocusing in the vertical one. The relative offset difference between the first and last bunch is -18% (focusing) and $+37\%$ (defocusing) respectively. Therefore, defocusing in the vertical direction dominates over the focusing in the horizontal one, and the overall impact on the luminosity is negative. Increasing the wakefield strength can lead to stronger focusing in the horizontal direction to the point of fully cancelling the initial offset.

The distributions of $r_{x,y}$ change significantly in the case where steel is used instead of copper as the vacuum chamber material, as shown in Figure 5.5. The onsets of the deviations from

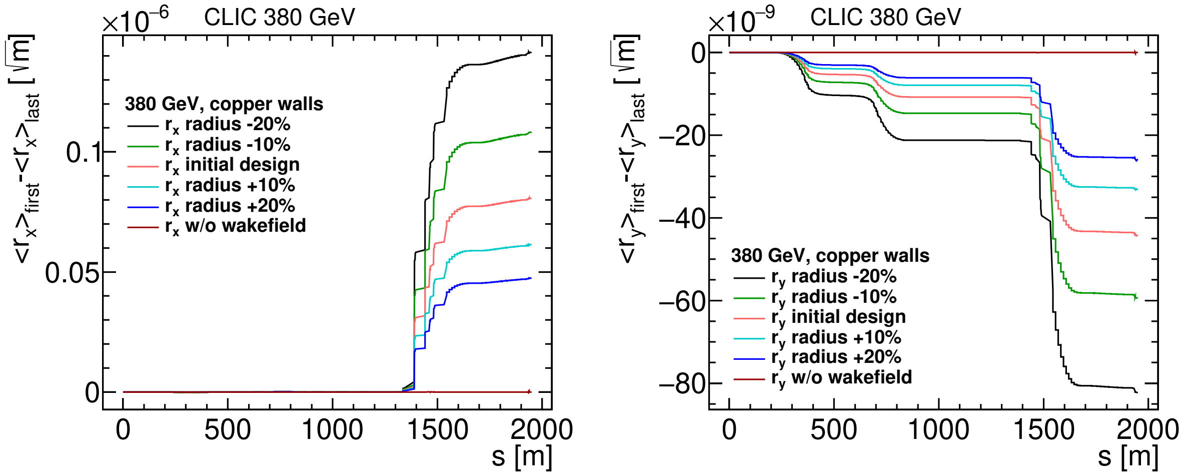

Figure 5.3: The impact of varying apertures in the Beam Delivery System on radii of the normalised phase-space at 380 GeV using copper vacuum chamber walls in the horizontal (left) and vertical (right) directions.

the benchmark distribution are located in the same lattice elements as when copper is used. However, the beam behaviour is significantly altered by wakefields, especially in the horizontal direction, as shown in Figure 5.5(left). The impact ordering with aperture radii observed when copper is used breaks down near $s \approx 1450\,\mathrm{m}$, where distributions which aperture radii were not increased, detach from the trend. The trend is followed in the case where the radii were increased by 10% or more. The lowest difference between the first and the last bunch in a train is observed in the case where apertures are reduced by 10%. This result is unexpected as, using Equation (5.18), the wakefield amplitude should increase when the aperture is reduced. In addition, such behaviour is not observed in the vertical direction, for example in Figure 5.5(right).

The lack of scaling with aperture size suggests a more dynamic behaviour of the beams with reduced radii, which cannot be fully quantified by merely comparing the $r_{x,y}$ between the beginning and end of a train. The impact on the beam quality at the IP and the luminosity cannot be predicted in this case, due to more unstable dynamics, strongly impacted by the resistive wall wakefield. The average offset distributions provide more information about the impact on the beams at the IP, which directly translates to luminosity performance, especially when compared with the beams transported through the copper vacuum chamber, as shown in Figure 5.6. The difference in offsets between the first and last bunch is greatly increased from 10 nm in the copper case to 70 nm with steel, with the change of sign of the offset in the middle of the train. The impact of the wakefield at the IP in the steel case can initially increase the luminosity as the offset decreases to zero, but then the luminosity should decrease as the offset quickly increases.

The impact of the resistive wall wakefield at 3 TeV in the horizontal direction shows similar dynamics to the one observed at 380 GeV. The ordering of $r_{x,y}$ sensitive to the aperture size, as observed at 380 GeV , is not maintained at 3 TeV , specifically in the vertical direction for aperture models where the radii were not extended, as visible in Figure 5.7(right). The sign of

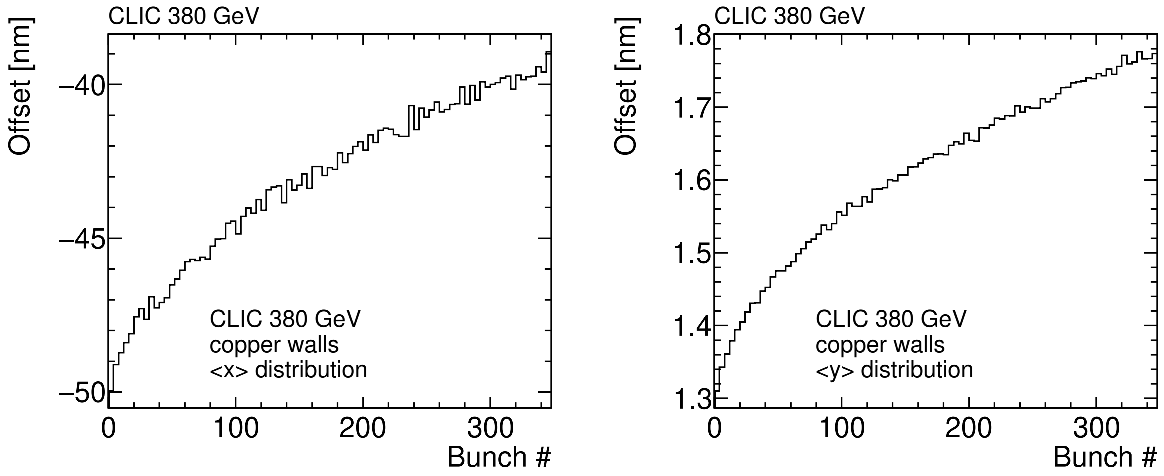

Figure 5.4: Average offset at the IP at 380 GeV for bunches transported through the BDS with copper vacuum chamber walls in the horizontal (left) and vertical (right) directions.

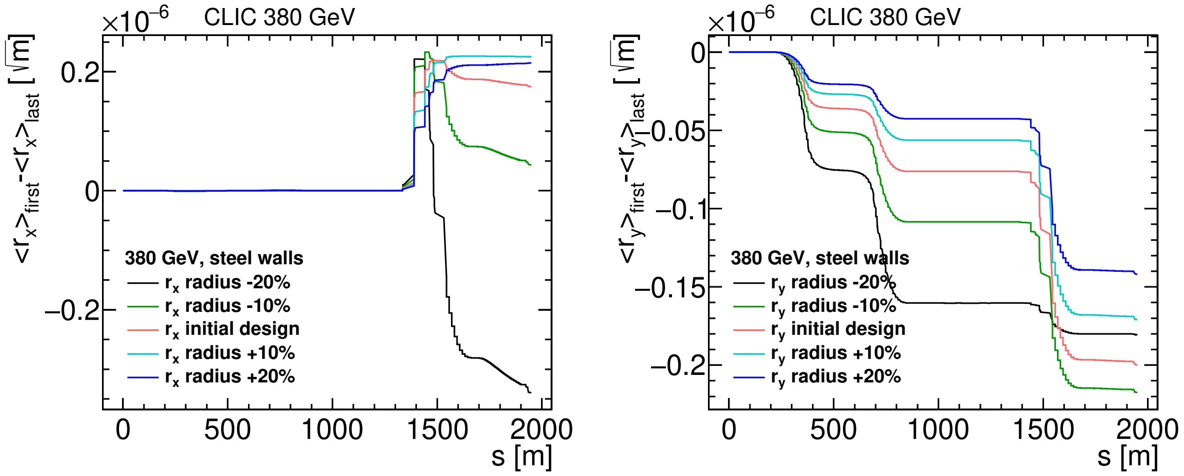

Figure 5.5: The impact of varying the apertures in the Beam Delivery System on radii of the normalised phase-space at 380 GeV using steel vacuum chamber walls in the horizontal (left) and vertical (right) directions.

the difference changes for options with reduced radii suggesting that these beams are under a strong influence of wakefields.

A decrease in apertures from the initial value by 10% leads to a 38% increase in the r_x difference between the beginning and the end of a bunch train. The same percentage increase of apertures leads to a 23% decrease in the sensitivity to the effect in the horizontal direction. The calculation in the vertical direction cannot be reliably done due to the unstable behaviour of the observed parameter.

The average offset distribution at the IP in the horizontal and vertical direction at 3 TeV is shown in Figure 5.8. The impact of wakefields is defocusing in the horizontal direction, and in the vertical direction it changes from defocusing to focusing in the first half of the bunch train. The change in the direction of the wakefield influence shows again a strong sensitivity

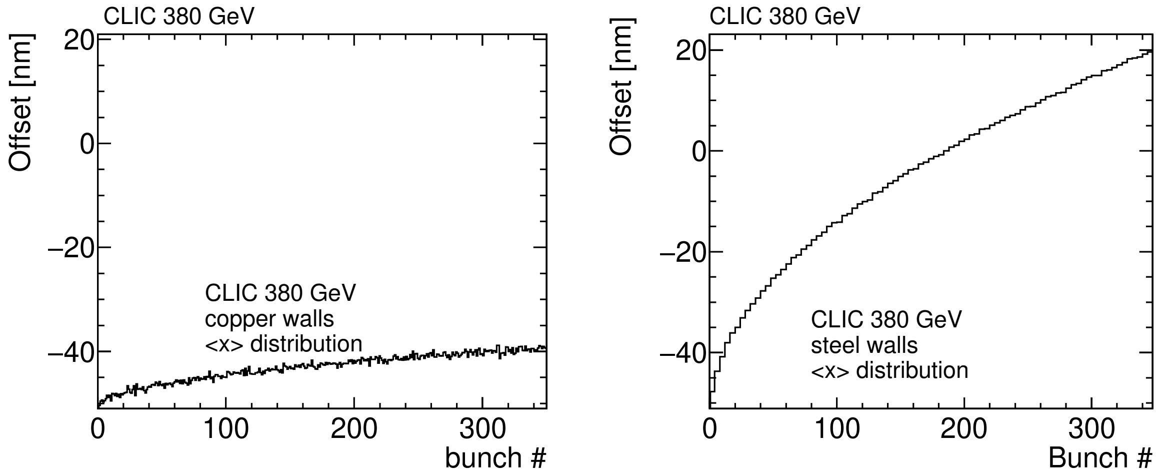

Figure 5.6: Average horizontal offset at the IP at 380 GeV for bunches transported through the BDS with copper (left) and steel (right) vacuum chamber walls.

to wakefields in this model. Larger offsets would lead to stronger distortions in the beams and more chaotic behaviour. Such a change of trend in the offset would also make it more challenging to correct by the intra-train beam feedback system [76] to restore the luminosity performance.

The use of a steel beam pipe instead of a copper one leads to larger differences in $r_{x,y}$ between the beginning and the end of the train, as shown in Figure 5.9. The increase in comparison with the use of copper is of about a factor of seven, consistent with scaling of the wakefield potential with $\sqrt{\frac{\sigma_{\mathrm{Cu}}}{\sigma_{\mathrm{Fe}}}}$. Similarly to the 380 GeV case, the scaling with apertures breaks down when steel is used. The change of the trend in beams with reduced apertures also takes place in the vertical direction.

The analysis of the phase-space radii difference between the beginning and the end of a train at 3 TeV suggests that the chosen minimum radius of 6 mm is too small and the beams are under a strong influence of the resistive wall wakefield. Therefore, the apertures should be extended by about 20% to ensure better beam stability. The full extend of the aperture extension can be established with the input from the analysis of the luminosity performance.

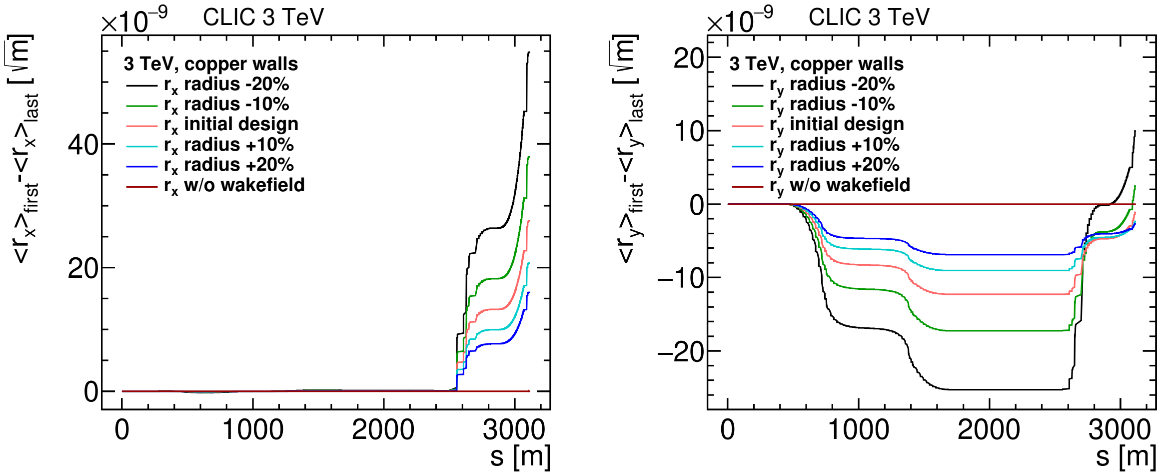

Figure 5.7: The impact of varying the apertures in the Beam Delivery System on radii of the normalised phase-space at 3 TeV using copper vacuum chamber walls in the horizontal (left) and vertical (right) directions.

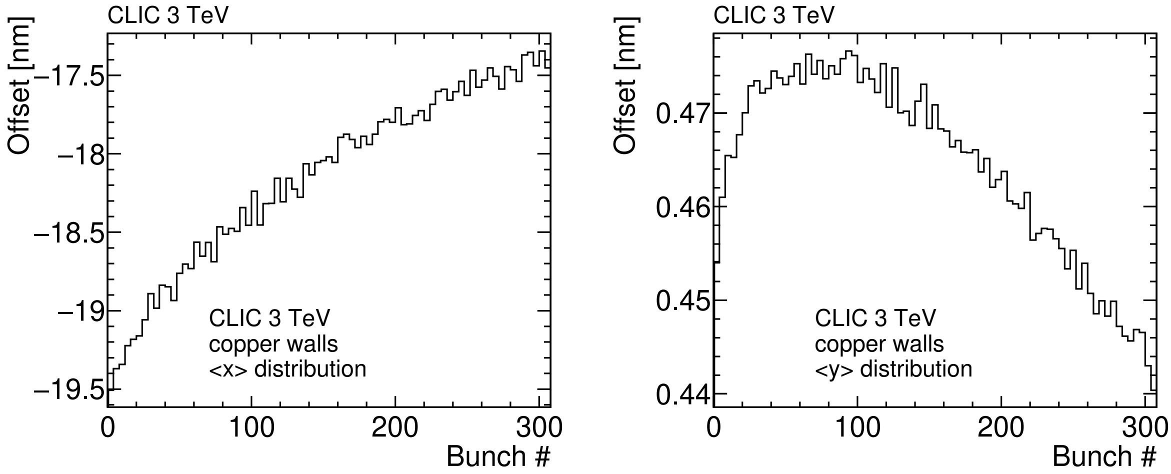

Figure 5.8: Average offset at the IP at 3 TeV for bunches transported through the BDS with copper vacuum chamber walls in the horizontal (left) and vertical (right) directions.

5.2.3.2 Luminosity performance

The luminosity along a bunch train allows quantifying the impact of the differences shown in the previous section. The instantaneous luminosity along the bunch train for copper and iron vacuum chambers are shown in Figure 5.10(left) for 380 GeV and in Figure 5.10(right) for 3 TeV.

The wakefield does not impact the luminosity in the benchmark case, and there is no trend in the instantaneous luminosity along the train, following the stability of $r_{x,y}$ distributions.

At 380 GeV, the luminosity at the end of the bunch train is 3% lower than in the benchmark case in the BDS with a copper vacuum chamber. The total luminosity loss over the train is just below 1%. For the steel BDS, the luminosity reduction along the train is much steeper resulting in a 14% loss at the end of a train with a total loss of 10%.

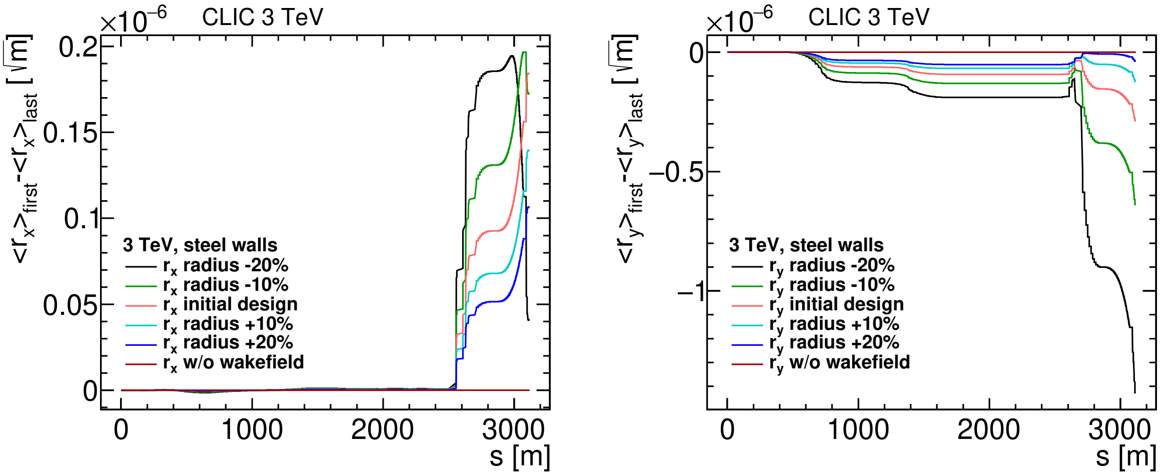

Figure 5.9: The impact of varying the apertures in the Beam Delivery System on radii of the normalised phase-space at 3 TeV using steel vacuum chamber walls in the horizontal (left) and vertical (right) directiosn.

The 3 TeV beams show a higher degree of sensitivity to wakefields than observed for 380 GeV, as can be seen in Figure 5.10(right). The luminosity at the beginning of the train is at the same level as in the benchmark case, and increases slightly along the train. At the end of the train, the luminosity is around 1% above the benchmark. This is caused by the wakefields focusing the beams in both the vertical and horizontal directions. While an increase in luminosity might look like a positive outcome, it is vital to notice that it is not a sign of beam stability and quality. The impact of wakefields changes the trend from defocusing to focusing in the vertical direction that causes the luminosity to surpass the benchmark value. However, an increase in the wakefield impact through a larger initial offset or lower conductivity of the vacuum chamber material would lead to an earlier onset of the change of trend and a steeper slope. The stronger wakefield eventually changes of sign of the offset, and its impact becomes again defocusing instead of focusing. The result is a severe luminosity loss, such as is observed when steel is used.

For the steel BDS, the luminosity along the train is non-monotonic, as shown in Figure 5.10(right). The luminosity initially falls, then increases above the benchmark case, and finally rapidly falls in the second half of the bunch train. The luminosity loss at the end of the train is 7%, and the total loss accounts to only 0.5% difference with the benchmark, due to the existence of the region with luminosity higher than the benchmark. The severe impact of the wakefields leads to outcomes which are challenging to predict and quantify.

The model derived in section 5.1 with a minimum aperture of 6 mm does not provide sufficiently stable beams and luminosity distribution along the bunch train, and therefore requires further optimisation. The sensitivity to the resistive wall wakefield of the 3 TeV beams is not entirely consistent with the conclusion of the previous study of the wakefield in the CLIC BDS [8], in which the 6 mm aperture was determined to provide sufficiently stable beams.

The previous study looked at the angle and position differences between the first and last bunch in the bunch train as a function of changing apertures. The apertures were assumed

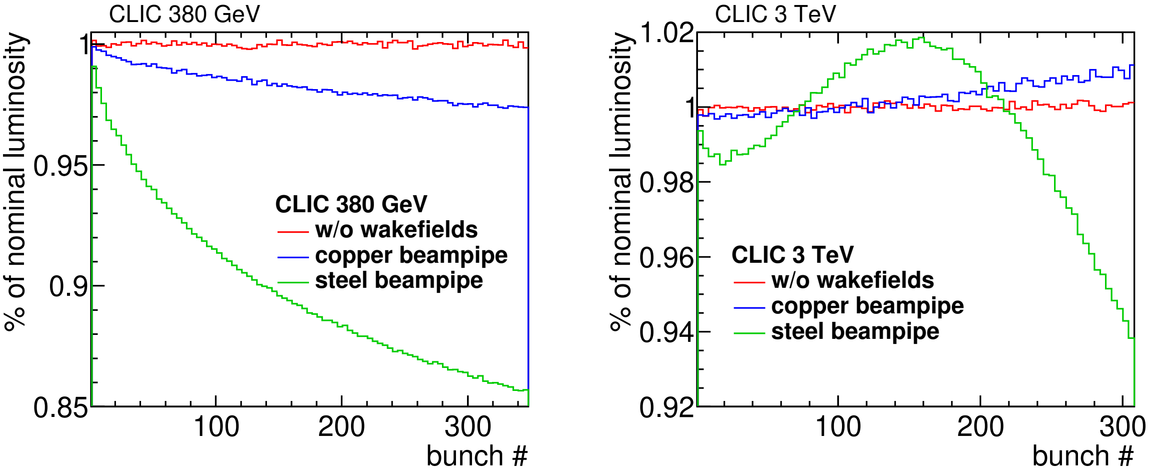

Figure 5.10: Instantaneous luminosity along the bunch train at 380 GeV (left) and 3 TeV (right) where copper or iron vacuum chamber walls are used. The nominal luminosity is the luminosity of the benchmark case, where the wakefield effects are not included.

to provide sufficient stability if the wakefields impact was converging, where the increase of aperture had diminishing impact on the position and angles, and was thus negligible or mostly due to numerical errors [8]. The analysis of the radii of the normalised phase-space is more robust as it combines the information of the beams position and momentum with the accelerator parameters. In addition, the luminosity has not been looked into, and it is the best parameter to quantify the beam quality and the impact of wakefields on the future accelerator performance.

The more robust analysis method of the PyHEADTAIL simulation excludes the use of minimum aperture of 6 mm at 3 TeV in the FFS, as proposed in the previous study. The use of a larger aperture of 8 mm, proposed there as the 'safer option', might be desirable and is considered in the optimisation process.

In summary, copper provides more stable behaviour of the beams and better luminosity performance at the same aperture in comparison with steel. Therefore, it is the preferred choice for both energy stages. The initial apertures at both energy stages lead to luminosity losses more significant than the 1% limit and require optimisation to increase the beam stability and better luminosity performance.

5.3 Aperture optimisation

The resistive wall wakefields impact the beams strongly at both energy stages. However, the impact leads to different results at each stage, that need separate approaches. At 380 GeV, the luminosity loss of 3% is the main concern, while at 3 TeV it is the non-monotonic beam behaviour. In both cases, the strong impact of the resistive wall effect can be addressed either by using a material with a higher conductivity than copper or by increasing the aperture radii.

The use of a more conductive material than copper does not offer a significant improvement in the simulated conditions, as silver is the only metal more conductive than copper at room temperature. The reduction in the wakefield amplitude, using Equation (5.18), scales with $\sqrt{\frac{\sigma_{\mathrm{Ag}}}{\sigma_{\mathrm{Cu}}}}$. Using 6.3 $\frac{1}{\Omega\mathrm{m}}$ as the conductivity of silver [75], in comparison with the conductivity of copper of 5.9 $\frac{1}{\Omega\mathrm{m}}$ [75], the wakefield would be only 2.7% smaller, which is an insufficient reduction.

Because the resistive wall wake potential depends strongly on the aperture (see Equation (5.18)), proportionally to the inverse of the third power of the radius, an increase in the aperture radii is the best approach to the wakefield reduction.

5.3.1 380 GeV BDS

The luminosity loss at 380 GeV is 3% at the end of the bunch train (see Figure 5.10(left)), and should be limited to 1%. To achieve this reduction, the resistive wall wakefield amplitude should be reduced by $\frac{2}{3}$. Using the formula from Equation (5.18), one can calculate an increase in the radius of 44% should lead to the desired wakefield reduction.

The beam is impacted by the wakefield mostly in the FFS, as can be seen in Figure 5.3, and thus it should suffice to extend the apertures only there. An aperture increase in the final quadrupole magnets is not desired due to cost considerations connected with a larger required magnetic field in their poles.

Simulations of the 380 GeV BDS with the final doublet apertures unchanged suggest that there is no impact on the beam quality and luminosity performance in comparison with extending these apertures. Therefore, the FD apertures can safely remain unchanged at this energy stage. The extended apertures in the FFS are shown in Figure 5.11. The increase in apertures can be accommodated and is not in conflict with the maximal allowable aperture imposed by the quadrupole magnets pole field limitation.

The result of the luminosity performance simulation with the extended apertures at 380 GeV is shown in Figure 5.12(left). The increase in aperture allows limiting the luminosity loss down to 1%, as calculated from the wakefield potential. The 44% extension provides an acceptable limitation of the luminosity loss due to the resistive wall effect, and does not require further intervention.

The average vertical offset distributions at the IP with both the nominal apertures design and the extended radii option for the FFS are shown in Fig. 5.12(right). The difference in offset between the first and last bunch for the initial design is equal to 16% of the vertical bunch size of 2.9 nm and this number is reduced to 7% for the extended radius option. The reduction

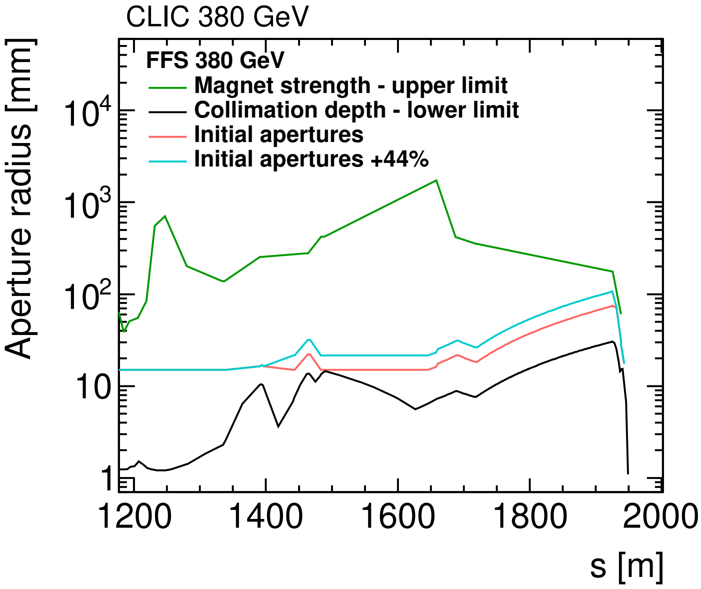

Figure 5.11: Initial and extended aperture models along the FFS with limits imposed from the beam collimation depth and the maximal allowable pole field strength in quadrupoles at 380 GeV.

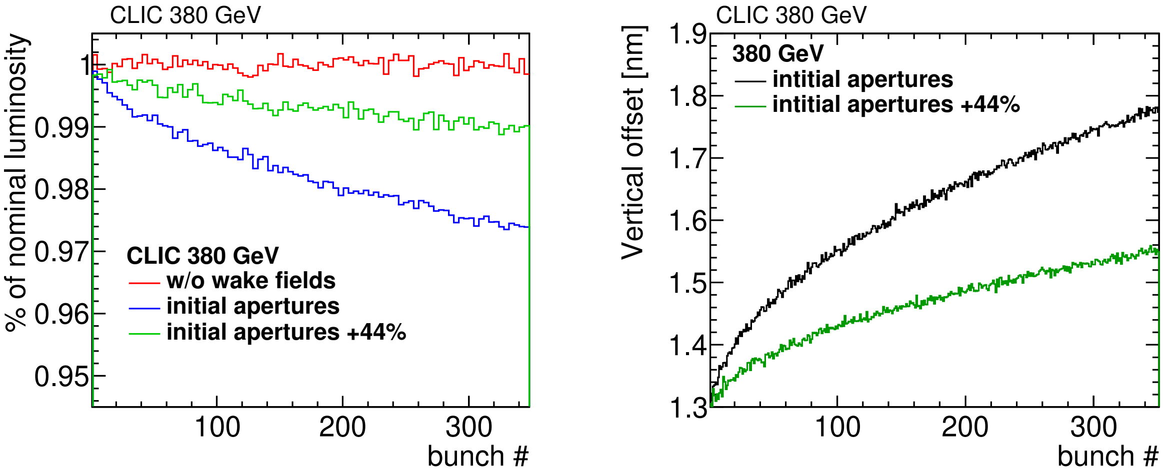

Figure 5.12: The impact on the instantaneous luminosity along a bunch train between the initial and extended aperture models at 380 GeV (left), and the average vertical offset at the IP along a bunch train for two aperture options: the nominal apertures and the extended option with 44% larger radii in the Final Focus System (right).

in the vertical offset at the end of a bunch train translates to a lower loss in the luminosity. In addition, the less steep offset behaviour is simpler to correct by the intra-train feedback system.

5.3.2 3 TeV BDS

The beam stability analysis at 3 TeV (see Figure 5.7) shows that the apertures should be extended by at least 20% to provide more predictable and monotonic beam behaviour. The impact of wakefields concentrates in the Final Focus System, similar to the situation observed at 380 GeV, thus the aperture is modified in the FFS.

In contrast to the situation at 380 GeV, the luminosity performance presented in the previous section (see Figure 5.10(right)) does not provide a definite number by which apertures should be extended. due to strong impact of wakefields in the vertical direction resulting in focusing of the beams and an increase in luminosity in comparison with the benchmark case.

The solution to the non-monotonous beam behaviour at the IP is found by gradually increasing the apertures in the FFS to the point where the beams monotonous. When that is achieved, a straightforward calculation based on the wakefield potential (Equation (5.18)) of the apertures needed for the desired luminosity performance is possible. The apertures need to be made more sensitive to the changing beam parameters than in the initial model. Therefore, the right-hand side of the maximum function is modified. The r_{wake} remains unchainged at 6 mm. The equation describing the extended aperture model at 3 TeV can be expressed as:

$$R_{\text{min}}[\text{mm}] = \max\{r_{\text{wake}},\ 0.1\,\text{mm} + a + \max\{15\sigma_x, 55\sigma_y\}\}, \tag{5.21}$$

where: $r_{\text{min}} = 6\,\text{mm}$ - minimal radius coming from beam stability considerations, 0.1 mm - safety margin for the offsets, the beam sizes calculated using Equation (5.1), and a is an expansion number depending on the position in the Final Focus System used to increase the dependence of the apertures on the beam parameters, parametrised as following:

$$a(s)[\text{mm}] = \begin{cases} 3.0 & \text{if} \quad s < 2450\,\text{m} \\ 5.0 & \text{if} \quad 2450\,\text{m} < s < 3090\,\text{m} \\ 3.5 & \text{if} \quad 3090\,\text{m} < s \end{cases}$$

The extended aperture model in the FFS is shown in Figure 5.13.

At 3 TeV, both the luminosity along the bunch train and the beam behaviour along the BDS was non-monotonic. Therefore, the normalised phase-space radii with a ±20% variation around the extended aperture need to be revisited. The distributions in the horizontal direction (Figure 5.14(left)) and the vertical one (Figure 5.14(right)) maintain the ordering observed at 380 GeV (see Figure 5.3) even if the radii are reduced by 20%. The Δr_x at the IP is 66% smaller than in the initial model, The δr_y is larger than in the initial model, although the comparison is not straight-forward due to the non-monotonous beam behaviour in the initial model in this direction. In the extended model, the vertical offset does not change the trend from defocusing to focusing, as can be seen in Figure 5.15(right), suggesting significantly lower sensitivity to wakefields.

The luminosity for the extended apertures model is shown in Figure 5.15(left). The luminosity along the bunch train is monotonic with a shallow negative slope. At the end of the

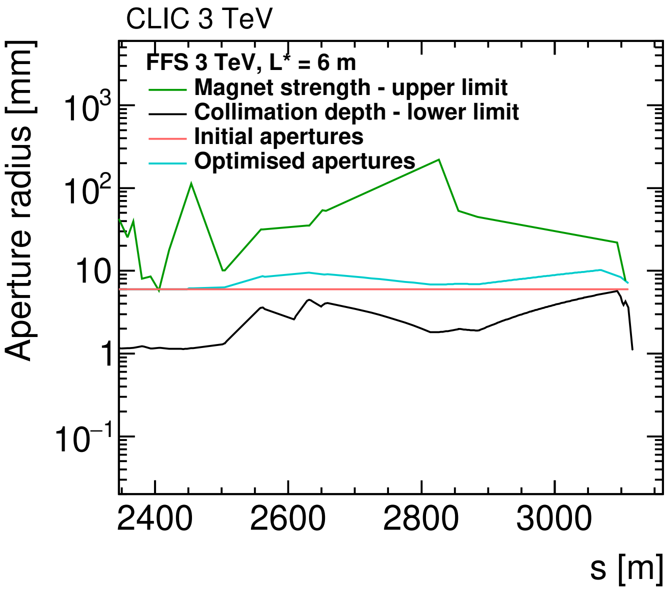

Figure 5.13: Initial and extended aperture models along the FFS with limits imposed from the beam collimation depth and maximal allowable pole field strength in quadrupoles at 3 TeV.

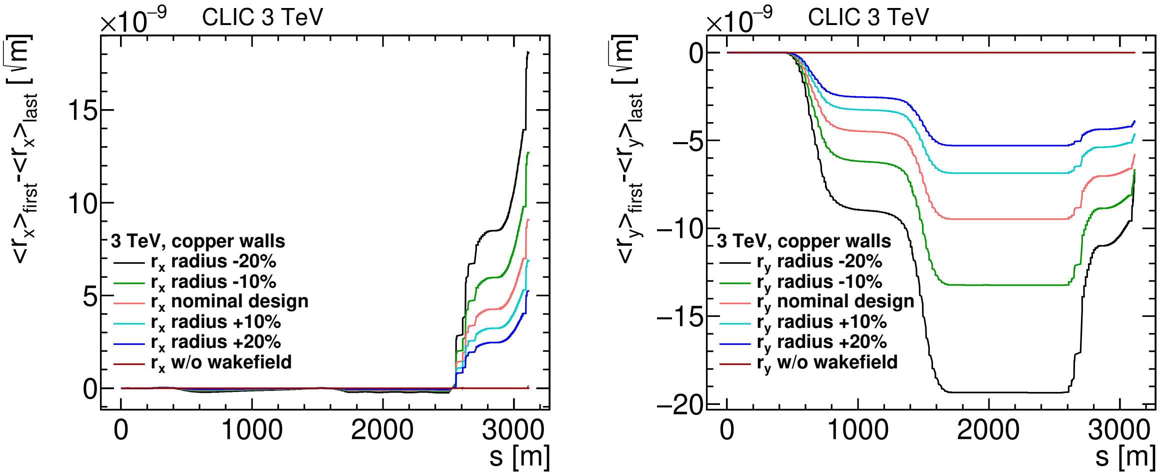

Figure 5.14: The sensitivity of radii of the normalised phase-space at 3 TeV in the horizontal (left) and vertical (right) directions to varying apertures in the Beam Delivery System with the optimised aperture model and copper vacuum chamber walls.

bunch train, the luminosity is 1% lower than the benchmark. The relative total luminosity loss is around 0.5% of the benchmark luminosity.

The 3 TeV beams with extended apertures show the expected sensitivity to aperture changes in the phase-space radii analysis, and show a monotonic behaviour in the offset distributions at the IP. The luminosity performance is more predictable than with the initial model, and the luminosity loss at the end of a train is within the imposed limit of 1%.

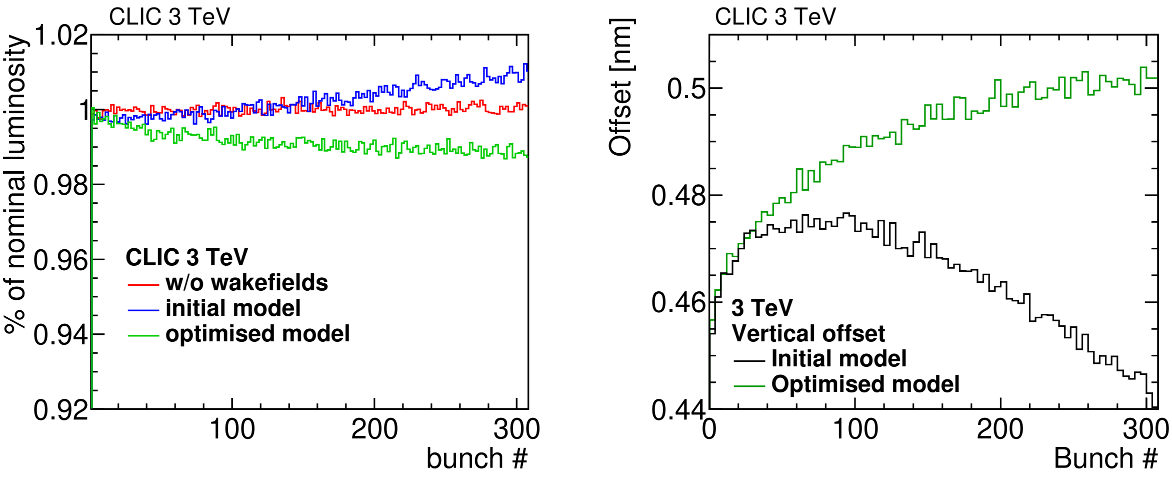

Figure 5.15: Comparison between the impact on the instantaneous luminosity along a bunch train between the initial and extended aperture models at 3 TeV (left) and average vertical offset along the bunch train at the IP. Two aperture options are shown, the initial aperture model and the extended option in Final Focus System (right).

Chapter 6

Simulations of synchrotron radiation

Synchrotron radiation is a severe effect that limits the performance of electron-positron circular colliders. However, it is also present at a linear accelerator and due to the possibility of reflections from the vacuum chamber walls, it can lead to substantial energy depositions in the detector.

This chapter describes the synchrotron radiation effects in the CLIC Beam Delivery System and their impact on the CLIC detector. First, the general properties of the radiation are derived in section 6.1. Photon reflections from metallic surfaces are discussed in section 6.1.1. The simulation methods using PLACET and Synrad+ are described in section 6.2. The impact of the synchrotron radiation in the CLIC BDS is shown in section 6.3, while the results impacting the detector performance are presented in section 6.4. Finally, the possible mitigations of the high fluxes of the SR in the detector region are discussed in section 6.5.

6.1 Synchrotron radiation emission and properties

Charged particles undergoing acceleration radiate power in the form of electromagnetic waves. It is possible to derive the intensity and angular distributions of the radiation emitted by a charged particle subjected to a small acceleration from Maxwell equations using retarded potentials. The most important steps of the derivation of the Larmor formula for the total emitted power and its relativistic generalisation version are presented, based on the Schwinger and Lee formulation [62, 77].

The position of an electron at time t' is $\vec{x'}(t')$, as shown in Figure 6.1, and the position of the observer is $\vec{x}$. The signal emitted by the electron reaches the observer at a time:

$$t = t' + \frac{|\vec{R}(t')|}{c}, \tag{6.1}$$

where: t' - retarded time (emitter time), t - observer time, $\vec{R}(t') = \vec{x} - \vec{x'}(t')$.
The velocity of the electron is specified by $\vec{x'}(t')$:

$$\frac{\mathrm{d}\vec{x'}}{\mathrm{d}t'} = \vec{\beta}c = -\frac{\mathrm{d}\vec{R}}{\mathrm{d}t'}. \tag{6.2}$$

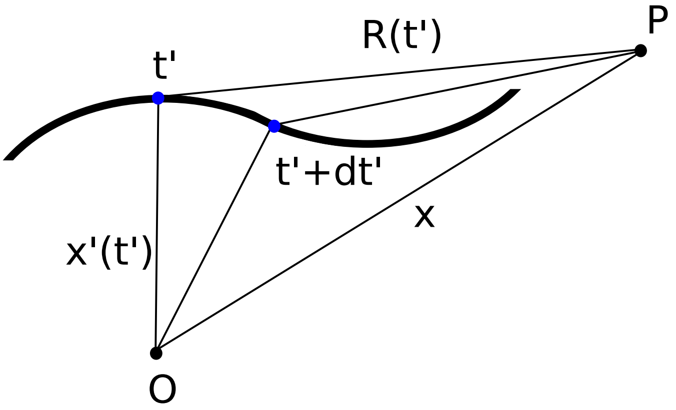

Figure 6.1: A graphic description of the coordinates used in the derivation of the synchrotron radiation emission. $\vec{x}'$ denotes the position of the electron, while $\vec{x}$ is the position of the observer. P signifies the position of the observer and $R(t')$ is a vector joining the charge and the observer.

The scalar Φ and vector $\vec{A}$ potentials of the electromagnetic field caused by the moving electron are [62]:

$$\begin{aligned}\Phi(\vec{x},t) &= \left.\frac{e}{4\pi\varepsilon_0}\frac{1}{\kappa R}\right|_{\text{retarded}}, \\ \vec{A}(\vec{x},t) &= \left.\frac{e}{4\pi\varepsilon_0 c}\frac{\vec{\beta}}{\kappa R}\right|_{\text{retarded}},\end{aligned} \tag{6.3}$$

where: $\kappa = \frac{\mathrm{d}t}{\mathrm{d}t'} = 1 + \frac{\mathrm{d}R}{c\mathrm{d}t'} = 1 - \hat{n}\cdot\vec{\beta}$, $\hat{n} = \frac{\vec{R}}{R} = \nabla R$.

The electric field can be obtained from the scalar and vector potentials: $\vec{E} = -\nabla\Phi - \frac{\partial\vec{A}}{\partial t}$, and the magnetic induction as: $\vec{B} = \nabla\times\vec{A}$. After transformations one can obtain:

$$\begin{aligned}\vec{E}(\vec{x},t) &= \frac{e}{4\pi\varepsilon_0}\left[\frac{\hat{n}-\vec{\beta}}{\kappa^2R^2} + \frac{\hat{n}}{c\kappa}\frac{\mathrm{d}}{\mathrm{d}t'}\left(\frac{1}{\kappa R}\right) - \frac{1}{c\kappa}\frac{\mathrm{d}}{\mathrm{d}t'}\left(\frac{\vec{\beta}}{\kappa R}\right)\right]_{\text{retarded}}, \\ \vec{B}(\vec{x},t) &= \frac{e}{4\pi\varepsilon_0 c}\left[\left(\frac{\vec{\beta}}{\kappa^2R^2} + \frac{1}{c\kappa}\frac{\mathrm{d}}{\mathrm{d}t'}\left(\frac{\vec{\beta}}{\kappa R}\right)\right)\times\hat{n}\right]_{\text{retarded}}.\end{aligned} \tag{6.4}$$

The magnetic field in Equation (6.4) is related to the electric field, where $\vec{B} = \frac{1}{c}\hat{n}\times\vec{E}$. It is therefore sufficient to calculate only the electric component of the field. The electric field can be simplified by a few manipulations, and using:

$$\begin{aligned}\frac{\mathrm{d}\vec{\beta}}{\mathrm{d}t'} &= \dot{\vec{\beta}}\text{, and} \\ \frac{\mathrm{d}(\kappa R)}{c\mathrm{d}t'} &= \beta^2 - \vec{\beta}\cdot\hat{n} - \frac{R}{c}\hat{n}\cdot\dot{\vec{\beta}},\end{aligned} \tag{6.5}$$

the electric field becomes:

$$\vec{E}(\vec{x},t) = \frac{e}{4\pi\varepsilon_0}\left[\frac{\hat{n}-\vec{\beta}}{\gamma^2\kappa^3R^2}\right]_{\text{retarded}} + \frac{e}{4\pi\varepsilon_0 c}\left[\frac{\hat{n}}{\kappa^3R}\times\left((\hat{n}-\vec{\beta})\times\dot{\vec{\beta}}\right)\right]_{\text{retarded}}, \tag{6.6}$$

where: $\gamma = \frac{1}{\sqrt{1-\beta^2}}$ - Lorentz factor.

The electric field in Equation (6.6) is composed of two terms; one is proportional to R^{-2} and the other to R^{-1}. The former is a static electric field which does not contribute to radiated energy. The field proportional to R^{-1} is the radiation field, which in further calculations is marked $\vec{E}_\text{a}$.

The flux of the field is expressed by the Poynting vector:

$$\vec{S} = \frac{1}{\mu_0}[\vec{E}\times\vec{B}] = \frac{1}{\mu_0 c}|\vec{E}|^2\hat{n}, \tag{6.7}$$

which can be used to calculate the power radiated per unit solid angle:

$$\frac{\mathrm{d}P}{\mathrm{d}\Omega} = (\hat{n}\cdot\vec{S})R^2\kappa. \tag{6.8}$$

In the non-relativistic case, where $\vec{\beta}\to 0$, and $\kappa\approx 0$, the accelerated field is:

$$\vec{E}_\text{a} = \frac{e}{4\pi\varepsilon_0 c}\left[\frac{\hat{n}\times(\hat{n}\times\dot{\vec{\beta}})}{R}\right]_{\text{retarded}}, \tag{6.9}$$

and the power radiated in solid angle becomes:

$$\frac{\mathrm{d}P}{\mathrm{d}\Omega} = \frac{1}{\mu_0 c}|\vec{E}_\text{a}|^2R^2 = \frac{r_\text{e}m_\text{e}c}{4\pi}\dot{\beta}^2\sin^2\theta, \tag{6.10}$$

where: r_e - classical radius of electron, m_e - mass of an electron, 511 keV [75], θ - angle between $\hat{n}$ and $\vec{\beta}$. Integration over all angles allows one to obtain the total power emitted by a charged particle undergoing acceleration $\dot{\beta}$:

$$P = \int_{\text{sphere}}\frac{\mathrm{d}P}{\mathrm{d}\Omega} = \frac{1}{6\pi\varepsilon_0}\frac{e^2}{c}\dot{\beta}^2. \tag{6.11}$$

Equation (6.11) is the Larmor formula in SI units. The formula can be also expressed in terms of a momentum change:

$$P = \frac{1}{6\pi\varepsilon_0}\frac{e^2}{m^2c^3}\left(\frac{\mathrm{d}p}{\mathrm{d}t}\right)^2. \tag{6.12}$$

The power emitted by a relativistic charged particle can be derived either through the Poynting vector using the electric field from Equation (6.6) or by transforming the Larmor formula into a relativistic equation. The latter approach will be now described, as the former requires approximations that use a priori knowledge about the synchrotron radiation properties, that have not been derived yet here.

Radiated energy and elapsed time transform in the same way under Lorentz transformation, proportionally to the Lorentz factor. Therefore, the radiated power is a Lorentz-invariant variable, and it remains unchanged regardless of the choice of an inertial frame of reference.

Let us first replace the time derivative with a derivative of the invariant proper time:

$$\mathrm{d}s^2 = c^2\mathrm{d}t^2 - (\mathrm{d}x^2 + \mathrm{d}y^2 + \mathrm{d}z^2) \tag{6.13}$$

Let us also replace the derivative of the momentum by an invariant combination:

$$\left(\frac{\mathrm{d}p}{\mathrm{d}s}\right)^2 \to \left(\frac{\mathrm{d}p}{\mathrm{d}s}\right)^2 - \frac{1}{c^2}\left(\frac{\mathrm{d}\mathcal{E}}{\mathrm{d}s}\right)^2, \tag{6.14}$$

where $\mathcal{E}$ is the energy of the electron.
In this generalisation, the Larmor formula is expressed by:

$$P = \frac{1}{6\pi\varepsilon_0}\frac{e^2}{m^2c^3}\left[\left(\frac{\mathrm{d}p}{\mathrm{d}s}\right)^2 - \frac{1}{c^2}\left(\frac{\mathrm{d}\mathcal{E}}{\mathrm{d}s}\right)^2\right] = \frac{1}{6\pi\varepsilon_0}\frac{e^2}{m^2c^3}\gamma^2\left[\left(\frac{\mathrm{d}p}{\mathrm{d}t}\right)^2 - \frac{1}{c^2}\left(\frac{\mathrm{d}\mathcal{E}}{\mathrm{d}t}\right)^2\right], \tag{6.15}$$

or in the conventional form:

$$P = \frac{e^2}{6\pi\varepsilon_0}\gamma^6\left[\dot{\vec{\beta}}^2 - (\vec{\beta}\times\dot{\vec{\beta}})^2\right]. \tag{6.16}$$

Total emitted power strongly depends on the particle momentum and mass, with the sixth power of the Lorenz γ factor. There are two relevant limiting cases of linear and transverse acceleration. In the linear case, the rate of momentum and energy change are connected by:

$$c^2p\frac{\mathrm{d}p}{\mathrm{d}t} = \mathcal{E}\frac{\mathrm{d}\mathcal{E}}{\mathrm{d}t}, \tag{6.17}$$

thus, the total emitted power is:

$$P_\mathrm{L} = \frac{1}{6\pi\varepsilon_0}\frac{e^2}{m^2c^3}\left(\frac{\mathrm{d}p}{\mathrm{d}t}\right)^2 = \frac{1}{6\pi\varepsilon_0}\frac{e^2}{m^2c^3}\left(\frac{\mathrm{d}\mathcal{E}}{\mathrm{d}x}\right)^2, \tag{6.18}$$

where: $\frac{\mathrm{d}\mathcal{E}}{\mathrm{d}x}$ - acceleration gradient.

In the transverse acceleration case, the rate of energy change is small in comparison with the momentum, thus:

$$P_\mathrm{T} = \frac{1}{6\pi\varepsilon_0}\frac{e^2}{m^2c^3}\gamma^2\left(\frac{\mathrm{d}p}{\mathrm{d}t}\right)^2 = \frac{1}{6\pi\varepsilon_0}\frac{e^2}{m^2c^3}\gamma^2\frac{\omega_0}{\rho}\beta^3\mathcal{E}^2, \tag{6.19}$$

where: $\left(\frac{\mathrm{d}p}{\mathrm{d}t}\right)^2 = \frac{\omega_0}{\rho}\beta^3\mathcal{E}^2$, ω_0 - instantaneous angular velocity and ρ - radius of the curvature of the trajectory. The ratio between power emitted in transverse and longitudinal acceleration is:

$$\frac{P_\mathrm{T}}{P_\mathrm{L}} \approx \gamma^2. \tag{6.20}$$

The SR emission during the longitudinal acceleration is at least a factor of γ^2 lower than in the transverse case, and is negligible in comparison with power gained from acceleration for accelerating gradients significantly below the gradient equivalent of gaining the energy corresponding to a stationary mass of an electron over a distance of classical electron radius ($2 \cdot 10^{20}\,\frac{\mathrm{eV}}{\mathrm{m}}$). The power emitted by electrons undergoing transverse acceleration, for example following a circular trajectory in a synchrotron, depends strongly on the particle energy, with the fourth power (see Equation (6.19)), and to a lesser degree on the curvature radius, only with a second power. This result suggests that there exists an upper energy limit reachable by the electron synchrotrons, beyond which they are not viable due to the required circumference and immense power needed to restore the energy lost to synchrotron radiation. This limit can be also understood in terms of luminosity limitation of synchrotrons. Higher collision energies can be reached at the cost of lowering the beam current, and thus lowering instantaneous luminosity, for a given accelerator circumference to keep the power lost to SR constant.

Let us express the Equations (6.18) and (6.19) in terms of the total emitted power radiated at time t in a unit solid angle about the direction $\hat{n}$ to obtain information about the angular distribution of synchrotron radiation. The power spectrum in the case of linear acceleration is then [77]:

$$P(\hat{n},t) = \frac{r_\mathrm{e}}{4\pi mc}\left(\frac{\mathrm{d}\vec{p}}{\mathrm{d}t}\right)^2 \frac{1}{\gamma^6}\frac{\sin^2\theta}{(1-\beta\cos\theta)^5}, \tag{6.21}$$

where: $\hat{n}$ - direction of observation, θ - angle between the velocity vector and emission direction.

For the transverse acceleration the total power is:

$$P(\hat{n},t) = \frac{r_\mathrm{e}}{4\pi mc}\left(\frac{\mathrm{d}\vec{p}}{\mathrm{d}t}\right)^2 \frac{1}{\gamma^2}\left[\frac{1}{(1-\beta\cos\theta)^3} - \frac{1}{\gamma^2}\frac{\sin^2\theta\cos^3\theta}{(1-\beta\cos\theta)^5}\right] \tag{6.22}$$

To evaluate the asymmetry of the radiation emission one can consider the mean value of $\sin^2\theta$, defined as:

$$< \sin^2\theta >= \int \sin^2\theta P(\hat{n},t)\mathrm{d}\Omega / P(t), \tag{6.23}$$

where: $P(\hat{n},t)$ is the power defined in either Equation (6.21) or Equation (6.22), and $P(t)$ is power as described in Equation (6.15).

For ultra-relativistic particles in both acceleration cases, the limit of the mean value of $\sin^2\theta$ is $\frac{1}{\gamma^2}$, and the angle between the direction of emission and of the motion of the electron is therefore:

$$\bar{\theta} = \sqrt{<\theta^2>} = \frac{1}{\gamma}. \tag{6.24}$$

The RMS value of the emission angle is $\frac{1}{\gamma}$, or equivalently the synchrotron radiation is emitted in a narrow cone with an opening angle proportional to $\frac{1}{\gamma}$.

It can be shown [77] that the power distribution as a function of the radiated frequency is described by:

$$P(\omega,t) = \frac{3\sqrt{3}}{4\pi}\frac{r_\mathrm{e}mc}{4\pi R}\gamma^4\frac{\omega\omega_0}{\omega_c^2}\int_{\omega/\omega_c}^{\infty} K_{5/3}(\eta)\mathrm{d}\eta, \tag{6.25}$$

where: R - instantaneous radius of curvature, $\omega_0 = \frac{c}{R}$, $\omega_\mathrm{c} = \frac{3}{2}\omega_0\gamma^3$ - critical frequency, $K_{5/3}$ - modified Bessel function [78].

Using Equation (6.25) one can calculate that the energy radiated into a frequency interval increases with frequency until $\omega \approx \omega_\mathrm{c}$, and beyond this value, for $\omega > \omega_\mathrm{c}$, the radiated energy

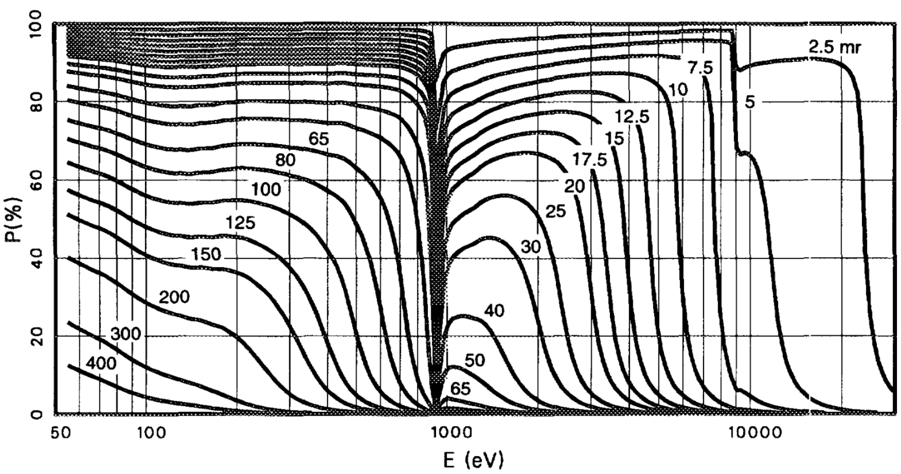

Figure 6.2: Reflectivity of copper as a function of energy and grazing angle available from the Henke database [47].

rapidly decreases. Therefore, the critical frequency splits the energy distribution in two regions. The distribution can be approximated by $(\omega/\omega_c)^{1/3}$ when $\omega \ll \omega_c$, and by $\sqrt{\omega/\omega_c}\, e^{\omega/\omega_c}$ when $\omega \gg \omega_c$.

The critical frequency is an important parameter to characterise the synchrotron radiation distribution. The critical energy of photons emitted from a beam travelling through a bending magnet, in convenient units, can be calculated using:

$$\mathcal{E}_c[\text{keV}] = \hbar\omega_c = \frac{3}{2}\frac{\hbar c}{\rho}\gamma^3 = 2.218\,\frac{\mathcal{E}^3\ [\text{GeV}]}{\rho\ [\text{m}]} = 0.665\,\mathcal{E}^2\ [\text{GeV}]\ \cdot B\ [\text{T}], \tag{6.26}$$

where: $\hbar$ - reduced Planck constant, ω_c - critical radial velocity, E - beam energy in GeV, ρ - bending radius in metres, B - induction of the magnetic field in T.

The average energy of photons is related to the critical energy, and can be calculated using:

$$<\mathcal{E}>= \frac{8}{15\sqrt{3}}\mathcal{E}_c. \tag{6.27}$$

The average energy of the emitted synchrotron radiation photons is a straight-forward parameter that can be used to check the validity of the used simulation models.

6.1.1 Specular and diffuse reflections

Reflection is a common phenomenon for photons belonging to the visible spectrum; however they can take place also for higher energy photons of up to about 30 keV. The probability of reflection depends strongly on the incident angle, especially at the higher energy of the photon. Reflectivity distributions as a function of energy and grazing angle for copper are shown in Figure 6.2.The minimum of reflectivity around the photon energy of 1 keV is caused by the proximity of the spectral L-line of copper at 931 eV, 951 eV and 1096 eV [75].

There are two types of reflections: specular, shown in Figure 6.3 (left), where the wavelength of a photon is much longer than the size of the irregularities of the reflective surface,

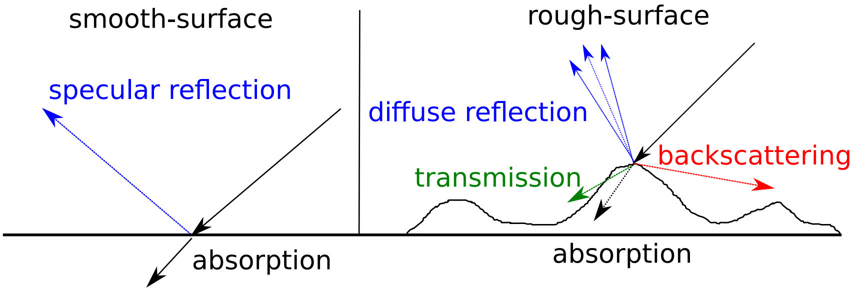

Figure 6.3: Possible outcomes of a photon interacting with a smooth surface (left) and a rough surface (right).

and diffuse, shown in Figure 6.3 (right), where the wavelength is comparable with the surface roughness. In the former case, the incident angle is equal to the outgoing angle. In a diffuse reflection the reflected angle has a distribution that depends on the surface properties, such as average roughness. Diffuse reflection can also lead to back-scattering.

Using the Kirchhoff scalar field integral, it is possible to derive the dependence of the reflection probability on the generalised surface properties [79]:

$$P_{\text{scattered}} \approx \mathrm{e}^{-g} \int \frac{\mathrm{d}\Omega}{P_0} \frac{\mathrm{d}P}{\mathrm{d}\Omega}\bigg|_{\text{specular}} + \int \frac{\mathrm{d}\Omega}{P_0} \frac{\mathrm{d}P}{\mathrm{d}\Omega}\bigg|_{\text{diffuse}} = P_{\text{specular}} + P_{\text{diffuse}}, \tag{6.28}$$

where the specular and diffuse reflection probabilities are:

$$\begin{aligned} P_{\text{specular}} &= \mathrm{e}^{-g} \int \frac{\mathrm{d}\Omega}{P_0} \frac{\mathrm{d}P}{\mathrm{d}\Omega}\bigg|_{\text{specular}} = \mathrm{e}^{-g} R, \\ P_{\text{diffuse}} &= \int \frac{\mathrm{d}\Omega}{P_0} \frac{\mathrm{d}P}{\mathrm{d}\Omega}\bigg|_{\text{diffuse}} = P_{\text{scattered}} - P_{\text{specular}} = (1 - \mathrm{e}^{-g}) R, \end{aligned} \tag{6.29}$$

and R - smooth surface field reflection coefficient, g - mean square surface height fluctuation.

The reflectivity of a metallic surface can be calculated from the refractive index using Fresnel formulas, as it is implemented in the reflection model of Synrad+ [80]:

$$R = \left| \frac{k_{\text{iz}} - k_{\text{oz}}}{k_{\text{iz}} + k_{\text{oz}}} \right|^2, \tag{6.30}$$

where: $k_{\text{iz}} = \frac{2\pi}{\lambda} \cos\theta$, λ - wavelength of the interacting photon, θ - grazing angle, $k_{\text{oz}} = \frac{2\pi}{\lambda}\sqrt{n^2 - \cos^2\theta}$, and n - complex refractive index.

The complex refractive index can be calculated from the atomic scattering factors:

$$n = \frac{r_{\text{e}}}{2\pi} \lambda^2 c_{\text{s}} f, \tag{6.31}$$

where: r_{e} - classical electron radius, c_{s} - concentration of atoms per unit volume, f - atomic scattering factor, a complex number where the imaginary part is a function of photo-absorption cross section, and the real part can be obtained from the imaginary through Kramers-Kronig dispersion relation.

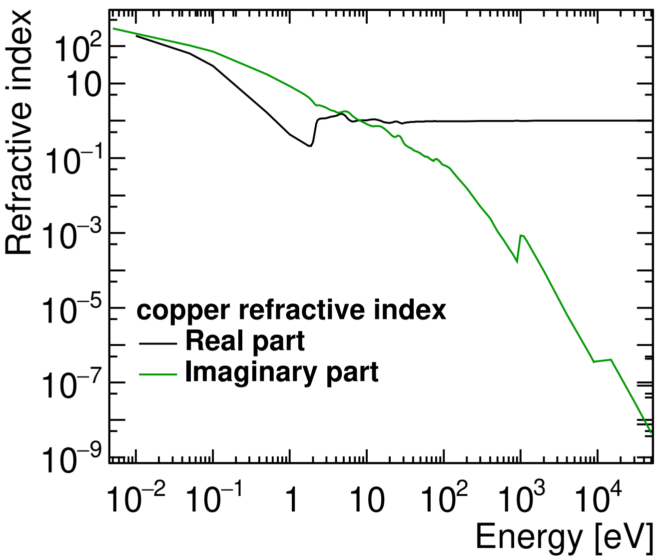

Figure 6.4: Real and imaginary part of copper refractive index and as a function of energy [82].

The scattering factors can be obtained from the Henke database [47] and the refractive indices for many materials are available in the Refractive Index Database [81]. An example of a distribution of the real and imaginary part of the refractive index in the case of copper is shown in Figure 6.4.

6.2 Simulation treatment

Simulations of the synchrotron radiation effects are done with PLACET and Synrad+. PLACET is used to obtain information regarding the total emitted power along the BDS, and the location of the SR emissions. The distributions of the photons created in the final doublet can also be studied with PLACET. The emitted SR photons are not tracked in the code, and thus the study of the photon interactions with the vacuum chamber is not possible with PLACET. For the interactions with the vacuum chamber walls, Synrad+ is used instead. The CLIC FFS is implemented in Synrad+ and the SR created along the accelerator are tracked until they reach the exit aperture of the QD0. From there, their impact on the CLICdet can be studied in full detector simulations using GEANT4.

A special version of the PLACET code is prepared, where more information about the SR is available. PLACET includes the SR effects in the form of energy loss of the particle moving through bending, quadrupole and multipole magnets. In the adapted version, the energy loss is translated into SR photons. The initial position and direction of velocities of a photon is the same as the direction of the particle that emitted it.

The photons get their angles from the emitting particle, as PLACET does not provide the information of the direction of the trajectory change due to the SR emission. However, the emission angle, as derived in Equation (6.24) is proportional to $\frac{1}{\gamma}$, and γ at CLIC energies is in the order of 10^5 at 380 GeV and 10^6 at 3 TeV, thus the error of assuming the SR emission exactly in the direction of the emitting particle is in the order of 30 nrad, and thus negligible.

Synrad+ is used for the treatment of the SR reflections in the CLIC Final Focus System. The entire BDS is not simulated in Synrad+, as the added length significantly slows down the computations, while not providing additional insight into the SR impact on the detector region. Most of the photons emitted in the BDS cannot reach the detector region without undergoing multiple interactions with the vacuum chamber wall surface that makes it highly unlikely for them to travel up to the IP. Therefore, omitting the photons produced prior to the FFS does not impact the results at the IP in a meaningful way. The energy and angular spectra of the emitted photons, as well as the total SR power, are compared with results from PLACET, and show good agreement.

The geometry of the simulated system is built using a software external to Synrad+, that takes as input a MAD-X output file with the parameters of the accelerator lattice, and creates a geometry readable by Synrad+. The information regarding magnetic regions of sector bending and quadrupole magnets is recorded, and put in the context of the aperture model. The apertures of the magnets can be provided directly, while the radii of the vacuum chamber in the drifts are interpolated as a linear transition between the apertures in the nearest magnetic regions.

The CLIC vacuum aperture shape is circular in all Synrad+ simulations. Polygons approximate the curved surfaces in Synrad+ and the circular vacuum chamber cross-section is split into 120 polygons to decrease the impact of the approximation, and obtain smoother distributions of reflected photons.

Synrad+ can accurately simulate seven orders of magnitude of the photon flux [80]. Therefore, the broad energy spectrum of photons is truncated to fulfil this requirement. Photons with energy below 4 eV do not carry enough power to be relevant in the study, and also cannot penetrate the vacuum chamber wall and interact with the sensitive elements of the detector. Photons with energies substantially above 30 keV have a negligible probability of reflection and are more likely to penetrate the vacuum chamber wall or be absorbed [47]. A choice of the range between 4 eV and 50 MeV was made. The truncation at 50 MeV does not impact the 380 GeV stage, however it does cut out the high energy tail of the SR distribution at 3 TeV.

Several types of materials provided with Synrad+ are used in the simulations of the CLIC FFS, namely: copper, iron, as well as some hypothetical materials such as the perfect absorber and more complicated shapes such as saw-tooth.

The perfect absorber material is used first to establish the impact of direct photons on the detector that can be compared with PLACET results, where the photon reflections are not included. This material is also used to obtain the information regarding the power emitted in the last few bending magnets and the final doublet that is carried by the SR photons traversing the QD0 magnet aperture.

Subsequently, copper and iron are used to study the impact of realistic reflectivities on the photon distributions at the QD0 aperture. In this case, iron approximates the stainless steel that is foreseen as the main material of the beam pipe for the CLIC BDS (with copper-coating inside). The impact of small differences in reflectivity between the application of copper and iron as the material for the CLIC BDS vacuum chamber is analysed. Different average roughnesses (R_a) are applied, with three main values used: 10 nm, 100 nm and 1 μm. The 100 nm average roughness is required in the CLIC ML [9], with precision machining reaching down to 10 nm [83]. The R_a requirements for the CLIC FFS are not established, however the FFS may not need to have such stringent requirements regarding the surface roughness, therefore several R_a values ranging from 1 μm down to 10 nm are studied to establish the sensitivity to different parameters and the related change in the photon flux and distributions at the QD0 exit.

The saw-tooth shape is used in the mitigation section. It is an equivalent effect surface of the saw-tooth used in the LHC beam screen [84] implemented in Synrad+. The computation cost of using a geometrically accurate saw-tooth in long elements of the accelerators is too high [80].

Photons are tracked in Synrad+ until the exit of the QD0 (at 380 GeV and 3 TeV) or the exit of the BeamCal (only at 3 TeV). Then, for each photon the three-dimensional position, the four-momentum vector and flux are stored for further analysis. In the general case, the beam pipe geometry between the QD0 exit and the IP is not simulated in Synrad+ due to its more complicated shape in the detector region that need not be implemented in Synrad+, as the SR photons can be embedded in a GEANT4 detector model containing all the necessary elements. However, it was found to be necessary for the 3 TeV energy stage.

Each photon stored at the QD0 exit aperture has a flux attached to it, making it a macroparticle (macrophoton) that represents a number of 'real' photons. The flux depends on the beam current and the magnetic region properties. It can be reduced during reflections, where only a fraction of the flux interacting with the beam pipe material is reflected. The photon flux is equivalent to a number of 'real' photons a stored macrophoton represents, and also the number of times the same macrophoton is embedded in the detector simulation.

The weight attached to each macrophoton is reduced in the procedure of normalisation the results to one bunch train. First, the simulation time has to be taken into account. The simulations run for a longer time than 1 s to obtain the required statistics of macrophotons. The fluxes attached to each macrophotons are given per second, thus all collected macrophoton fluxes need to be divided by the simulation running time provided by Synrad+. Then, the assumption present in Synrad+ that the beams represent a continuous current needs to be corrected. The bunch train time is used to multiply the flux attached to each photon, and is calculated for each energy stage:

$$t_{\text{train}} = N_{\text{bunches/train}} \times t_{\text{spacing}}, \tag{6.32}$$

where $N_{\text{bunches/train}}$ is the number of bunches per train and t_{spacing} is the time between bunches in a bunch train, equal to 0.5 ns.

The inputs to the GEANT4 simulations need to be translated to LCIO files and properly rotated before embedding them in the detector model. Photons created in PLACET and Synrad+ are created in the beamline frame of reference and need to be rotated by half of the crossing angle to translate them properly into the detector frame of reference. Positions and momenta in the vertical direction remain unchanged, while in the horizontal and longitudinal are rotated:

$$\begin{pmatrix} x \\ z \end{pmatrix}_{\text{detector}} = \begin{pmatrix} \cos\frac{\theta}{2} & \sin\frac{\theta}{2} \\ -\sin\frac{\theta}{2} & \cos\frac{\theta}{2} \end{pmatrix} \begin{pmatrix} x \\ z \end{pmatrix}_{\text{beamline}}, \tag{6.33}$$

where: $\theta = 20$ mrad at 3 TeV and 16.5 mrad at 380 GeV [21].

Hit distributions coming from the detector response are summed with a distribution that is mirrored against the XY-plane, where the Z-axis is colinear with the longitudinal detector axis, to take into account the existence of photons coming from the opposite direction, produced in the second BDS. The safety factor for photons is assumed to be equal to two to take into account the uncertainty of the SR photons interactions with the material of the detector.

The main figure of merit is the occupancy level in the CLIC detector caused by the SR photons. All of the considered material choices and roughnesses are compared in terms of the visible energy of the photons in the detector. Out of them, a few representative examples are chosen for full detector simulations. The energy of a photon is recorded as visible if the photon has energy above 1 keV and a polar angle $\theta_{\text{QD0}} > 3.3$ mrad. The polar angle is calculated from the centre axis at the exit of the QD0. The 3.3 mrad corresponds to the BeamCal aperture of 32 mm located on the opposite side of the detector. The occupancies are calculated according to the methods described in section 3.2.1.

The initial aperture models derived in section 5.1 are compared with their extended versions described in section 5.3, and the impact of slight changes of the apertures on the photon fluxes at the exit of QD0 is analysed. However, the extended versions are used by default for the simulations and optimisations of the FFS at 380 GeV and at 3 TeV in Synrad+.

Table 6.1: Beam parameters at the IP at the 3 TeV energy stage, when the synchrotron radiation effects are not taken into account ('Without SR') and when they are included in the simulation ('With SR'). Simulations performed using PLACET.

	σ_x [nm]	σ_y [nm]	$< E >$ [GeV]	σ_E [%]
Without SR	41.0	1.1	1500.1	0.35
With SR	48.3	1.2	1499.8	0.35
change [%]	18	9	-0.02	$<1 \cdot 10^{-2}$

6.3 Impact in the BDS

The emission of synchrotron radiation leads to several effects that can impact the machine and beams negatively. The beams lose energy by emitting photons, and their interactions with the vacuum chamber can lead to absorption of the radiation, and thus heating, transmission, which would increase the radiation levels in the tunnel, or reflection which allows the SR to travel much further downstream the accelerator. In addition, the interactions of photons with the surface of the beam pipe can create photo-electrons that lead to desorption of gas particles attached to the surface, which is detrimental to vacuum pressure and quality.

6.3.1 Energy loss and beam quality

Synchrotron radiation emission impacts the beams negatively through the loss of energy and increase of the transverse beam sizes. The energy of the beams after the acceleration in the ML is fixed, and the power lost to SR in the BDS cannot be replenished. Therefore, the loss is irreversible.

The average energy loss per particle along the BDS can be derived from the SR photon energy distributions and the average number of photons emitted per beam particle. The SR photon energy distributions of all photons emitted in the BDS at both 380 GeV and 3 TeV are shown in Figure 6.5. The average photon energy is 45 keV at 380 GeV and is a factor about ninety larger at 3 TeV. The average energy loss along the BDS is 1.1 MeV at 380 GeV and 240 MeV at 3 TeV, which accounts to only $6 \cdot 10^{-4}\%$ and 0.02% of the beam energy, respectively. The energy loss at 380 GeV is significantly below the 0.35% relative energy spread initially present in the beams leaving the ML and negligible when compared with the beam energy. The situation is different at 3 TeV, where the energy loss per particle is a factor 200 larger, while the energy increased only by a factor of eight. The energy loss is comparable with the energy spread and cannot be neglected.

The beam parameters coming from PLACET of 3 TeV beams that are impacted by the emission of SR and when the SR effects are not included in the simulation are summarized in Table 6.1. Particles in both beams have their initial energy correlated with the position in a bunch, as required by the BNS damping. The energy spread remains unchanged at 0.35%. The energy spread would increase if the initial beams had no energy spread, or the energy spread had a uniform distribution. The average energy is slightly lower in the case where the SR effects are present, and the difference is equal to the average energy loss per particle of 0.02% of their initial energy.

The biggest difference between these two situations is in the transverse beam sizes. The beam core sizes are significantly increased in comparison with the beams not impacted by the SR. The transverse beam distributions at the IP simulated with PLACET for the two cases are shown in Figure 6.6. The SR emission leads to a significant increase in the number of particles travelling far away from the beam centre, especially in the vertical direction. The presence of these tails is detrimental to the achievable luminosity and the luminosity quality.

In summary, the energy loss due to SR is negligible at 380 GeV in comparison with the initial energy spread and the beam energy. However, it is relevant at 3 TeV and cannot be neglected. The SR emission impacts the beam quality negatively at the higher energy stage by increasing the transverse beam sizes.

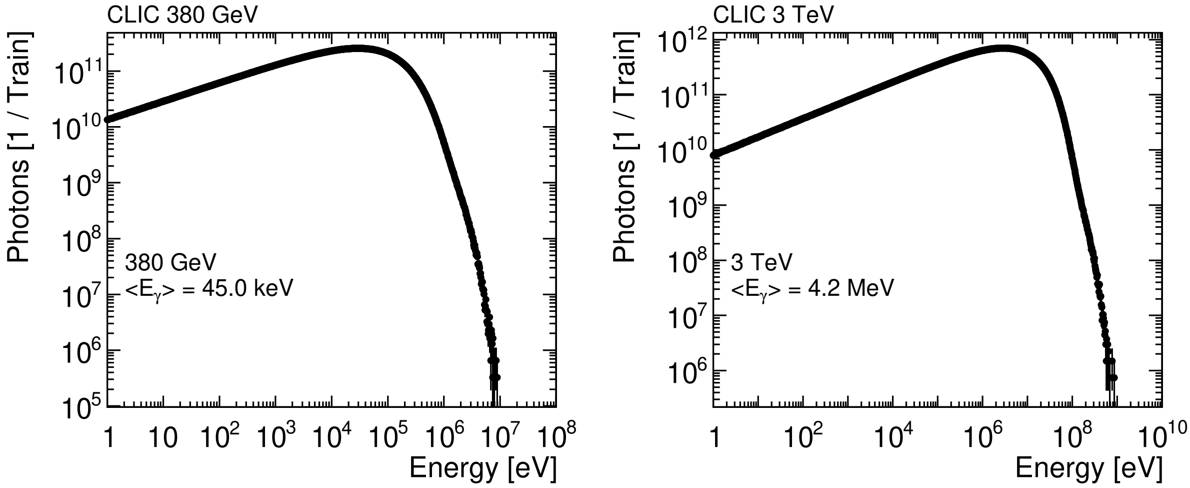

Figure 6.5: Distributions of synchrotron radiation photon energies for all photons emitted along the CLIC BDS at 380 GeV(left) and 3 TeV(right) simulated in PLACET. The horizontal axes of the distributions have variable bin sizes that are invariant in the logarithmic scale.

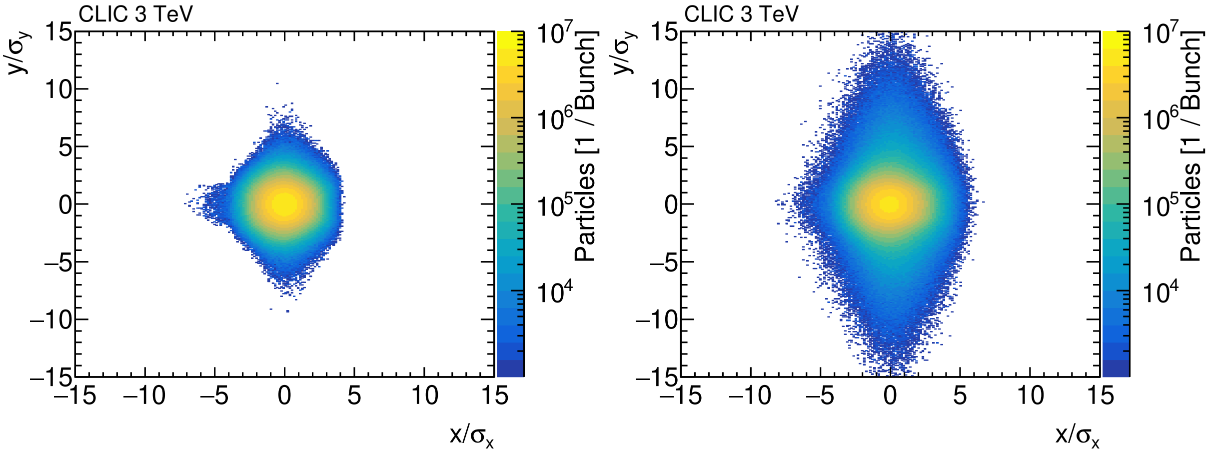

Figure 6.6: Transverse beam distributions at the IP at the 3 TeV energy stage when the synchrotron radiation effects were not taken into account in the simulation (left) and with the SR effects impacting the beams (right). The beam sizes are expressed in terms of nominal beam sizes at 3 TeV, shown in Table 2.1.

6.3.2 Radiation levels in the tunnel

The probability of the SR photons penetrating the vacuum chamber walls is low, due to small grazing angles of the photons. Simple geometric considerations conclude that the wall thickness t at a grazing angle θ is increased proportionally to:

$$t = \frac{d}{\sin\theta}, \tag{6.34}$$

where: d - vacuum chamber wall thickness, assumed to be 1 mm, θ - grazing angle.

The attenuation of the photon flux traversing the material of the vacuum chamber can be described in terms of exponential attenuation, defined as:

$$I = I_0\, \mathrm{e}^{-t/\lambda}, \tag{6.35}$$

where: I_0 - initial photon flux, t - material thickness in $\frac{g}{\mathrm{cm}^2}$ units, $t = d \cdot \rho$ where d - thickness of the material and ρ - material density, λ - photon mass attenuation length, that can be read out from Figure 6.7. The average thickness of the beam pipe of 1 mm and the density of iron of 7.87 $\frac{g}{\mathrm{cm}^3}$ [75] are used.

At 380 GeV, where the average photon energy is in the keV range, as can be seen in Figure 6.5(left), photons interact with matter through the photoelectric effect and Compton scattering. For photons emitted in the bending magnets, the grazing angle is closely related to the bending angle of the magnets. In the 380 GeV CLIC BDS, the bending magnets in the final 400 m have bending angles in the order of 10 µrad, and length of 2.5 m each. A photon emitted tangentially to the beam trajectory in the centre of the vacuum chamber will hit the vacuum chamber after around 24 magnets, assuming the inner aperture radius of 15 mm. Therefore, the average grazing angle is in the order of 0.24 mrad. For such a grazing angle, the perceived wall thickness, using Equation (6.34) is about $4.2 \cdot 10^3$ mm.

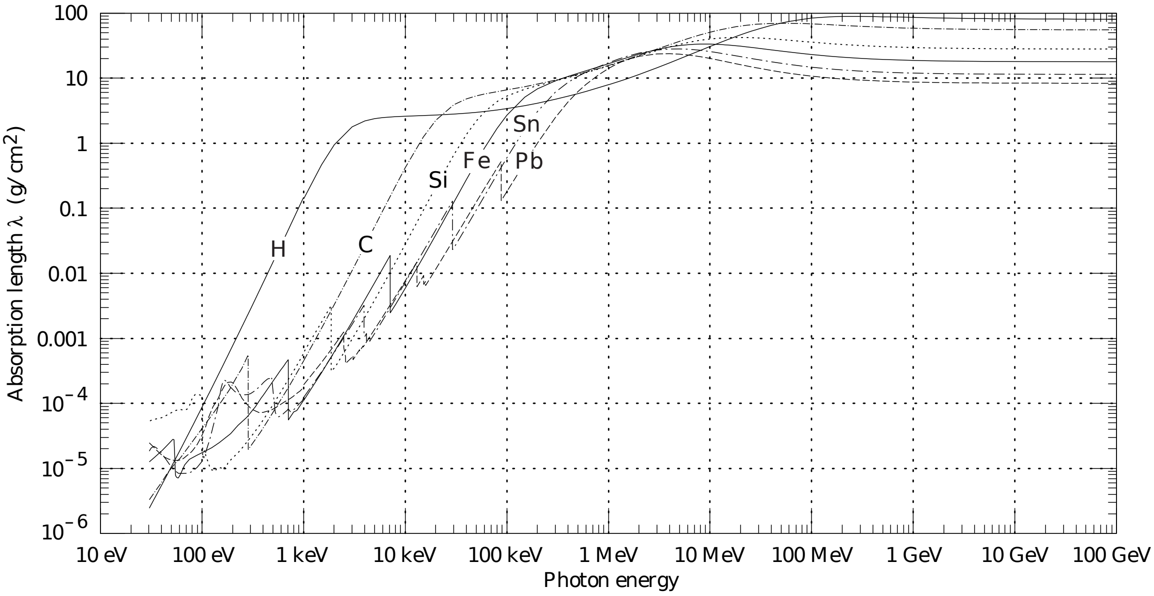

Figure 6.7: Photon mass attenuation lengths for various materials as a function of the photon energy [85].

Using the average energy of the SR photon from Figure 6.5(left) the mean free path is about $1\,\frac{\mathrm{g}}{\mathrm{cm}^2}$. Assuming exponential attenuation in the wall material, and using Equation (6.35), one can conclude that all of the photons are absorbed, and the radiation in the tunnel does not increase. Assuming conservatively the highest energy observed in the photon spectrum at 380 GeV of 10 MeV, for which the attenuation coefficient is around $30\,\frac{\mathrm{g}}{\mathrm{cm}^2}$, and increasing the grazing angle to the bending angle of all one hundred bending magnets combined in the final 400 m metres of the FFS, the photons are still fully attenuated in the vacuum chamber material. The intensity of the photon flux remains below 1% of the photon flux in the vacuum chamber for grazing angles lower than 170 mrad and for a photon of average energy at this energy stage.

The average energy of photons at 3 TeV is in the MeV range, as can be seen in Figure 6.5(right). Photons in this energy range can create pairs, as well as electromagnetic cascades. The average bending angle of the bending magnets located in the final metres of the 3 TeV BDS is lower than at 380 GeV. It is around 1 µrad, while the magnet length is similar. Assuming conservatively that the grazing angle is equal to the bending angle of all of the bending magnets combined, it is around 0.4 mrad. The perceived thickness is thus around $2.8 \cdot 10^3$ mm. For the average photon energy, using Figure 6.5(right), the attenuation length from Figure 6.7 is around $30\,\frac{\mathrm{g}}{\mathrm{cm}^2}$, while for the maximal observed energy of almost 1 GeV the mass attenuation is about $20\,\frac{\mathrm{g}}{\mathrm{cm}^2}$. Using Equation (6.35), the photons emitted in the 3 TeV BDS are completely attenuated in the vacuum chamber walls. The intensity of the photon flux remains below 1% of the photon flux in the vacuum chamber for grazing angles lower than 9 mrad and for a photon of average energy at this energy stage.

In conclusion, the radiation level in the tunnel is estimated to not be increased by the SR produced in the BDS, assuming the grazing angles determined by the bending magnets and exponential photon attenuation. Therefore, no additional shielding of the beam pipe is required. However, these estimates do not take into account possible scattering in the material, that can significantly change the grazing angle while a photon is traversing the material, and thus allow some of the photons to penetrate the beam pipe and enter the tunnel. In addition, the development of an electromagnetic shower in the vacuum chamber wall increases the proportion of the energy that can leak into the tunnel. A more detailed study of the grazing angles and full simulations of the photon interactions with the beam pipe wall material might be required in the future.

6.3.3 Heating of the beam pipe

The power emitted in the form of SR heats up the beam pipe and can create conditions that require a dedicated cooling system to protect the machine elements. The SR heating can be a problem especially in cryogenic systems, where the extraction of the unwanted heat is inefficient due to low efficiency of the Carnot cycle for low temperature difference systems [86]. Heating of superconducting elements can lead to loss of superconductivity, and for example, magnet quenches. The cooling can also be required for normal-conducting elements if the heat load is deemed too high.

The total power emitted in the form of the SR photons in the BDS coming from PLACET is 16 W at 380 GeV and 2.3 kW at 3 TeV, from which 11.4 W and 442 W, respectively, are emitted in the FFS. The numbers concerning the FFS can be compared between PLACET and Synrad+. Synrad+ predicts that the total power loss to SR is 11.2 W at 380 GeV and 332 W at 3 TeV. The results at 380 GeV are in excellent agreement, with less than 3% relative difference between the codes. The situation is different at 3 TeV, where the relative discrepancy reaches 33%. However, the difference can be explained by the photon top energy cut off at 50 MeV present in Synrad+ simulations. When the same energy range is imposed on the PLACET spectrum, the total power comes down to 367 W in the FFS, and the relative difference shrinks to about 10%. The remaining discrepancy is due to a more realistic beam representation in PLACET, where the energy spread and non-linear beam dynamics are taken into account. Wherever applicable, the PLACET prediction of the total power is used, as it is free from energy spectrum limitations imposed on Synrad+ simulation.

The energy emitted in the form of the SR radiation along the CLIC BDS simulated with PLACET is shown in Figure 6.8. From the detector perspective, the most significant SR emissions take place in the final doublet quadrupoles at both energy stages, due to the proximity of the emission point and the high energy carried by photons. However, in terms of the total emitted power, the photons emitted in the bending magnets in the last 400 m of the FFS are more relevant at both energy stages. These photons become especially relevant when the SR reflections are included in simulations. At 380 GeV 70% of the power is emitted in the FFS, while at 3 TeV it is only 20%, due to intense emissions in the collimation section. The average linear power density is 8 mW/m in the entire BDS, and 14 mW/m in the FFS at 380 GeV, and 0.7 W/m and 0.6 W/m respectively at 3 TeV. For the heating estimates in this section, the larger value is used for each energy stage.

To estimate the impact of the SR heat several assumptions are made. Assumed are adiabatic conditions, an average beam pipe aperture of 15 mm at 380 GeV and 6 mm at 3 TeV with a uniform thickness of 1 mm, as well as instantaneous heating of the entire beam pipe element.

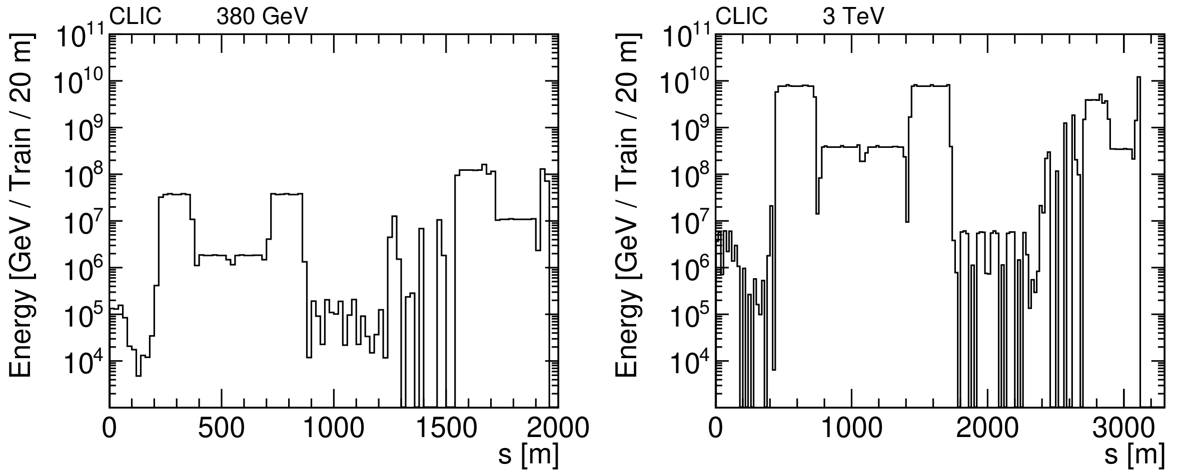

Figure 6.8: Distributions of energy emitted in the form of synchrotron radiation photons along the CLIC BDS at 380 GeV(left) and 3 TeV(right) simulated in PLACET.

The structure of the CLIC beam pipe consists of iron that is copper-coated on the inner surface. This coating is neglected in the following estimates. Using these assumptions, the temperature increase due to SR at each point of the distributions shown in Figure 6.8 can be calculated using:

$$\Delta T = \frac{P_{\mathrm{SR}}\Delta t}{V\rho\sigma_{\mathrm{Fe}}}, \tag{6.36}$$

where: P_{SR} - SR power at given point, Δt - elapsed time, V - volume of the beam pipe material per bin length, ρ - density of iron, 7.87 $\frac{\mathrm{g}}{\mathrm{cm}^3}$ [75], σ_{Fe} - specific heat of iron, 0.449 $\frac{\mathrm{J}}{\mathrm{g}\cdot\mathrm{K}}$ [75].

The temperature increase distribution along the BDS at both energy stages is shown in Figure 6.9. In the calculation of the temperature increase per hour, no cooling and heat dissipation are assumed. In addition, complete absorption of the entire SR power is assumed at the point of emission. In the actual machine, the SR power is going to be more diluted along the accelerator, reducing the height of the maximal temperature. The last assumption does not impact the average temperature increase.

The maximal temperature increase per hour at 380 GeV is just below 0.7 K difference between the beam pipe and the ambient temperature in the accelerator tunnel. At 3 TeV, the temperature increase is substantially more significant, leading to an unacceptable increase in the collimation region of up to 80 K/hr. The temperature increase at the very end of the BDS is linked with the SR emission in the final doublet. This energy is safely removed from the detector region and does not interact with the beam pipe in the detector region so that it can be safely neglected when only the incoming beamline is considered. The temperature increase at 3 TeV needs to be addressed by a dedicated active cooling solution, while at 380 GeV active cooling may not be required.

Either passive or active cooling can be envisaged to address the heat load. First, let us estimate the efficiency of radiative and convective cooling, by calculating the equilibrium temperature difference between the beam pipe outer wall and the tunnel air.

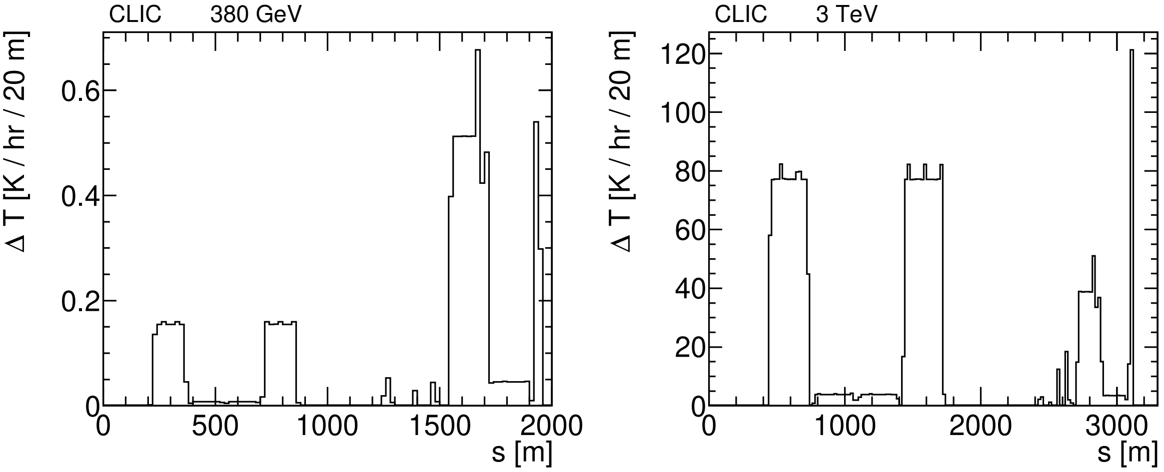

Figure 6.9: Distributions of the temperature increase due to absorption of synchrotron radiation energy over one hour of machine running at 380 GeV(left) and 3 TeV(right). No power dissipation or cooling is assumed.

The power emitted by the beam pipe at a temperature T_{pipe} in a tunnel with a temperature T_{ambient}, assuming a gray-body radiation follows the Stefan–Boltzmann formula:

$$P = \varepsilon A \sigma_{\mathrm{SB}} (T^4_{\mathrm{pipe}} - T^4_{\mathrm{ambient}}), \tag{6.37}$$

where: P - radiated power, ε - material emissivity: 0.1–0.94 for iron [87], A - emitting surface, $\sigma_{\mathrm{SB}} = 5.67 \cdot 10^{-8} \frac{\mathrm{W}}{\mathrm{m^2 K^4}}$ - Stefan–Boltzmann constant, T_{ambient} - air temperature in the tunnel surrounding the beam pipe, assumed to be 293 K.

In the equilibrium condition, the power received from the SR and emitted in the radiative cooling are equal, thus allowing one to calculate the equilibrium temperature difference using Equation (6.38).

$$T_{\mathrm{pipe}} = \left(\frac{P_{\mathrm{SR}}}{\varepsilon A \sigma_{\mathrm{SB}} + T^4_{\mathrm{ambient}}} \right)^{1/4}. \tag{6.38}$$

This results in the maximum temperature increase in the range from 100 K at 380 GeV to 340 K at 3 TeV. Even if the high emissivity of 0.94 is assumed, the beam pipe would need to heat up about 60 K above the ambient temperature at 380 GeV and 200 K at 3 TeV. Such a temperature rise is not acceptable, taking into account the tight precision and stability requirements of the elements on the micrometre-level and the impact of the thermal expansion of the beampipe.

The equilibrium temperature along the BDS, when the radiative cooling with 0.1 emissivity is assumed is shown in Figure 6.10. The radiative cooling at both energy stages is not a viable choice, as it requires substantial temperature differences between the beam pipe and the ambient temperature. At 3 TeV, the temperature increase is limited to below 340 K in the collimation region, an increase that cannot be allowed due to the safety of the machine components. Therefore, radiative cooling is not sufficient to stabilise the beam pipe temperature on average and

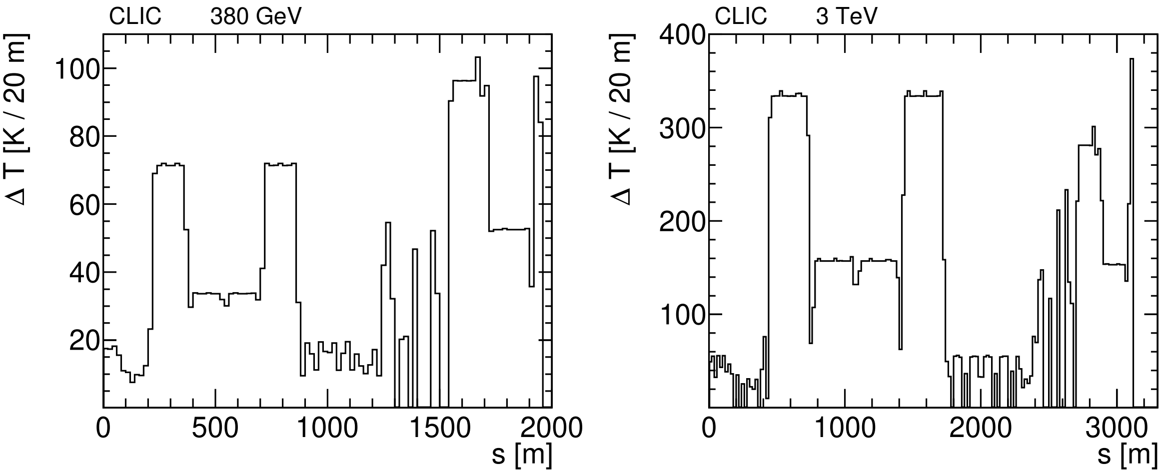

Figure 6.10: Distributions of the equilibrium temperature increase above the ambient temperature at 380 GeV(left) and 3 TeV(right), assuming radiative cooling and 0.1 emissivity.

especially not in the regions where the SR emission is the highest.

The other method to cool the beam pipe is by the means of convection. Convective heat transfer is a complex phenomenon that depends on the shape of the heat-emitting object and the surrounding environment conditions. The exact description of this process is beyond the scope of this work, therefore a simplified approach to estimate the natural convection cooling of a beam pipe is used. The following equation describes the general expression for the convection heat exchange:

$$P = hA\Delta T, \tag{6.39}$$

where: h - heat transfer coefficient, A - area of the emitting surface, ΔT - temperature difference between the emitting surface and the surrounding environment.

For free (natural) laminar convection of air under normal pressure the heat transfer coefficient ranges from $0.5\,\frac{\mathrm{W}}{\mathrm{Km^2}}$ to $1000\,\frac{\mathrm{W}}{\mathrm{Km^2}}$ [88]. The lower value is used as a conservative estimate. To obtain the increase of the beam pipe temperature in the equilibrium condition, the heat transferred to air in the laminar convection must be equal to the power received from the SR:

$$\Delta T = \frac{P_{\mathrm{SR}}}{hA}. \tag{6.40}$$

The equilibrium temperature difference when the convective cooling with a heat transfer coefficient of 0.5 is assumed is shown in Figure 6.11. The convective cooling, even with such a low heat transfer coefficient is sufficient to stabilise the beam pipe temperature within 1 K from the ambient temperature at 380 GeV. At 3 TeV, the temperature increase is up to 150 K in the collimation region. The heat exchange coefficient needs to be at least $80\,\frac{\mathrm{W}}{\mathrm{Km^2}}$ to maintain the temperature increase due to SR heating within 1 K from the ambient temperature.

In conclusion, at 380 GeV, the average power of the synchrotron radiation is low, and the associated temperature rise under the asssumed conditions is negligible. The situation is different at 3 TeV, where the average power per metre is about 90 times larger. The estimate of

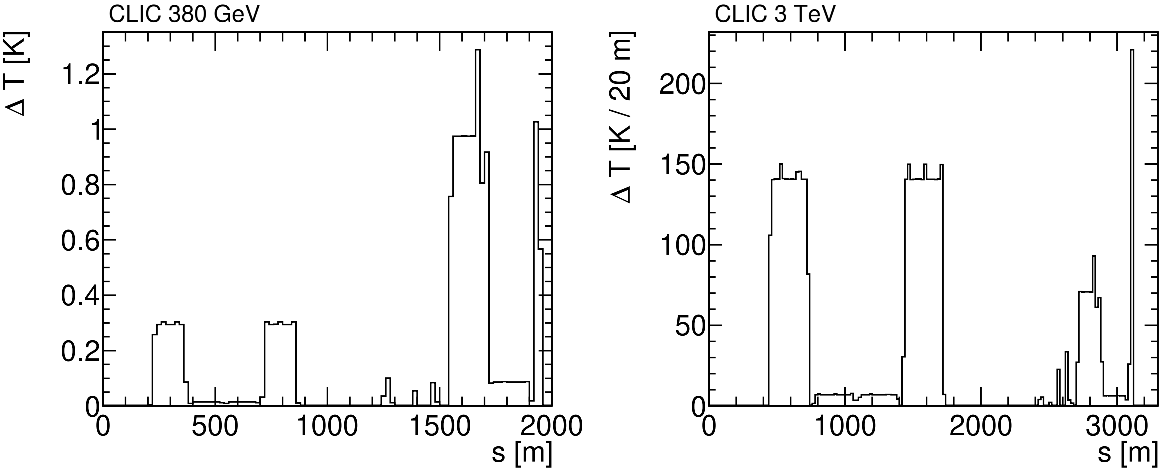

Figure 6.11: Distributions of the equilibrium temperature increase at 380 GeV(left) and 3 TeV(right) assuming convective cooling with heat transfer coefficient $h = 0.5\,\frac{\mathrm{W}}{\mathrm{Km}^2}$.

passive cooling efficiencies shows a substantial increase in the beam pipe temperature. Therefore, a dedicated cooling system for the beam pipes in the CLIC BDS at 3 TeV should be studied in more detail in the future, especially for the collimation region.

6.3.4 Photo-desorption and outgassing

Synchrotron radiation photons can cause significant photo-desorption, and the increased outgassing leads to a pressure rise in the vacuum system. It is the main source of the gas load in electron–positron storage rings such as LEP [89] or FCC-ee [90], and is also a major concern for the LHC vacuum system [91]. The synchrotron radiation reflections increase the area impacted by photons and thus increase the outgassing rates in the CLIC BDS.

The outgassing rate due to the synchrotron radiation desorption, assuming only the photoelectric effect, is defined as [91]:

$$Q'\,[\mathrm{mbar} \cdot \mathrm{l/s}] = K\eta\Gamma, \tag{6.41}$$

where: η - desorption yield ($2 \cdot 10^{-6}$ molecule/photon [90]), K - conversion from molecules to pressure ($4.01 \cdot 10^{-20}$ mbar·l/molecule at 298 K), Γ - photon yield (photons/s)

To maintain the average pressure $< P >$ an effective pumping pressure S' is required:

$$S'[\mathrm{l/s}] = Q'/ < P >, \tag{6.42}$$

where: Q' is defined as in Equation (6.41), and $< P >$ is $2 \cdot 10^{-9}$ mbar in order to limit the beam losses to 10^{-5} [9].

The photon fluxes, related gas loads, and required pumping speeds are summarised in Table 6.2. The photon fluxes are coming from Synrad+ simulations, where copper vacuum chamber walls with an average roughness of 100 nm and no SR absorbers are used. The obtained numbers for FCC-ee are quoted per length in the arcs, so the CLIC numbers from the FFS are

Table 6.2: Comparison of maximum and average outgassing loads in the CLIC BDS simulated with Synrad+ and FCC-ee [90] due to the photo-desorption.
$i = 1$ for FCC-ee and CLIC average data, while $i = 2$ for the maximal fluxes of photons interacting with vacuum chamber in the CLIC FFS.

	photon flux [ph/s/m^i]	gas load [mbar·l/s/m^i]	pumping speed [l/s/m^i]
CLIC 380 GeV max	$3.6 \cdot 10^{16}$	$2.9 \cdot 10^{-9}$	1.5
CLIC 380 GeV average	$1.4 \cdot 10^{12}$	$1.1 \cdot 10^{-13}$	$5.5 \cdot 10^{-5}$
CLIC 3 TeV max	$6.5 \cdot 10^{15}$	$5.2 \cdot 10^{-10}$	$2.6 \cdot 10^{-1}$
CLIC 3 TeV average	$7.2 \cdot 10^{11}$	$5.8 \cdot 10^{-14}$	$2.9 \cdot 10^{-5}$
FCC-ee 91.2 GeV	$7.1 \cdot 10^{17}$	$5.7 \cdot 10^{-8}$	28.7
FCC-ee 365 GeV	$1.2 \cdot 10^{16}$	$9.5 \cdot 10^{-10}$	$4.7 \cdot 10^{-1}$

made comparable by extracting average flux per metre. The maximal fluxes and outgassing loads provided by Synrad+ are given per square metre.

The photon fluxes and outgassing rates are more significant at 380 GeV than at 3 TeV. The photon emissions are more intense at the lower energy stage due to the higher beam current and a factor of two stronger weak bending magnets in the Final Focus System.

The maximal photon fluxes per area in CLIC BDS are located directly in front of the QD0 entrance. The average numbers are estimated using the total number of absorbed photons along the FFS divided by the total length of the system. The average and maximal pumping speed required in the CLIC FFS are not challenging in comparison with the requirements for FCC-ee. The pumping speeds can be easily met with the planned use of Non-Evaporative Getter (NEG) pumps [9]

The SR-induced outgassing was found [90] to be a challenging issue that needs to be addressed at FCC-ee, while at CLIC the outgassing rates in the FFS are not significant. The maximal outgassing rate is at 380 GeV, and remains a factor ten below the average level of FCC-ee at 91.2 GeV (Z-boson pole). The required average and maximum pumping speeds in CLIC FFS are below the FCC-ee in the arcs at the Z-pole and do not constitute a threat to the quality of the vacuum system.

A full vacuum pressure study in the CLIC FFS with coupled Synrad+ and Molflow+ [40] simulations should be pursued in the future to have the full knowledge of the vacuum quality along the CLIC BDS and FFS in particular. The gas pressure increase due to inclusion of Compton scattering and pair production should also be included.

6.4 Impact in the detector region

Synchrotron radiation at CLIC can be an issue also in the detector region. Photons with energies surpassing 1 keV can penetrate the beam pipe and leave significant energy deposits in the sensitive material of the detector, especially in the vertex and tracker.

First, the transverse photon distributions at the exit of the QD0 magnet are presented, and their impact on the beam pipe aperture choice in the detector region is discussed in section 6.4.1. The impact of the vacuum chamber material on the photon polar angle and energy distributions is shown in section 6.4.2. Finally, the hit densities and related occupancy level in the tracking detectors are presented in section 6.4.3.

6.4.1 Beam pipe aperture optimisation in the detector region

The apertures of the incoming beam pipe in the BeamCal region need to be optimised at both the 380 GeV and 3 TeV energy stages to take into account the transverse SR photons distributions. The SR photons tranverse position distributions at the exit of the QD0 with fully absorbing walls of the vacuum chamber and two roughness options for copper are shown in Figure 6.12. Photons are concentrated centrally and along the X-axis. In all cases, the photons around the centre are coming mainly from the final doublet, and the elongated distribution along the X-axis comes from emissions in the last few bending magnets. The photons with positive X position are coming predominantly from reflections from the vacuum chamber walls in the FFS. Higher reflectivity of the vacuum chamber walls leads to photons filling out the entire available transverse space of the QD0 aperture [92].

It is a design requirement [9] that the photons emitted in the final quadrupole doublet do not interact with the material of the detector. To fulfil this requirement, the beam pipe aperture design in the detector region needs to be revisited. The goal can be achieved by increasing the apertures of the incoming beamline in the BeamCal region. The apertures should be increased to match the QD0 aperture at each energy stage. Direct photons have a very low divergence; thus, this extension is sufficient to ensure the safety of the kicker system, and minimises scattering in the BeamCal region.

The updated beam pipe design in the detector region for the 380 GeV energy stage is summarised in Table 6.3 and in Table 6.4 for 3 TeV, using the CLICdet detector model design as the starting point [14]. The inner aperture between the longitudinal position of 2700 mm and 3500 mm in the incoming beamline is extended from 2.7 mm to 17.5 mm at 380 GeV, and from 2.7 mm to 7.6 mm in the 3 TeV detector model. The beam pipe thickness is kept at 1 mm.

The detector models with updated apertures are used instead of the model described in the CLICdet Note [14], in the full-detector simulations of the SR photons impact on the occupancy levels.

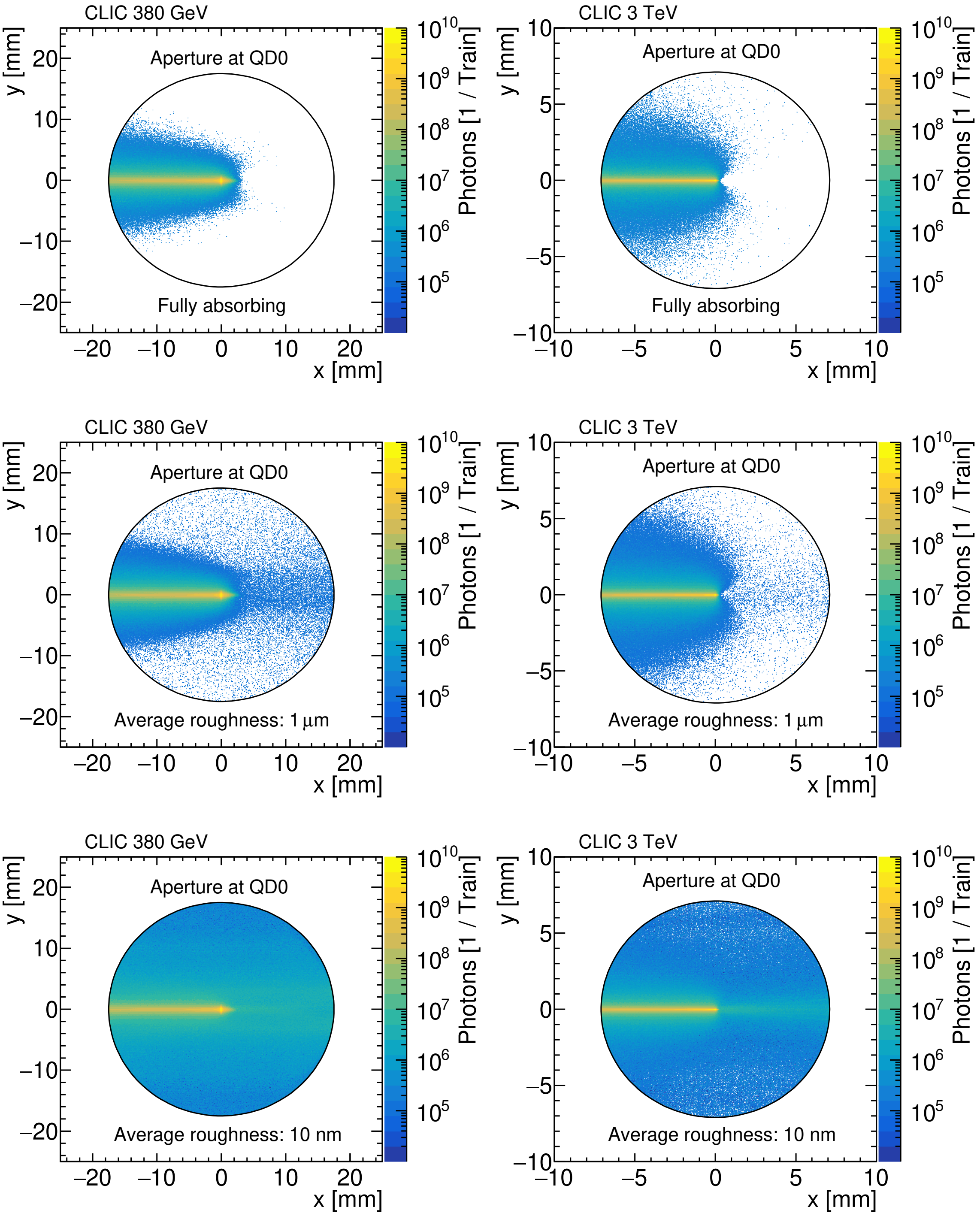

Figure 6.12: Transverse position distributions of synchrotron radiation photons at the QD0 exit at 380 GeV (left column) and 3 TeV (right column) assuming fully absorbing walls (top), copper walls with 1 µm roughness (middle), copper walls with 10 nm roughness (bottom).

Table 6.3: Beam pipe apertures in the detector region implemented in the simulation model for the 380 GeV energy stage based on the CLICdet model [14].

&[A]	Z_1 [mm]	Z_2 [mm]	R_1^{In} [mm]	R_2^{In} [mm]	R_1^{Out} [mm]	R_2^{Out} [mm]
0	0	308	29.4	29.4	30.0	30.0
0	308	337	29.4	29.4	30.0	33.4
0	337	2080	29.4	235.2	33.4	240.0
0	2080	2528	235.2	235.2	240.0	240.0
0[B]	2528	2531	0.0	98.0	240.0	240.0
2	2531	3170	98.0	98.0	99.0	99.0
2[C]	3170	3173	17.5	31.0	99.0	99.0
2	3173	3500	31.0	31.0	32.0	32.0
2[D]	3500	12500	31.0	125.0	32.0	127.0
1	3173	3281	17.5	17.5	18.5	18.5
1	3281	3835	17.5	17.5	18.5	18.5
1	3835	3845	17.5	17.5	18.5	18.5
1	3845	12500	17.5	17.5	18.5	18.5

Each element has a circular aperture and is a cylinder barrel or a cone located between Z_1 and Z_2. The radii $R_{1,2}^{\mathrm{In,Out}}$ are the inner and outer radii at position Z_1 and Z_2 respectively.

[A] Alignment of the beam pipe element: 0 - aligned on the detector axis, 1 - aligned on the incoming beam axis, 2 - aligned on outgoing beam axis.

[B] Beam pipe end in front of LumiCal: R_1^{Out} is the size of the hole where the beam pipe inside LumiCal is connected. The hole is centred on the outgoing beam axis.

[C] Beam pipe end in front of BeamCal: R_1^{In} is the size of the hole for the incoming beam pipe,
R_1^{Out} is the size of the hole for the outgoing beam pipe.

[D] Conical beam pipe with a half-opening angle of 10 mrad.

Table 6.4: Beam pipe apertures in the detector region implemented in the simulation model for the 3 TeV energy stage.
The parameter descriptions are the same as for the 380 GeV design in Table 6.3. [14].

&[A]	Z_1 [mm]	Z_2 [mm]	R_1^{In} [mm]	R_2^{In} [mm]	R_1^{Out} [mm]	R_2^{Out} [mm]
0	0	308	29.4	29.4	30.0	30.0
0	308	337	29.4	29.4	30.0	33.4
0	337	2080	29.4	235.2	33.4	240.0
0	2080	2528	235.2	235.2	240.0	240.0
0[B]	2528	2531	0.0	98.0	240.0	240.0
2	2531	3170	98.0	98.0	99.0	99.0
2[C]	3170	3173	17.5	31.0	99.0	99.0
2	3173	3500	31.0	31.0	32.0	32.0
2[D]	3500	12500	31.0	125.0	32.0	127.0
1	3173	3281	7.6	7.6	8.6	8.6
1	3281	3835	7.6	7.6	8.6	8.6
1	3835	3845	7.6	7.6	8.6	8.6
1	3845	12500	7.6	7.6	8.6	8.6

6.4.2 Photon distributions at the QD0 exit

The photons propagated through the FFS geometry by Synrad+ are stored at the exit of the final focus quadrupole magnet, QD0. The transverse and angular distributions of the SR photons at this position determine the radiation impact on the CLIC detector. The parameter used to quantify the impact is the θ_{QD0} angle that signifies the polar angle where the reference point is located in the centre of the beampipe at the QD0 exit, 6 m upstream from the IP.

Polar angles are calculated for each SR photon to estimate the flux and energy that can be deposited in the detector. Polar angle distributions of the SR photons are shown in Figure 6.13. The distributions are split into two parts depending on the origin of photons. Direct photons, coming from the last few bending magnets and the final focus quadrupoles are emitted with low polar angles and occupy the left-hand side of the figure. The flux of direct photons dominates the distribution, however they do not contribute towards the total energy visible in the detector. The reflected photons have significantly larger polar angles, spanning from 1 mrad to almost $\frac{\pi}{2}$. Due to larger apertures, the reflected photons are more numerous at 380 GeV in comparison with the 3 TeV energy stage, by a factor of about ten when using the same material and roughness.

Photons with polar angles $\theta_{\mathrm{QD0}} > 3.3\,\mathrm{mrad}$, as shown in Figure 6.13, where the reference point is located in the centre of the beam pipe at the QD0 exit, 6 m upstream from the IP, are capable of interacting at least with the material of the BeamCal located on the opposite side (later referred to as 'far-side') of the detector. Photons with such polar angles are recognised visible in the detector, and the total energy they carry in each studied case are summarised in Table 6.5.

The polar angle distributions of photons coming from a BDS with a fully absorbing vacuum chamber walls at both energy stages are constrained to the low polar angles, as only the direct photons traverse the QD0 aperture. Therefore, in the case when the fully absorbing walls are used in the FFS the SR photons do not interact with the material of the detector, fulfilling the detector safety requirement. This result is consistent with PLACET simulations, where photons produced in the final doublet and the last few bending magnets cannot interact with the sensitive material of the detector. The absence of the SR photons in the acceptance of the detector is the desired experimental condition. It ensures there are no accidental hits and unwanted energy depositions in the tracking detector, also in the form of additional heat.

The application of realistic reflectivities of copper and iron leads to a substantial amount of visible energy that can be deposited in the detector. The photon distributions strongly depend on the reflectivity of the material and its average roughness. A change of $\mathrm{R_a}$ by a factor of ten, from 1 µm to 100 nm, increases the number of reflected photons that can hit the sensitive material of the detector by a factor of fifteen at 380 GeV and twenty-five at 3 TeV. The number of photons quickly decreases with increasing polar angle in all studied cases.

The visible energy of the SR photons is abundant, even where a rough copper surface with $\mathrm{R_a}$ of 1 µm is used, as shown in Table 6.5. The visible energy surpasses the nominal collision energy at 380 GeV, and is comparable with the collision energy at 3 TeV. The amount of energy is higher at 380 GeV than at 3 TeV when copper is used as the vacuum chamber material, but the opposite is true when the vacuum chamber is made of iron. The difference in the number

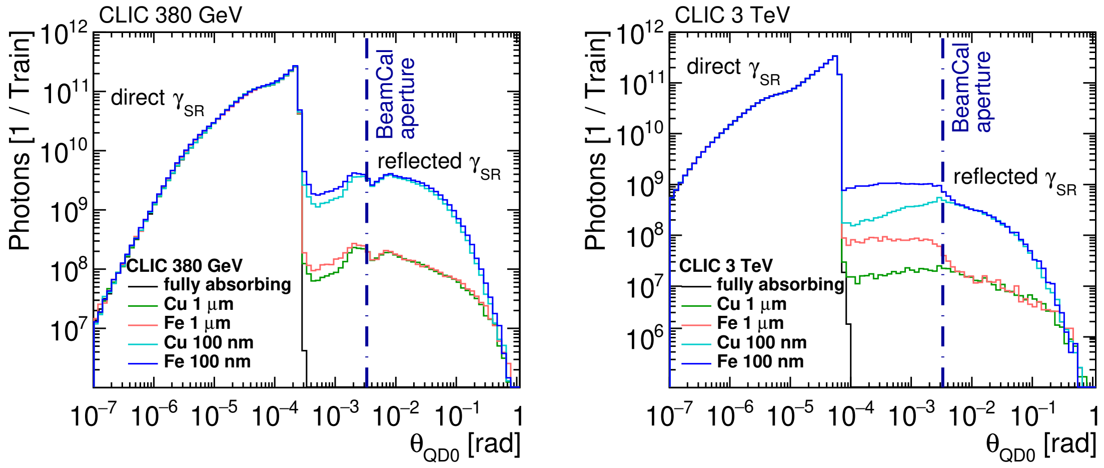

Figure 6.13: Polar angle distributions of synchrotron radiation photons at the QD0 exit at 380 GeV(left) and 3 TeV(right) with copper and iron vacuum chamber walls with 1 µm and 100 nm average surface roughness simulated with Synrad+ [92]. θ_{QD0} signifies the polar angle where the reference point is located in the centre of the beampipe at the QD0 exit, 6 m upstream from the IP. The marked BeamCal aperture refers to the BeamCal located on the opposite side of the detector.

Table 6.5: The energy carried by photons with polar angle $\theta_{\mathrm{QD0}} > 3.3$ mrad per bunch train with various beam pipe wall material and roughness assumptions. The energy that can be deposited in the detector is two times larger than the presented numbers, as two beamlines meet in the interaction region. Safety factors are not included.

	visible energy [TeV]	
	380 GeV	3 TeV
fully absorbing	0.0	0.0
Cu 1 µm	7.0	0.9
Fe 1 µm	8.6	50
Cu 100 nm	85	11
Fe 100 nm	$1.2 \cdot 10^2$	$6.0 \cdot 10^2$
Cu 10 nm	$3.9 \cdot 10^2$	$1.1 \cdot 10^2$
Fe 10 nm	$6.0 \cdot 10^2$	$3.7 \cdot 10^3$

of reflected photons between copper or iron vacuum chamber, as shown in Figure 6.13, is not as large as the difference in the visible energy. The angular distribution of the energy carried by photons that provides an explanation to this observation is shown in Figure 6.14. The difference in the distributions is the result of a harder energy spectrum at the higher energy stage, that leads to a lower probability of reflections. The other factor is the higher reflectivity of iron in comparison with copper. The use of iron for the vacuum chamber wall results in significantly more copious amounts of energy deposited in the detector region in comparison when copper of the same roughness is used, and thus the use of iron should be avoided.

Larger apertures allow photons to travel longer distances before they hit a vacuum chamber surface. The result is a smaller of interactions that can remove photons and a greater number of

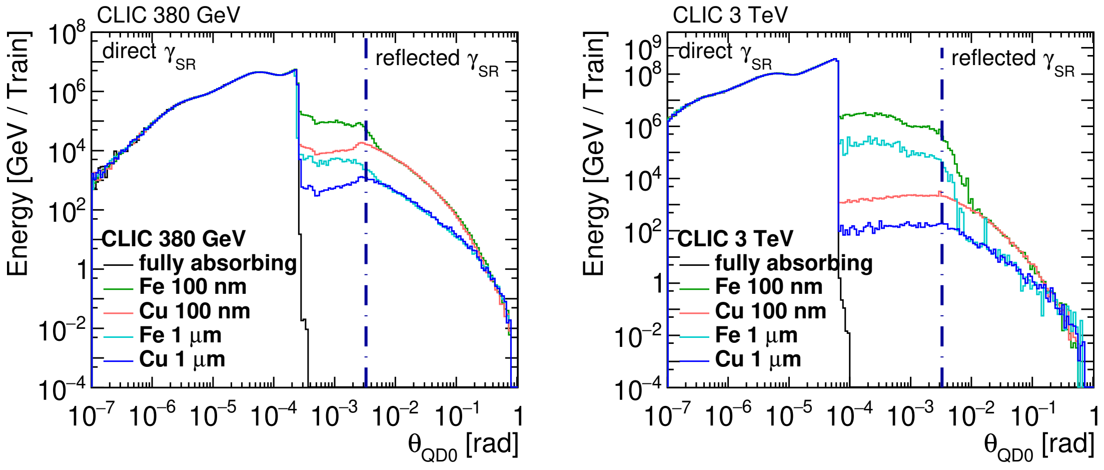

Figure 6.14: The angular distribution of the energy carried by synchrotron radiation photons at the QD0 exit at 380 GeV(left) and 3 TeV(right) with copper and iron vacuum chamber walls with 1 µm and 100 nm average surface roughness simulated with Synrad+. θ_{QD0} signifies the polar angle where the reference point is located in the centre of the beampipe at the QD0 exit, 6 m upstream from the IP. The marked BeamCal aperture refers to the BeamCal located on the opposite side of the detector.

photons reaching the detector region. Therefore, the extended apertures provide a more challenging environment for the detector. A comparison of the polar angle distributions between the initial and extended apertures of the 380 GeV BDS and 3 TeV BDS is shown in Figure 6.15. There are no significant differences in the polar angle distributions of the SR photons in the case of the 380 GeV BDS, and the total visible energy is similar between the initial and the extended design, within a 5% relative difference. The lack of a significant increase in the photon flux can be explained by the design of the extended aperture model, where the final doublet quadrupole aperture remains unchanged. The smaller aperture at the end of the FFS works as an absorber for the SR photons travelling at large offsets from the vacuum chamber axis. Therefore, when these photons are removed, the result is similar regardless of the extension.

For 3 TeV, the polar angle distributions differ significantly between the initial and the extended apertures. The extended apertures lead to a substantial increase of reflected photons (with $\theta_{\mathrm{QD0}} > 100\,\mu\mathrm{rad}$) in each of the roughness options, similarly to the 380 GeV design, the aperture in the QD0 magnet is slightly smaller than in the preceding magnets. The aperture is 7.6 mm in comparison with 8.4 mm in the first magnet of the final doublet. The reduction is equal to only a 10% difference, while at 380 GeV it is more substantial, with a 40% difference between the apertures of the QF1 and QD0. The smaller difference than at 380 GeV leads to not removing the photons travelling at large offsets to the beam pipe centre. Since these divergent photons are not removed, the amount of visible energy in the detector region is substantially increased in the extended aperture case, by around 40%.

The energy distributions of the SR photons traversing the QD0 aperture, similarly to the polar angle distributions, have contributions from both direct photons produced in the final

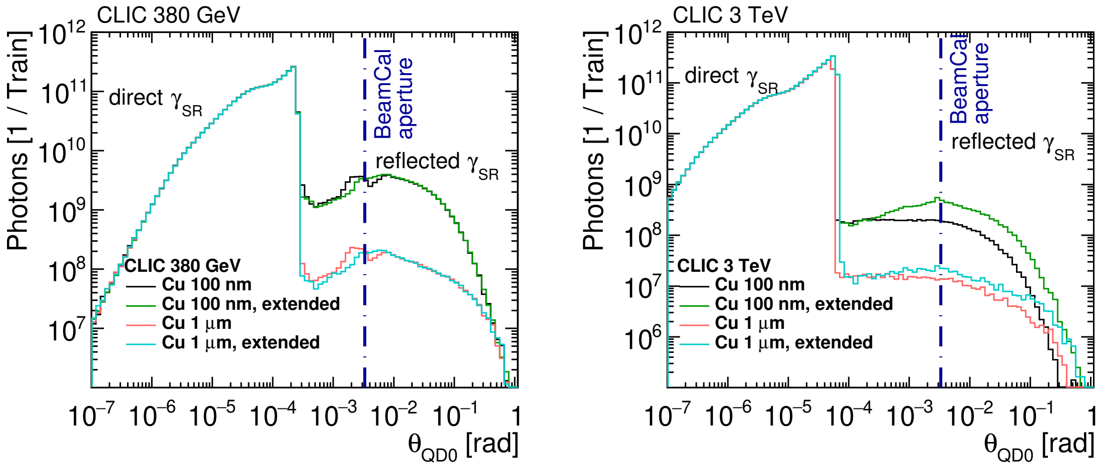

Figure 6.15: Polar angle distributions of synchrotron radiation photons at the QD0 exit at 380 GeV(left) and 3 TeV(right) using the initial and extended apertures derived in section 5.1 and section 5.3, respectively. The vacuum chamber walls are made of copper, with 1 μm and 100 nm average surface roughness and simulated with Synrad+.

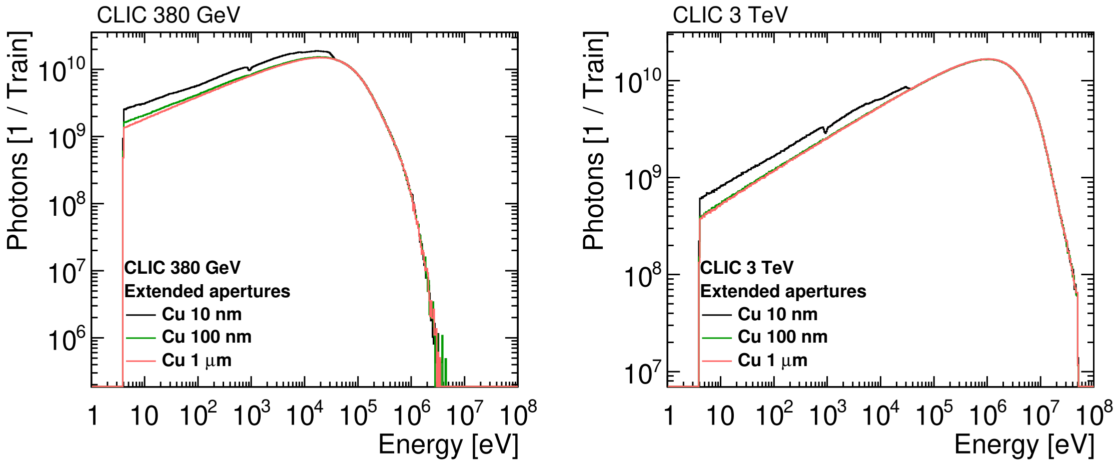

Figure 6.16: Energy distributions of synchrotron radiation photons at the QD0 exit at 380 GeV(left) and 3 TeV(right), using copper vacuum chamber walls with 1 μm, 100 nm, and 10 nm surface roughness simulated with Synrad+.

doublet quadrupoles and the last few bending magnets and the photons that underwent reflections. Direct photons dominate over the reflected ones, and define the shape of the distributions, as shown in Figure 6.16. Direct photons are all photons with energy above 30 keV, and constitute most of the photons.

The contribution from the reflected photons enhances the number of low energy photons for an average roughness below 100 nm, as can be seen in Figure 6.16. However, the impact of the enhancement on the average photon energy is limited and is not larger than 8% of the relative value between material choices and roughnesses. The average photon energy is in the 100 keV range at 380 GeV, and is a factor forty larger at 3 TeV, reaching the MeV-range.

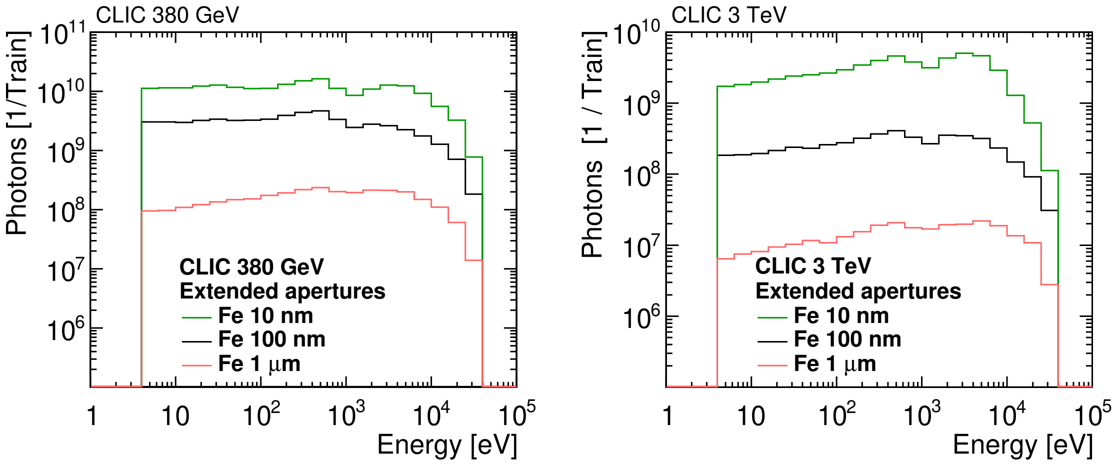

Figure 6.17: Energy distributions of synchrotron radiation photons with $\theta_{\mathrm{QD0}} > 3.3\,\mathrm{mrad}$ at the QD0 exit at 380 GeV(left) and 3 TeV(right), using copper vacuum chamber walls with 1 µm, 100 nm and 10 nm surface roughness simulated with Synrad+.

The critical energy in the weak bending magnets, as calculated using Equation (6.26), is fifty-six times larger at 3 TeV than at 380 GeV, even though the magnets have a factor ten lower bending angle. The difference in the average photon energy is smaller than the difference in the critical energy in the bending magnets. The emission of lower energy photons in the bending magnets at 380 GeV is compensated by the emission of higher energy photons in the quadrupole magnets at the lower energy stage, caused by larger beam divergence and size than at 3 TeV.

The average SR photon energies at the exit of the QD0 magnet are smaller than the average energy of all the photons emitted in the BDS at each respective stage. Less intense and energetic emissions in the weak bending magnets and quadrupole in the final metres of the FFS in comparison with the stronger bending magnets in the collimation region of the BDS explain the observed discrepancy. The distribution at the QD0 exit lacks the higher energy photons produced upstream because photons with energies above 30 keV have negligible reflectivity and therefore do not reach the detector region.

The energy distributions of the photons with polar angle above 3.3 mrad are shown in Figure 6.17. The shape of the distributions is sensitive to the used material and average roughness. The higher reflectivity cases have a larger dip in the 1–2 keV energy range that splits the distribution into two parts. The dip is caused by a minimum of reflectivity in this energy range. An increase in reflectivity changes especially the low energy part of the distribution, as these photons have the highest probability of reflection while the higher energy range is fully determined by the direct photons emitted in the weak bending magnets and final focus quadrupoles. Therefore, the average energy of photons decreases with increasing reflectivity. The average energy varies from 1.8 keV to 2.3 keV at 380 GeV and from 2.0 keV to 3.2 keV at 3 TeV. The average energy of emitted photons differ significantly between the energy stages, by a factor of forty, but the average energy of photons that can impact the detector are similar.

The low energy part, with photons below 1 keV does not constitute a risk of increasing the

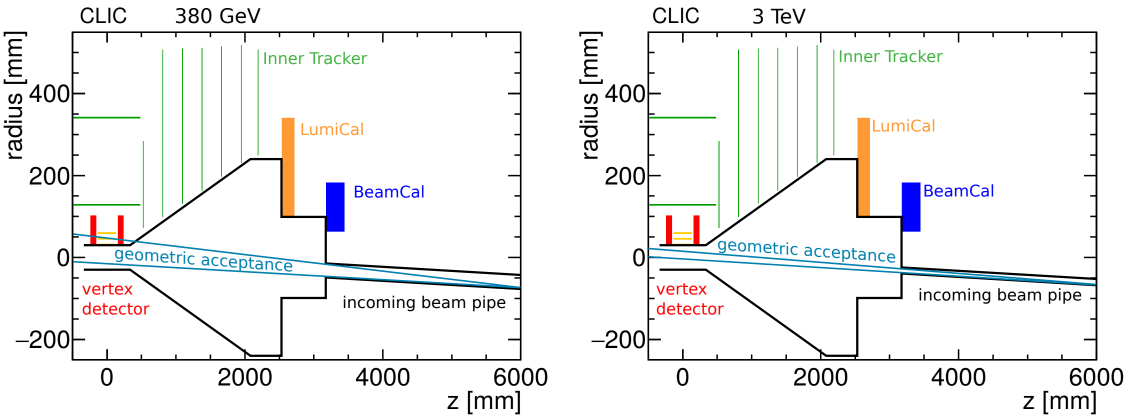

Figure 6.18: Geometric acceptance of synchrotron radiation photons taking into account the detector geometry at 380 GeV (left) and 3 TeV (right).

occupancy level in the detector, as the energy deposits are below the energy threshold for all of the detectors. These photons can lead mostly to the heating of the beam pipe in the detector region, and the detectors located closest to the IP region. However, the low energy photons can also induce radiation damage after a long exposition. The total power carried by the SR photons passing through the QD0 aperture is equal to 0.5 W at 380 GeV and 25 W at 3 TeV. The visible photons carry only a small fraction of the photon beam power, 2.8 mW at 380 GeV and 0.9 W at 3 TeV, but is still substantial enough to cause damage, especially at the higher energy stage. Therefore, the radiation damage from the unmitigated SR in the detector region may be a concern, and the energy depositions in the tracking detector need to be simulated in GEANT4.

In summary, the desired experimental conditions without the unwanted SR photons in the acceptance of the detector are provided at both energy stages by using fully absorbing vacuum chamber walls. Realistic material reflectivities lead to substantial amounts of energy to be visible in the detector. The use of iron as the material for the beam pipe is not advised, as for the same aperture and average roughness it provides a larger number of photons that can impact the detector negatively in comparison with copper. The energy that is visible in the detector scales strongly with the average material roughness used in the FFS. Based on realistic material reflection tables, the best experimental conditions are provided by a copper surface with an average roughness around 1 µm.

6.4.2.1 Geometric acceptance of the photons

Direct SR photons can interact with the sensitive material of the detector if their polar angle is larger than 3.3 mrad. However, for direct photons the polar angle also needs to be lower than the limit imposed by the beam pipe aperture of the incoming beamline, so the SR photons do not interact with the beam pipe multiple times. Otherwise, only indirect interaction is possible, where a photon needs to scatter to reach larger polar angles to be able to interact with the sensitive material of the detector. The borders of the geometric acceptance limited by the aperture in the BeamCal region is shown in Figure 6.18.

The synchrotron radiation photons that are travelling through the QD0 aperture can interact directly with the vertex detector barrel and disks at 380 GeV. The remaining of the tracking detector is outside of the geometric acceptance, thus are expected to receive a significantly smaller number of hits than the vertex detector. At 3 TeV, even the vertex detector is outside the geometric acceptance, as shown in Figure 6.18(right). Therefore, at 3 TeV, the photons can interact with the sensitive material of the trackers indirectly, after scattering in the beam pipe in the BeamCal region.

Photons with considerable angles $\theta_{\mathrm{QD0}} \approx \frac{\pi}{2}$ can interact with the material of the yoke endcap and the HCal endcap. The high energy threshold of 300 keV for detection in the HCal endcap cells surpasses the maximum energy of photons in the detector acceptance by a factor of ten. Multiple simultaneous hits from the SR photons could leave energy depositions above the threshold. However, this case is not observed in the full detector simulations.

The MuonID system can be impacted, as the energy threshold of the gaseous sensitive elements is only 300 eV, if photons can penetrate the beam pipe and find themselves between the iron yoke plates. Similar to the HCal endcap, the energy depositions above threshold are not observed in full detector simulations.

The ECal endcap, with the energy threshold of the silicon sensors of 40 keV, which is above the maximal energy of the visible photons, should not be impacted negatively by SR. In addition, the ECal endcap is shielded by the HCal endcap from the SR photons entering the detector. The SR photons cannot point directly at the far-side ECal endcap, as the required polar angle is at least 31 mrad, while the limitation imposed by the BeamCal aperture is below this number at both energy stages.

The ECal and HCal barrels and the MuonID barrel are also safe from the SR due to their distant position from the central beam pipe and the low probability of photons scattering in the centre of the detector to gain the necessary polar angle to point towards these subdetectors. The scattered photons would need to traverse all of the material between the IP region and leave energy depositions over threshold in the sensitive elements of these detectors, which is highly unlikely.

The SR photons are also unlikely to impact the forward calorimeters, even on the near-side of the detector. The BeamCal shadows the LumiCal, and therefore the latter remains safe from the SR. The SR photons need to penetrate the beam pipe at low grazing angles and then traverse through tungsten absorber plates to reach the sensitive material of the BeamCal.

The only detectors that can be strongly impacted by the SR photons are the vertex and Inner Tracker detectors, due to their position close to the beam pipe, and relatively low energy threshold in the keV range.

The larger beam pipe aperture in the 380 GeV detector model leads to a larger possibility that the sensitive material receives significant energy depositions in comparison with the 3 TeV design. At 3 TeV, photons need to scatter in the beam pipe material in the detector region to increase their polar angle to make the hits in the tracking detectors possible. Therefore, the hit rates for the same total energy of photons with polar angles above 3.3 mrad should be significantly lower at 3 TeV than at 380 GeV. The larger beam pipe aperture in the 380 GeV detector model leads to a larger proportion of the visible energy that can interact with the sensitive elements of the detector than at 3 TeV.

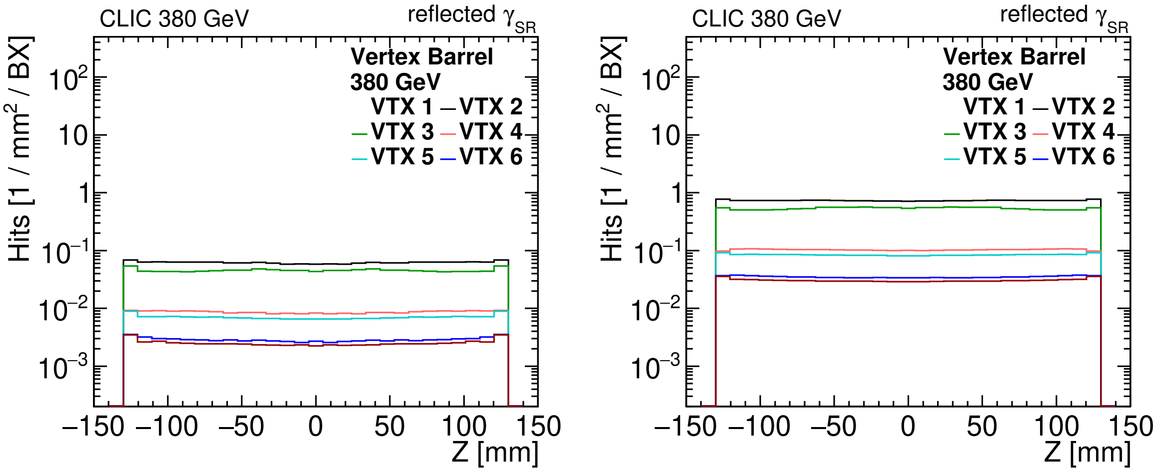

Figure 6.19: Distribution of the hit densities per bunch crossing in the vertex barrel at 380 GeV coming from the reflected synchrotron radiation photons assuming average roughness of the copper vacuum chamber wall of 1 µm (left) and 100 nm (right).

6.4.3 Hit densities and occupancies in silicon trackers

The hit densities are calculated using Equation (3.3). There is no limit imposed on the maximal number of hits per bunch crossing as well as the maximal occupancy level. The occupancies coming from these hit densities are calculated using Equation (3.4), assuming a cluster size of five in the vertex detector and of two in the tracker, and including a safety factor of two. In the full detector simulations, the SR photons coming from the BDS with copper vacuum chamber walls and two roughness options: 1 µm and 100 nm are used.

The SR photons used for the hit densities simulations and calculations are coming from the Synrad+ simulations with an electron beam. The detector is impacted by SR photons coming also from the positron beam. To take this into account and to remove asymmetry coming from using a beam coming only from one direction, the hit distribution that comes directly from GEANT4 simulations is added with itself mirrored against the transverse XY-plane.

6.4.3.1 380 GeV

The hit densities from the reflected SR photons in the vertex barrel are shown in Figure 6.19(left) when the 1 µm average roughness copper is used, and in Figure 6.19(right) when 100 nm average roughness (R_a) is used. The factor of ten decrease in roughness leads to a proportional increase in the number of hits observed in the vertex detector. The occupancy linked with these hit rates surpasses 100% in the 100 nm roughness case, as shown in Figure 6.20. In both cases, the occupancy is significantly above the 3% acceptable limit in the first double layer and severely impacts the detector performance when R_a is 1 µm, and renders it unusable when R_a is at or below 100 nm.

The hit densities of the vertex disks are shown in Figure 6.21. At the lowest radii, the hit densities are even larger than in the vertex barrel, due to the lower polar angles of the disks located on the other side of the IP. The occupancy, shown in Figure 6.22, reaches 30% in the

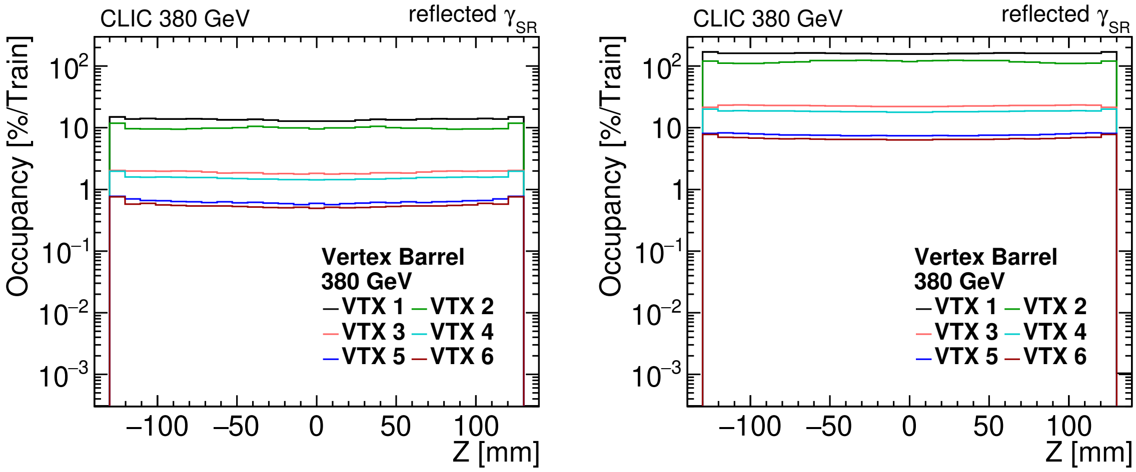

Figure 6.20: Distribution of the occupancies per bunch train in the vertex barrel at 380 GeV coming from the reflected synchrotron radiation photons assuming average roughness of the copper vacuum chamber wall of 1 µm (left) and 100 nm (right).

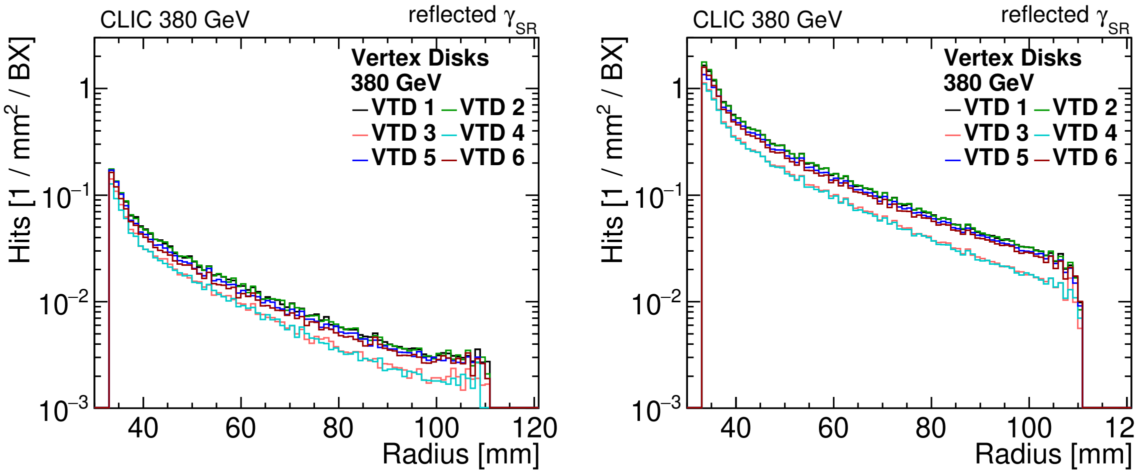

Figure 6.21: Distribution of the hit densities per bunch crossing in the vertex disks at 380 GeV coming from the reflected synchrotron radiation photons assuming average roughness of the copper vacuum chamber wall of 1 µm (left) and 100 nm (right).

rough copper case and is more than a factor ten larger at the lowest radii when a smoother vacuum chamber surface is used in the FFS.

The disks located in the middle of the forward region of the vertex detector, namely disks VTD3 and VTD4, have consistently lower hit rates than either disks VTD 1 and 2 or VTD 5 and 6. The lower hit rates can be explained by shielding of the disks in the middle, provided by the disks located on either side.

The hit densities and occupancies are much lower in the Inner and Outer Tracker barrel than in the Vertex detector, especially for layers located further away from the beam pipe. The most impacted is the first Inner Tracker layer, as shown in Figure 6.23, where the hits caused by the SR photons have a 'hat'-like distribution. Such hit density is a result of the transition between being impacted by the 'direct' photons that travelled in almost straight-line from the QD0 exit, and the hits are coming from photons that underwent scattering while traversing

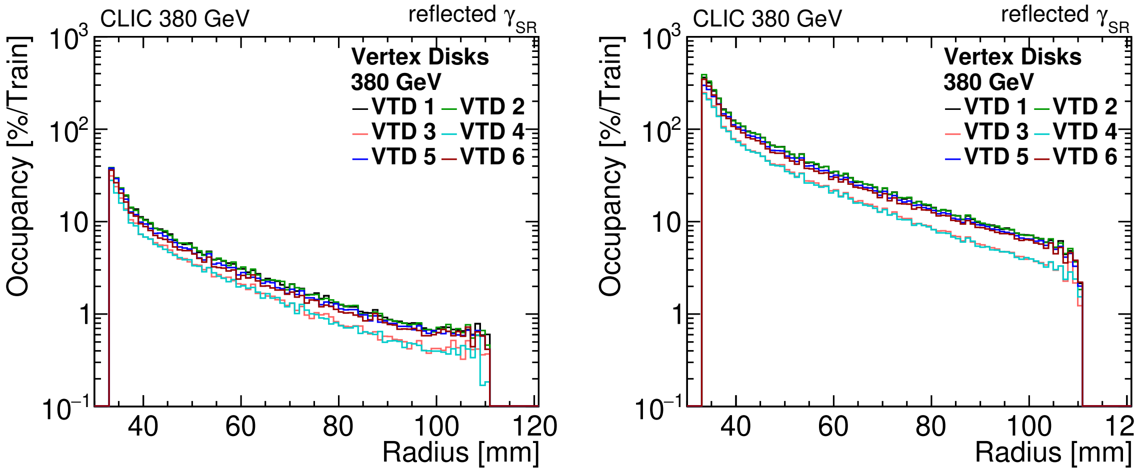

Figure 6.22: Distribution of the occupancies per bunch train in the vertex disks at 380 GeV coming from the reflected synchrotron radiation photons assuming average roughness of the copper vacuum chamber wall of 1 µm (left) and 100 nm (right).

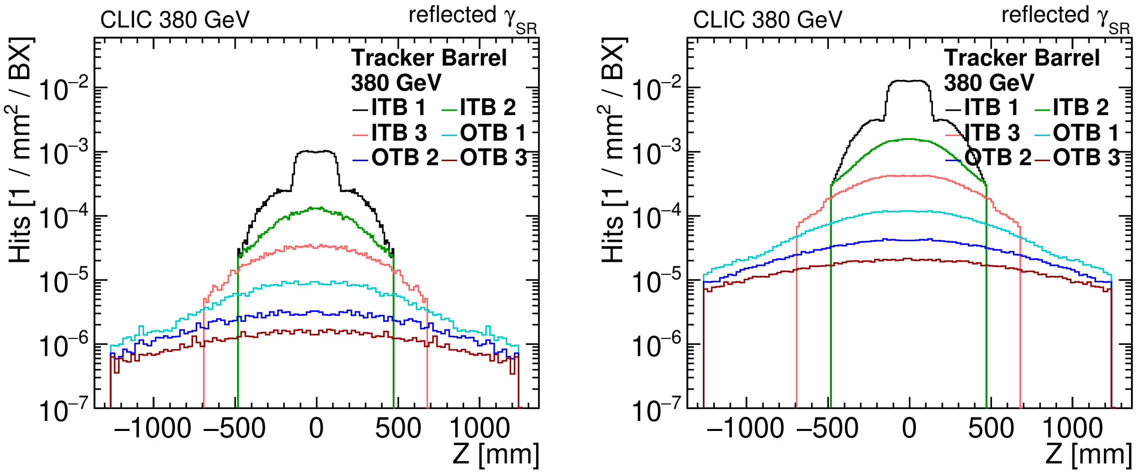

Figure 6.23: Distribution of the hit densities per bunch crossing in the tracker barrel at 380 GeV coming from the reflected synchrotron radiation photons assuming average roughness of the copper vacuum chamber wall of 1 µm (left) and 100 nm (right).

material of the beam pipe or inner detectors, including the support structures.

The occupancy distributions of the tracker barrel are shown in Figure 6.24. The maximal occupancy is close to the 3% limit for the first layer of the Inner Tracker when 1 µm roughness is used, and safely below the limit for layers located further away from the beam pipe. When higher reflectivity copper is used, the photon impact on the tracker is more severe, and only the last layer of the Inner Tracker is below the occupancy limit.

The impact of the SR photons in the tracker disks is much lower than in the other tracking subdetectors. The hit densities are shown in Figure 6.25. The low hit rates are due to the position the detector behind the conical beam pipe with a 4 mm thick steel walls, that provide shielding. With an exception of the lowest radius of the first disk, the disks cannot be impinged by 'direct' photons without additional scattering, as the required polar angle is larger than the limit imposed on the photons in the BeamCal region, which further reduces the probability of

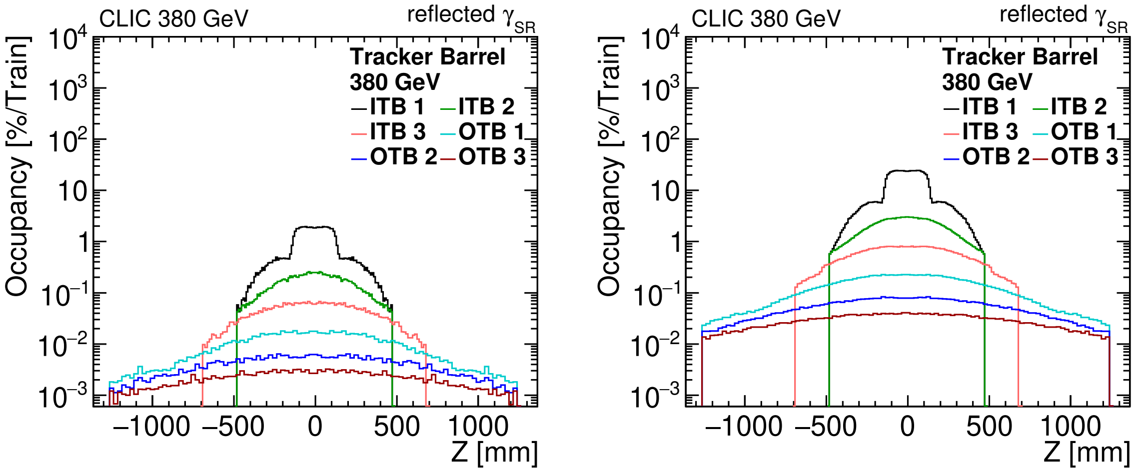

Figure 6.24: Distribution of the occupancies per bunch train in the tracker barrel at 380 GeV coming from the reflected synchrotron radiation photons assuming average roughness of the copper vacuum chamber wall of 1 µm (left) and 100 nm (right).

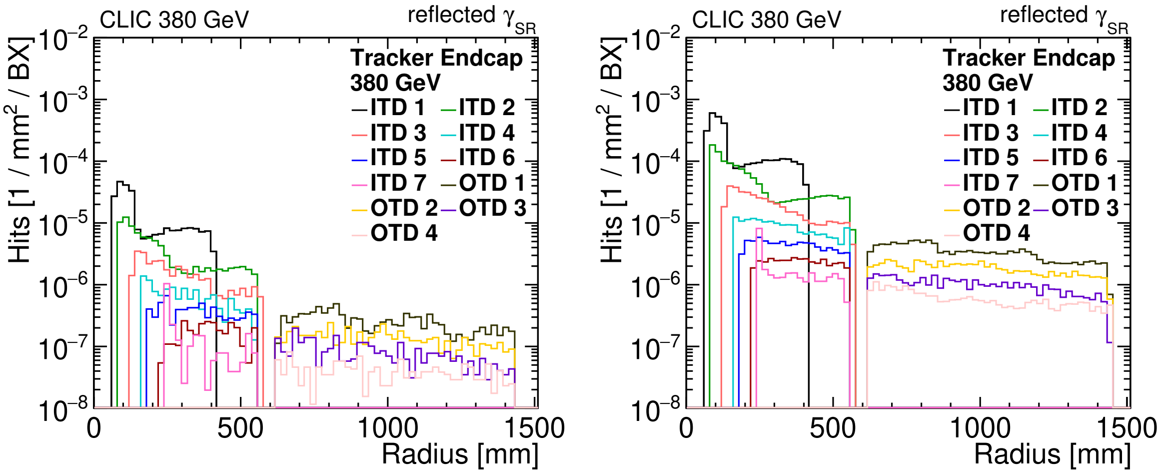

Figure 6.25: Distribution of the hit densities per bunch crossing in the tracker disks at 380 GeV coming from the reflected synchrotron radiation photons assuming average roughness of the copper vacuum chamber wall of 1 µm (left) and 100 nm (right).

receiving a hit.

The most impacted elements are the two first disks of the Inner Tracker, and especially at their lowest radii, located the nearest to the beam pipe. The occupancies, shown in Figure 6.26, reach up to 0.4% for the smooth beam pipe option and are below 0.03% when the beam pipe in the FFS is rougher.

Only a fraction of the total visible energy, as shown in Table 6.5, is deposited in the tracking detectors. The total energy deposit per bunch train is equal to 1% of the visible energy when the 1 µm R_a copper is used and reaches 7% in the 100 nm roughness case.

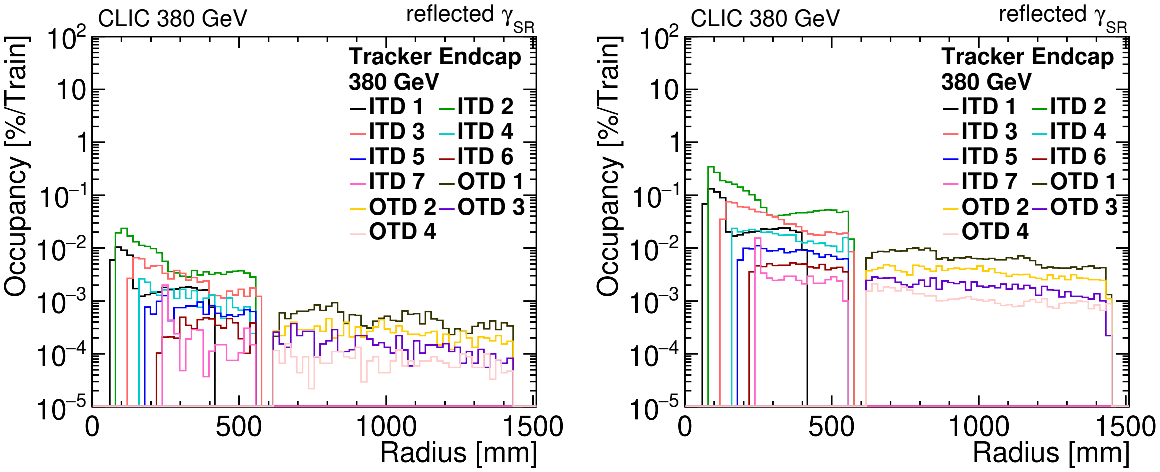

Figure 6.26: Distribution of the occupancies per bunch train in the tracker disks at 380 GeV coming from the reflected synchrotron radiation photons assuming average roughness of the copper vacuum chamber wall of 1 µm (left) and 100 nm (right).

6.4.3.2 3 TeV

The SR photon distributions coming from the 3 TeV FFS Synrad+ simulations and embedded in the CLIC detector model with optimised beam pipe apertures result in zero hits recorded the sensitive material of the detector. The photons simulated in GEANT4 are entirely absorbed in the beam pipe walls before they reach the material of the vertex and tracker.

The lower hit density at 3 TeV than at 380 GeV is expected due to the lower visible energy per bunch train (see Table 6.5), and the smaller geometric acceptance for the SR photons, that excludes the vertex detector (see Figure 6.18(right)). However, a complete lack of energy depositions is not expected. Taking into account the shortcomings of the GEANT4 description of the low-energy photons, as described in section 3.1.5, a change in the simulation conditions needs to be done.

A possible approach is to track the SR photons further downstream, up to the end of the BeamCal at 3170 mm from the IP. This approach changes the total energy of photons in the acceptance of the detector from 0.9 TeV to 0.4 TeV per bunch train when 1 µm average roughness copper is used, and from 11 TeV to 5.1 TeV when R_a is 100 nm. These are about a 50% reduction in the energy that can be deposited in the sensitive material of the vertex and tracker detectors.

The hit densities from the reflected SR photons in the vertex barrel are shown in Figure 6.27(left) when the 1 µm average roughness copper is used, and in Figure 6.27(right) when 100 nm average roughness (R_a) is used. Similar to the 380 GeV results, a factor of ten decrease in roughness leads to a proportional increase in the number of hits observed in the vertex detector. The occupancy linked with these hit rates reaches 10% in the 100 nm roughness case, as shown in Figure 6.28. In the case with rougher copper surface of 1 µm, the occupancy in the vertex barrel reaches 1% for the first double layer and is below for layers located at larger radii.

The hit densities of the vertex disks are shown in Figure 6.29. At the lowest radii, the hit densities are significantly larger than in the vertex barrel, due to the lower polar angles of the disks located on the other side of the IP. The occupancy, shown in Figure 6.30, reaches 5% in the 1 µm copper case and is about 40% at the lowest radii when a smoother vacuum chamber surface is used in the FFS.

As observed in for the 380 GeV energy stage, the disks located in the middle of the forward vertex detector, namely disks VTD3 and VTD4, have consistently lower hit rates than either disks VTD 1 and 2 or VTD 5 and 6. The explanation is the same as for the 380 GeV results.

The hit densities and occupancies are much lower in the Inner and Outer Tracker barrel than in the Vertex detector, especially for layers located further away from the beam pipe. The most impacted is the first Inner Tracker layer, as shown in Figure 6.31, where the hits caused by the SR photons again have a 'hat'-like distribution. The occupancy distributions of the tracker barrel are shown in Figure 6.32. The maximal occupancy is close to 1% for the first layer of the Inner Tracker when 100 nm roughness is used, well below the 3% acceptable occupancy. The layers located further away from the beam pipe are not significantly impacted by the SR photons, and have occupancy levels below 0.1% . When rougher copper surface is used, the photon impact on the tracker is even smaller, and all of the Inner Tracker layers are below the 0.1% occupancy level.

Similarly to the 380 GeV energy stage results, the impact of the SR photons in the tracker disks is much lower than in the other tracking subdetectors. The hit densities are shown in Figure 6.33. The hit rates are significantly below the 380 GeV levels, by about a factor of 30. This is a more substantial difference than can be expected from a simple comparison of the visible energy in Table 6.5, where the visible energy of the SR photons at 3 TeV is smaller only by a factor of 7 than at 380 GeV. The occupancies, shown in Figure 6.34, are negligible and are below 0.01% level for the smooth beam pipe option and a factor of ten lower when the beam pipe in the FFS is rougher.

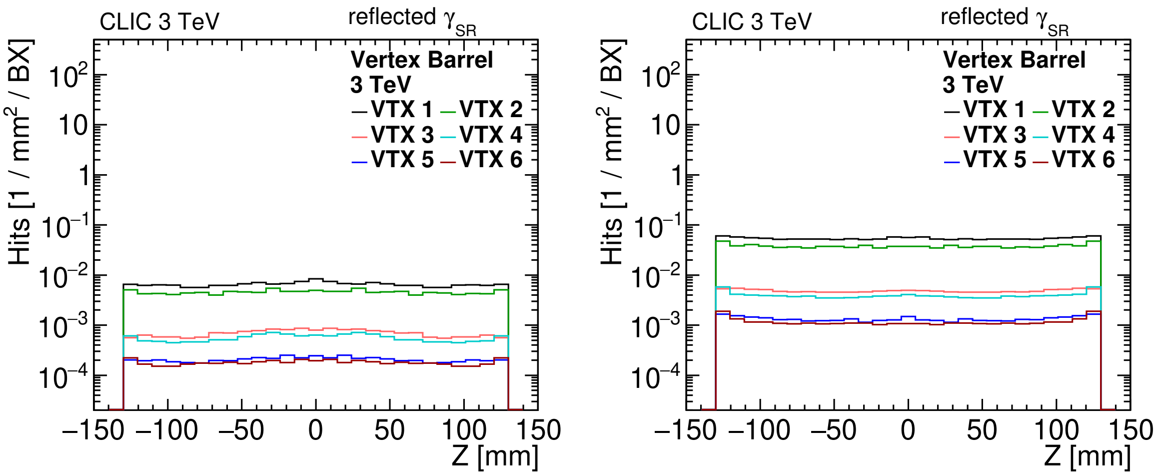

Figure 6.27: Distribution of the hit densities per bunch crossing in the vertex barrel at 3 TeV coming from the reflected synchrotron radiation photons assuming average roughness of the copper vacuum chamber wall of 1 µm (left) and 100 nm (right).

6.4.3.3 Summary of hit densities and occupancies

The hit densities and related occupancy levels coming from the SR photons are high at both energy stages, but especially at 380 GeV. There, the detector is under a strong influence of the SR photons even when the beam pipe surface is rough, with an average roughness of 1 µm. An increase of reflectivity in the FFS translates to more numerous photons in the acceptance of the detector and higher hit rates, proportionally to the increase in the visible energy.

The vertex detector is the most impacted subdetector, due to its proximity to the beam pipe and lower energy threshold. The average occupancy of the first double layer surpasses the 10% level at 380 GeV with rough beam pipe, and it is around 1% at 3 TeV in the same conditions. The tracker barrel and disks, except for the first layer of the Inner Tracker, receive a much lower number of hits. These numbers are not negligible, especially when the FFS vacuum chamber has the average roughness of 100 nm. At 380 GeV, the occupancy of the first layer of the Inner Tracker reaches 2% when the rough beam pipe surface is used and is about 20% in the smoother case. At 3 TeV, even when the smoother beam pipe is used the occupancy is below 1% level. At both energy stages, the occupancy levels in the tracking detectors, especially vertex, need to be addressed with a mitigation method that minimises the energy visible in the detector acceptance.

The method used to obtain the hit and occupancy distributions has certain limitations related to the available statistics of synchrotron radiation macrophotons. Ideally, the macrophoton representation would not be necessary, and the uncertainty linked with its use would vanish. However, in order to do so, a running time of several thousand times longer is required. This is not possible to achieve without the use of distributed computing resources, such as the WLCG, with Windows operating system and the software that can be used in batch mode. Synrad+ does not offer this functionality, and thus the analysed statistics remains limited. Further studies of the hit rates with a different software that contains a description of SR interactions with matter and allows the user to benefit from distributed computing resources would be

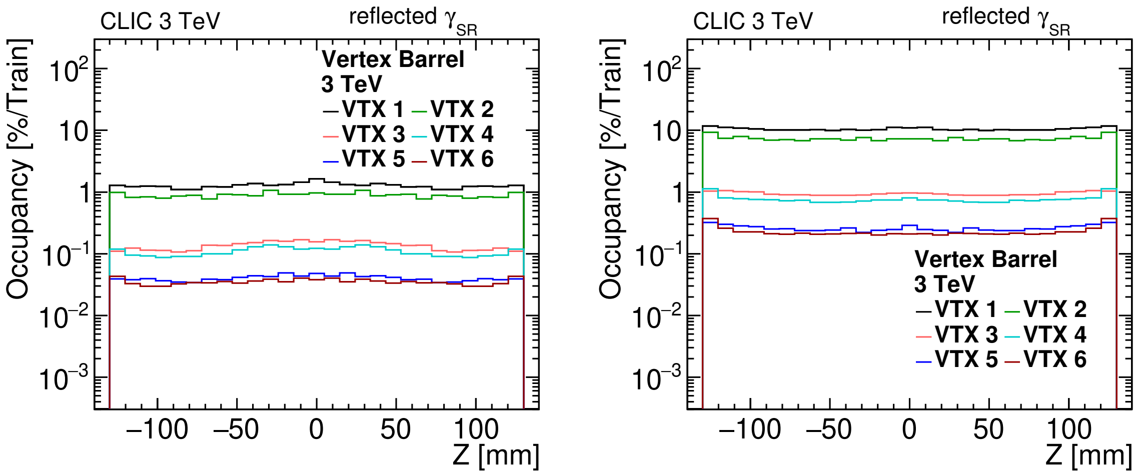

Figure 6.28: Distribution of the occupancies per bunch train in the vertex barrel at 3 TeV coming from the reflected synchrotron radiation photons assuming average roughness of the copper vacuum chamber wall of 1 µm (left) and 100 nm (right).

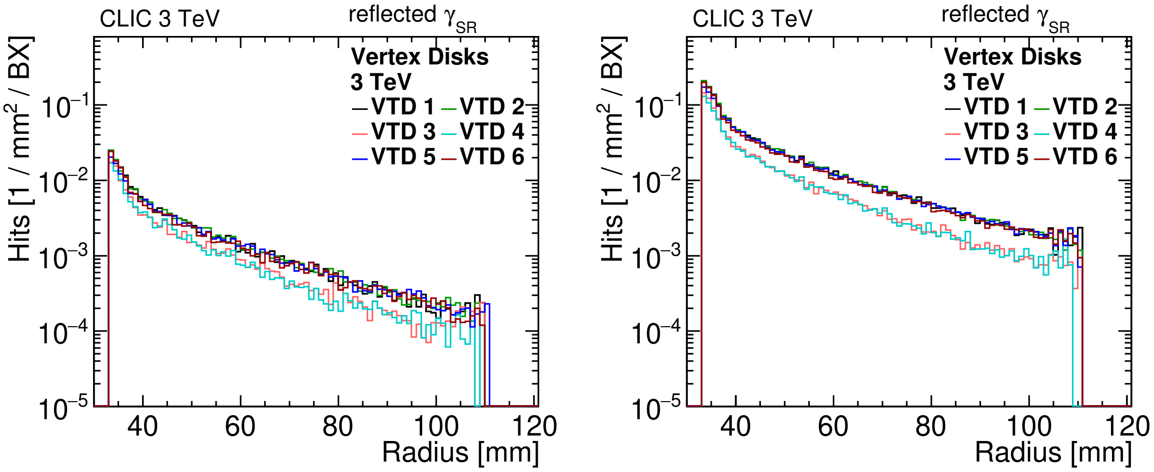

Figure 6.29: Distribution of the hit densities per bunch crossing in the vertex disks at 3 TeV coming from the reflected synchrotron radiation photons assuming average roughness of the copper vacuum chamber wall of 1 µm (left) and 100 nm (right).

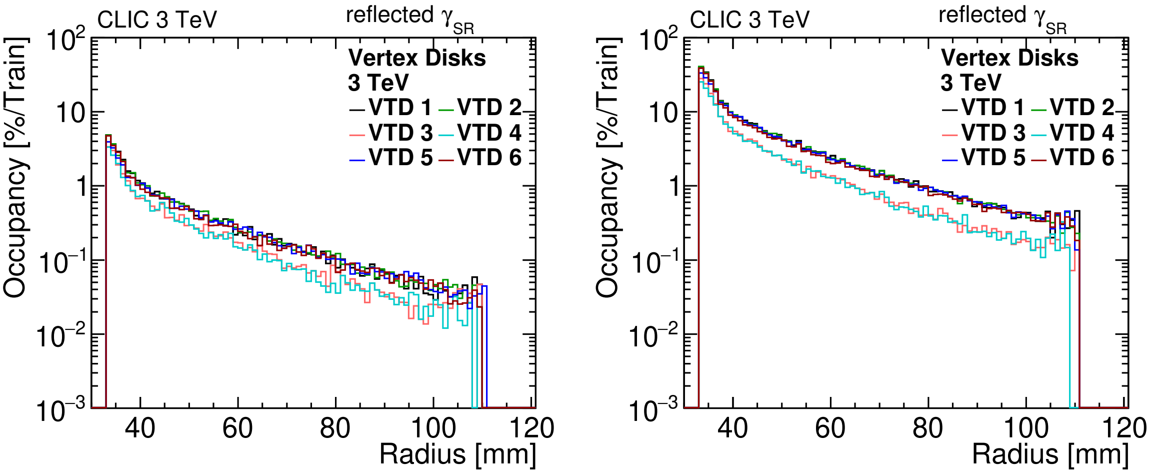

Figure 6.30: Distribution of the occupancies per bunch train in the vertex disks at 3 TeV coming from the reflected synchrotron radiation photons assuming average roughness of the copper vacuum chamber wall of 1 µm (left) and 100 nm (right).

beneficial to ensure the safety of the detector.

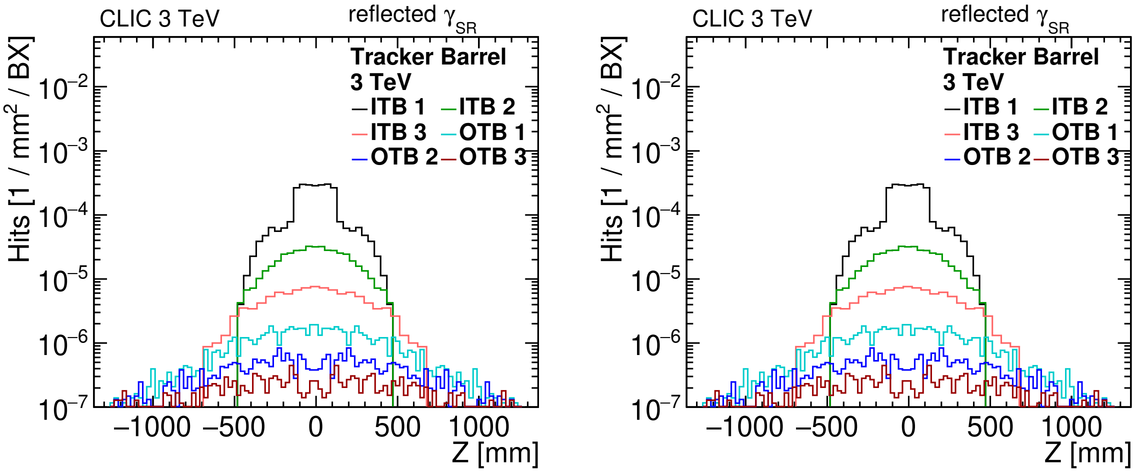

Figure 6.31: Distribution of the hit densities per bunch crossing in the tracker barrel at 3 TeV coming from the reflected synchrotron radiation photons assuming average roughness of the copper vacuum chamber wall of 1 µm (left) and 100 nm (right).

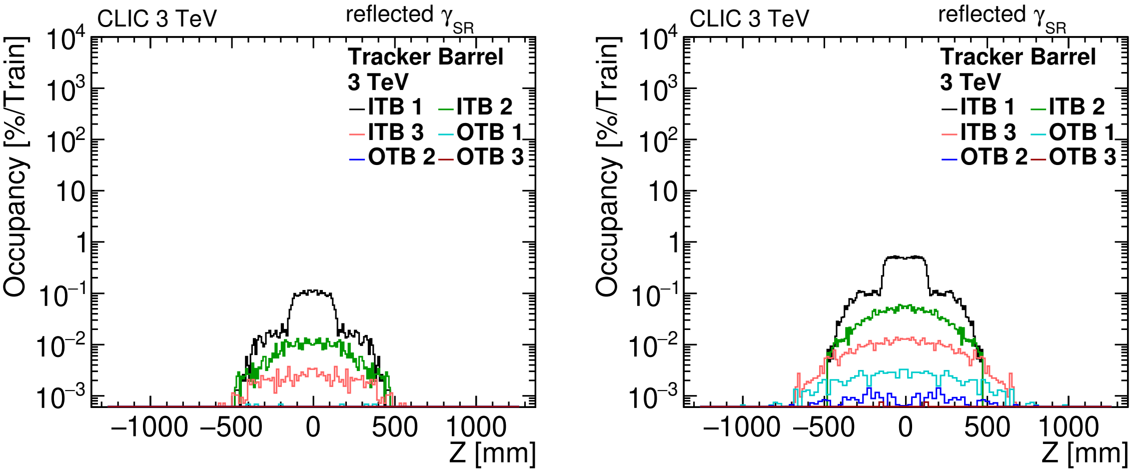

Figure 6.32: Distribution of the occupancies per bunch train in the tracker barrel at 3 TeV coming from the reflected synchrotron radiation photons assuming average roughness of the copper vacuum chamber wall of 1 µm (left) and 100 nm (right).

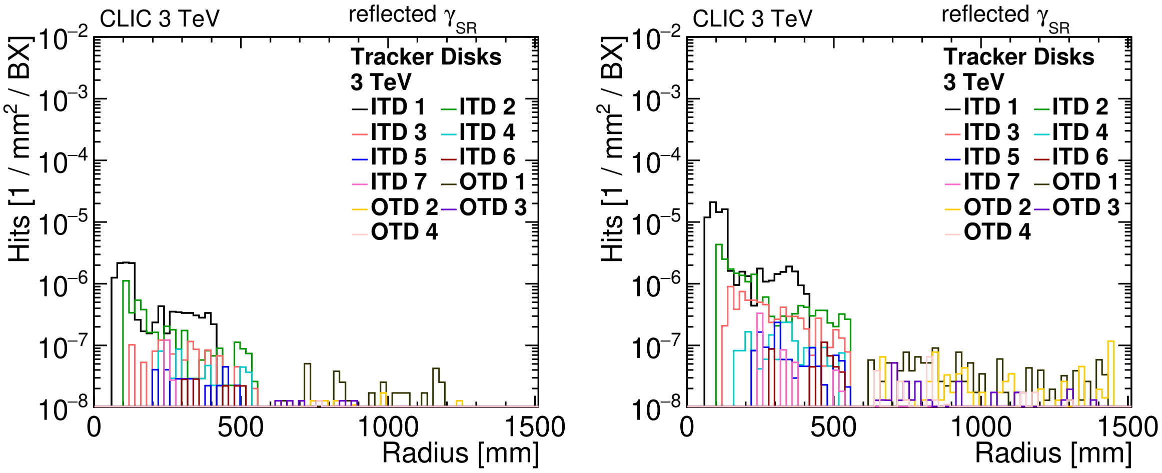

Figure 6.33: Distribution of the hit densities per bunch crossing in the tracker disks at 3 TeV coming from the reflected synchrotron radiation photons assuming average roughness of the copper vacuum chamber wall of 1 µm (left) and 100 nm (right).

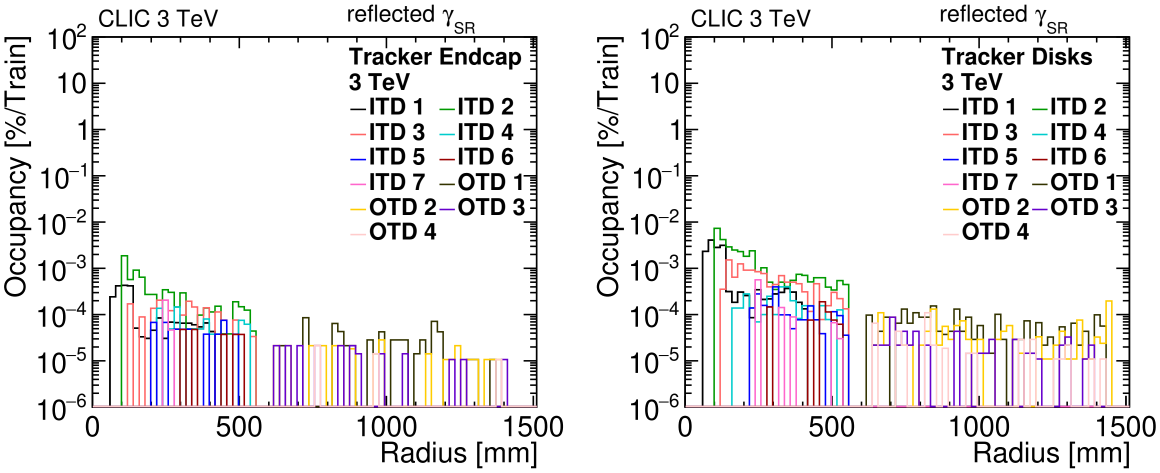

Figure 6.34: Distribution of the occupancies per bunch train in the tracker disks at 3 TeV coming from the reflected synchrotron radiation photons assuming average roughness of the copper vacuum chamber wall of 1 µm (left) and 100 nm (right).

6.5 Mitigation methods

The impact of the SR photons on the detector is severe at 380 GeV. The observed occupancies render the vertex and Inner Tracker detectors unusable when the average surface roughness of copper is below 1 µm. The situation is different at 3 TeV, where the occupancy levels are significantly smaller, due to the geometry of the interaction region that makes it unlikely for the SR photons to hit sensitive elements linked with the small apertures in the BeamCal region limiting the maximal polar angle θ_{QD0} of the photons. However, the visible energy of the SR photons is still substantial and the occupancy levels in the 100 nm average roughness case are high at 3 TeV. Therefore, a mitigation method should be put in place for maximal safety of the detector at both energy stages.

The desired experimental conditions are ensured when there are no SR photons in the detector acceptance. In the case when the SR photons are impossible to be entirely removed, the mitigation should aim to minimise the visible energy in the detector, and the occupancy levels. Such conditions are provided when the vacuum chamber is assumed to be completely non-reflective. Therefore, a mitigation method providing similar conditions to ensure the detector safety and performance has to be derived.

There are a few ways the high fluxes of the SR photons in the detector acceptance can be addressed. The first is to reduce the reflectivity of the vacuum chamber by increasing the average roughness of the surface. The R_a equal to 7 µm for the 380 GeV BDS is sufficient to minimise the impact of the SR photons in the detector region. The average visible energy per bunch train is not reduced to zero; however, according to full detector simulations in GEANT4 photons do not leave significant energy deposits in the tracking detectors, and the maximal occupancies are reduced to below 1% level in the vertex detector.

The required increase of surface roughness can be achieved, for example, through laser ablation. The laser treatment of the surface is a stable and inexpensive method of increasing the average roughness [93]. The surface treated with a laser has the additional advantage of lowering the yield of secondary electrons emitted when interacting with the SR photons, thus lowering the outgassing rate and suppressing the creation of an electron cloud [93, 94].

The main disadvantage of the roughness increase approach is the increase of the impedance that is a direct result of the roughness increase [95]. The beams would be under a stronger impact of wakefields, and their performance would deteriorate. To mitigate wakefields an increase in apertures would be desirable. However, a general increase of circular vacuum chamber radii in the FFS, in turn, increases the photon flux in the detector region and counteracts the benefits from this mitigation approach.

A similar method aiming to reduce the reflectivity is based on installing a saw-tooth shape on the inner wall of the vacuum chamber on the side where reflections of the synchrotron radiation take place. An example of such saw-tooth, based on the experiences of the LHC vacuum chamber design [84] is shown in Figure 6.35(right). The layout of the circular vacuum chamber with a saw-tooth shape installed, as simulated with Synrad+, is shown in Figure 6.35(left). The saw-tooth shape of similar design is also foreseen for the FCC-hh [96].

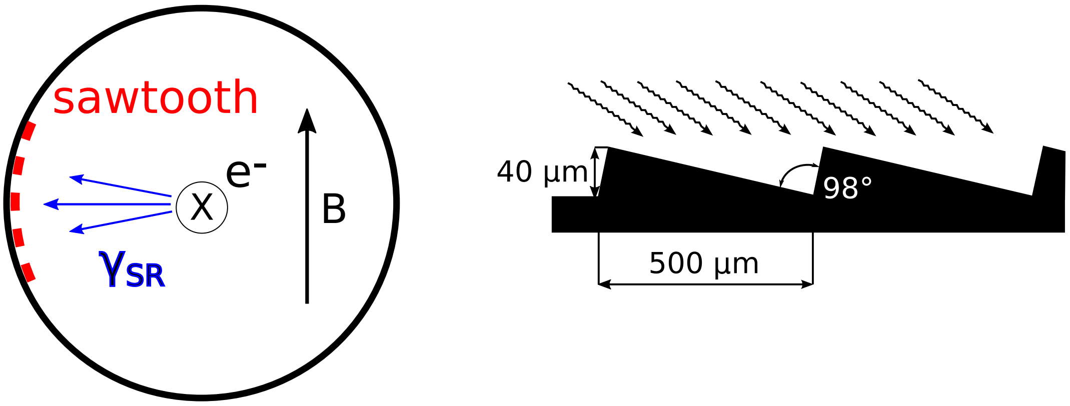

Figure 6.35: Saw-tooth beam pipe layout inside the beam pipe as used in the Synrad+ model of the CLIC FFS (left) and z-axis projection of the saw-tooth with design details (right) [92].

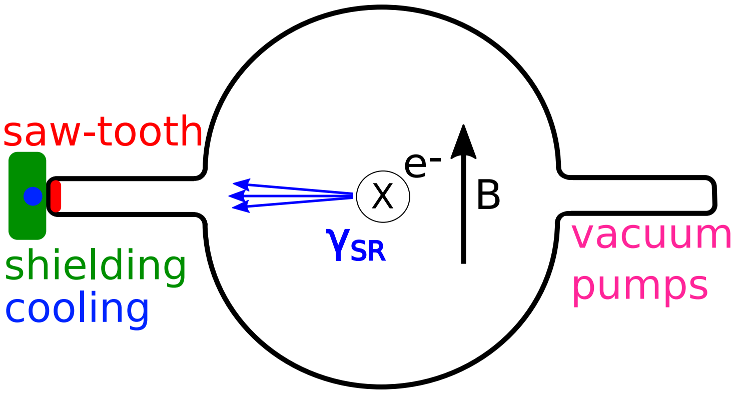

Figure 6.36: Winglet aperture shape based on the vacuum system under development for FCC-ee [90] with saw-tooth shape located further away from the beam pipe centre axis and schematic position of possible shielding.

The saw-tooth shape is one of the available “materials” in Synrad+, and its impact on the SR photons flux in the detector region can be studied with the already developed tools. The simulations suggest that it is sufficient to install the saw-tooth in the final 30 m of the FFS, or equivalently, from the last bending magnet to the QD0 exit, to reduce the reflectivity to the point, where the SR photons are not visible in the detector acceptance. The result at both energy stages is achieving the same experimental conditions as if the vacuum chamber was fully absorbing along the entire FFS. A safety margin can be ensured by extending the region where the saw-tooth is installed by an additional 100 m upstream (about 25 bending magnets), and downstream up to the kicker system.

The disadvantage of installing the saw-tooth is the same as in the roughness increase approach: an increase in impedance, and consequently in wakefields experienced by the beams. The impact of the increased impedance can be mitigated in both cases by extruding the circular vacuum chamber to create a ’winglet’-shaped aperture. In one of the extruded arms, sufficiently distant from the beam pipe axis, the saw-tooth or a rough surface can be placed to limit the negative impact on the beam stability. Such a design, based on the idea developed for the FCC-ee vacuum chamber [90] is shown in Figure 6.36. The winglet could be cooled or shielded on the side irradiated by the SR photons if it were found to be necessary.

An alternative method to mitigate the large photon fluxes is to install SR masks in the detector region, similar to the approach used in LEP2 [97]. A collimator or a synchrotron radiation mask needs to be installed upstream from the BeamCal and the Kicker on the incoming beamline to protect these elements from the SR irradiation. Such a mask, made of lead or tungsten can be implemented in the GEANT4 detector model as a reduction in vacuum chamber aperture. Given the available space constraints in the forward region, tungsten is the preferred material.

Taking into account only the photons with $\theta_{\mathrm{QD0}} > 3.3\,\mathrm{mrad}$ which are in the acceptance of the detector, it is sufficient to reduce the aperture upstream from the BeamCal down to 6 mm. Photons that cause high occupancy levels have energy below 30 keV, where electromagnetic cascades or neutron photo-emissions do not take place. Therefore, these photons do not cause significant scattering in the forward region of the detector when they interact with the beam pipe material. However, the SR mask necessarily needs to absorb all photons that are at a larger offset than 6 mm. The photons with energies higher than 30 keV and at offset larger than 6 mm were travelling through the detector region without interacting with any material of CLICdet. When the SR mask is implemented, these higher energy photons will cause scattering in the forward detector region, which makes a design of such a mask more challenging. The number of photons further away from the beam pipe axis increases with increasing reflectivity, as was shown in Figure 6.12, t herefore more energy needs to be absorbed in the high reflectivity cases.

The maximal energy of the SR photons is 5 MeV at 380 GeV and about 100 MeV at 3 TeV, as can be read from Figure 6.16. Using GEANT4 simulations, it was found that a 100 mm long tungsten mask is sufficient to reduce the energy of the SR photons at 3 TeV to below 1 MeV, and the 5 MeV photons to 80 keV.

The disadvantages of the SR mask are related to both the beam stability and detector safety. The required mask aperture is lower than the limit imposed by the resistive wall wakefield at the 380 GeV energy stage. However, as it was found in section 5.3 and using PyHEADTAIL simulations, a short-length aperture limitation located close to the IP should not impact the beam quality at the IP significantly. Therefore, the risk related to the beam quality is low. The detector safety is connected with the efficiency of the mask, and the margin of safety when using GEANT4 to simulate the effects related to the low-energy photons. The collimator introduces scattering of the SR photons in the detector region, that becomes a source of background itself in the forward detector region

A combination of methods can also be envisioned. In this approach, the winglet shape is used in the final metres of the FFS, and in the detector region, the arm that hosts the saw-tooth shape is fully filled with a short radiation length material instead. The photons in the winglet would be then absorbed, and the decrease of aperture would not impact the beam stability.

In summary, two main approaches to the mitigation of large SR photon fluxes found in the detector can be pursued. The most promising from the safety perspective is to remove the photons before they can reach the detector. The number of the SR photons that can interact with the sensitive material of the detector can be limited by reducing the reflectivity of the vacuum chamber surface, either by modifying the surface or installing the saw-tooth shape. The reflectivity reduction should be placed in the extruded arms of the 'winglet' shape, located further away from the centre of the beam pipe to reduce wakefields. The advantage of this approach is that it is independent from the GEANT4 predictions and its precision of describing the low-energy electromagnetic processes. However, it depends on the precision of the Synrad+ reflectivity model, which has been validated [80].

Chapter 7

Estimate of the beam-induced backgrounds impact

7.1 Central silicon detectors

This section describes the results obtained for hit densities and occupancies in the vertex and tracker subdetectors. The statistics used in this occupancy study is equivalent to about three bunch trains, with 1069 and 1044 bunch crossings at 380 GeV and 3 TeV respectively, of the incoherent pairs results, and 13700 and 2272 bunch trains respectively of the $\gamma\gamma \to$ hadron events.

A maximal occupancy of 3% per bunch train can be tolerated, if safety factors are included [59]. This number corresponds to less than two hits from background particles per 1 mm^2 per bunch train in the vertex detector. Respecting this 3% limit allows to reach the required position resolution without requiring electronics with multi-hit capability [12].

7.1.1 Occupancies in the Vertex detector

The hit rates are the highest in the detector layers positioned closest to the beam line, as can be expected from simple geometric considerations. Most of the hits are expected to come from the incoherent pairs. This is due to the larger number of incoherent pairs than the $\gamma\gamma \to$ hadron events, and the differences in momentum distributions, as shown in Figures 4.4 and 4.6. The number of incoherent pairs that have sufficient momentum and polar angle pointing towards the vertex detector ($13.5^\circ < \theta < 90^\circ$) decreases with increasing radius of the layers. In addition, the region close to the beam pipe is influenced the most by the backscattered particles produced in the forward calorimeters region.

The longitudinal hit distributions in the vertex barrel are shown in Figures 7.1 and 7.2 and the radial hit distributions in the vertex disks are presented in Figures 7.3 and 7.4. The differences in hit densities between vertex layers are larger for the incoherent pairs than for the $\gamma\gamma \to$ hadron events, as expected from their respective momentum distributions. The hit densities in the disks are very consistent between all disks, due to their low material budget and similar angular acceptance. The dominant source of the background hits in the vertex detector are the incoherent pairs, with a factor one-hundred more hits than caused by the $\gamma\gamma \to$ hadron events at 380 GeV and a factor of ten at 3 TeV.

The time structure of the hits at 3 TeV can be found in Figure 7.5 for the vertex barrel and in Figure 7.6 for the vertex disks. The time distributions are consistent between the 380 GeV and 3 TeV results with an increase in the share of backscattered particles in the case of the incoherent pairs. However, the distributions differ significantly between the incoherent pairs nad $\gamma\gamma \to$ hadrons. The vast majority of the hits from $\gamma\gamma \to$ hadrons particles take place within 10 ns following a bunch crossing, as shown in Table 7.1. A secondary peak around 20 ns is present in the vertex disks, while it is not as prominent in the vertex barrel. The 20 ns time of flight corresponds to twice the distance between the vertex detector and BeamCal region, where the scattering with LumiCal and BeamCal material takes place. The time structure of the hits in the vertex barrel coming from $\gamma\gamma \to$ hadron events has a secondary peak at 4 ns, which can be attributed to scattering in the conical beam pipe at $Z = 0.5$ m, and a rapidly decreasing tail spanning over many nanoseconds. The multiple scattering of the background particles in the BeamCal and LumiCal region is the origin of the long tails. In the case of the incoherent pairs, most of the hits takes place within 10 ns following a bunch crossing in both vertex barrel and disks. A secondary peak around 20 ns, seen in Figures 7.5(left) and 7.6(left) after a bunch crossing has a factor ten lower amplitude to one of the particles travelling directly from the IP. The secondary peak is connected with a large influx of backscattered particles coming from the forward calorimeter region.

The maximum and average occupancies from both the incoherent pairs and $\gamma\gamma \to$ hadron events are summarised in Table 7.2. At 380 GeV, the occupancies in the vertex barrel are a factor of three lower than at 3 TeV, and in the disks about a factor of two. The occupancies reach 1% at 380 GeV in the first layer of the vertex barrel and 1.5% in the innermost region of the vertex disks from the incoherent pairs (Figure 7.7(left)). The impact of $\gamma\gamma \to$ hadron events at this energy stage is negligible (Figure 7.8(left)). The occupancies at the 380 GeV energy stage were found to be well below the 3% limit and thus do not pose additional constraints on the CLICdp vertex design. Taking into account the low occupancy level, it is possible to reduce the radius of the beam pipe in the centre of the detector, allowing to place the first vertex detector layer closer to the interaction point. The lower radius of the vertex detector would be beneficial for vertexing performance. More details on the possible inner radius change of the first double layer are given in section 8.1.

At 3 TeV, the number of produced background particles is larger, and the hit densities and occupancies increase accordingly. The most radical change occurs with the $\gamma\gamma \to$ hadron events which become a significant source of background at this higher energy stage. The hit densities from incoherent pairs (Figures 7.1(right) and 7.3(right)) and $\gamma\gamma \to$ hadron events (Figures 7.2(right) and 7.4(right)) are in agreement with previous findings for CLIC_ILD [60], although the occupancy estimates (Figures 7.7(right) and 7.8(right))differ. This is caused by a different pixel sensor pitch, which has changed from $20 \times 20\,\mu\text{m}^2$ to $25 \times 25\,\mu\text{m}^2$ for CLICdet [14]. With the larger pixel pitch, the combined occupancy from both incoherent pairs and $\gamma\gamma \to$ hadrons exceeds the 3% mark by a small margin in the first layer of the vertex barrel. The smallest radii region of the vertex disks is especially impacted at 3 TeV. With averaging using 1 mm long radial bins, the combined occupancy from both the incoherent pairs and $\gamma\gamma \to$ hadron events reaches up to 4.7% at the lowest radii of the disk placed farthest from the IP (Figures 7.9(right) and 7.10(right)). With averaging over larger radial bins of 10 mm, which are closer to a realistic read-out scenario, one can expect the occupancy to be just marginally above

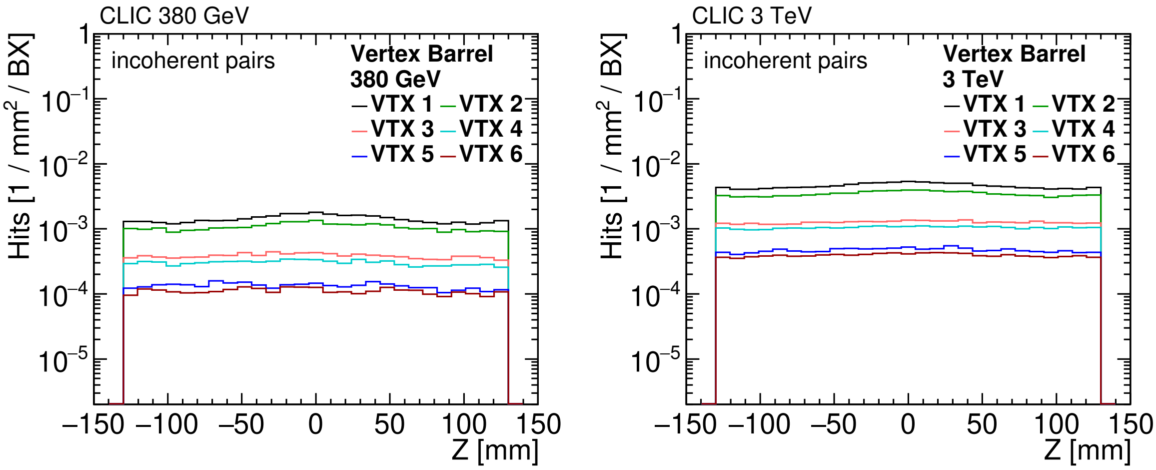

Figure 7.1: Longitudinal distribution of the hit density per bunch crossing from incoherent electron–positron pairs in the vertex barrel at 380 GeV (left) and 3 TeV (right). Safety factors are not included.

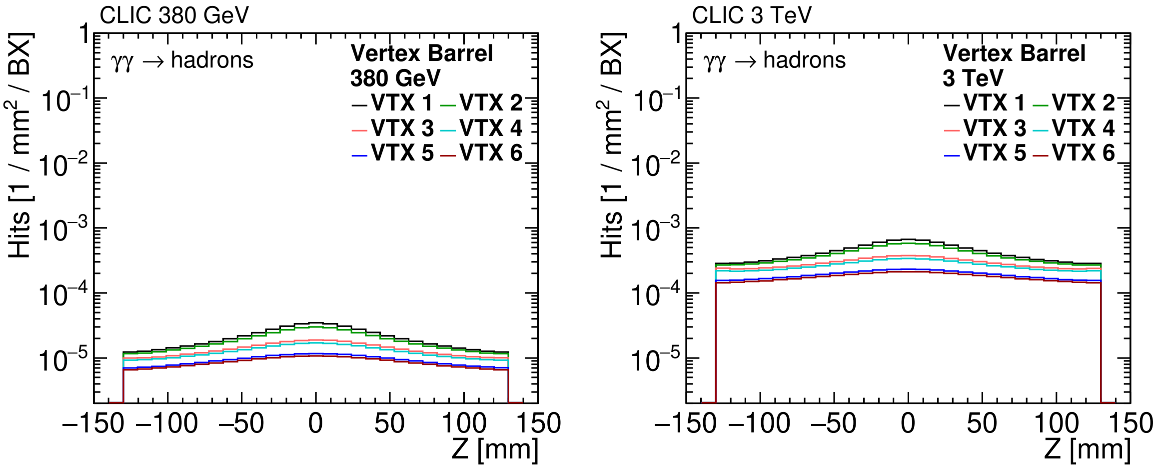

Figure 7.2: Longitudinal distribution of the hit densities per bunch crossing from $\gamma\gamma \rightarrow$ hadron events in the vertex barrel at 380 GeV (left) and 3 TeV (right). Safety factors are not included.

the 3% at 3 TeV.

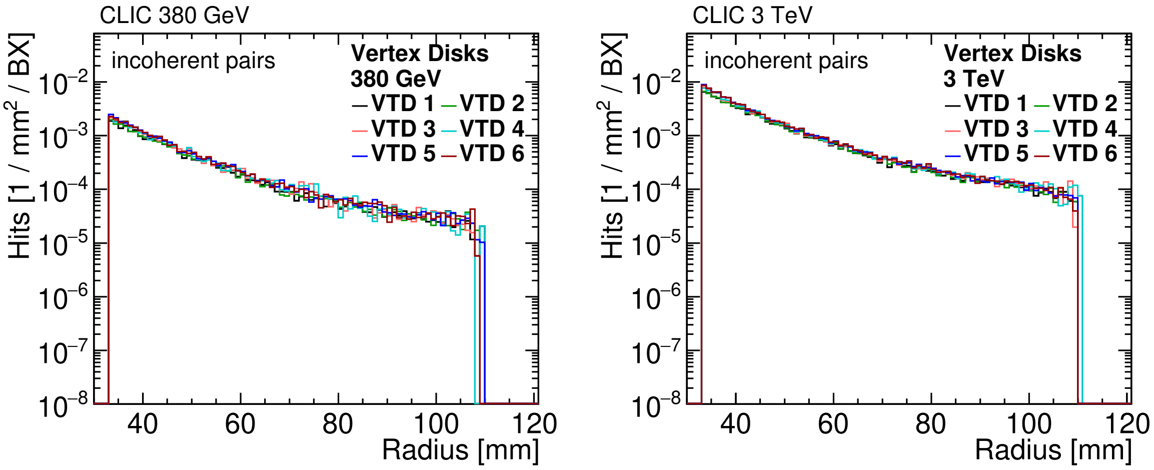

Figure 7.3: Radial distribution of the hit densities per bunch crossing from incoherent electron–positron pairs in the vertex disks at 380 GeV (left) and 3 TeV (right). Safety factors are not included.

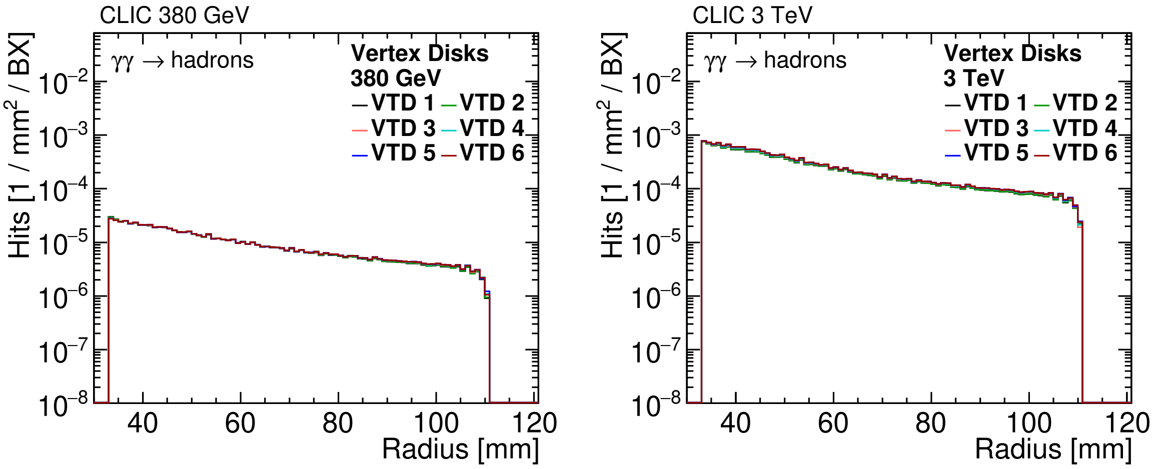

Figure 7.4: Radial distribution of the hit densities per bunch crossing from $\gamma\gamma \rightarrow$ hadron events in the vertex disks at 380 GeV (left) and 3 TeV (right). Safety factors are not included.

Table 7.1: Percentage of hits recorded in the vertex detector more than 10 ns after a bunch crossing.

Energy stage	380 GeV		3 TeV	
Subdetector	incoherent pairs [% after 10ns]	$\gamma\gamma \to$ hadrons [% after 10ns]	incoherent pairs [% after 10ns]	$\gamma\gamma \to$ hadrons [% after 10ns]
VTX barrel 1	16 %	6 %	18 %	6 %
VTX barrel 2	16 %	6 %	18 %	6 %
VTX barrel 3	21 %	8 %	20 %	8 %
VTX barrel 4	23 %	9 %	22 %	9 %
VTX barrel 5	23 %	11 %	27 %	11 %
VTX barrel 6	23 %	12 %	28 %	12 %
VTX disk 1	23 %	4 %	27 %	4 %
VTX disk 2	22 %	4 %	25 %	4 %
VTX disk 3	21 %	4 %	24 %	4 %

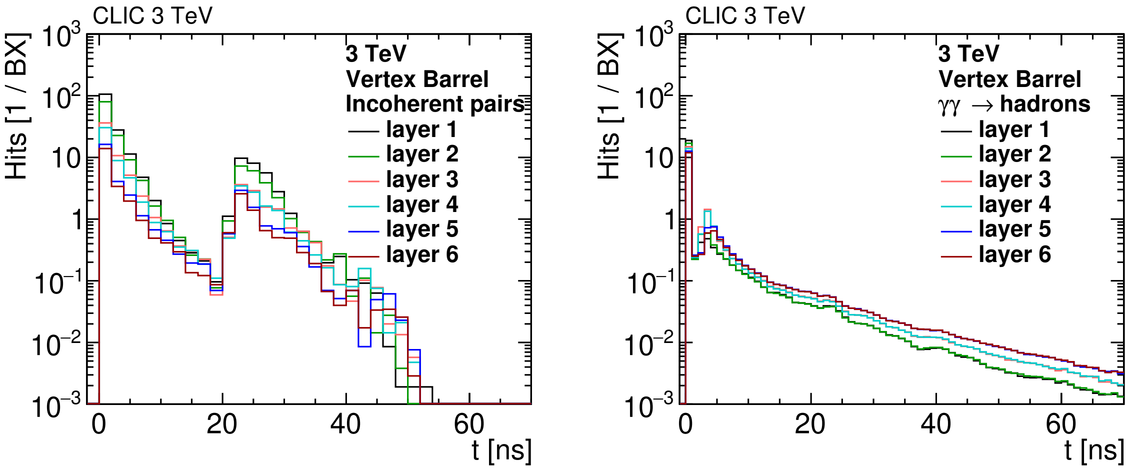

Figure 7.5: Time distribution of the hits per bunch crossing in the vertex barrel at 3 TeV from incoherent electron–positron pairs (left) and $\gamma\gamma \to$ hadron events (right). Safety factors are not included.

Table 7.2: The maximum and average occupancy in the vertex detector from the incoherent pairs and $\gamma\gamma \to$ hadron events at 380 GeV and 3 TeV.

Energy stage	380 GeV		3 TeV	
Subdetector	maximum [%]	average [%]	maximum [%]	average [%]
VTX barrel 1	1.0	0.7	2.8	2.1
VTX barrel 2	0.7	0.5	2.1	1.6
VTX barrel 3	0.3	0.2	0.7	0.6
VTX barrel 4	0.2	0.2	0.6	0.5
VTX barrel 5	0.1	0.1	0.3	0.2
VTX barrel 6	0.1	0.1	0.3	0.2
VTX disk 1	1.1	0.1	2.4	0.4
VTX disk 2	1.3	0.1	2.7	0.5
VTX disk 3	1.4	0.1	2.8	0.5

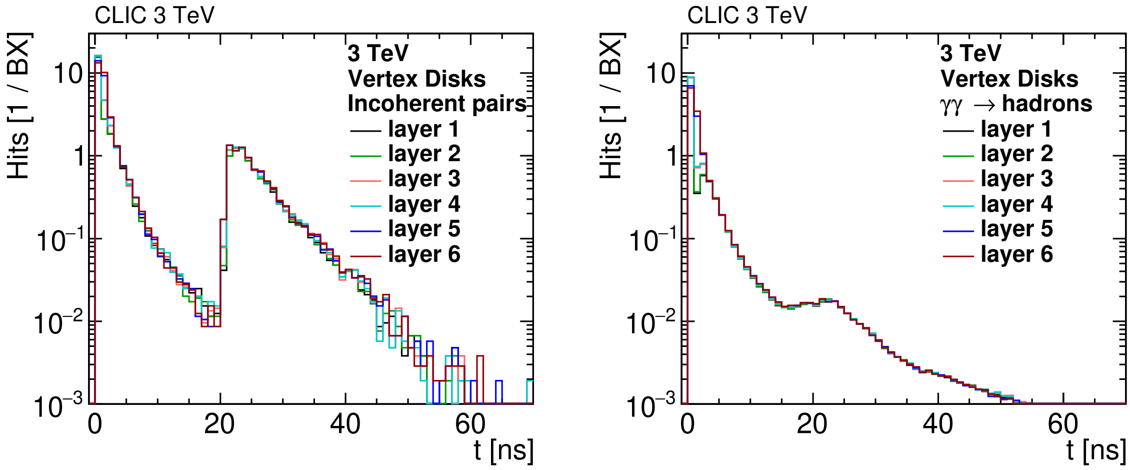

Figure 7.6: Time distribution of the hits per bunch crossing in the vertex disks at 3 TeV from incoherent electron–positron pairs (left) and $\gamma\gamma \rightarrow$ hadron events (right). Safety factors are not included.

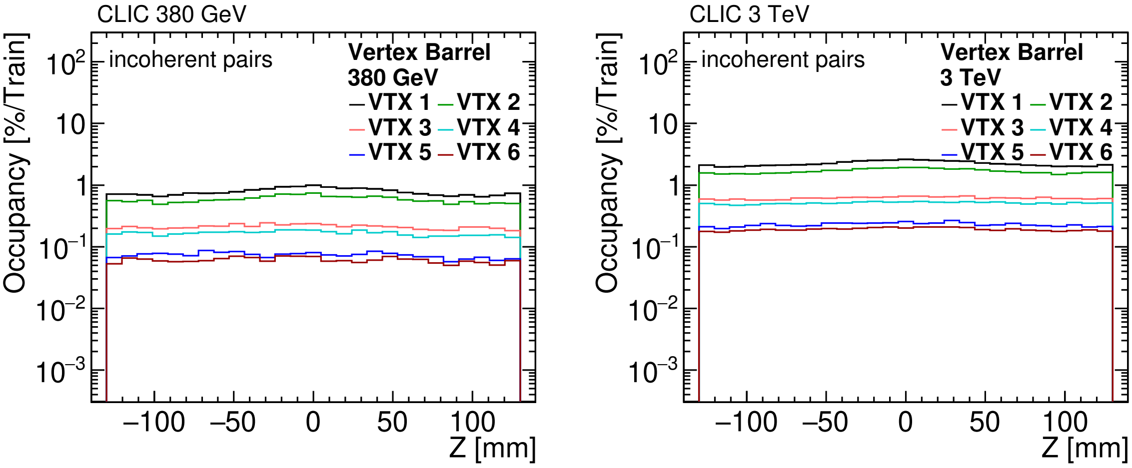

Figure 7.7: Longitudinal distribution of the occupancies per bunch train from incoherent electron–positron pairs in the vertex barrel at 380 GeV (left) and 3 TeV (right). Safety factors are included.

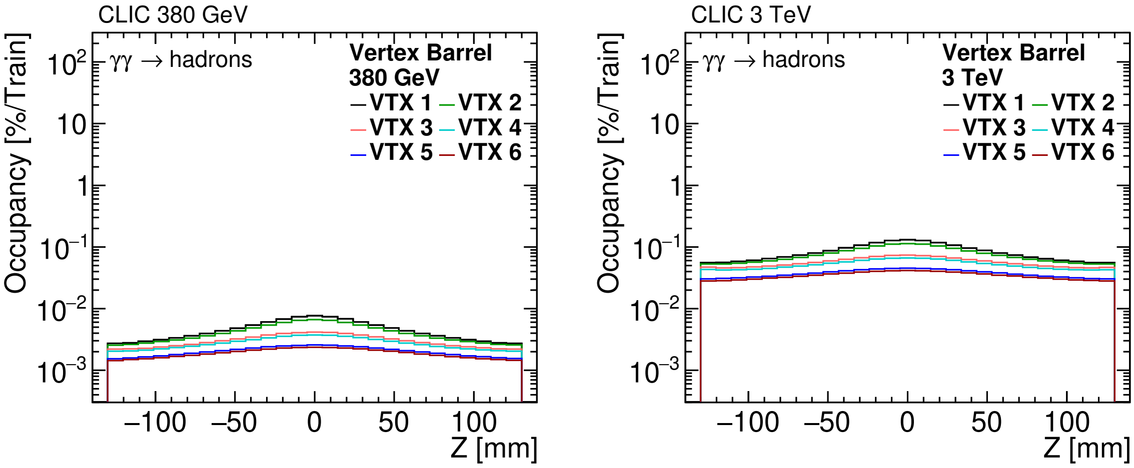

Figure 7.8: Longitudinal distribution of the occupancies per bunch train from $\gamma\gamma \to$ hadrons in the vertex barrel at 380 GeV (left) and 3 TeV (right). Safety factors are included.

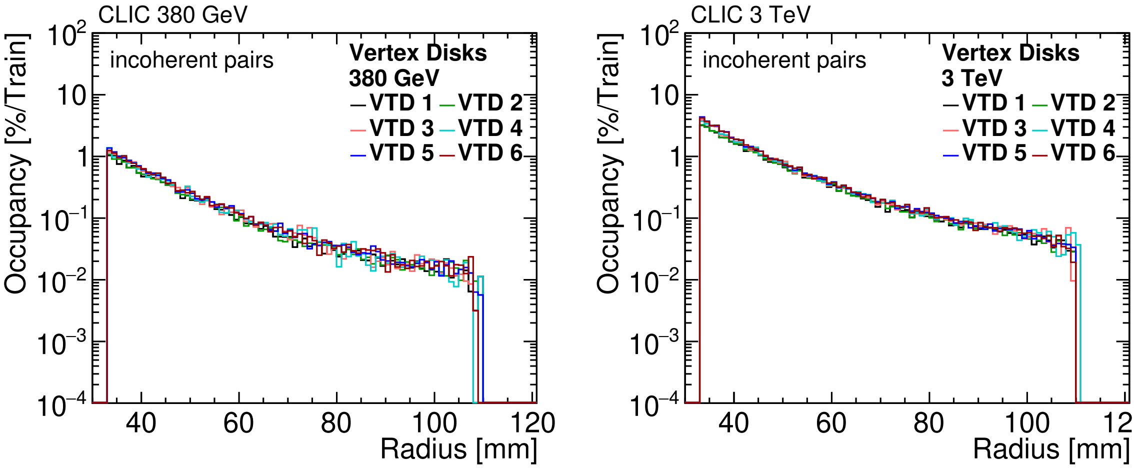

Figure 7.9: Radial distribution of the occupancies per bunch train from incoherent electron–positron pairs in the vertex disks at 380 GeV (left) and 3 TeV (right). Safety factors are included.

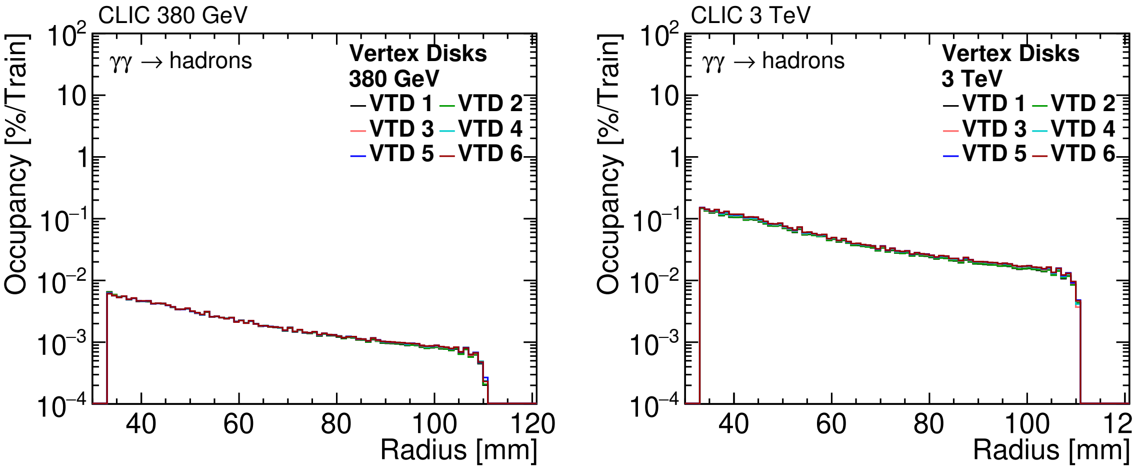

Figure 7.10: Radial distribution of the occupancies per bunch train from $\gamma\gamma \to$ hadrons in the vertex disks at 380 GeV (left) and 3 TeV (right).

7.1.2 Occupancies in the Tracker detector

At 380 GeV, the dominant source of the hits in the tracker are the incoherent electron–positron pairs. They are produced in larger quantities than the $\gamma\gamma \rightarrow$ hadron particles, and there are more of them in the detector acceptance. In addition, they cause backscattering in the forward calorimeter region thus further increasing the hit densities in the tracker region. The pairs cause five times more hits than $\gamma\gamma \rightarrow$ hadron events in the first layers of the tracker barrel, as shown in Figures 7.11 and 7.12

The hit density in the tracker at 3 TeV is five times larger than at 380 GeV for the incoherent pairs, as shown in Figures 7.11 and 7.13. The hit density of $\gamma\gamma \rightarrow$ hadron events increases more rapidly than the incoherent pairs between 380 GeV and 3 TeV, by a factor of twenty compared to less than a factor of three for the incoherent pairs, as shown in Figures 7.12 and 7.14.

The hit densities for incoherent pairs fall more rapidly between the vertex barrel and the tracker than for the $\gamma\gamma \rightarrow$ hadron events, as shown in Figures 7.11 and 7.12. The hit density in the first layer of the tracker barrel is a factor ten lower than in the last layer of the vertex barrel for the incoherent pairs, while it is a factor of three for $\gamma\gamma \rightarrow$ hadron events. This difference can be explained by comparing the transverse momentum distributions of the sources. In the case of the incoherent pairs a significant portion of the particles is boosted in the beam direction. The density of particles that are pointing towards the central barrel and have a sufficient transverse momentum to reach the outer layers of the tracker decreases rapidly, as shown in Figure 4.4. The transverse momentum distribution of $\gamma\gamma \rightarrow$ hadron events is different, with particle density increasing between the vertex and tracker detector, as shown in Figure 4.6.

The occupancies arising from the hit densities caused by both incoherent pairs and $\gamma\gamma \rightarrow$ hadron events can be found in Figures 7.15 and 7.16 for the tracker barrel, and in Figures 7.17 and 7.18 for the tracker disks.

The detectors are impacted by particles produced in the interaction region, which depends mainly on the transverse momentum distributions of the background particles, and by particles coming from scattering in the BeamCal and LumiCal region. A significant portion of the hits in the tracker barrel and disks occurs after 10 ns. The time distributions of the hits in the Inner Tracker are shown in Figures 7.19 and 7.21, and in the Outer Tracker are in Figures 7.20 and 7.22. These time distributions differ significantly between the $\gamma\gamma \rightarrow$ hadron events and incoherent pairs, similarly to what is observed in the vertex detector. A large fraction of the hits from $\gamma\gamma \rightarrow$ hadron events take place within 10 ns after the bunch crossing, with a slowly decreasing tail containing a small number of hits. Due to the transverse momentum distribution of $\gamma\gamma \rightarrow$ hadron events, most of the hits are direct, and the produced particles do not backscatter in the forward region in large numbers. The incoherent pairs do not cause numerous direct hits in the tracker, although they deposit significant energy in the LumiCal and BeamCal resulting in a large number of electron–positron pairs and neutrons in the forward region [98]. A fraction of these particles are scattering backwards towards the central barrel region and cause hits in the tracker. The large angular acceptance of the tracker barrel and disks for the backscattered particle and a lower hit density from the direct particles causes the tracker to be relatively more influenced by the backscattered particles than the vertex detector. In absolute terms, the vertex barrel receives more hits from backscattered particles than the tracker barrel, although they

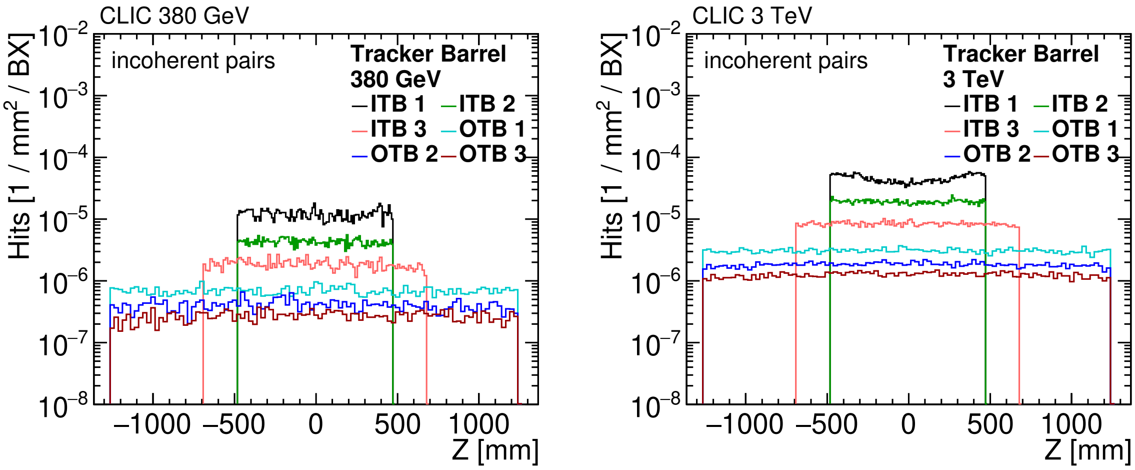

Figure 7.11: Longitudinal distribution of the hit densities per bunch crossing from incoherent electron–positron pairs in the tracker barrel at 380 GeV (left) and 3 TeV (right). Safety factors are not included.

constitute a lower fraction of all hits, due to a large flux of direct particles. The fraction of hits in the tracker layers and disks, occurring later than 10 ns after a bunch crossing is summarised in Table 7.3.

The Inner Tracker Barrel is relatively more impacted than the Outer Tracker barrel by the backscattered particles from the incoherent pairs. The effect is due to the closer position to the beam pipe of the former. The backscattered particles need lower transverse momentum and are traversing less material to reach the Inner Tracker Barrel.

In the case of the Inner and Outer tracker disks, most of the hits received from the $\gamma\gamma \to$ hadron events are direct, although the fraction of late hits increases in the more forward disks, as shown in Figures 7.21 and 7.22. The time distribution of the hits from the incoherent pairs is entirely different. For each disk three distinct peaks are visible, with the first peak corresponding to direct hits from particles travelling from the IP, the secondary peak around 15-20 ns from the near-side forward calorimeter region scattering positioned and the tertiary around 25-30 ns from the far-side forward calorimeter region. The far-side scattering impacts the outer tracker disks relatively more than the near-side. This is due to the shielding provided by the ECal and HCal endcaps from the particles coming from the near-side forward calorimeters.

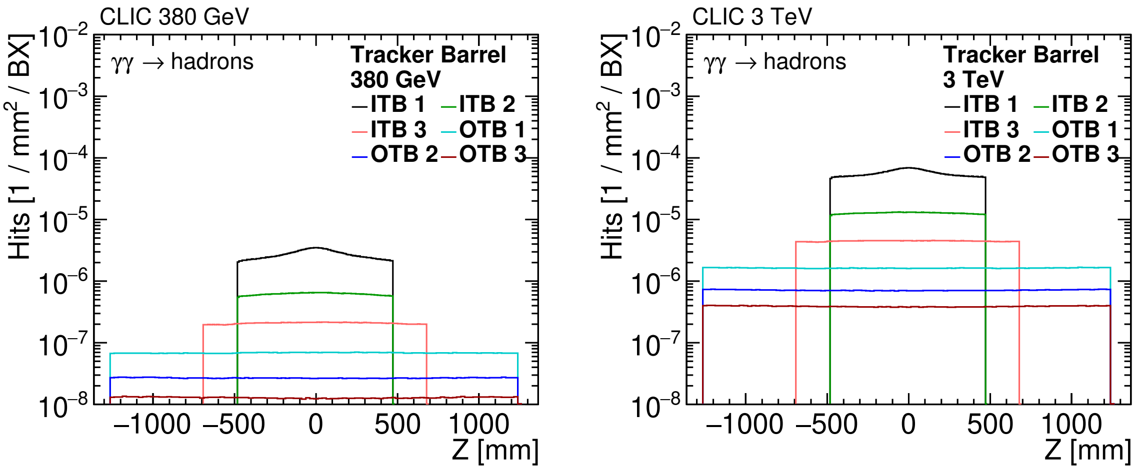

Figure 7.12: Longitudinal distribution of the hit densities per bunch crossing from $\gamma\gamma \to$ hadrons in the tracker barrel at 380 GeV (left) and 3 TeV (right). Safety factors are not included.

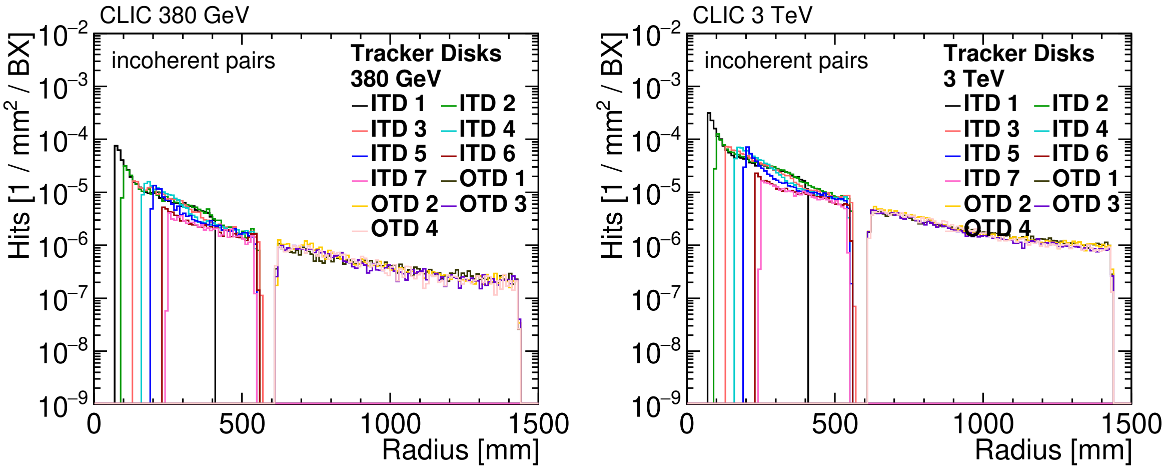

Figure 7.13: Radial distribution of the hit densities per bunch crossing from incoherent electron–positron pairs in the tracker disks at 380 GeV (left) and 3 TeV (right). Safety factors are not included.

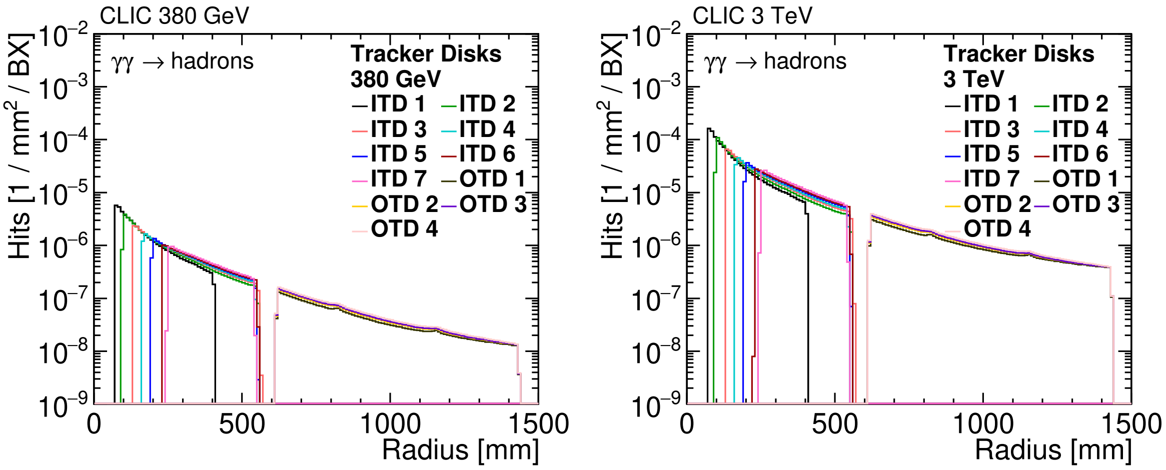

Figure 7.14: Radial distribution of the hit densities per bunch crossing from $\gamma\gamma \to$ hadron events in the tracker disks at 380 GeV (left) and 3 TeV (right). Safety factors are not included.

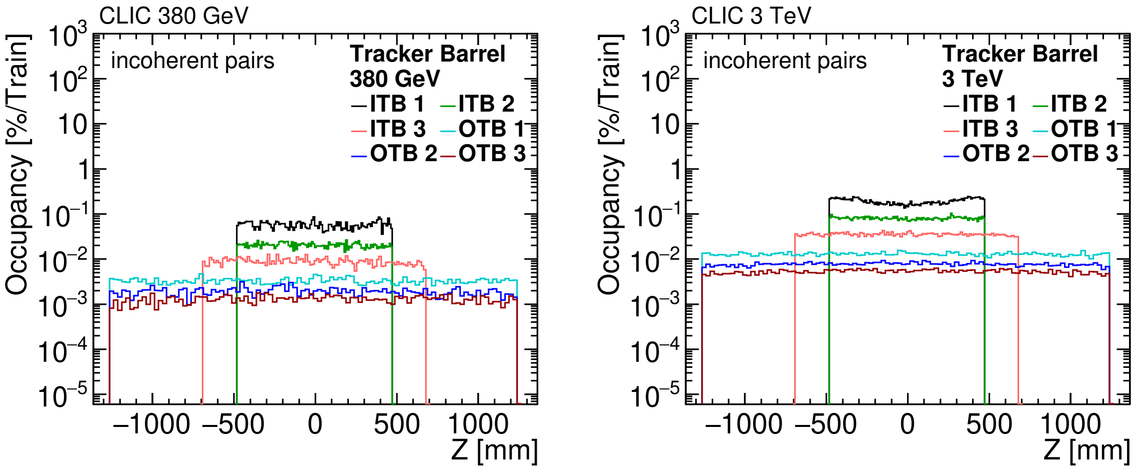

Figure 7.15: Longitudinal distribution of the occupancies per bunch train from incoherent electron–positron pairs in the tracker barrel at 380 GeV (left) and 3 TeV (right).

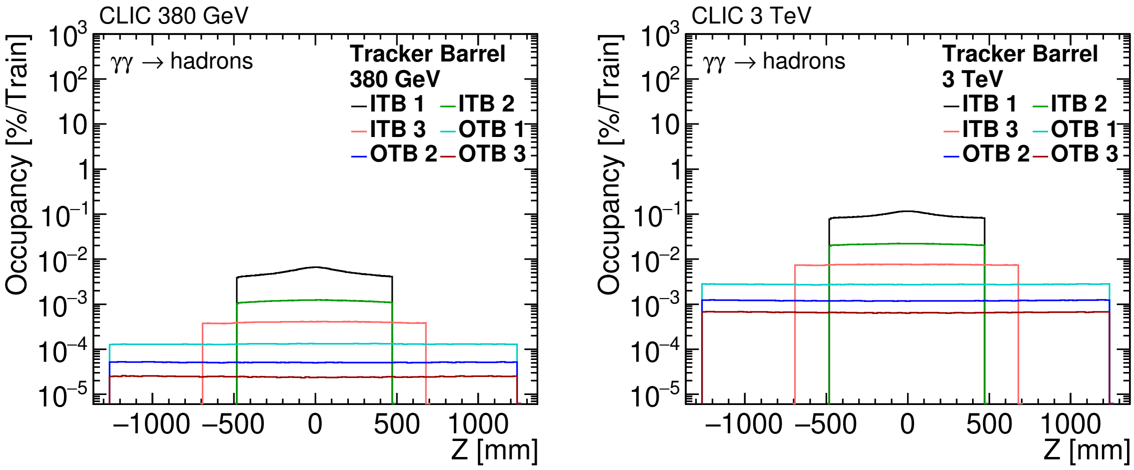

Figure 7.16: Longitudinal distribution of the occupancies per bunch train in the tracker barrel at 380 GeV (left) and 3 TeV (right) from γγ → hadrons.

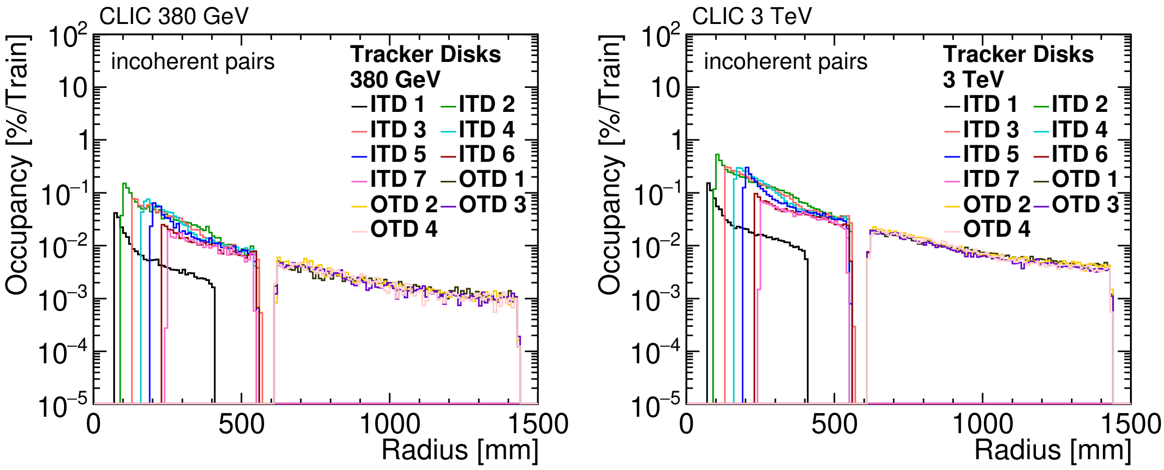

Figure 7.17: Radial distribution of the occupancies per bunch train from incoherent electron–positron pairs in the tracker disks at 380 GeV (left) and 3 TeV (right).

Table 7.3: Percentage of hits recorded in the tracking detector more than 10 ns after a bunch crossing.

Energy stage	380 GeV		3 TeV	
	incoherent pairs [% after 10ns]	$\gamma\gamma \rightarrow$ hadrons [% after 10ns]	incoherent pairs [% after 10ns]	$\gamma\gamma \rightarrow$ hadrons [% after 10ns]
Inner Tracker Barrel 1	48 %	29 %	55 %	28 %
Inner Tracker Barrel 2	89 %	46 %	90 %	47 %
Inner Tracker Barrel 3	88 %	52 %	90 %	52 %
Outer Tracker Barrel 1	83 %	57 %	84 %	56 %
Outer Tracker Barrel 2	85 %	60 %	86 %	60 %
Outer Tracker Barrel 3	86 %	60 %	87 %	61 %
Inner Tracker Disk 1	62 %	13 %	69 %	13 %
Inner Tracker Disk 2	74 %	17 %	79 %	16 %
Inner Tracker Disk 3	77 %	19 %	81 %	18 %
Inner Tracker Disk 4	80 %	22 %	84 %	20 %
Inner Tracker Disk 5	77 %	25 %	80 %	24 %
Inner Tracker Disk 6	71 %	30 %	73 %	28 %
Inner Tracker Disk 7	60 %	31 %	66 %	29 %
Outer Tracker Disk 1	85 %	48 %	87 %	50 %
Outer Tracker Disk 2	78 %	47 %	84 %	48 %
Outer Tracker Disk 3	79 %	49 %	83 %	49 %
Outer Tracker Disk 4	74 %	48 %	78 %	46 %

Table 7.4: The maximum and average occupancy in the Tracker detector from the incoherent pairs and $\gamma\gamma \rightarrow$ hadron events at 380 GeV and 3 TeV. Safety factors are included.

Energy stage	380 GeV		3 TeV	
	maximum [%]	average [%]	maximum [%]	average [%]
Inner Tracker Barrel 1	0.1	0.06	0.4	0.3
Inner Tracker Barrel 2	0.03	0.02	0.1	0.1
Inner Tracker Barrel 3	0.01	0.01	0.1	0.04
Outer Tracker Barrel 1	0.004	0.003	0.02	0.01
Outer Tracker Barrel 2	0.003	0.002	0.01	0.01
Outer Tracker Barrel 3	0.002	0.001	0.01	0.01
Inner Tracker Disk 1	0.05	0.004	0.2	0.02
Inner Tracker Disk 2	0.1	0.02	0.7	0.1
Inner Tracker Disk 3	0.1	0.02	0.4	0.1
Inner Tracker Disk 4	0.1	0.02	0.4	0.1
Inner Tracker Disk 5	0.1	0.01	0.4	0.1
Inner Tracker Disk 6	0.03	0.01	0.1	0.05
Inner Tracker Disk 7	0.02	0.01	0.1	0.05
Outer Tracker Disk 1	0.005	0.001	0.03	0.01
Outer Tracker Disk 2	0.006	0.001	0.03	0.01
Outer Tracker Disk 3	0.005	0.001	0.03	0.01
Outer Tracker Disk 4	0.005	0.001	0.03	0.01

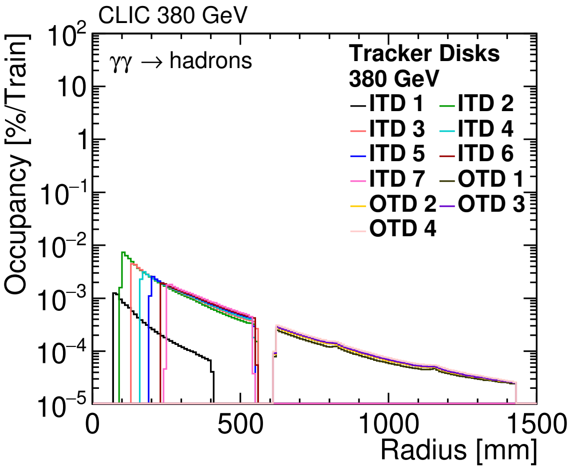

Figure 7.18: Radial distribution of the occupancies per bunch train from $\gamma\gamma \rightarrow$ hadrons in the tracker disks at 380 GeV (left) and 3 TeV (right).

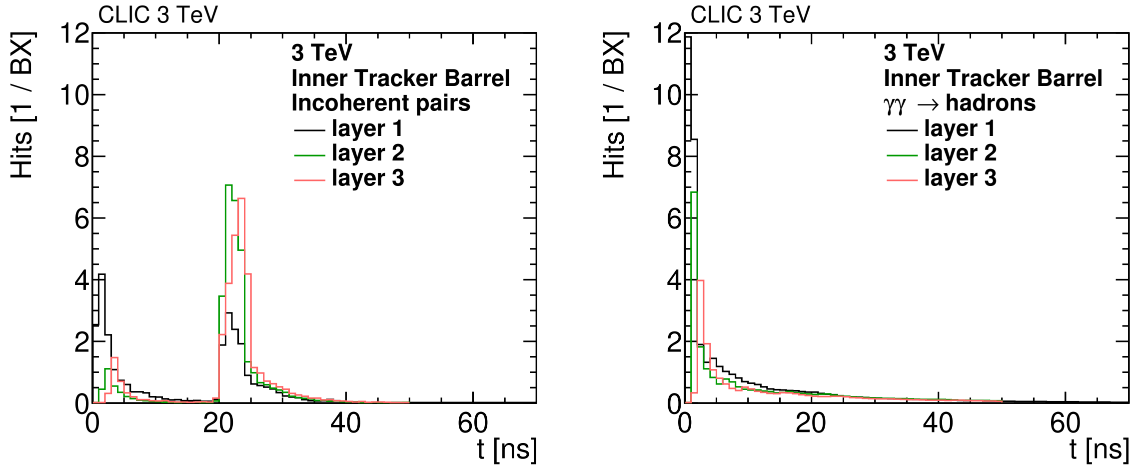

Figure 7.19: Time distribution of the hits per bunch crossing in the Inner Tracker barrel at 3 TeV from incoherent electron–positron pairs (left) and $\gamma\gamma \rightarrow$ hadron events (right). Safety factors are not included.

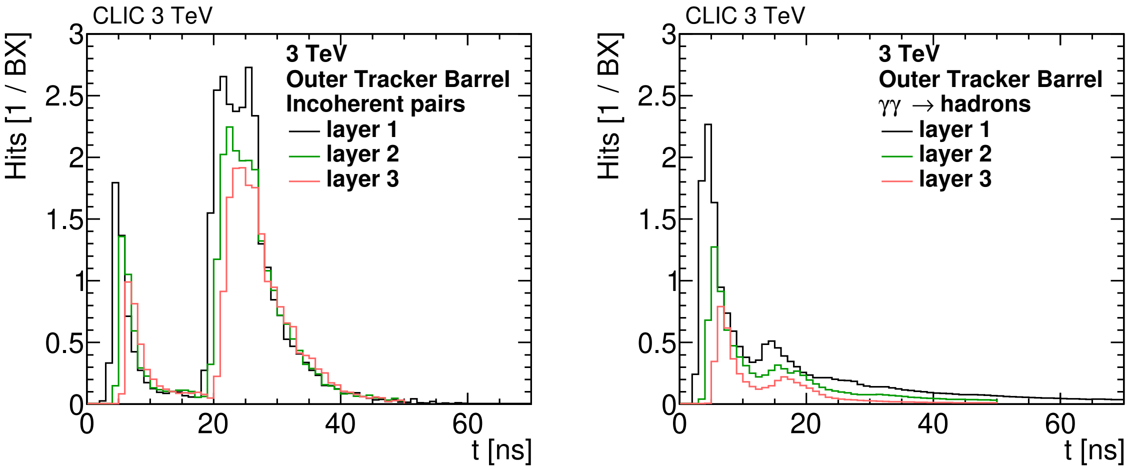

Figure 7.20: Time distribution of the hits per bunch crossing in the Outer Tracker barrel at 3 TeV from incoherent electron–positron pairs (left) and $\gamma\gamma \rightarrow$ hadron events (right). Safety factors are not included.

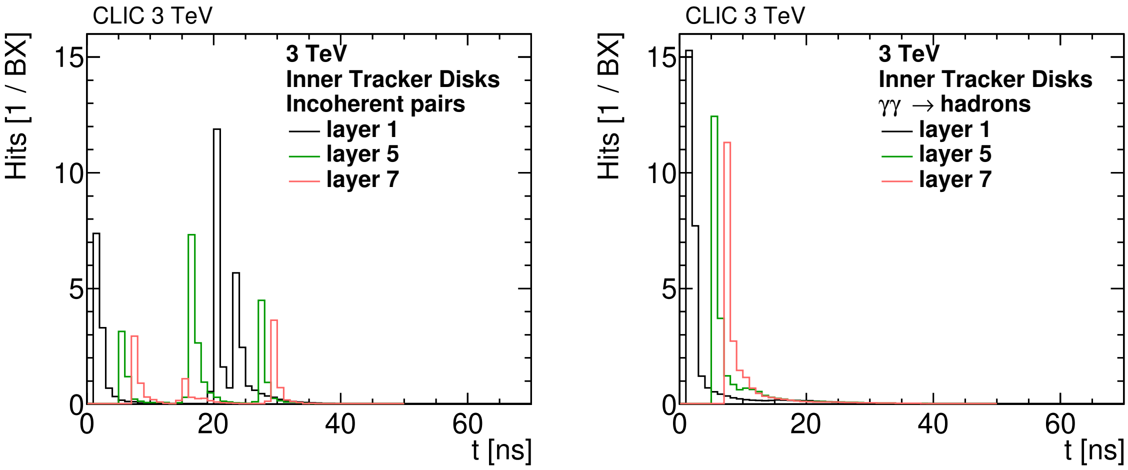

Figure 7.21: Time distribution of the hits per bunch crossing in the Inner Tracker disks at 3 TeV from incoherent electron–positron pairs (left) and $\gamma\gamma \rightarrow$ hadron events (right). Safety factors are not included.

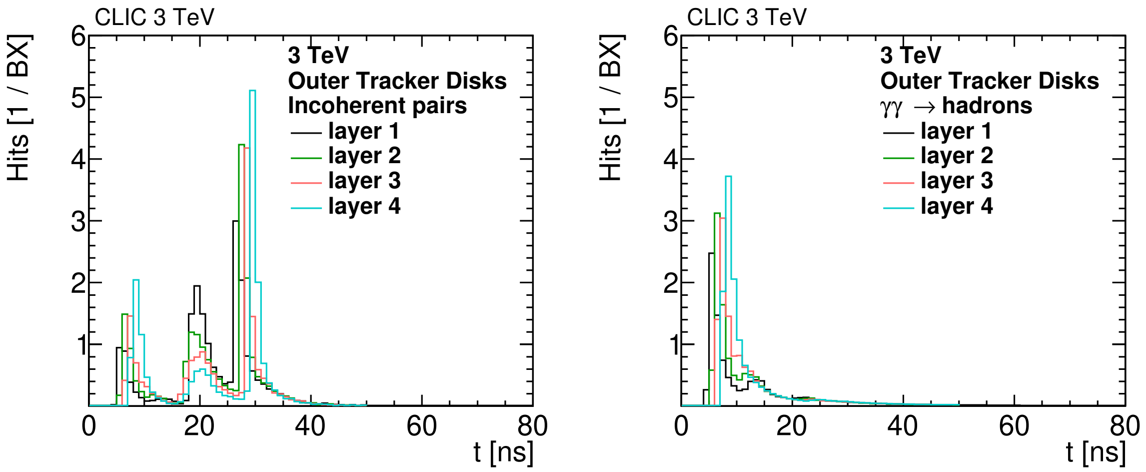

Figure 7.22: Time distribution of the hits per bunch crossing in the Outer Tracker disks at 3 TeV from incoherent electron–positron pairs (left) and $\gamma\gamma \to$ hadron events (right). Safety factors are not included.

7.2 Energy depositions and occupancies in the calorimeters

In this section, the energy depositions and occupancies in the calorimeter barrel detectors and calorimeter endcaps are described. The statistics used and the methods of calculating the occupancy are given for each region.

The statistics used in the study of occupancies in the barrel calorimeters consists of three bunch trains, i.e. 1056 bunch crossings at 380 GeV and 936 at 3 TeV, of the incoherent pairs results, and 6446 bunch trains at 380 GeV and 1087 bunch trains at 3 TeV of the $\gamma\gamma \to$ hadron events.

A significant amount of energy from the background particles is deposited in CLIC calorimeters. The incoherent pairs and the products of their scattering in the BeamCal region impact mainly the HCal endcap and leave significant energy depositions at both energy stages. The total reconstructed energy in the calorimeter is the energy deposited by the simulated particles multiplied by the relevant energy calibration factors, 38.3 for the ECal and 53.6 for the HCal. The calibration procedure sets the constants used in the detector simulations for both the digitisation, the estimation of energy deposits in the absorber material of the calorimeters based on the energy deposited in the active material [99]. The total energy deposited in the endcaps rises by a factor of four from 380 GeV to 3 TeV. The reconstructed energy in the calorimeter barrel and endcaps are summarised in Table 7.5. The energy reconstructed in the HCal endcap at both 380 GeV and 3 TeV significantly surpasses the nominal collision energy. Assuming there is one hard interaction relevant for the CLIC physics programme per bunch train, it would be challenging to reconstruct accurately the deposits from such an event in the HCal endcap due to the large energy deposited there by background particles.

7.2.1 Calorimeter barrel detectors

Two calorimeters that surround the tracking detectors are envisioned in the CLICdet model: an electromagnetic calorimeter and a hadronic one.

The barrel calorimeters do not suffer significantly from beam-induced backgrounds due to their distance from the IP and the large transverse momentum of more than 900 MeV a charged background particle would need to reach them. Using the distributions of particles from $\gamma\gamma \to$

Table 7.5: The energy depositions per bunch train in ECal and HCal at 380 GeV and 3 TeV taking into account the energy calibration factors. Safety factors not included.

	380 GeV		3 TeV	
	pairs [TeV]	$\gamma\gamma \to$ hadrons [TeV]	pairs [TeV]	$\gamma\gamma \to$ hadrons [TeV]
ECal barrel	0.1	0.1	0.4	1.9
ECal endcap	0.2	0.2	0.7	5.0
HCal barrel	$1.6 \cdot 10^{-3}$	$6.8 \cdot 10^{-3}$	$7.5 \cdot 10^{-3}$	0.2
HCal endcap	75.3	0.1	310.4	7.7
Total calorimeter	75.6	0.4	311.5	14.8

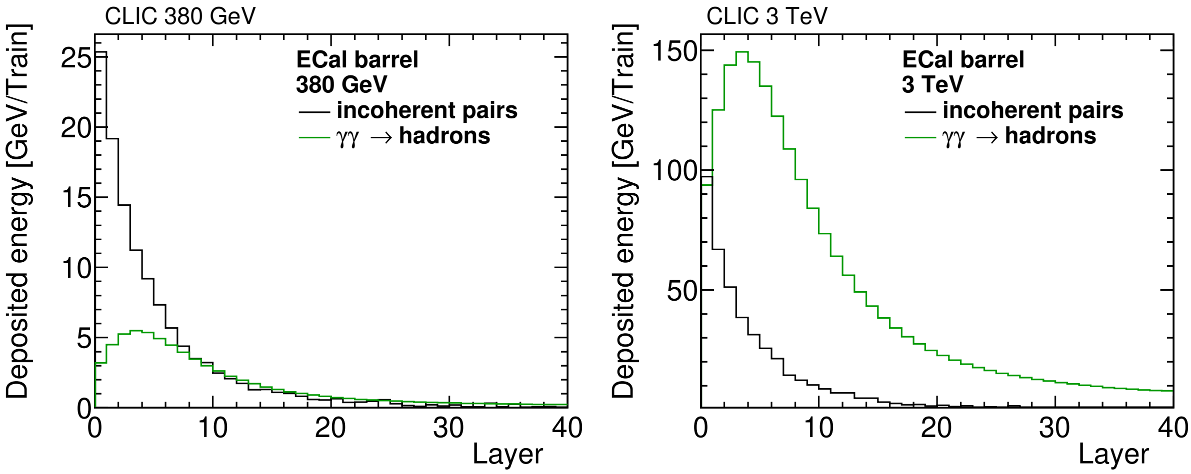

Figure 7.23: Distribution of the energy depositions per bunch train in the ECal barrel at 380 GeV (left) and 3 TeV (right) from incoherent electron–positron pairs and $\gamma\gamma \to$ hadrons. Safety factors are included.

hadron events from section 4.5, and incoherent pairs from section 4.4, one can estimate the energy carried by the particles which can potentially reach the ECal or HCal barrel region. This calculation does not take into account the possible interaction with detectors placed between the interaction point and the calorimeters. At 380 GeV and 3 TeV it is estimated that 2.7% and 3.9%, respectively, of charged particles from $\gamma\gamma \to$ hadrons (3×10^{-5}% and 5×10^{-5}% of incoherent pairs) reach the first layer of the ECal. In addition, there are no significant sources of secondary and backscattered particles in proximity of the barrel calorimeters.

7.2.1.1 ECal barrel

The energy depositions for the ECal barrel are presented in Figure 7.23, and the occupancy distributions can be found in Figure 7.24. The occupancies in the case where the integration time has not been split into 25 ns time windows are available in Figure 7.25. The electromagnetic calorimeter in the first few layers is most impacted by incoherent electron–positron pairs, while the $\gamma\gamma \to$ hadron events impact mainly the deeper layers. The energy depositions and occupancy at 380 GeV energy stage is dominated by the incoherent pairs. At 3 TeV the integrated energy deposition from $\gamma\gamma \to$ hadron events surpasses that of the incoherent pairs. This is not fully reflected in the occupancy levels, with the pairs being the most important source of occupancy at 3 TeV as well. The maximal occupancy, including the safety factors, is generally low and does not exceed 0.06% and 0.23% at 380 GeV and 3 TeV respectively when the 25 ns time slicing is applied. With the use of one slice per total integration time these numbers increase to 0.48% and 1.8% respectively.

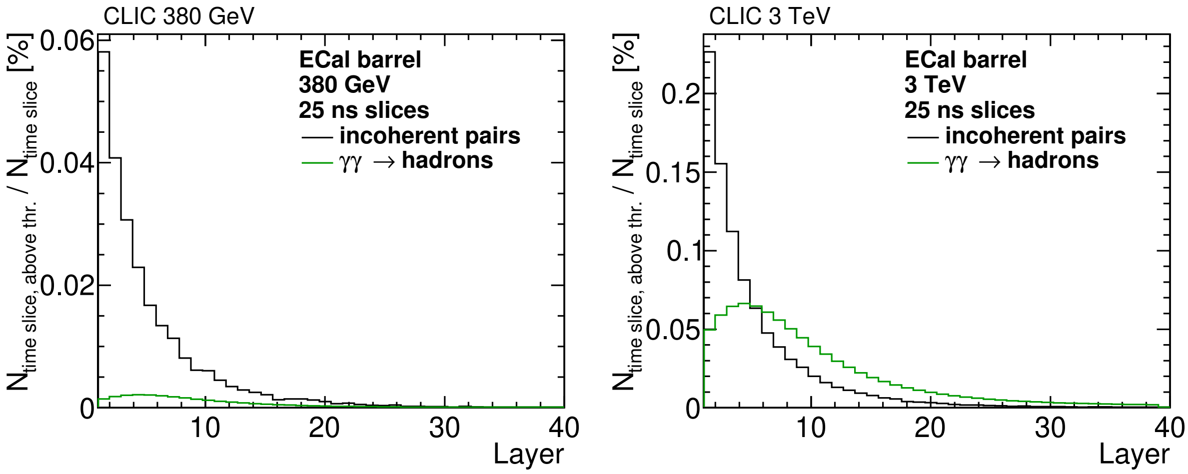

Figure 7.24: Distribution of the occupancy per time slice, with time slices of 25 ns, in the ECal barrel at 380 GeV (left) and 3 TeV (right) from incoherent electron–positron pairs and $\gamma\gamma \rightarrow$ hadrons. Safety factors are included.

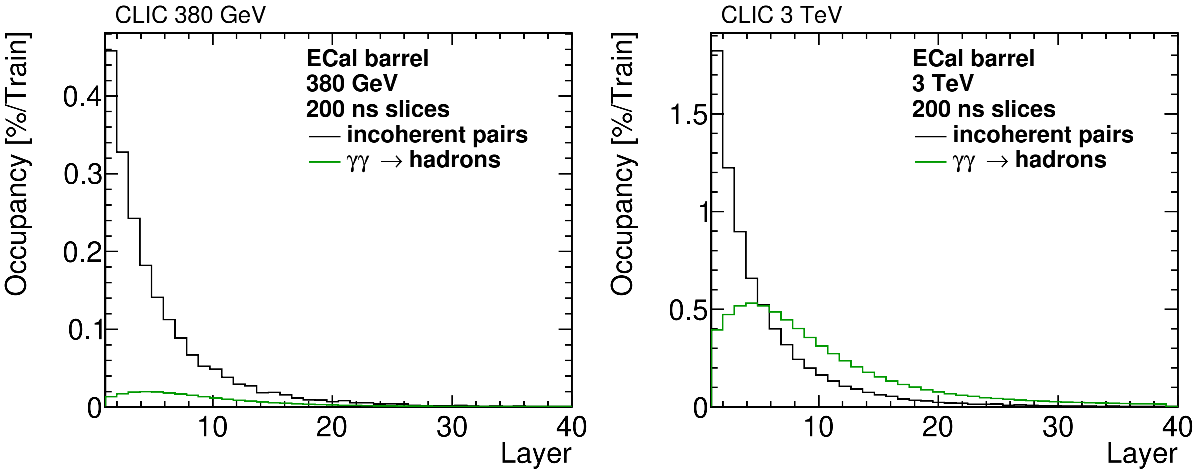

Figure 7.25: Distribution of the occupancy per bunch train in the ECal barrel at 380 GeV (left) and 3 TeV (right) from incoherent electron–positron pairs and $\gamma\gamma \rightarrow$ hadrons. The total integration time has not been separated into time windows. Safety factors are included.

7.2.1.2 HCal barrel

In the hadronic calorimeter barrel, as can be observed in Figures 7.26 and 7.27, the impact of incoherent pairs is limited due to the containment of electrons, positrons and photons in the electromagnetic calorimeter. Thus, the flux of background particles is dominated by $\gamma\gamma \rightarrow$ hadrons. The observed secondary peak in the incoherent pairs energy depositions in the fifth layer of the HCal at 380 GeV is caused by statistical fluctuations. The limited size of the simulated samples makes the conclusions more qualitative than for the ECal. Taking into account all relevant sources of background and the safety factors the occupancies are found to be low in the HCal

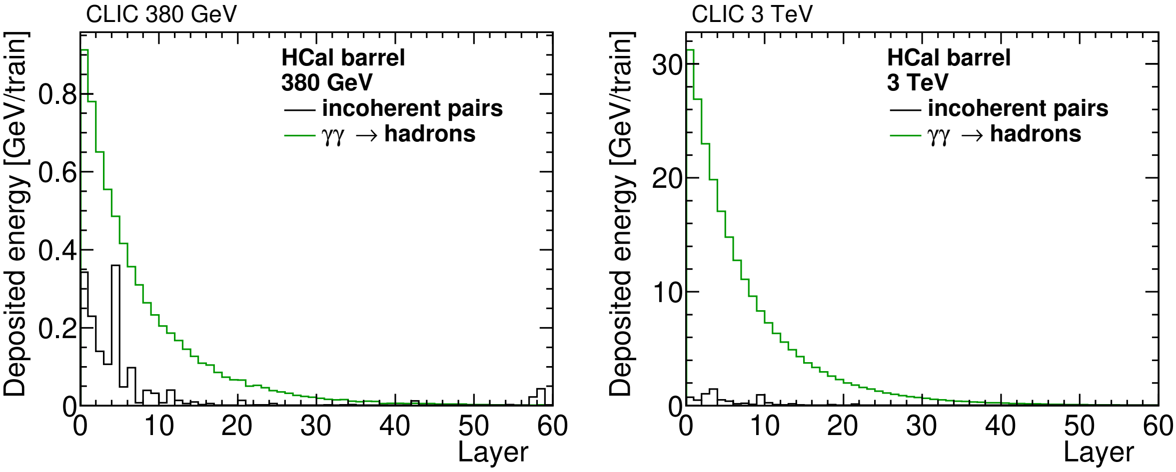

Figure 7.26: Distribution of the energy depositions per bunch train in the HCal barrel at 380 GeV (left) and 3 TeV (right) from incoherent electron–positron pairs and $\gamma\gamma \to$ hadrons. Safety factors are included.

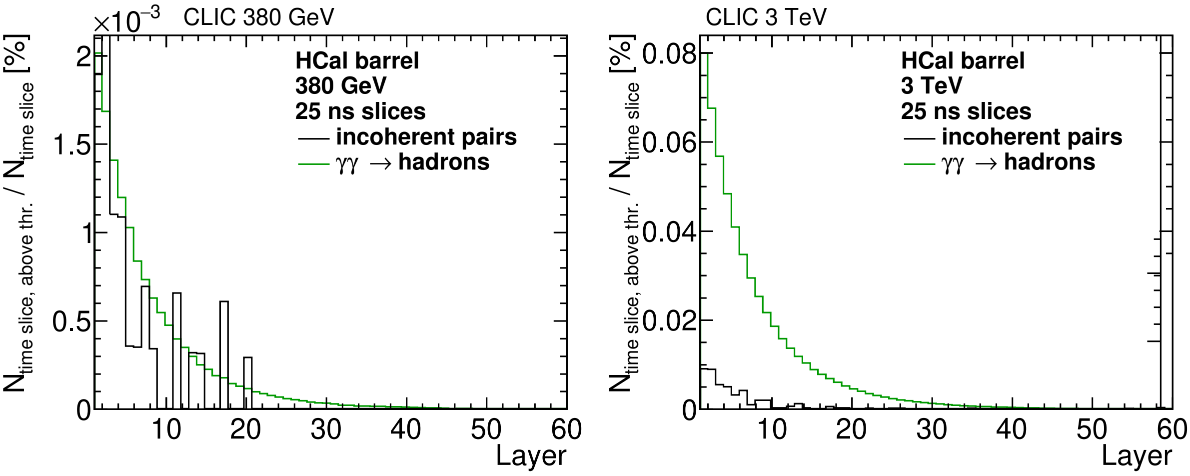

Figure 7.27: Distribution of the occupancy per time slice, with time slices of 25 ns, in the HCal barrel at 380 GeV (left) and 3 TeV (right) from incoherent electron–positron pairs and $\gamma\gamma \to$ hadrons. Safety factors are included.

barrel. The occupancy levels are less than $2 \cdot 10^{-3}$% and 0.08% at 380 GeV and 3 TeV respectively with 25 ns slicing time. The case where the integration time has not been split into time windows is shown in Figure 7.28, where the occupancies are less than 0.02% and 0.8% respectively. With occupancies considerably below 1% at both energy stages, the performance of the HCal barrel detectors are not expected to be significantly impacted. The data rates caused by backgrounds are also not expected to be large [35].

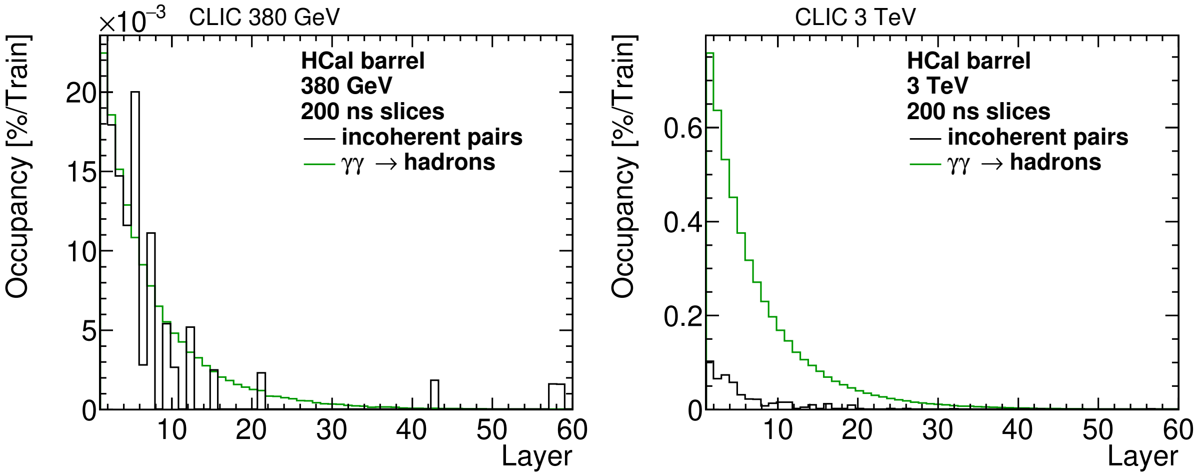

Figure 7.28: Distribution of the occupancy per bunch train in the HCal barrel at 380 GeV (left) and 3 TeV (right) from incoherent electron–positron pairs and $\gamma\gamma \rightarrow$ hadrons. The total integration time has not been separated into time windows. Safety factors are included.

7.2.2 Calorimeter endcap detectors

The calculation of the occupancy for the ECal and HCal endcaps consists of several steps. It starts with transportation of background particles through the CLICdet detector model using GEANT4. The energy depositions in each calorimeter layer are integrated and the cells occupancy per bunch train is calculated with Equation (3.5). The distribution of occupied cells and time windows (25 ns long) is stored as a function of radius. These radial distributions of occupied cells are normalised by dividing them by a radial distribution of all cells of the current calorimeter endcap layer, in analogy to the radial surface distributions described in section 7.1. The resulting numbers are scaled by the respective safety factors, as expressed in Equation (3.6). Finally, the occupancy distributions coming from different sources can be combined using Equation (3.8).

The maximum and average occupancies for the ECal and HCal endcaps at both 380 GeV and 3 TeV are summarised in Table 7.6. The occupancy level is significantly larger in the HCal endcap, and reaches 100% at both energy stages. The maximum occupancy of the ECal endcap is below the acceptable level of about 10%, with a maximum of 7.1% at 3 TeV.

7.2.2.1 ECal endcap

The energy depositions in the electromagnetic calorimeter are comparable between the incoherent pairs and $\gamma\gamma \to$ hadron events at the 380 GeV energy stage, while at 3 TeV the influence of $\gamma\gamma \to$ hadron events is dominant. The radial distributions of energy depositions in the ECal endcap can be found in Figure 7.29. The energy deposition distributions for both the incoherent pairs and $\gamma\gamma \to$ hadron events show an exponential decrease with radius.

The occupancy, using 25 ns time windows, is presented as a function of radius and layer number in Figures 7.30 and 7.31 for 380 GeV and 3 TeV respectively. The region with highest occupancy is at the lowest radii. The shape of the impacted region in Figures 7.30 and 7.31 depends on the type of background and the energy stage. The incoherent pairs leave deposits mainly in the front ten layers and also at a larger radius than the particles from $\gamma\gamma \to$ hadron events. The $\gamma\gamma \to$ hadrons event occupancy distributions have a maximum between layers eight and twelve, and the impacted region is bigger and positioned at a larger radius than for the incoherent pairs. In the 2D occupancy distributions in Figures 7.30 and 7.31, the gap between ECal and ECal plug at the radial position of 400 mm is visible as a white line.

Table 7.6: The maximal and average values of the ECal and HCal endcaps occupancy with 25 ns time slices at 380 GeV and 3 TeV. The granularity is $5 \times 5\,\text{mm}^2$ for the ECal endcap and $30 \times 30\,\text{mm}^2$ for the HCal endcap. Safety factors are included.

	380 GeV		3 TeV	
	max [%]	average [%]	max [%]	average [%]
ECal	1.7	0.1	7.1	0.3
HCal	100	1.6	100	2.7

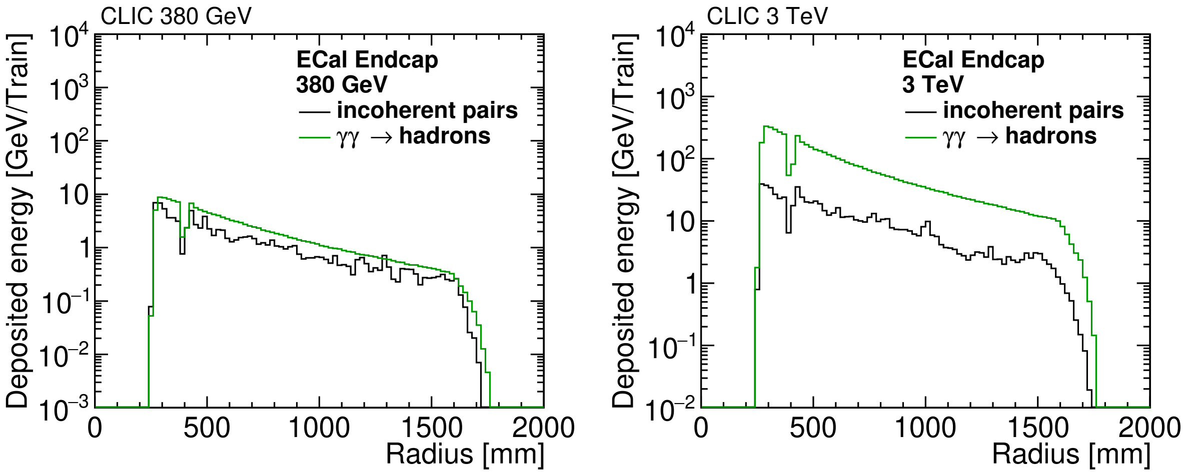

Figure 7.29: Distribution of the energy depositions per bunch train in the ECal endcap at 380 GeV (left) and 3 TeV (right) from incoherent electron–positron pairs and γγ → hadrons. Safety factors are included.

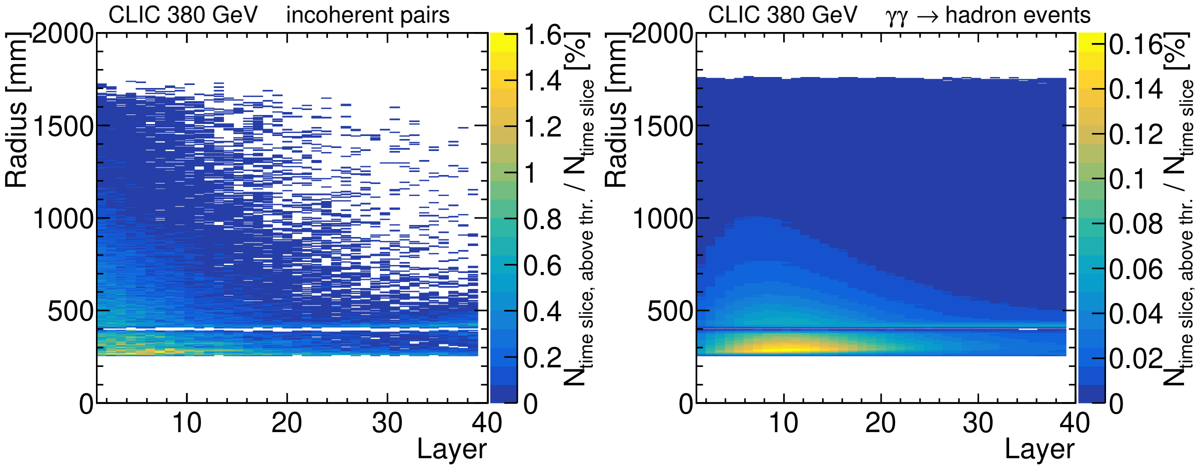

Figure 7.30: Distribution of occupancy per time slice, with time slices of 25 ns, as a function of radius and layer number in the ECal endcap at 380 GeV from incoherent electron–positron pairs (left) and γγ → hadrons (right). Safety factors are included.

The radial distribution of occupancy is presented in Figure 7.32 as an average over six layers in the region with the highest occupancy between layers five and ten. The radial projection provides a focused view of the occupancy in the chosen layers and allows for comparison of the impact of different background sources. The occupancy levels at 380 GeV are generally low, reaching the radial average of 0.3% for the smallest radii. The radial average is a weighted mean, where the number of cells at each radial bin is used as the weight. At 3 TeV, the occupancy reaches a maximum of 3%. The dominant source of background in the ECal at 380 GeV is incoherent pairs, while at 3 TeV the γγ → hadron events yield most of the hits. The observed difference is a result of the difference in the transverse momentum distributions of the background sources.

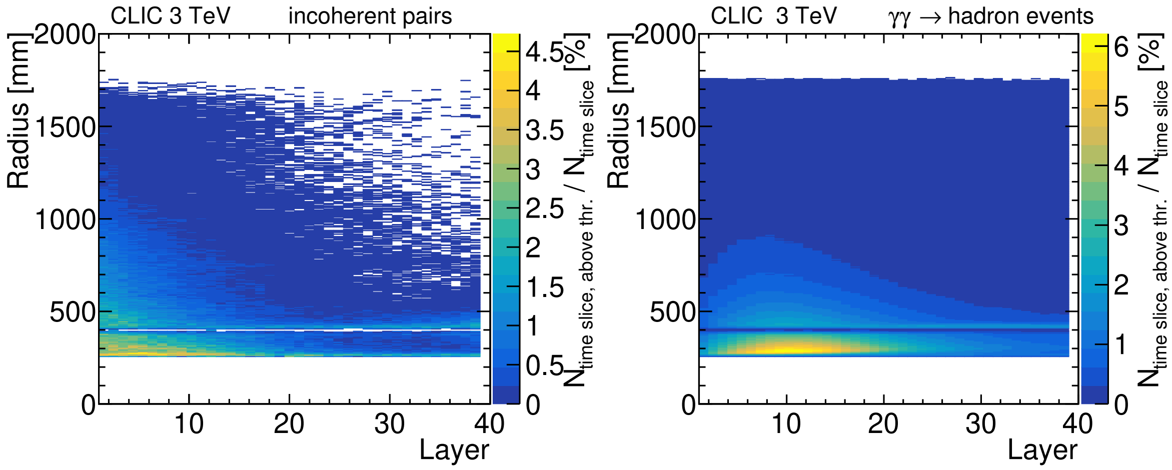

Figure 7.31: Distribution of occupancy per time slice, with time slices of 25 ns, as a function of radius and layer number in the ECal endcap at 3 TeV from incoherent electron–positron pairs (left) and γγ → hadrons (right). Safety factors are included.

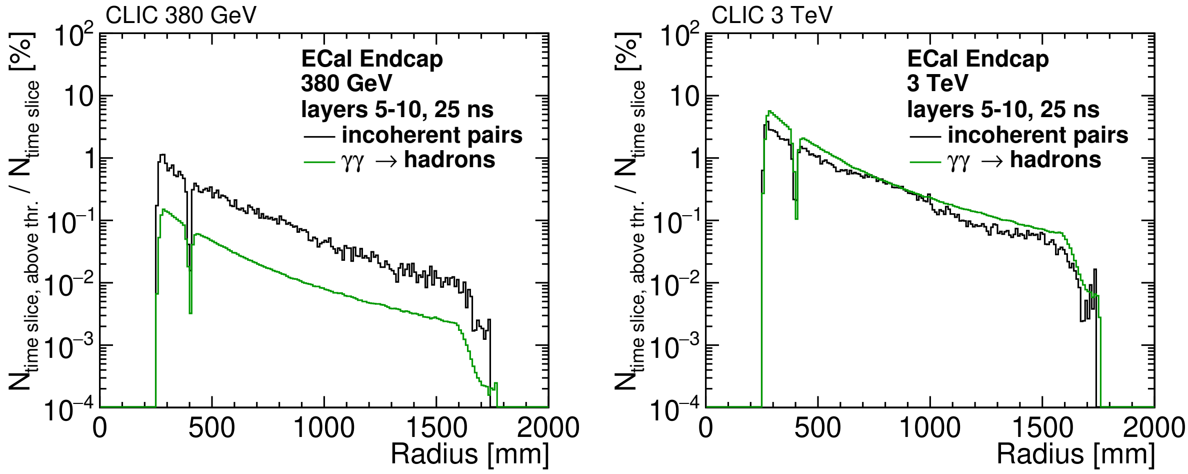

Figure 7.32: Distribution of the occupancy per time slice, with time slices of 25 ns, in the ECal endcap at 380 GeV (left) and 3 TeV (right) from incoherent electron–positron pairs and γγ → hadrons. The occupancy is averaged over layers 5 to 10, the region with the highest occupancy. Safety factors are included.

7.2.2.2 HCal endcap

The radial distributions of energy depositions in the HCal can be found in Figure 7.33. In the hadronic calorimeter the impact of the incoherent pairs is significantly larger than of the γγ → hadron events, especially at the lowest radii. This suggests that there is a large influx of low-energy particles in the innermost region of the HCal that lose most of their energy in the first 400 mm radially of the calorimeter. Particles with higher energy travel deeper into the HCal and leave an exponentially decreasing energy deposition. Such a characteristic is consistent with the incoherent pairs scattering in the BeamCal that cause an influx of photons with a wide energy spectrum up to the GeV range and neutrons with a dominant energy of

1 MeV in the HCal endcap [98].

The occupancy in the HCal endcap is significantly higher than in the ECal, and reaches full saturation due to the direct and indirect impact of the incoherent pairs. The incoherent pairs hit the BeamCal, producing neutrons and photons that deposit large amounts of energy in the HCal. In Figures 7.34 and 7.35 the distribution of occupancy as a function of radius and layer number is shown for 380 GeV and 3 TeV respectively. The radial distribution of the occupancy averaged over thirteen layers, twenty-three to thirty-five, is shown in Figure 7.36. The region most impacted by hadrons is located at a depth of around 50 mm from the subdetector's inner radius. The gap in the ECal calorimeter, through which some hadrons travel to the HCal is visible. This is not observed in the incoherent pairs occupancy distribution. The impact from the incoherent pairs dominates at both energy stages, especially at 380 GeV. The depth of the highly impacted region, defined as having an occupancy above 10%, increases with the collision energy, reaching 450 mm at 380 GeV and 600 mm at 3 TeV. There are two maxima of occupancy located in layers 22-26 and around layer 46, in proximity to the BeamCal. The scattering of high energy electrons and positrons in the BeamCal region gives rise to high fluxes of photons and neutrons, which impact the HCal endcap and is the dominant source of the occupancy. The high occupancy requires mitigation, which is discussed in section 8.3.

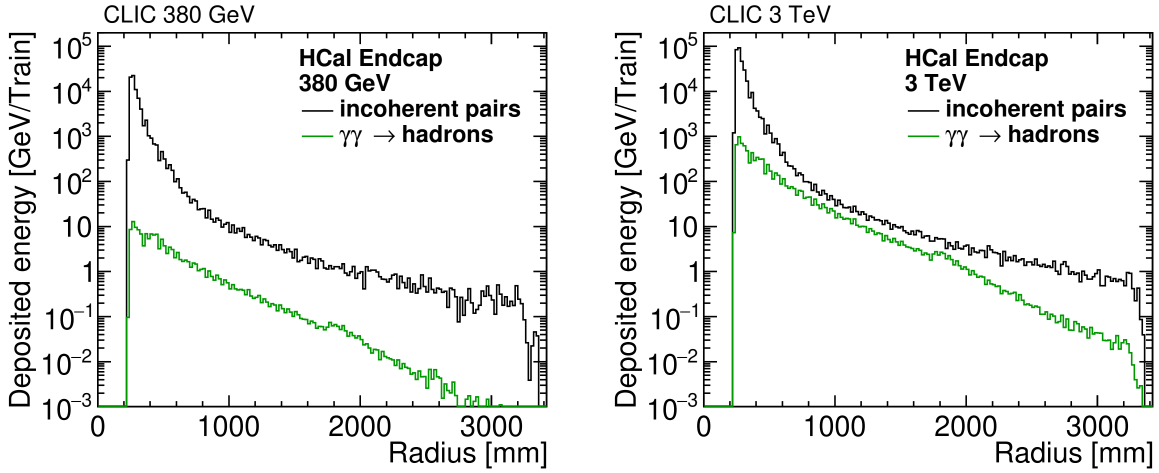

Figure 7.33: Distribution of the energy depositions per bunch train in the HCal endcap at 380 GeV (left) and 3 TeV (right) from incoherent electron–positron pairs and $\gamma\gamma \to$ hadrons. Safety factors are included.

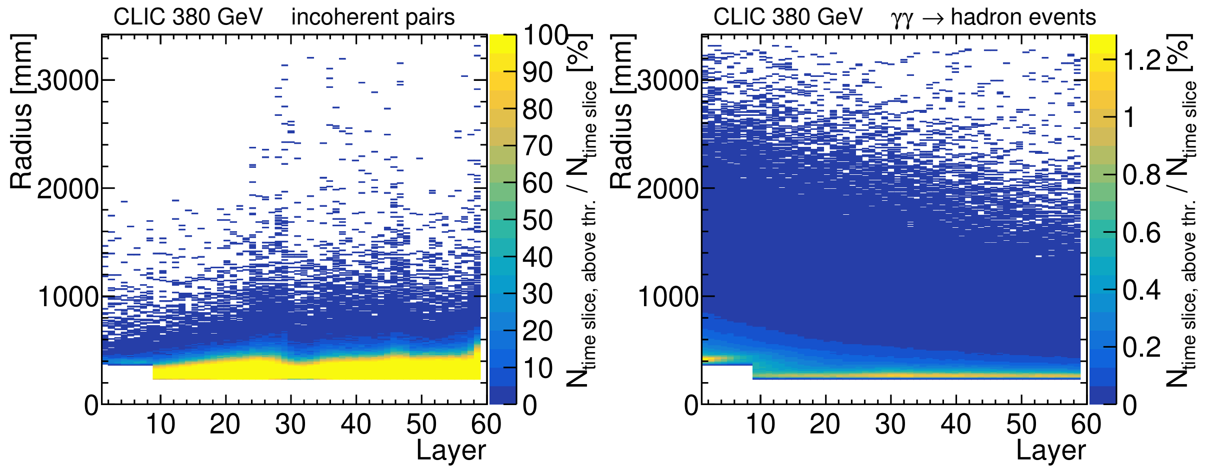

Figure 7.34: Distribution of occupancy per time slice, with time slices of 25 ns, as a function of radius and layer number in the HCal endcap at 380 GeV from incoherent electron–positron pairs (left) and $\gamma\gamma \to$ hadrons (right). Safety factors are included.

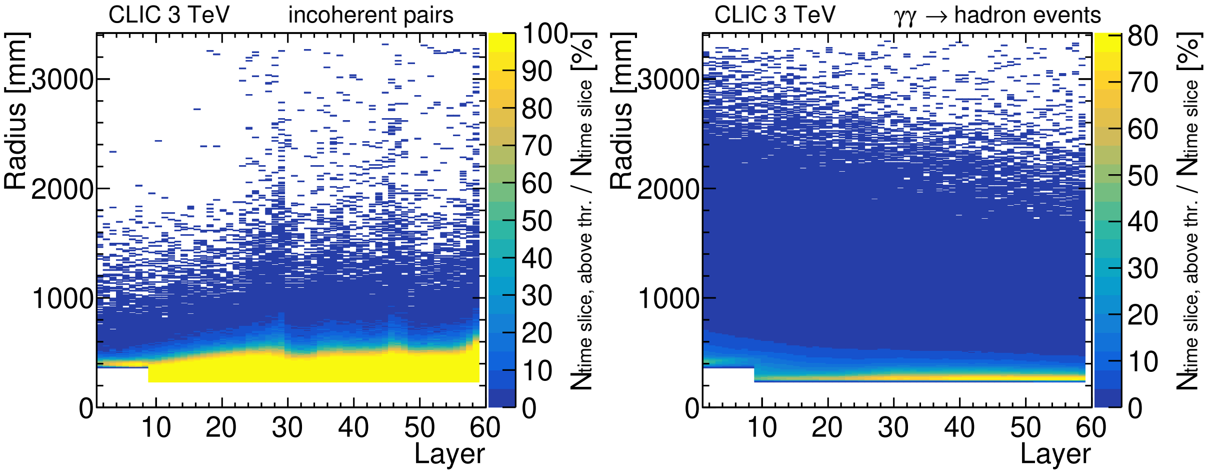

Figure 7.35: Distribution of occupancy per time slice, with time slices of 25 ns, as a function of radius and layer number in the HCal endcap at 3 TeV from incoherent electron–positron pairs (left) and $\gamma\gamma \to$ hadrons (right). Safety factors are included.

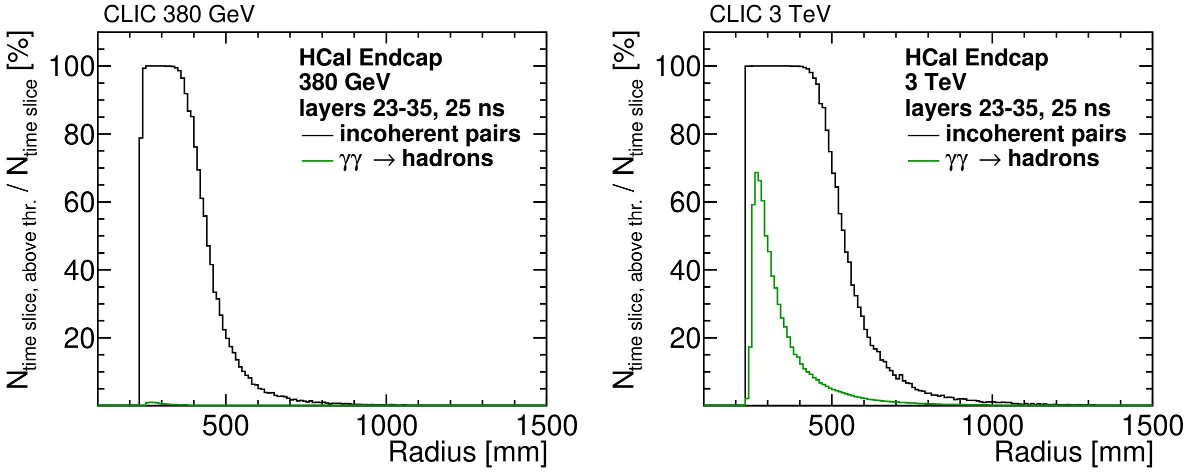

Figure 7.36: Distribution of the occupancy per time slice, with time slices of 25 ns, in the HCal endcap at 380 GeV (left) and 3 TeV (right) from combined incoherent electron–positron pairs and $\gamma\gamma \to$ hadrons. The occupancy is averaged over layers 23 to 35, the region containing the maximum occupancy. Safety factors are included.

7.3 Muon Identification System

The Muon Identification System (MuonID) consists of six layers of resistive plate chambers (RPCs) inserted in the iron return yoke. The RPC cell size is $30 \times 30\,\mathrm{mm}^2$. Since the sensor of the RPCs is a thin layer of gas, the energy threshold in the MuonID simulations is only 300 eV (0.3 MIP) [60]. Changing the forward region of the dtector model, from CLIC_ILD to CLICdet, led to a change of the MuonID endcap design. The inner radius in CLICdet is 490 mm, compared to 690 mm in CLIC_ILD.

The occupancy calculation method used in the analysis of the MuonID and the data normalization are the same as used for the calorimeters. No time-slicing is assumed, leading to a time window for hits in the MuonID of 200 ns. The statistics used to obtain the results in this section corresponds to three bunch trains at each energy stage: 1056 bunches and 936 bunches at 380 GeV and 3 TeV, respectively, in the case of incoherent pairs, and 170 bunch trains of $\gamma\gamma \rightarrow$ hadron events for both energy stages. An experimental cavern is not included in the simulations of CLICdet. The impact of including the experimental cavern in the simulation model is presented in section 8.4.

7.3.1 MuonID barrel occupancies

The occupancies in the MuonID barrel are presented in Figure 7.37. With the MuonID barrel placed further from the IP than the calorimeter barrel the hit rates are low, similar to the outer layers of the HCal barrel (see section 7.2.1). The outer layers of the MuonID barrel are not receiving a single energy deposition above threshold from background particles. Incoherent pairs and $\gamma\gamma \rightarrow$ hadron particles can thus be assumed to not impair the muon identification efficiency nor cause any noticeable data rates. Particles that have sufficient transverse momentum to reach the MuonID barrel need to traverse both the ECal and the HCal barrel.

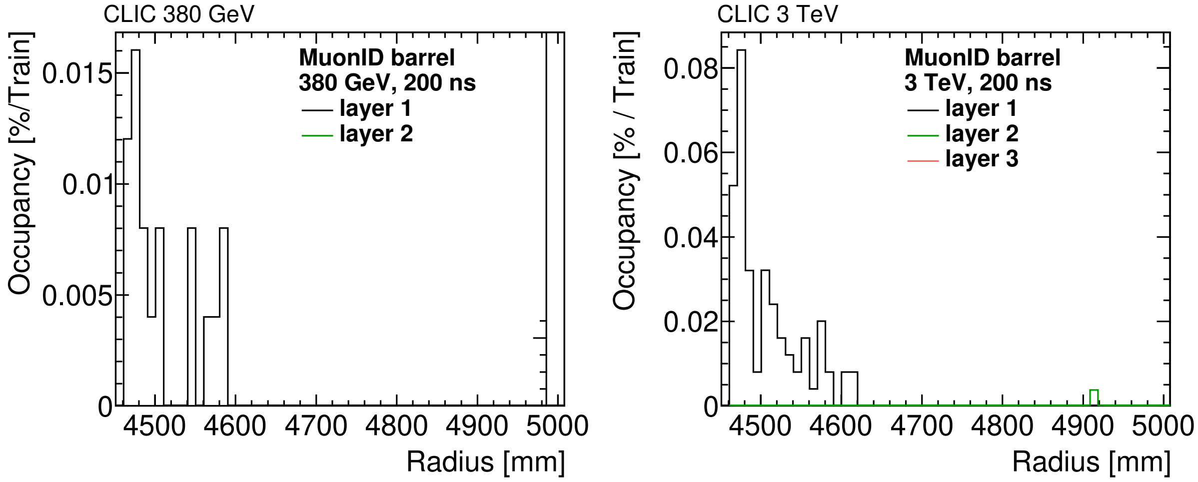

Figure 7.37: Distribution of the occupancy per bunch train in the Muon Identification System barrel at 380 GeV (left) and 3 TeV (right) from combined incoherent electron–positron pairs and $\gamma\gamma \rightarrow$ hadrons. Safety factors are included.

Table 7.7: The maximal and average values of the occupancy in all layers of the MuonID endcap at 380 GeV and 3 TeV. Safety factors are included.

	380 GeV		3 TeV	
	max [%]	average [%]	max [%]	average [%]
Layer 1	100	1.05	100	1.65
Layer 2	100	1.06	100	1.67
Layer 3	100	1.00	100	1.63
Layer 4	100	0.93	100	1.51
Layer 5	100	0.93	100	1.52
Layer 6	100	1.14	100	2.06

7.3.2 MuonID endcap occupancies

The muon endcap detector is strongly affected by the presence of unwanted particles, especially the incoherent pairs and the products of their interactions with material in the BeamCal region, as can be observed in Figure 7.38. The radial distributions of the occupancy are presented in Figure 7.39, split between subdetector layers. The hit density is uniform where the statistical fluctuations are low. The density is not concentrated in any layer but persists along the entire subdetector at a similar level, thus averaging over all the layers to reduce the statistical fluctuations does not introduce a systematic bias. The uniformity of the occupancy level in the inner part of the MuonID endcap can also be observed in Figure 7.40, where the occupancies are presented as a function of radius and layer number.

The occupancy level reaches 100% at the lowest radii at both energy stages, and the radial depth of the impacted region is larger at 3 TeV. The average and maximal occupancy is summarised in Table 7.7. Layer 6 of the MuonID endcap sees the highest average occupancy, coming mainly from $\gamma\gamma \rightarrow$ hadrons and incoherent pairs scattering downstream the detector. The beam pipe implemented in the CLICdet simulation model is 12 m long, and no other material that would be present in the tunnel, such as magnets or the experimental cavern are present. Thus, the background particles produced in the electron–positron interactions at the IP can travel up to 12 m, interact with the beam pipe between the outer edge of the detector and the products of their interactions with the beam pipe can travel back towards the detector leading to increased occupancy levels. The mitigation of this high occupancy, including the implementation of the experimental cavern and accelerator tunnel, is discussed in section 8.4.

The obtained occupancy is significantly higher than was estimated for the CLIC_ILD detector model. The high occupancy level can be attributed to the changes in detector geometry between CLIC_ILD and CLICdet, namely the removal of the material of the QD0 magnet and anti-solenoid that provided shielding, and the reduction of the inner radius from 690 mm to 490 mm.

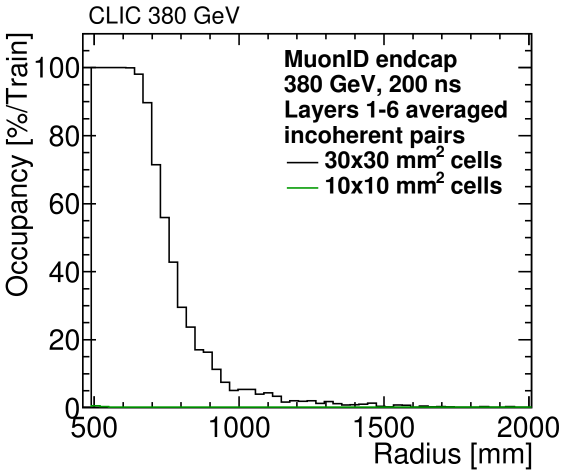

Figure 7.38: Radial distribution of the occupancy per bunch train in the Muon Identification System endcap at 380 GeV (left) and 3 TeV (right) from combined incoherent electron–positron pairs and $\gamma\gamma \rightarrow$ hadrons. Safety factors are included.

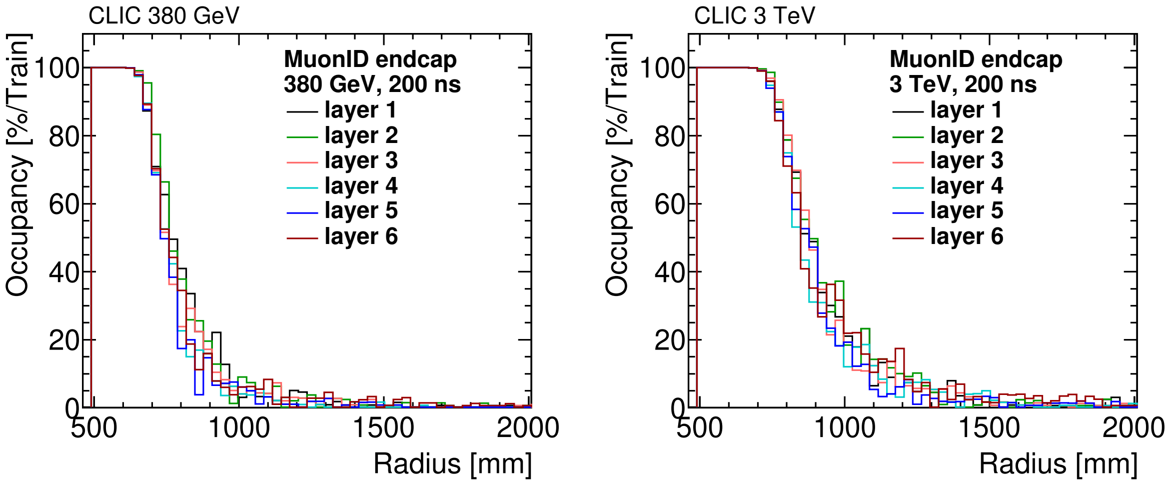

Figure 7.39: Radial distribution of the occupancy per bunch train in the Muon Identification System endcap averaged over Layer 1 to 6 at 380 GeV (left) and 3 TeV (right) from combined incoherent electron–positron pairs and $\gamma\gamma \rightarrow$ hadrons. Safety factors are included.

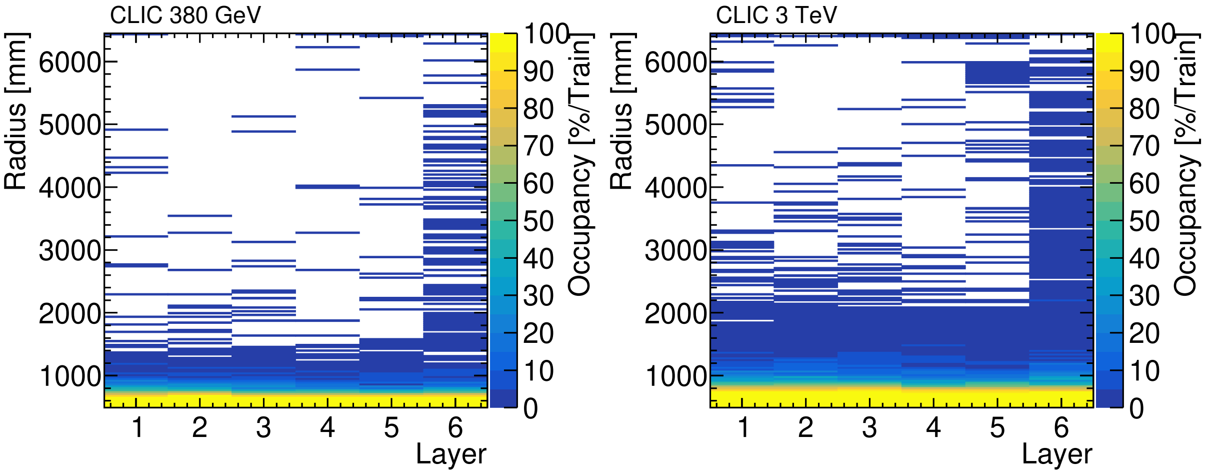

Figure 7.40: Distribution of the occupancy per bunch train by layer as a function of radius in the Muon Identification System endcap at 380 GeV (left) and 3 TeV (right) from combined incoherent electron–positron pairs and $\gamma\gamma \rightarrow$ hadrons. Safety factors are included.

Chapter 8

Optimisation of the detector geometry

The high occupancies found in the analysis of beam-induced backgrounds, in some regions of CLICdet, call for modifications to the detector layout. On the other hand, low occupancies found in the vertex detector for the 380 GeV centre-of-mass energy stage lead to studying the vertex detector layout, with the aim of reducing the inner radius of the vertex barrel and thus improving the impact parameter resolution of CLICdet. These studies are discussed in the first part of this section. Proposed changes in the vertex detector, BeamCal, HCal endcap and MuonID endcap regions are then described. These changes include modifying the acceptance, increasing the granularity or introducing additional shielding.

8.1 Vertex detector

The hit densities and occupancy levels in the vertex detector at 380 GeV are significantly below the 3% limit. Therefore, either the sensor pitch requirements can be eased from $25 \times 25\,\mu\text{m}^2$ to about $40 \times 40\,\mu\text{m}^2$, or the vertex detector can be placed closer to the interaction point. The sensor design change is disfavoured, as it would be detrimental to the resolution of the vertex reconstruction. Alternatively, a reduction of the inner radius of the vertex barrel detector can be envisaged, which will be beneficial for impact parameter resolution.

The lower limit ensuring the safety of the vertex detector comes from the transverse distribution of the SR photons (see Figure 6.12). The central beam pipe aperture cannot be smaller than the QD0 aperture to ensure the safe transport of the SR photons in the detector region. At 380 GeV, this aperture is 17.5 mm.

The inner radii of the first double layer of the vertex barrel and central beam pipe are simultaneously reduced. Special attention is made to connect the conical beam pipe element with the central beam pipe. The 7° opening angle of the conical beam pipe is not maintained, due to software implementation of the detector model. As a result, the conical beam pipe does not point towards the IP for lower radii of the central beam pipe than 31 mm, that increases the probability of scattering of direct particles produced at the IP. Therefore, the used implementation and obtained results represent a worst-case scenario.

The occupancy distribution as a function of the inner radius of the first double layer is shown in Figure 8.1(left). Initially, between 31 mm and 25 mm, the occupancy increases linearly, with a shallow slope represented by the blue line. Below 25 mm, the occupancy increases with a significantly steeper slope, represented by the red line. The acceptable limit of 3% per bunch

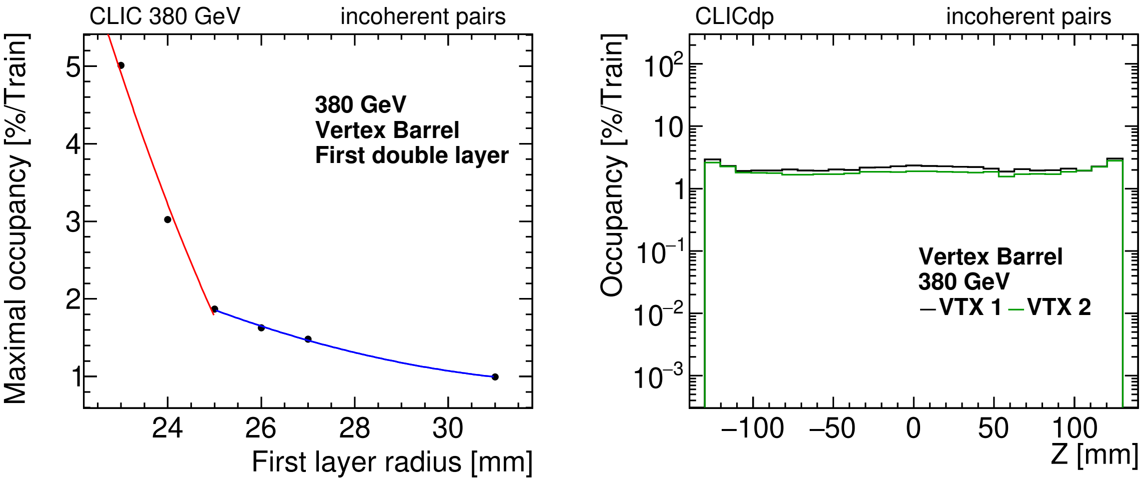

Figure 8.1: Distribution of the occupancy as a function of the inner radius of the first double layer of the vertex detector at 380 GeV coming from incoherent electron–positron pairs (left) and a longitudinal distribution averaged over $r\phi$ of the occupancy when 24.5 mm inner radius is assumed (right). The red line is a second order polynomial fit to the points between 22 mm and 25 mm, and the blue line is the same function fitted in the range between 25 mm and 31 mm. Safety factors are included.

train is reached at the radius of about 24 mm. The change of slope is caused by encountering of a high density of incoherent pairs, that have a parabolic distribution in this region [60]. The optimised radius of 24.5 mm is slightly lower than the value estimated in the previous study for the 500 GeV energy stage (25 mm) [60]. However, the presented results are obtained using the full detector simulations that are more robust in comparison with the fast simulations used for 500 GeV.

The longitudinal distribution of the occupancy in the case where the inner radius of 24.5 mm is used is shown in Figure 8.1(right). In comparison with the 31 mm radius, as shown in Figure 7.7(left) in section 7.1.1, the occupancy increases especially at the edges of the barrel. This is caused by the angular and transverse momentum distribution of the incoherent pairs.

8.2 BeamCal layout

The BeamCal in CLICdet was optimised for the 3 TeV beam conditions with $L^* = 3.5\,\mathrm{m}$, where the last quadrupole was placed inside of the detector. The extension of the L^* from 3.5 m to 6 m changed the beam conditions in the BeamCal region, and the impact of this modification on the required aperture has to be taken into account. The other reason to consider a geometry modification of the BeamCal is the difference in the transverse beam sizes, which at 380 GeV are around three times larger than at 3 TeV (see Table 2.1).

The inner radius of the incoming beam pipe in the BeamCal region in CLICdet is 2.7 mm [14]. This is found to be below the radius required to ensure safety of the machine and beam stability when the resistive wall effects are taken into account [69]. The lower limit of the beam pipe radius comes from minimising the impact of the resistive wall wakefield and machine safety. The machine safety is understood as the depth to which the beam halo has to be collimated to ensure that particles that can contribute to the backgrounds in the detector region are removed. The collimation depth coefficients of $15\sigma_x, 55\sigma_y$ were chosen to be the same at both energy stages and to be equal with the previously used values for the 3 TeV and 500 GeV Beam Delivery System designs [70]. Taking both the collimation depth requirements and the resistive wall effect into account in the necessary increase of the inner radius of the incoming beam pipe to 7 mm at 3 TeV and 17.5 mm at 380 GeV.

The synchrotron radiation also poses a limitation on the minimum beam pipe radius. The photon distribution, which includes photons reflected from the vacuum chamber walls, has a transverse size similar to the inner diameter of the vacuum chamber at the exit of the QD0 magnet [92]. To ensure the safe passage of the synchrotron radiation and minimise the effect of possible scattering, the beam pipe aperture in the BeamCal should not be smaller than the size of the transverse distribution of the synchrotron radiation photons. The proposed values of the inner radii taking into account the synchrotron radiation are: 7.6 mm at 3 TeV and 17.5 mm at 380 GeV, which are similar to those determined from the resistive wall wakefield study [69]. The increase in the incoming beam pipe radius results in a reduction of the BeamCal sensitive area of the BeamCal by 1.4% at 3 TeV and by 8.6% at 380 GeV.

The use of smaller aperture of the incoming beam pipe in the BeamCal region could be possible if the beam halo effect was minimised and a dedicated synchrotron radiation mask was placed upstream from the BeamCal. A design of such an element can use the approach used in LEP2 [97, 100]. An SR mask will limit the flux of reflected synchrotron radiation in the detector acceptance, although the photon interactions with the mask material and the impact on the occupancy levels would have to be studied.

The second modification of the BeamCal is the result of the BeamCal efficiency study [36]. It was found that the LumiCal creates a ‘shadow’ on the outermost part of BeamCal, such that particles coming from the IP with polar angles larger than 38 mrad can not reach BeamCal. As a result, the BeamCal in this region receives a negligible number of hits from high energy electrons and a reduction in the radius is possible without a negative impact on its performance. Such a reduction in angular acceptance has the benefit of providing additional space between BeamCal and the HCal endcap, which can be used to introduce additional shielding of the latter. The BeamCal acceptance reduction takes into account the edge of the shadowed region at 38 mrad and a safety margin of one Moliere radius in tungsten of 9.3 mm. As a result the BeamCal angular acceptance has been reduced to 41 mrad from 46 mrad, corresponding to a change of the outer radius from 150 mm to 130 mm.

8.3 HCal endcap

The occupancies in the HCal endcaps described in section 7.2.2 are unacceptably high at both of the considered energy stages. The maximal allowable occupancy can be deduced from the need to avoid confusion during reconstruction. Two hits should not be located next to each other on a 3×3 cell grid, which can be achieved on average with an occupancy lower than $1/9 = 11\%$. At 380 GeV, the region with occupancies surpassing 10% ranges from 250 mm to 450 mm radially, while at 3 TeV this region reaches up to 700 mm.

There are several possible ways to reduce the occupancy in the most impacted region, based on the understanding of the origin of the backgrounds, as well as on the parameters defining the occupancy (see Equation (3.5). One solution is to make the time slices shorter, allowing for a lower number of hits to be integrated in each time window. An alternative option is to increase the calorimeter's granularity which would decrease the number of hits per cell. It is possible to reduce the occupancy levels without changing the HCal parameters, through the use of shielding that could protect the HCal endcap from the influx of unwanted particles. It can be expected that the approach yielding the best outcome consists of a combination of the methods described above. For combination of methods, the most promising solution from each of the studied mitigations is chosen, taking into account the existing constraints.

In the search for the optimal solution to the high occupancy issue, the existing physical and technical constraints need to be identified and taken into account. One constraint comes from the space available for shielding. There is 80 mm radially between the BeamCal and the inner radius of the HCal endcap between layers 9 to 60 that can be filled with shielding material. It is possible to have a thicker shield in the region not occupied by other systems, e.g. between the longitudinal position of 3500 mm (outer edge of the BeamCal) to 5700 mm (outer edge of the return yoke). Alternatively, the shield can be extended radially into the region currently occupied by the HCal endcap at the cost of acceptance. This approach would be proposed only if other methods did not lead to a sufficiently large reduction of the occupancy.

The length of time slices also cannot be changed freely and has a lower bound at around 10 ns, due to the limits in the current state-of-art electronics, signal pile-up and power consumption [101]. Time slices shorter than 10 ns face issues of collecting enough charge to generate a signal in the given time frame.

The granularity can only be increased to the point where manufacturing and read-out of small sizes of scintillator-based cells are not viable. Recent studies indicate that the limit is around cell sizes of 1 cm^2 [102], and smaller cells require the use of silicon sensors. An example of these limits is the design of CMS HGCal, where minimal scintillator-based cells of 4 cm^2 are used, below which the silicon sensors are employed [103].

8.3.1 Varying time slicing

The impact on the occupancy of varying the time slicing is shown in Figure 8.2. The occupancy at the lowest radii is lower than 100% when the time slices are shorter than 200 ns due to lower energy per time window deposited in the cells located in this region, as the electromagnetic shower develops in the calorimeter. The reduction in the maximal occupancy is limited. Only

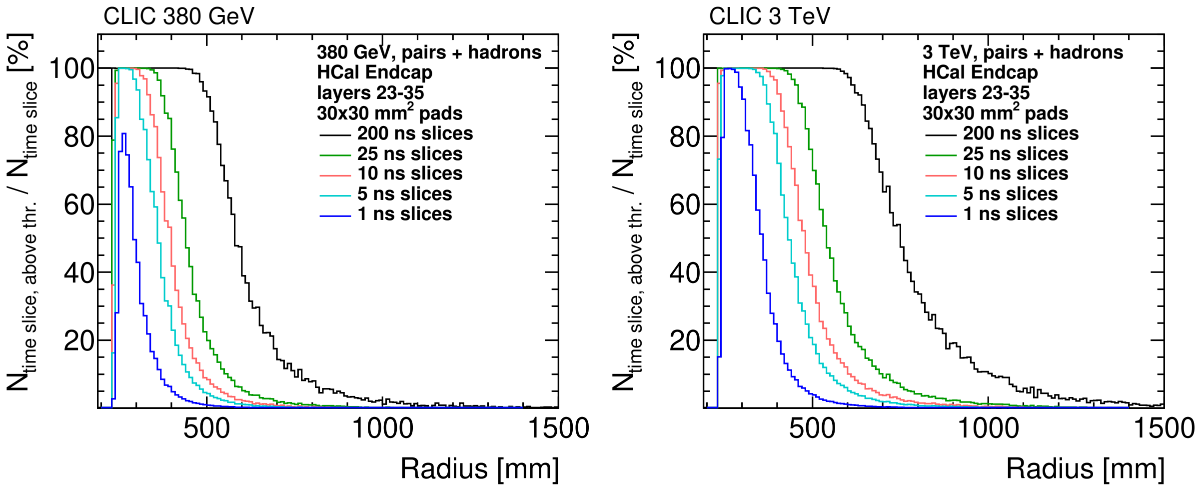

Figure 8.2: Radial distributions of the occupancy per time slice, with varying time per slice, in the HCal endcap at 380 GeV (left) and 3 TeV (right) from incoherent electron–positron pairs and $\gamma\gamma \rightarrow$ hadrons with different assumptions about the integration time window length. Safety factors are included.

Table 8.1: The maximal and average values of the HCal endcap occupancy with different time slicing assumptions at 380 GeV and 3 TeV. 200 ns is used for data rates estimate and 25 ns is assumed in the occupancy calculation. The granularity is $30 \times 30\,\mathrm{mm}^2$. Safety factors are included.

	380 GeV		3 TeV	
	max [%]	average [%]	max [%]	average [%]
200 ns	100	3.3	100	6.0
25 ns	100	1.6	100	2.7
10 ns	100	1.1	100	1.9
5 ns	100	0.9	100	1.5
1 ns	80	0.4	100	0.8

slicing with an unrealistic value of 1 ns, that is comparable with the shower development time, limits the maximal occupancy to below 100% at 380 GeV. The maximum occupancy remains at 100% in all slicing scenarios at 3 TeV. The average occupancy values with different sampling times are presented in Table 8.1. The design of the HCal read-out is not currently finalised, but a time slice shorter than 10 ns would be challenging. A 10 ns time window length is chosen to be combined with other mitigation methods. The main disadvantage of decreasing the sampling time is a large increase of the data rates in the region where the high occupancy persists.

8.3.2 Varying granularity

The sensitivity to the variation of the pad sizes is presented in Figure 8.3. The increase in granularity has a limited impact on the maximal occupancy, while the average occupancy change more significantly, as shown in Table 8.2. The radial depth of the most impacted region is reduced with higher granularity, although the innermost cells still have high levels of occupancy, reaching saturation at both energy stages. The impact on data rates is also significant where the full saturation with background persists. The increase of granularity translates directly into a proportional increase in the data rate, e.g. by a factor of four with $15 \times 15\,\text{mm}^2$ pads and a factor 36 with the smallest pads considered in the region. In addition, cell dimensions of $5 \times 5\,\text{mm}^2$ require a change of the sensitive material from scintillator to silicon. For the $5 \times 5\,\text{mm}^2$ cells, the sensor thickness is assumed to be the same as what is proposed for the ECal, with 500 µm of silicon.

In conclusion, the modification in the granularity cannot be considered as a stand-alone solution to the high occupancy issue, as it does not reduce the maximal occupancy below the full saturation. Instead, the $15 \times 15\,\text{mm}^2$ scintillator cells and $5 \times 5\,\text{mm}^2$ silicon sensor cells are considered for combination with other methods.

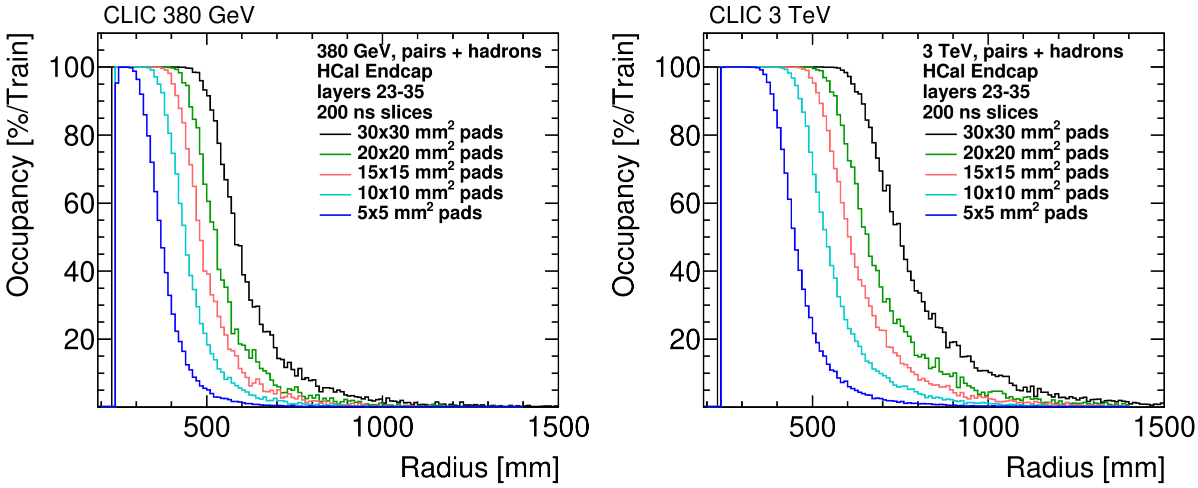

Figure 8.3: Radial distributions of the occupancy per bunch train in the HCal endcap at 380 GeV (left) and 3 TeV (right) from incoherent electron–positron pairs and $\gamma\gamma \rightarrow$ hadrons with different assumptions about the HCal cell sizes. Safety factors are included.

Table 8.2: The maximal and average values of the HCal endcap occupancy with different granularity assumptions at 380 GeV and 3 TeV. The $30 \times 30\,\text{mm}^2$ is the granularity assumed in the CLICdet model. 200 ns time slicing is used. Safety factors are included.

	380 GeV		3 TeV	
	max [%]	average [%]	max [%]	average [%]
$30 \times 30\,\text{mm}^2$	100	3.3	100	6.0
$20 \times 20\,\text{mm}^2$	100	2.4	100	4.3
$15 \times 15\,\text{mm}^2$	100	2.0	100	3.5
$10 \times 10\,\text{mm}^2$	100	1.5	100	2.6
$5 \times 5\,\text{mm}^2$ (Si sensors)	100	0.8	100	1.5

8.3.3 Introducing shielding

The shielding solution presented in this section is based on the experience with mitigating the background impact at 3 TeV on the CLIC_ILD detector design [98]. The beam conditions are comparable between the $L^* = 3.5\,\mathrm{m}$ and the current $L^* = 6\,\mathrm{m}$; however, the detector model has changed. The QD0 magnet has been removed and does not provide shielding for the HCal endcap, hence a new shield design needs to be proposed.

High energy photons and neutrons originating from incoherent pairs scattering in the BeamCal region impact the HCal endcap. This composition of background particles requires the use of materials with that have short radiation lengths to aborb or reduce the energy of photons, and materials with large concentration of hydrogen atoms to moderate the neutrons.

Various configurations and materials for the shield have been studied using a simplified model of a shield implemented in GEANT4. Simulations were performed with photon and neutron beams travelling perpendicular to the shield, and with the energy distributions that are expected to be produced in the vicinity of the HCal endcap [98]. The goal was to minimise the energy flux leaking through the shield from both of the sources, taking into account the space limitations present between the BeamCal and the HCal endcap. The results show that a monolithic shield made of either a short radiation length material, such as lead or tungsten, or a neutron absorber such as polyethylene cannot shield the HCal endcap effectively from the unwanted particles. The best solution found is a two-layer composite approach: a layer of tungsten or lead in the innermost region, with a mixture of polyethylene and boron carbide on the outside, as shown in Figure 8.4. The maximal thickness of the shield that can be fitted between the modified BeamCal and the HCal endcap without reducing the HCal acceptance is around 80 mm. It was also found that extending the radius of the neutron absorbing material beyond 50% of the short radiation length material does not improve the shielding efficiency.

The best solution is a 50 mm layer tungsten and a 30 mm layer of 5%-borated high-density polyethylene, such as SWX-201HD [104]. The proposed shield starts at a longitudinal position of 2720 mm and extends to the end of the yoke at 5700 mm.

The radial occupancy distributions in the HCal with various shields installed coming from full detector simulations are shown in Figure 8.5. The presence of a shield significantly reduces the region with 100% occupancy, and the average occupancy levels, which are shown in Table 8.3. The use of lead as the short radiation length material shows slightly lower shielding efficiency than tungsten. Taking into account the ease of manufacturing and price considerations, lead is more favourable as the choice for the shielding material. The 80 mm shield with lead allows one to reduce the outer radius of the most impacted region from 650 mm to 500 mm at 380 GeV and from 700 mm to 600 mm 3 TeV. This shield also reduces the reconstructed energy in the HCal endcap, as summarised in Table 8.4. The use of shielding significantly reduces the energy in the HCal at both energy stages, especially the depositions caused by the incoherent pairs, and to a lesser extent by the $\gamma\gamma \rightarrow$ hadron events. The occupancy level remains high and it is not possible to fully mitigate the occupancy issue using shielding alone.

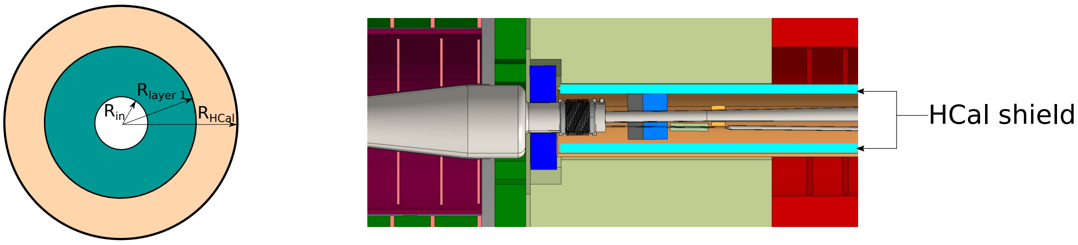

Figure 8.4: Layout of the proposed HCal shield (left) and the shield position in the CLICdet forward region (right). $R_{\text{in}} = 168\,\text{mm}$, $R_{\text{layer 1}}$ is design dependent, and R_{HCal} is the inner radius of the HCal less 2 mm and is also design dependent; a maximal shield that can be fitted without impacting the HCal acceptance has $R_{\text{HCal}} = 248\,\text{mm}$.

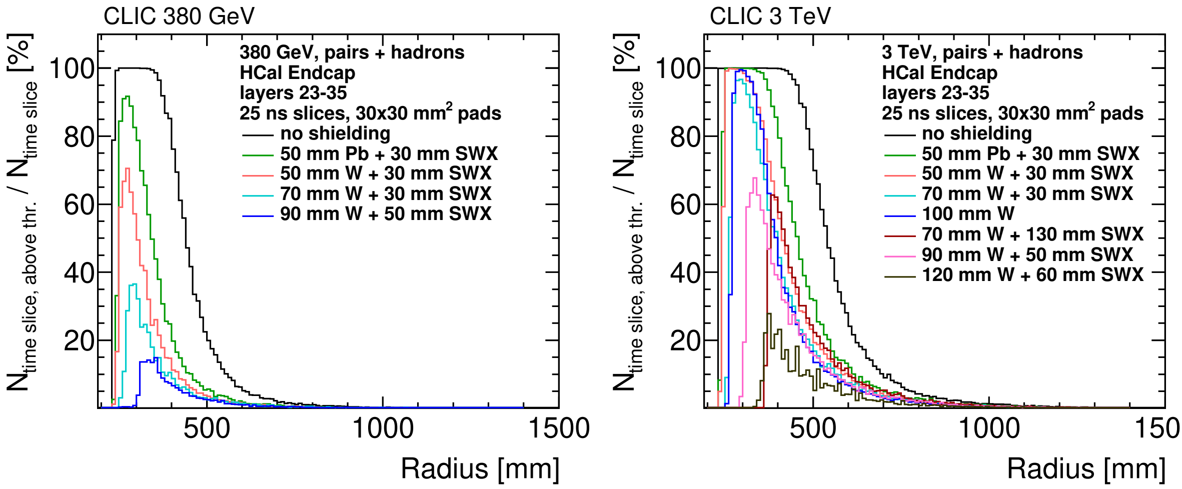

Figure 8.5: Distribution of the occupancy per time slice, with time slices of 25 ns, in the HCal endcap at 380 GeV (left) and 3 TeV (right) from incoherent electron–positron pairs and $\gamma\gamma \rightarrow$ hadrons with different assumptions about the proposed shielding between the outgoing beam pipe and the HCal endcap. Safety factors are included.

Table 8.3: The maximal and average values of the HCal endcap occupancy with different shielding assumptions at 380 GeV and 3 TeV. Assumed are $30 \times 30\,\text{mm}^2$ cell sizes and 200 ns integration time with one time window. Safety factors are included.

	380 GeV		3 TeV	
	maximum [%]	average [%]	maximum [%]	average [%]
no shield	100	3.3	100	6.0
50 mm W + 30 mm SWX	100	1.4	100	4.0
50 mm Pb + 30 mm SWX	100	1.9	100	4.4
70 mm W + 30 mm SWX	100	1.1	100	2.7
90 mm W + 50 mm SWX	100	0.8	100	3.5

Table 8.4: The reconstructed energy in the HCal endcap at 380 GeV and 3 TeV with and without the shielding, taking into account the energy calibration factors. Safety factors are not included.

	380 GeV		3 TeV	
	incoherent pairs [TeV]	$\gamma\gamma \to$ hadrons [TeV]	incoherent pairs [TeV]	$\gamma\gamma \to$ hadrons [TeV]
no shielding	75.3	0.14	310.4	7.7
50 mm Pb + 30 mm SWX	3.5	0.11	15.1	5.5
Deposit reduction [%]	95	21	95	29

8.3.4 Combining mitigation measures

The occupancy level can be best improved if the mitigation methods presented above are combined. The following parameters are combined for an optimised mitigation: $15 \times 15\,\mathrm{mm}^2$ or $5 \times 5\,\mathrm{mm}^2$ cell sizes, 10 ns time slices, and the 50 mm of tungsten or lead shield with 30 mm of polyethylene. The results of combining these assumptions are shown in Figure 8.6; the average and maximal occupancies for all HCal endcap layers are shown in Table 8.5.

The combined effect of the increase in granularity by a factor of four with either the increase of the number of time slices or the implementation of shielding allows for a reduction of the average occupancy by a factor of around four at both energy stages. However, it does not reduce the maximal occupancy below full saturation.

When all of the proposed approaches are combined they provide substantial mitigation of both the maximal and average occupancy at both energy stages, reducing the average occupancy to 1.5% and 5.7% of their unmitigated value at 380 GeV and 3 TeV respectively.

Further reduction of the maximal value of the occupancy can be achieved by reducing the cell sizes in the HCal endcaps to $5 \times 5\,\mathrm{mm}^2$ and using silicon as the sensitive material. In this case, the occupancy at 380 GeV is at the desired level of below 11%, while it is still at 27.9% at 3 TeV due to the harsher background environment at this energy stage. A possible remedy could be to insert a thicker shield, with 70 mm or even 90 mm of lead. The disadvantage of this approach would be the reduction of the HCal endcap acceptance.

Table 8.5: The maximal and average values of the HCal endcap occupancy with different mitigation methods at 380 GeV and 3 TeV. Safety factors are included.
'Shield' denotes a shield composed of 50 mm of lead and 30 mm of SWX. '100 mm shield' considers the alternative shield for the 3 TeV energy stage with a thicker lead plate of 70 mm.

	380 GeV		3 TeV	
	max [%]	average [%]	max [%]	average [%]
no mitigation – 200 ns, $30 \times 30\,\mathrm{mm}^2$	100.0	3.30	100.0	6.01
$30 \times 30\,\mathrm{mm}^2$ + 7shield + 10 ns	65.4	0.15	98.9	0.65
$15 \times 15\,\mathrm{mm}^2$ cells + 10 ns	100.0	0.70	100.0	1.25
shield + $15 \times 15\,\mathrm{mm}^2$ cells + 200 ns	100.0	0.68	100.0	2.12
shield + $15 \times 15\,\mathrm{mm}^2$ cells + 10 ns	22.8	0.05	73.0	0.34
shield + $5 \times 5\,\mathrm{mm}^2$ Si cells + 10 ns	8.1	0.01	27.9	0.05
100 mm shield + $5 \times 5\,\mathrm{mm}^2$ Si cells + 10 ns	3.1	0.01	11.1	0.02

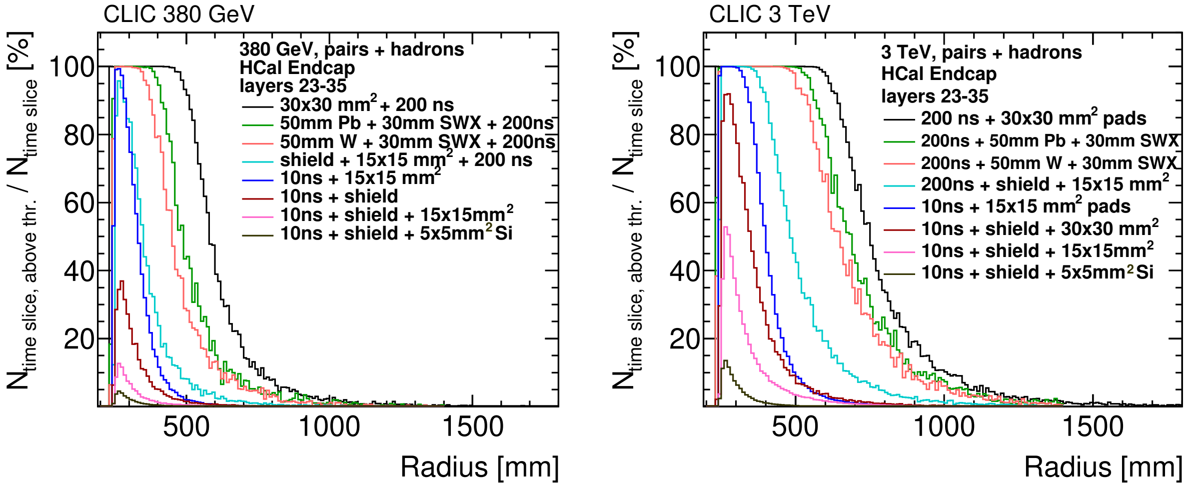

Figure 8.6: Distribution of the occupancy per time slice, with time slices of 10 ns, in the HCal endcap at 380 GeV (left) and 3 TeV (right) from incoherent electron–positron pairs and $\gamma\gamma \rightarrow$ hadrons with different mititgation methods applied. Safety factors are included. 'Shield' signifies the use of a composite shield made of 50 mm lead and 30 mm of SWX.

8.3.5 Two granularity regions

In the previous section, a mitigation approach is proposed that combines an increase in the number of time slices, higher granularity, and the use of shielding. From the radial distribution of the occupancy in Figure 8.6, it is clear that it is not necessary to implement the highly granular cells in the entire HCal endcap. Such a modification would increase the number of channels by a factor thirty-six, from 4.5 million to 162 million. In addition, it does not bring any further mitigation of the beam-induced backgrounds in regions further away from the inner edge. It is possible to split the HCal endcap into two regions of different granularity to optimise the number of channels and observed occupancy, in a similar fashion to the CMS HGCal design, although due to different reasons [103].

To find the optimal radial position for the transition between granularity regions, Figure 8.6

is used, in particular, the distributions with 10 ns slices and shielding. Following the target of having less than 11% occupancy, the transition radius is located at 430 mm at 380 GeV and at 500 mm at 3 TeV. Since it is envisioned to use the same calorimeter design at both energy stages, with the exception of the vertex detector and forward calorimeter region, the latter radius is chosen.

The inner region ('Inner HCal') is proposed to be built using $5 \times 5\,\mathrm{mm}^2$ cells with silicon sensors, and the outer region ('Outer HCal') uses $30 \times 30\,\mathrm{mm}^2$ cells with scintillator material. The silicon sensor and its PCB follow the implementation in the ECal [14], with 500 µm of silicon that replaces 3 mm of plastic scintillator, and a slightly thicker PCB of 1.3 mm instead of 1 mm. Due to the difference in the thickness of the used materials, a gap of 1.9 mm is created if the absorber plates are kept aligned. It is possible to fill the available space with additional stainless steel absorber, although it is not found to be beneficial to limit the occupancies. Instead, following the CMS HGCal design [103] this gap is filled with air. The implementation of the proposed design results in an increase in the number of channels from 4.50 million to 6.90 million (+53%) with the 80 mm shield or 6.76 million (+51%) with the 100 mm shield. The position of the Inner HCal and the layout of its layers are shown in Figure 8.7.

The radial distribution of the occupancy is shown in Figure 8.8, and the maximal and average occupancies over the entire HCal endcap are summarised in Table 8.6. The maximal occupancy at both energy stages is high due to the large number of backscattered particles created by incoherent pairs interactions with the material downstream. The high occupancy is concentrated in the last layer of the HCal and mostly impacts the lower granularity region. The influx of backscattered particles is reduced if the space between the beamline and the inner radius of the MuonID endcap is filled with shielding material and a cavern is added to the simulation model. A further reduction of the high occupancy is possible through the addition of shielding material in the available space between the inner radius of the proposed shield and the beamline (see Figure 8.4(right)). The average occupancy is higher than in the uniformly high granularity case when comparing the numbers in the last two rows of Table 8.5, due to the existence of two occupancy peaks: the first in the highly granular region and the second in the baseline granularity region. The second reason is the lower number of available cells in the design with two granularity regions in comparison with the design with uniform high granularity.

In summary, the best approach to reduce the high occupancy in the HCal endcap consists of simultaneous implementation of 100 mm composite shield, split into 70 mm of lead and 30 mm of polyethylene mixture, using time slices of 10 ns, and a reduction of cell sizes to $5 \times 5\,\mathrm{mm}^2$. This proposed solution is best implemented by splitting the HCal into two granularity regions where the design benefits from the increased granularity where it is the most needed while keeping the occupancy at acceptable levels.

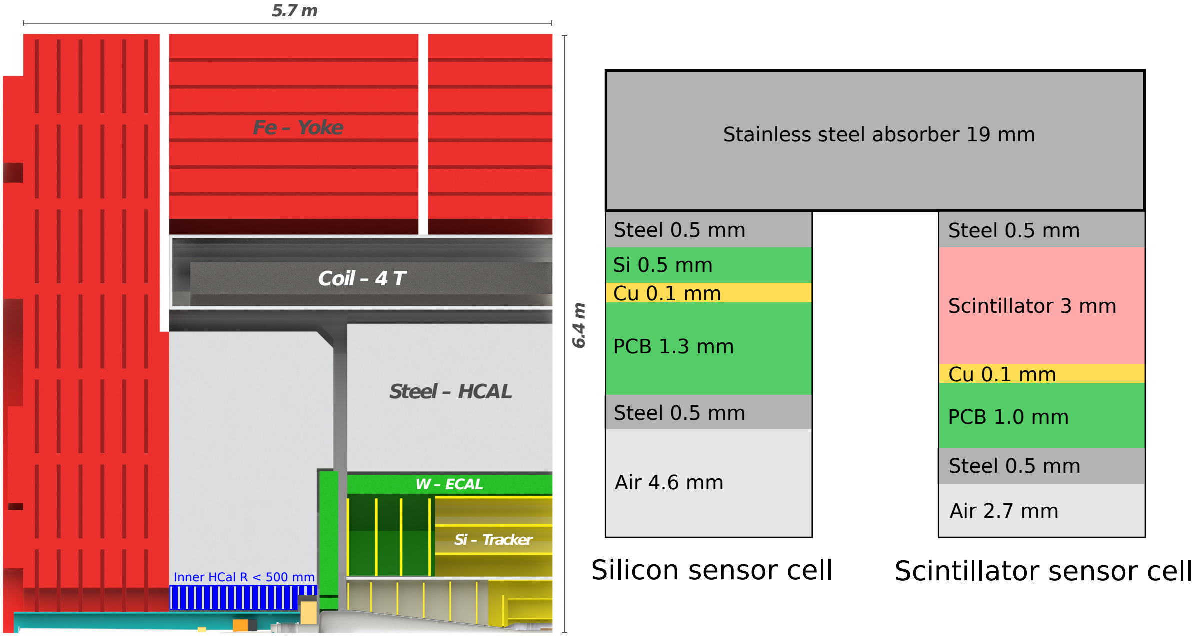

Figure 8.7: The region with higher granularity superimposed over the quarter top of the CLICdet layout (left) and schematic cross-section of cells with scintillator or silicon as sensitive materials (right). Safety factors are included.

Table 8.6: The maximal and average values of the occupancy with different mitigation method at 380 GeV and 3 TeV. Safety factors are included.
‘Option 1’ denotes a mitigation approach combining the use of 10 ns time slices, a shield composed of 50 mm of lead and 30 mm of SWX and 5 × 5 mm^2 silicon sensors.
‘Option 2’ is similar to ‘option 1’ however with a thicker lead plate of 70 mm instead of 50 mm.
‘w/cavern’ is the result where a large mass of concrete approximates the experimental cavern (see Figure 8.9(left)) in the simulation model.

	380 GeV		3 TeV	
	max [%]	average [%]	max [%]	average [%]
no mitigation	100.0	3.30	100.0	6.01
option 1 Inner HCal	7.6	0.63	27.0	2.63
option 1 Outer HCal	24.3	0.04	76.2	0.22
option 2 Inner HCal	2.9	0.25	11.1	1.14
option 2 Outer HCal	11.4	0.03	37.3	0.18
option 2 Outer HCal /w cavern	9.0	0.03	28.1	0.16

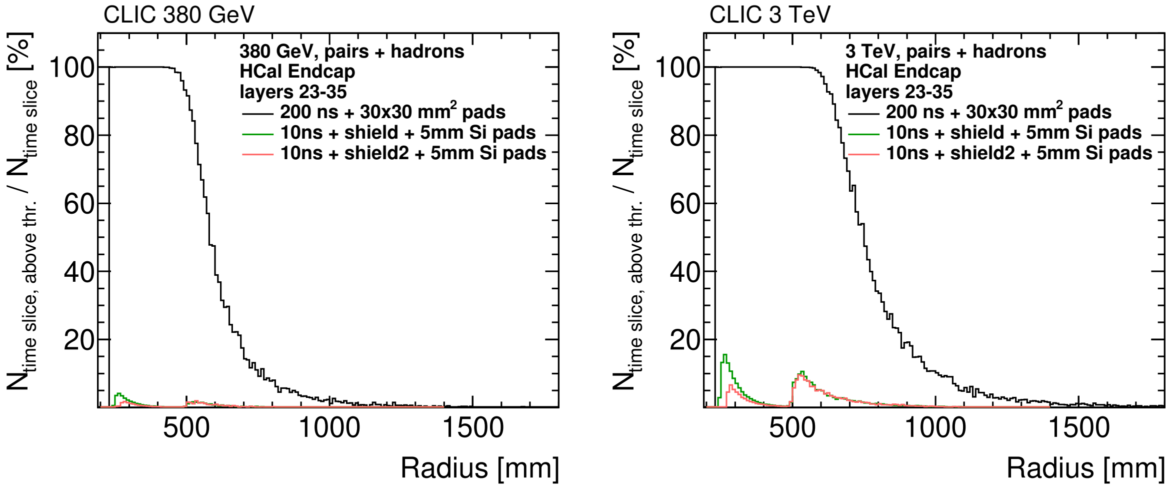

Figure 8.8: Distribution of the occupancy per time slice, with time slices of 10 ns, in the HCal endcap at 380 GeV (left) and 3 TeV (right) from incoherent electron–positron pairs and $\gamma\gamma \to$ hadrons with different mititgation methods applied. 'Shield' signifies use of a composite shield made of 50 mm lead and 30 mm mixture of polyethylene and boron carbide, while 'shield2' represents the same shield layout although with a thicker lead layer of 70 mm.

8.4 Muon Identification System endcap

The MuonID endcap detectors are severely impacted by the background particles at both 380 GeV and 3 TeV, in particular the sensors at the lowest radii of all layers. The main reason is that there is very little material between the subdetector's innermost sensors and the sources of unwanted particles. These particles come either directly from the IP, are a result of scattering in the BeamCal region or of interactions with the outgoing beam pipe. The latter is not expected to be a significant source of background in the real machine, due to the existence of an experimental cavern encompassing the detector.

It has been shown that an implementation of the cavern surrounded by concrete would lower the occupancy levels in the MuonID endcap [105]. For this reason, large volumes of concrete are added to the simulation model, in an attempt to approximate the detector cavern. The layout of the implementation is shown in Figure 8.9(left). The concrete volume starts directly outside the detector yoke at the radial distance from the IP of 6.7 m and longitudinal position of 5.8 m. A transition region between the detector region and the tunnel consists of a wall 0.4 m thick with an opening of radius 0.25 m, intended to fit the incoming and outgoing beam pipes and the QD0 magnet [12]. The tunnel aperture limits the background particles scattering off the outgoing beam pipe. A tunnel with a diameter of 5.6 m is added to the detector model [9]. The impact on the average occupancy levels in the MuonID endcap when the cavern described above is implemented is shown in Figure 8.10. At both energy stages, one can observe a significant reduction in the average occupancy in the last layer of the MuonID system, which is connected with a reduction in the flux of backscattered particles coming from downstream scattering outside of the detector. However, the maximal occupancies remain high, reaching saturation in all layers at the lowest radii at both energy stages. Different occupancy levels between the two options observed in layers 1 and 2 for 380 GeV energy stage results are due to statistical fluctuations.

The occupancy level can be further reduced in several ways. The granularity of the RPC cells can be increased or the readily available space can be used to install a shield. An increase in granularity by a factor of nine, resulting in cells of $10 \times 10\,\text{mm}^2$ allows for a reduction in the average occupancy by a factor of four and two at 380 GeV and 3 TeV respectively. The maximum occupancy is limited to under 40% at 380 GeV, however it remains at 100% at 3 TeV, as shown in Figure 8.11. The change in granularity does not provide sufficient mitigation on its own, although it could be considered an addition to the shielding solution.

The primary approach is to fill the available space between the inner radius of the support tube ($R = 250\,\text{mm}$) and the MuonID endcap inner radius (490 mm) with material that can shield the sensitive elements of the MuonID endcap, as shown in Figure 8.9(right). The results of this approach are shown in Figure 8.12. The proposed shield for the HCal endcap extends up to the end of the return yoke and can provide some additional shielding for the MuonID system as well. However, the sole use of the HCal shield does not provide a sufficient mitigation. The use of a composite shield, that combines both polyethene and steel or other short radiation length material, was also considered. However, it does not provide an improvement over the steel shield. The best result can be achieved with a combination of the HCal shield with a shield

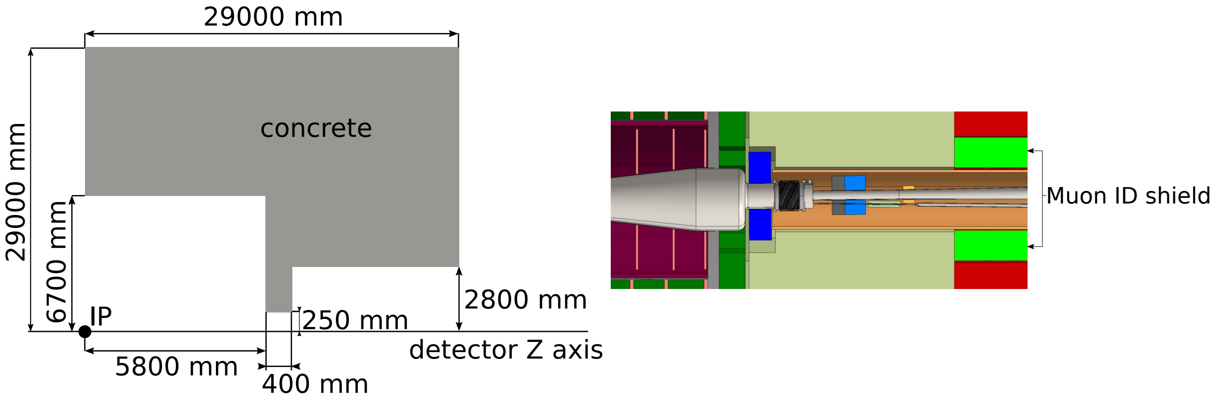

Figure 8.9: Schematic layout of the concrete volume around the CLICdet (left) and the proposed MuonID shield placement position in the CLICdet forward region (right).

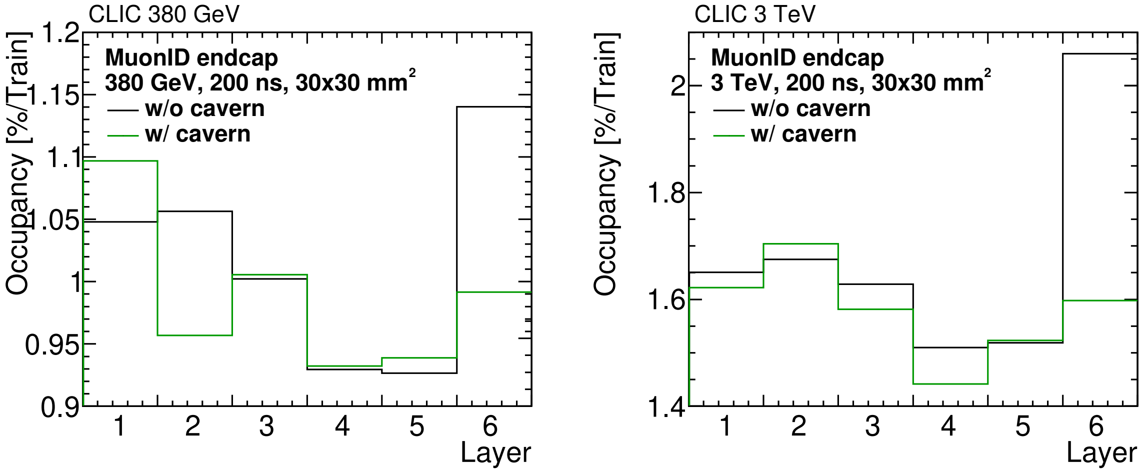

Figure 8.10: A comparison between the distributions of the average layer occupancy per bunch train in the Muon Identification System endcap at 380 GeV (left) and 3 TeV (right) from incoherent electron–positron pairs and $\gamma\gamma \to$ hadrons with or without the experimental cavern included in the simulation model6. Safety factors are included.

made of 240 mm of stainless steel. Such a shield allows limiting the maximal occupancy per layer of all layers to below 1% at 380 GeV and to below 5% at 3 TeV, using the same occupancy calculation method as in section 7.3 and cell sizes of $30 \times 30\,\text{mm}^2$.

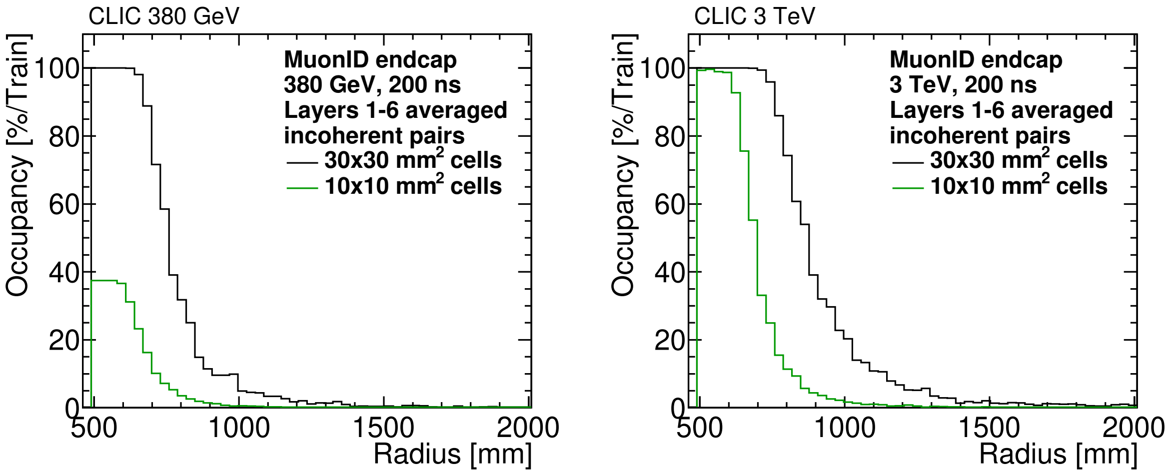

Figure 8.11: Distributions of the average layer occupancy per bunch train in the Muon Identification System endcap at 380 GeV (left) 3 TeV (right) from incoherent electron–positron pairs with two granularity options. Safety factors are included.

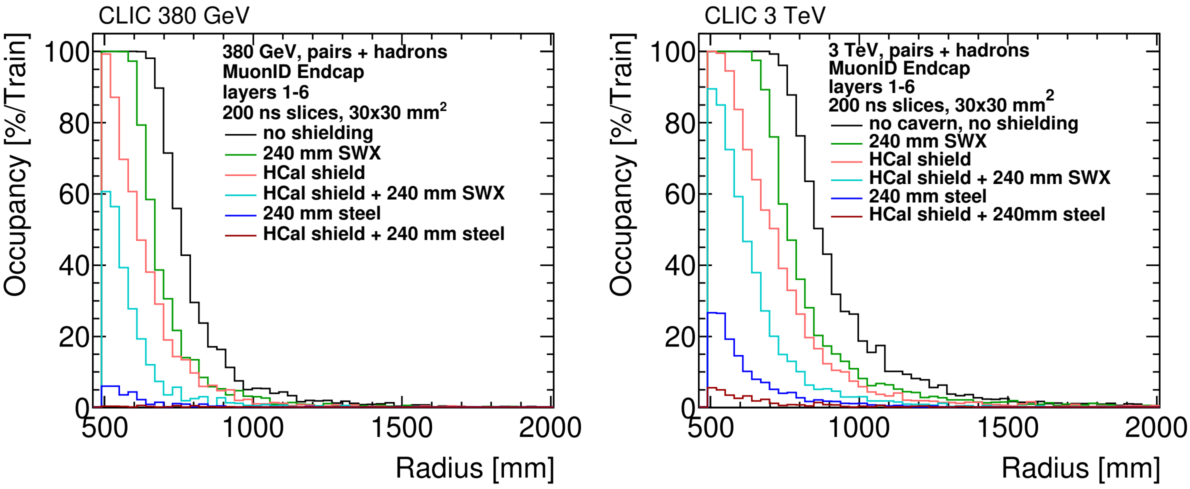

Figure 8.12: Distribution of the occupancy per bunch train in the MuonID endcap at 380 GeV (left) and 3 TeV (right) from incoherent electron–positron pairs and $\gamma\gamma \rightarrow$ hadrons with different shielding applied. 'HCal shield' signifies the shield proposed earlier for the HCal with 50 mm of lead and 30 mm of polyethylene. Safety factors are included.

Chapter 9

Summary and outlook

The results of the performance of the Beam Delivery System and the CLIC detector, taking into account the resistive wall wakefields, the emission of the synchrotron radiation and the impact of the beam-induced backgrounds have been presented.

The apertures in the CLIC Final Focus System have been optimised at two energy stages: 380 GeV and 3 TeV. The optimisation took into account the disturbances coming from the resistive wall wakefields and the aperture limit imposed by the use of normal-conducting quadrupole magnets. The impact of wakefields has been minimised by extending the apertures in the FFS by a uniform 44% at 380 GeV, and by varying the radii by a constant in the range from 3 mm to 5 mm, depending on the position in the accelerator, at 3 TeV. The result is a significantly reduced impact of the wakefields, which reduces luminosity losses caused by offsets, that are less challenging to correct by the intra-train beam feedback system.

The optimised beam pipes apertures were used as input in Synrad+ simulations of the synchrotron radiation reflections in the FFS. The radii extension does not impact the energy visible in the detector at 380 GeV, but it significantly increases the visible energy in the detector at 3 TeV, by around 40%.

The wholly absorbing walls provide optimal experimental conditions, where there are no SR photons in the acceptance of the detector. The materials that can be used for the vacuum chamber walls have non-negligible reflection probability up to a photon energy of about 30 keV. This leads to a large number of photons that travel significantly further along the accelerator and can interact with the sensitive material of the detector.

The power lost to the SR is negligible at 380 GeV with a total of 16 W and an average of 14 $\frac{\text{mW}}{\text{m}}$ along the BDS, while it is substantial at 3 TeV with the total power of 2.2 kW and the average power of 0.7 $\frac{\text{W}}{\text{m}}$. The heating caused by the SR photons interacting with the beam pipe material does not cause a significant increase of the temperature at 380 GeV while at 3 TeV, the heating is substantial and needs to be addressed by adedicated active cooling system, especially in the collimation region. The energy loss of the beam particles to the SR photons is negligible in comparison with the beam energy at both energy stages. However, the transverse beam sizes are significantly increased, lowering the luminosity performance.

The situation in the detector region at each energy stage is the opposite to the severity of the impact in the BDS. At 380 GeV, the SR photons cause large hit rates in the vertex and tracker detectors, while their impact in the BDS is negligible. At 3 TeV, the heating in the BDS is significant, while the hit rates coming from full detector simulations using GEANT4 are lower than at 380 GeV, due to the aperture limitations in the BeamCal region.

The occupancy in the vertex detector at 380 GeV is significantly above the 3% limit, even when the copper vacuum chamber surface is rough with an average roughness of 1 µm. Using a smoother surface with 100 nm average roughness leads to occupancies reaching 100% in the vertex barrel and endcaps. At 3 TeV, the occupancies reach 10% for the first double layer when the 100 nm roughness is used, and is below 1% when the roughness is 1 µm. For both energy stages, the hit rates are significantly lower in the tracker barrel and endcaps. The thick walls of the conical beam pipe shield the endcap disks. Most of the tracker barrel layers are not directly visible from the QD0 exit and every hit that they receive comes from a photon that had to scatter while traversing the material of the detector. This significantly lowers the probability of receiving a hit.

The high occupancies render the vertex detector unusable and significantly deteriorate the performance of the tracker. The non-reflective vacuum chamber surface in the FFS provides the desired experimental conditions, thus approaches based on reducing the reflectivity offer mitigation of the high photon fluxes. A reduction of reflectivity can be achieved by increasing the roughness of the surface or by the implementation of a saw-tooth absorber similar to the LHC design. It is sufficient to cover the final 30 m of the FFS to achieve the same outcome as if the vacuum chamber walls were wholly absorbing along the entire FFS. However, the roughness increase or the installation of a saw-tooth absorber increases the impedance and leads to stronger wakefields that decrease the quality of the beam. To counteract the increase of wakefields, the saw-tooth can be placed in an extruded arm of the circular beam pipe, creating a 'winglet' shape that is foreseen to be used in the vacuum system of the FCC-ee. The result of the implementation of this approach is the absence of the SR photons in the detector acceptance and the optimal experimental conditions.

The impact of beam-induced backgrounds, in particular the incoherent pairs and $\gamma\gamma \rightarrow$ hadron events on the CLIC detector has been studied at two energy stages of 380 GeV and 3 TeV.

The hit densities and occupancy levels have been estimated in the vertex and tracker detectors. The occupancies do not surpass the 3% level, and at 3 TeV are consistent with CLIC_ILD results. The time structure of the hits has been analysed. Most of the hits in the vertex detector are direct, while the tracker is relatively more impacted by particles backscattered in the forward calorimeter region. From the hit density and occupancy level stance, it is feasible to use either the $300 \times 30\,\mu\text{m}^2$ pixel sensor for the tracker or the strixels. In the latter case, the maximal and average occupancies would be higher but at acceptable levels.

The energy depositions and occupancy levels have been estimated for calorimeter barrel and endcap regions. The calorimeter barrel receives a few hits per bunch crossing, and the maximal occupancies at both energy stages are significantly below 1% in both the ECal and the HCal. The situation is different in the calorimeter endcaps that receive significant energy depositions in the order of TeV. The ECal endcap is impacted chiefly by incoherent pairs at 380 GeV and by both incoherent pairs and $\gamma\gamma \rightarrow$ hadron events at 3 TeV. The maximal occupancy reaches 1% and 7% respectively, when 25 ns time slices are used. The HCal endcap suffers from high fluxes of background, reaching 100% occupancy at a radius below 400 mm at 380 GeV and below 500 mm at 3 TeV.

Various mitigation approaches have been investigated, including varying the time slice length, increasing the granularity of sensitive elements and implementation of shielding. The best solution involves simultaneous use of 10 ns time slices, increased granularity with $5 \times 5\,\text{mm}^2$ silicon-sensor cells and implementation of a 100 mm composite shield. The proposed shield is made of two layers of materials. The inner layer is made of 70 mm of lead, and the outer layer consists of 30 mm of borated polyethylene. The shield is placed between the BeamCal and HCal endcap and reduces the acceptance of the subdetector by increasing the inner radius of the HCal endcap by 20 mm. The high granularity needs to be implemented only in the innermost region, at radius below 500 mm. Therefore, it is proposed for the HCal endcap to be split into two granularity regions: high granularity close to the beamline and the $30 \times 30\,\text{mm}^2$ granularity in the outer region. This way, the number of channels increases by 50% in comparison with the baseline CLICdet design, while the occupancy is kept at low levels.

The occupancy has also been estimated in the Muon Identification System. The barrel region, placed behind the barrel calorimeters, sees even fewer hits and most of the layers do not receive a single hit per bunch train from the beam-induced backgrounds. The conditions are different in the MuonID endcap, that is under a strong influence of the background particles and the maximal occupancy in the innermost region reaches 100%. An introduction of a simplified experimental cavern to the simulation model and filling of the available space between the inner radius of the MuonID endcap and the HCal endcap with stainless steel removes most of the unwanted particles. In the case where the HCal shield and the additional material in the MuonID system are implemented, the maximal occupancy does not surpass the 5% level.

The BeamCal outer radius has been reduced from 150 mm to 130 mm, as that region was shadowed by the LumiCal and did not receive hits from the high energy electrons or photons it is intended to measure. The acceptance reduction provides additional 20 mm of radial space that is used for shielding of the HCal endcap. In addition, the incoming beampipe radii have been optimised at both 380 GeV and 3 TeV to minimise the scattering of the synchrotron radiation in the BeamCal region. The proposed radii are 17.5 mm at 380 GeV and 7.6 mm at 3 TeV. As a result, the sensitive area of the BeamCal is reduced by 1.9% and 0.3% respectively.

The future works can expand on and use the results from the three parts of this study: the resistive wall wakefields, synchrotron radiation simulations and beam-induced backgrounds.

For the resistive wall wakefield study, dedicated simulations of the BDS collimation region at the 380 GeV energy stage can improve the precision of the predictions. The imperfections introduced to the beams in this region can increase the impact of the wakefields in the FFS and therefore require a separate optimisation.

The results of the simulations of the synchrotron radiation in the FFS can be used as input for the study of the active cooling of the beam pipe, which was found to be especially relevant at 3 TeV. Additional simulations in GEANT4 or FLUKA of the saw-tooth element should be pursued to optimise the height and thickness of the teeth fully for the CLIC synchrotron radiation energy spectrum.

Another subject where the simulations of the synchrotron radiation simulations can be improved in the future is an extension of the GEANT4 description of the low-energy photon physics. An implementation of the reflections to the *gamma* photon particle type in GEANT4 would allow one to obtain more reliable estimates of the hit rates from low energy ($E < 30\,\text{keV}$) photons in the detector.

For the study of beam-induced backgrounds, the most significant improvement can be made through the implementation of a more realistic hit recording algorithm. An addition of the time element and read-out window, similar to the implementation in the calorimeters, that resembles more the data acquisition in the future detector would improve the precision of the hit rates estimate.

All of the studies presented can be done also for the intermediate CLIC energy stage of 1.5 TeV. The only requirement is a design of the BDS lattice in a MADX or PLACET-compatible format.

List of Figures

List of Tables

Appendix A

Guinea-Pig configuration file

```
$ACCELERATOR:: CLIC380
{ energy     = 190 ;
  particles  = 0.52 ;
  beta_x     = 8.0 ;
  beta_y     = 0.1 ;
  sigma_z    = 70 ;
  emitt_x    = 0.95 ;
  emitt_y    = 0.03 ;
}
$ACCELERATOR:: CLIC350
{ energy     = 175;
  particles  = 0.364;
  beta_x     = 8.0;
  beta_y     = 0.1;
  sigma_z    = 70;
  emitt_x    = 0.95;
  emitt_y    = 0.03;
}
$ACCELERATOR:: CLIC3000
{ energy     = 1500 ;
particles  = 0.372 ;
beta_x    = 7.0 ;
beta_y    = 0.12 ;
sigma_z    = 44 ;
emitt_x    = 0.66 ;
emitt_y    = 0.02 ;
}

$PARAMETERS:: lumi
{
n_x=128;
n_y=640;
n_z=25;
n_t=1;
n_m=100000;
cut_x=12.0*sigma_x.1;
```

```
cut_y=64.0*sigma_y.1;
cut_z=3.0*sigma_z.1;
integration_method=2;
force_symmetric=0;
do_espread=1;
do_eloss=1;
beam_size=1;
electron_ratio=1.0;
ecm_min=0.99*energy.1*energy.2;
do_photons=1;
store_photons=2;
photon_ratio=1.0;
do_hadrons=3;
store_hadrons=1;
do_pairs=1;
track_pairs=1;
store_pairs=1;
do_prod=0;
grids=7;
load_beam=3;
charge_sign=-1.0;
do_lumi=7;
num_lumi=1000000;
num_lumi_eg=1000000;
num_lumi_gg=1000000;
store_beam=1;
do_coherent=1;
do_trident=1;
}
```

References

[1] M. Benedikt et al., *Future Circular Collider* (2018), CERN-ACC-2018-0058,
URL: `http://cds.cern.ch/record/2651300`.

[2] CEPC Study Group, *CEPC Conceptual Design Report: Volume 1 - Accelerator* (2018), IHEP-CEPC-DR-2018-01, arXiv: `1809.00285 [physics.acc-ph]`.

[3] G. Aad et al., *Observation of a new particle in the search for the Standard Model Higgs boson with the ATLAS detector at the LHC*, Phys. Lett. **B716** (2012) 1,
DOI: `10.1016/j.physletb.2012.08.020`, arXiv: `1207.7214 [hep-ex]`.

[4] S. Chatrchyan et al.,
Observation of a New Boson at a Mass of 125 GeV with the CMS Experiment at the LHC, Phys. Lett. **B716** (2012) 30, DOI: `10.1016/j.physletb.2012.08.021`,
arXiv: `1207.7235 [hep-ex]`.

[5] T. Behnke et al.,
The International Linear Collider Technical Design Report - Volume 1: Executive Summary (2013), arXiv: `1306.6327 [physics.acc-ph]`.

[6] R. Wilson, *The Stanford Two-Mile Accelerator*, Science **164** (1969) 674,
DOI: `10.1126/science.164.3880.674-a`.

[7] J. Seeman, *SLC beam dynamics issues*, AIP Conf. Proc. **255** (1992) 19,
DOI: `10.1063/1.42326`.

[8] R. Mutzner et al., *Multi-bunch effect of resistive wall in the Beam Delivery System of the Compact Linear Collider. Multi-bunch Effect of Resistive Wall in the CLIC BDS* (2010), CERN-ATS-2010-072, URL: `https://cds.cern.ch/record/1269903`.

[9] M. Aicheler et al.,
A Multi-TeV Linear Collider Based on CLIC Technology: CLIC Conceptual Design Report, CERN Yellow Report (2012), CERN, DOI: `10.5170/CERN-2012-007`,
URL: `http://cds.cern.ch/record/1500095`.

[10] A. Muennich, A. Sailer,
The CLIC ILD CDR Geometry for the CDR Monte Carlo Mass Production (2012), LCD-Note-2011-002, URL: `https://cds.cern.ch/record/1443543`.

[11] C. Grefe, A. Muennich,
The CLIC SiD CDR Detector Model for the CLIC CDR Monte Carlo Mass Production (2011), LCD-Note-2011-009, URL: `http://cds.cern.ch/record/1443533`.

[12] L. Linssen et al., *CLIC Conceptual Design Report: Physics and Detectors at CLIC*, CERN Yellow Report (2012), DOI: `10.5170/CERN-2012-003`, arXiv: `1202.5940 [physics.ins-det]`.

[13] P. Burrows, et al, *Updated baseline for a staged Compact Linear Collider* (2016), CERN-2016-004, URL: `http://dx.doi.org/10.5170/CERN-2016-004`.

[14] N. Alipour Tehrani et al., *CLICdet: The post-CDR CLIC detector model* (2017), CLICdp-Note-2017-001, URL: `https://cds.cern.ch/record/2254048`.

[15] H. Abramowicz et al., *Higgs physics at the CLIC electron–positron linear collider*, Eur. Phys. J. **C77** (2017) 475, DOI: `10.1140/epjc/s10052-017-4968-5`, arXiv: `1608.07538 [hep-ex]`.

[16] ATLAS Collaboration, *Standard Model Summary Plots Summer 2019* (2019), ATL-PHYS-PUB-2019-024, URL: `http://cds.cern.ch/record/2682186`.

[17] J. de Blas et al., *The CLIC Potential for New Physics* (2018), CERN-2018-009-M, DOI: `10.23731/CYRM-2018-003`, arXiv: `1812.02093 [hep-ph]`.

[18] M. Benedikt et al., *Future Circular Collider* (2018), CERN-ACC-2018-0057, URL: `http://cds.cern.ch/record/2651299`.

[19] P. N. Burrows et al., *The Compact Linear Collider (CLIC) - 2018 Summary Report*, CERN Yellow Report (2018), DOI: `10.23731/CYRM-2018-002`, arXiv: `1812.06018 [physics.acc-ph]`.

[20] M. Ge et al., *Low-temperature Baking and Infusion Studies for High-gradient ILC SRF Cavities*, Proc., 29th International Linear Accelerator Conference (LINAC18): Beijing, China, September 16-21, 2018, DOI: `10.18429/JACoW-LINAC2018-TUPO057`.

[21] M. Aicheler et al., *The Compact Linear Collider (CLIC) - Project Implementation Plan*, CERN Yellow Report (2019), DOI: `10.23731/CYRM-2018-004`, arXiv: `1903.08655 [physics.acc-ph]`.

[22] H. Abramowicz et al., *Top-Quark Physics at the CLIC Electron-Positron Linear Collider* (2018), arXiv: `1807.02441 [hep-ex]`.

[23] Compact Linear Collider Project, *CLIC accelerator schematic diagrams* (2019), OPEN-PHO-ACCEL-2019-002, URL: `https://cds.cern.ch/record/2655160`.

[24] A. Latina, P. Eliasson, D. Schulte, *Implications of a Curved Tunnel for the Main Linac of CLIC* (2006), URL: `http://cds.cern.ch/record/971881`.

[25] R. Corsini, *Experimental Verification of the CLIC Two-beam Scheme, Status and Outlook*, Conf. Proc. **C1205201** (2012) 1101, URL: `https://cds.cern.ch/record/1464099`.

[26] V. B. A. Novohatsky, V. Smirnov, Proc., 12th International Conference on High-Energy Accelerators, HEACC 1983, Fermilab, Batavia, IL, 1984, p. 119, URL: `http://www-spires.fnal.gov/spires/find/books/www?cl=QC786.IN81::1983`.

[27] N. Blaskovic Kraljevic, D. Arominski, D. Schulte, *Intra-Bunch Energy Spread Minimisation for CLIC Operation at a Centre-of-Mass Energy of 350 GeV*, Proc., 10th International Particle Accelerator Conference (IPAC2019): Melbourne, Australia, May 19-24, 2019, DOI: `10.18429/JACoW-IPAC2019-MOPMP016`.

[28] S. Kuroda, *ATF2 for Final Focus Test Beam for Future Linear Colliders*, Nucl. Part. Phys. Proc. **273-275** (2016) 225, DOI: `10.1016/j.nuclphysbps.2015.09.030`.

[29] T. Okugi, *Achievement of Small Beam Size at ATF2 Beamline*, Proc., 28th International Linear Accelerator Conference (LINAC16): East Lansing, Michigan, September 25-30, 2016, DOI: `10.18429/JACoW-LINAC2016-MO3A02`.

[30] P. Burrows et al., *Progress towards Electron-beam Feedback at the Nanometre Level at the Accelerator Test Facility (ATF2) at KEK*, Proc., 6th International Particle Accelerator Conference (IPAC 2015): Richmond, Virginia, USA, May 3-8, 2015, DOI: `10.18429/JACoW-IPAC2015-MOPTY083`.

[31] A. C. Dexter et al., *CLIC crab cavity design optimisation for maximum luminosity*, Nucl. Instrum. Meth. **A657** (2011) 45, DOI: `10.1016/j.nima.2011.05.057`.

[32] I. R. R. Shinton et al., *Beam dynamic simulations of the CLIC crab cavity and implications on the BDS*, Nucl. Instrum. Meth. **A657** (2011) 126, DOI: `10.1016/j.nima.2011.05.059`.

[33] G. L. Bayatian et al., *CMS Physics: Technical Design Report Volume 1: Detector Performance and Software* (2006), CERN-LHCC-2006-001, URL: `https://cds.cern.ch/record/922757`.

[34] J. S. Marshall, A. Muennich, M. A. Thomson, *Performance of Particle Flow Calorimetry at CLIC*, Nucl. Instrum. Meth. **A700** (2013) 153, DOI: `10.1016/j.nima.2012.10.038`, arXiv: `1209.4039 [physics.ins-det]`.

[35] D. Dannheim et al., *Detector Technologies for CLIC*, CERN Yellow Report (2019), DOI: `10.23731/CYRM-2019-001`, arXiv: `1905.02520 [physics.ins-det]`.

[36] D. Arominski et al., *A detector for CLIC: main parameters and performance* (2018), CLICdp-Note-2018-005, URL: `http://cds.cern.ch/record/2649437`.

[37] A. Oeftiger, *An Overview of PyHEADTAIL* (2019), CERN-ACC-NOTE-2019-0013, URL: `http://cds.cern.ch/record/2672381`.

[38] D. Schulte, *Beam-Beam Simulations with GUINEA-PIG* (1999), CERN-PS-99-014-LP, URL: `http://cds.cern.ch/record/382453`.

[39] A. Latina et al., *Improvements in the Placet tracking code*, Conf. Proc. **C1205201** (2012), URL: `http://cds.cern.ch/record/1463325`.

[40] R. Kersevan, M. Ady, *Recent Developments of Monte-Carlo Codes Molflow+ and Synrad+*, Proc., 10th International Particle Accelerator Conference, Melbourne, Australia, May 19-24, 2019, DOI: `10.18429/JACoW-IPAC2019-TUPMP037`.

[41] M. Frank et al., *DD4hep: A Detector Description Toolkit for High Energy Physics Experiments*, J. Phys. Conf. Ser. **513** (2014) 022010, DOI: `10.1088/1742-6596/513/2/022010`.

[42] C. Grefe et al., *ILCDIRAC, a DIRAC extension for the Linear Collider community*, J. Phys.: Conf. Ser. **513** (2013) 032077, DOI: `10.1088/1742-6596/513/3/032077`.

[43] I. Antcheva et al., *ROOT: A C++ framework for petabyte data storage, statistical analysis and visualization*, Comput. Phys. Commun. **180** (2009) 2499, DOI: `10.1016/j.cpc.2009.08.005`, arXiv: `1508.07749 [physics.data-an]`.

[44] O. Tange, *GNU Parallel - The Command-Line Power Tool*, The USENIX Magazine **36** (2011) 42, DOI: `http://dx.doi.org/10.5281/zenodo.16303`.

[45] L. Robertson, *Computing Services for LHC: From Clusters to Grids*, From the web to the grid and beyond: Computing paradigms driven by high-energy physics, DOI: `10.1007/978-3-642-23157-5_3`.

[46] *MADX - Methodological Accelerator Design*, Accessed: 12.05.2021, URL: `http://madx.web.cern.ch/madx/`.

[47] B. L. Henke, E. M. Gullikson, J. C. Davis, *X-Ray Interactions: Photoabsorption, Scattering, Transmission, and Reflection at E = 50-30,000 eV, Z = 1-92*, Atom. Data Nucl. Data Tabl. **54** (1993) 181, DOI: `10.1006/adnd.1993.1013`.

[48] E. Gabriel et al., *Open MPI: Goals, Concept, and Design of a Next Generation MPI Implementation*, Proc., 11th European PVM/MPI Users' Group Meeting, Budapest, Hungary, 2004.

[49] T. Sjostrand, S. Mrenna, P. Z. Skands, *PYTHIA 6.4 Physics and Manual*, JHEP **05** (2006) 026, DOI: `10.1088/1126-6708/2006/05/026`, arXiv: `hep-ph/0603175 [hep-ph]`.

[50] S. Agostinelli et al., *Geant4—a simulation toolkit*, Nucl. Instrum. Methods Phys. Res. A **506** (2003), DOI: `https://doi.org/10.1016/S0168-9002(03)01368-8`.

[51] *Penelope Geant4 Physics List*, Accessed: 12.05.2021, URL: `https://geant4.web.cern.ch/node/1621`.

[52] *Livermore Geant4 Physics List*, Accessed: 12.05.2021, URL: `https://geant4.web.cern.ch/node/1619`.

[53] *QGSP_BERT Geant4 Physics List*, Accessed: 12.05.2021, URL: `https://geant4.web.cern.ch/node/628`.

[54] *Physics lists electromagnetic constructors*, Accessed: 12.05.2021, URL: `https://geant4.web.cern.ch/node/1731#opt4`.

[55] K. Amako et al., *Comparison of Geant4 electromagnetic physics models against the NIST reference data*, IEEE Trans. Nucl. Sci. **52** (2005) 910, DOI: `10.1109/TNS.2005.852691`.

[56] M. Petric et al., *Detector simulations with DD4hep*, J. Phys. Conf. Ser. **898** (2017) 042015, DOI: `10.1088/1742-6596/898/4/042015`.

[57] A. Tsaregorodtsev et al., *DIRAC3: The new generation of the LHCb grid software*, J. Phys. Conf. Ser. **219** (2010) 062029, DOI: `10.1088/1742-6596/219/6/062029`.

[58] S. Aplin et al., *LCIO: A Persistency Framework and Event Data Model for HEP* (2012), SLAC-PUB-15296, DOI: `10.1109/NSSMIC.2012.6551478`.

[59] A. M. Nurnberg, D. Dannheim, *Requirements for the CLIC tracker readout* (2017), CLICdp-Note-2017-002, URL: `http://cds.cern.ch/record/2261066`.

[60] D. Dannheim, A. Sailer, *Beam-Induced Backgrounds in the CLIC Detectors* (2012), LCD-Note-2011-021, URL: `http://cds.cern.ch/record/1443516`.

[61] L. Z. Rivkin, *Beamstrahlung and disruption*, Advanced accelerator physics. Proc., 5th Course of the CERN Accelerator School, Rhodos, Greece, September 20-October 1, 1993. Vol. 1, 2, 1993, p. 557.

[62] S. Y. Lee, *Accelerator physics*, Singapore, World Scientific (1999).

[63] K. Yokoya, P. Chen, *Beam-beam phenomena in linear colliders*, Lect. Notes Phys. **400** (1992) 415, DOI: `10.1007/3-540-55250-2_37`.

[64] P. Chen, *Beamstrahlung and the QED, QCD backgrounds in linear colliders*, 9th International Workshop on Photon-Photon Collisions (PHOTON-PHOTON '92) San Diego, California, March 22-26, 1992, p. 418, URL: `http://www-public.slac.stanford.edu/sciDoc/docMeta.aspx?slacPubNumber=SLAC-PUB-5914`.

[65] A. A. Sokolov, A. V. Borisov, V. C. Zhukovskii, *Synchrotron radiation from relativistic electrons in intense magnetic fields*, Soviet Physics Journal **18** (1975), DOI: `10.1007/BF00895789`.

[66] *Quantum aspects of beam physics*, Proc., Joint 28th Advanced Beam Dynamics and Advanced and Novel Accelerator Workshop, QABP'03, Hiroshima, Japan, January 7-11, 2003, ed. by P. Chen, K. Reil, URL: `http://www-public.slac.stanford.edu/sciDoc/docMeta.aspx?slacPubNumber=slac-r-630`.

[67] G. Abbiendi et al., *Total Hadronic Cross-Section of Photon-Photon Interactions at LEP.* Eur. Phys. J. C **14** (1999) 199, DOI: `10.1007/s100520000352`, URL: `http://cds.cern.ch/record/391920`.

[68] T. Barklow et al., *Simulation of $\gamma\gamma \to$ hadrons background at CLIC* (2012), LCD-Note-2011-020, URL: `http://cds.cern.ch/record/1443518`.

[69] D. Arominski, A. Latina, D. Schulte,
Resistive Wall Effects in the CLIC Beam Delivery System, Proc. 10th International Particle Accelerator Conference, Melbourne, Australia, 19-24 May 2019,
DOI: `doi:10.18429/JACoW-IPAC2019-MOPGW071`.

[70] J. Resta-Lopez et al., *Status report of the baseline collimation system of CLIC.* (2011), CLIC-Note-883, URL: `https://cds.cern.ch/record/1344627`.

[71] F. Plassard, *Optics optimization of longer L* Beam Delivery System designs for CLIC and tuning of the ATF2 final focus system at ultra-low using octupoles*, Presented 06 Jul 2018, PhD thesis, 2018, URL: `http://cds.cern.ch/record/2646086`.

[72] S. Sgobba, *Physics and measurements of magnetic materials*, Proc., 2009 CAS-CERN Accelerator School: Specialised course on Magnets: Bruges, Belgium, June 16 - 25, 2009, arXiv: `1103.1069 [physics.acc-ph]`.

[73] A. W. Chao, *Physics of collective beam instabilities in high energy accelerators*, Wiley, New York, NY, 1993, URL: `http://cds.cern.ch/record/246480`.

[74] W. K. H. Panofsky, W. A. Wenzel, *Some Considerations Concerning the Transverse Deflection of Charged Particles in Radio-Frequency Fields*,
Review of Scientific Instruments (1956) 967, DOI: `10.1063/1.1715427`.

[75] J. R. Rumble, *Handbook of chemistry and physics*,
Taylor and Francis, Chemical Rubber Co, Boca Raton, FL, 2019,
URL: `http://cds.cern.ch/record/244291`.

[76] R. Bodenstein et al.,
Intra-beam IP Feedback Studies for the 380 GeV CLIC Beam Delivery System
(2016), CLIC-Note-1093, DOI: `10.18429/JACoW-IPAC2016-WEPOR009`.

[77] J. Schwinger, *On the Classical Radiation of Accelerated Electrons*, Phys. Rev. **75** (1949),
DOI: `10.1103/PhysRev.75.1912`.

[78] *NIST Digital Library of Mathematical Functions*, Accessed: 12.05.2021,
URL: `https://dlmf.nist.gov/10.25#E1`.

[79] G. Dugan, D. Sagan,
Simulating synchrotron radiation in accelerators including diffuse and specular reflections,
Phys. Rev. Accel. Beams **20** (2017) 020708,
DOI: `10.1103/PhysRevAccelBeams.20.020708`.

[80] M. Ady, *Monte Carlo simulations of ultra high vacuum and synchrotron radiation for particle accelerators*, Presented 03 May 2016, PhD thesis,
URL: `http://cds.cern.ch/record/2157666`.

[81] M. N. Polyanskiy, *Refractive index database*, Accessed: 12.05.2021,
URL: `https://refractiveindex.info`.

[82] H.-J. Hagemann, W. Gudat, C. Kunz, *Optical constants from the far infrared to the x-ray region: Mg, Al, Cu, Ag, Au, Bi, C, and Al2O3*, J. Opt. Soc. Am. **65** (1975) 742,
DOI: `10.1364/JOSA.65.000742`.

[83] F. Mirapeix et al., *High Precision Manufacturing for LINAC's*, Proc., 27th Linear Accelerator Conference, LINAC2014: Geneva, Switzerland, August 31-September 5, 2014, URL: `http://jacow.org/LINAC2014/papers/tupp077.pdf`.

[84] G. Guillermo, D. Sagan, F. Zimmermann, *Examining mitigation schemes for synchrotron radiation in high-energy hadron colliders*, Phys. Rev. Accel. Beams **21** (2018) 021001, DOI: `10.1103/PhysRevAccelBeams.21.021001`.

[85] C. Patrignani et al., *Review of Particle Physics*, Chin. Phys. **C40** (2016) 100001, DOI: `10.1088/1674-1137/40/10/100001`.

[86] Y. Bar-Cohen, *Low Temperature Materials and Mechanisms*, Taylor and Francis, Boca Raton, FL, 2016, DOI: `https://doi.org/10.1201/9781315371962`.

[87] P. E. Liley, *Emissivity of solids*, Department of Chemical Engineering, Imperial College London, UK, DOI: `10.1615/hedhme.a.000530`.

[88] *Engineering ToolBox, (2003). Convective Heat Transfer.* Accessed: 12.05.2021, URL: `https://www.engineeringtoolbox.com/convective-heat-transfer-d_430.html`.

[89] J. C. Billy et al., *The pressure and gas composition evolution during the operation of the LEP accelerator at 100 GeV*, Vacuum **60** (2001) 183, DOI: `10.1016/S0042-207X(00)00383-3`.

[90] R. Kersevan, C. Garion, *Design of the Vacuum System of the FCC-ee Electron-Positron Collider*, Proc. 10th International Particle Accelerator Conference (IPAC2019): Melbourne, Australia, May 19-24, 2019, 2019, DOI: `10.18429/JACoW-IPAC2019-TUPMP035`.

[91] O. Groebner, *Dynamic outgassing* (1999), CERN-OPEN-2000-275, DOI: `10.5170/CERN-1999-005.127`.

[92] D. Arominski et al., *Synchrotron Radiation Reflections in the CLIC Beam Delivery System*, Proc. 10th International Particle Accelerator Conference (IPAC'19), Melbourne, Australia, 19-24 May 2019, DOI: `doi:10.18429/JACoW-IPAC2019-WEPTS104`.

[93] R. Valizadeh et al., *Reduction of secondary electron yield for E-cloud mitigation by laser ablation surface engineering*, Appl. Surf. Sci. **404** (2017) 370, DOI: `10.1016/j.apsusc.2017.02.013`.

[94] Y. Wang et al., *Establishing a Laser Treatment to Suppress the Secondary Electron Emission*, Proc. 10th International Particle Accelerator Conference (IPAC'19), Melbourne, Australia, 19-24 May 2019, DOI: `doi:10.18429/JACoW-IPAC2019-TUPMP029`.

[95] S. Arsenyev, D. Schulte,
Modelling Wake Impedance of a Rough Surface in Application to the FCC-hh Beamscreen,
Proc. 9th International Particle Accelerator Conference (IPAC'18), Vancouver, BC,
Canada, April 29-May 4, 2018, DOI: `doi:10.18429/JACoW-IPAC2018-MOPMF031`.

[96] L. Gonzalez et al., *Results on the FCC-hh Beam Screen Sawtooth at the Kit Electron Storage Ring Kararesults on the Fcc-Hh Beam Screen Sawtooth at the Kit Electron Storage Ring Kara*,
Proc. 10th International Particle Accelerator Conference (IPAC'19), Melbourne,
Australia, 19-24 May 2019, DOI: `doi:10.18429/JACoW-IPAC2019-TUPMP036`.

[97] P. Lepeule, C. Menot, R. J. M. Veness,
Design and implementation of synchrotron radiation masks for LEP2
(1996), CERN-LHC-96-008-VAC, URL: `http://cds.cern.ch/record/307861`.

[98] S. van Dam, A. Sailer,
The occupancy in the Hadronic Calorimeter endcap of the CLIC detector
(2014), CLICdp-Note-2014-004, URL: `http://cds.cern.ch/record/1751528`.

[99] *DD4hep-based CLIC Detector Calorimeter Calibration*, Accessed: 12.05.2021,
URL: `https://twiki.cern.ch/twiki/bin/view/CLIC/DD4hepClicDetectorCaloCalibration`.

[100] G. Von Holtey, W. Niessen, P. Roudeau, *Synchrotron radiation masks for LEP2* (1994),
URL: `http://cds.cern.ch/record/266590`.

[101] M. Idzik et al.,
A 10-bit multichannel digitizer ASIC for detectors in particle physics experiments,
IEEE Trans. Nucl. Sci. **59** (2012) 294, DOI: `10.1109/TNS.2011.2181189`.

[102] L. Varga, *Characterization and optimization of Silicon Photomultipliers and small size scintillator tiles for future calorimeter applications*, MSc Thesis, Presented 23 Jun 2017,
2017, URL: `http://cds.cern.ch/record/2277248`.

[103] CMS Collaboration, *The Phase-2 Upgrade of the CMS Endcap Calorimeter*
(2017), CERN-LHCC-2017-023, URL: `https://cds.cern.ch/record/2293646`.

[104] *Shieldwerx - a Polyethylene-Based Shielding manufacturer*, Accessed: 12.05.2021, URL:
`http://www.shieldwerx.com/poly-based-shielding.html#swx201hd`.

[105] A. Sailer, *Radiation and Background Levels in a CLIC Detector due to Beam-Beam Effects: Optimisation of Detector Geometries and Technologies*, PhD thesis, HU Berlin, 2013,
URL: `http://cds.cern.ch/record/1506163`.

Acknowledgements

The successful completion of this work would not be possible without the many people I had an opportunity to discuss with and learn.

First and foremost, I would like to express my gratitude towards my supervisors: Andre Sailer and Andrea Latina for their continuous support and knowledge and experience they shared with me. I would also like to thank Adam Kisiel, my supervisor, since the Bachelor and Master theses, for support and removing all of the obstacles from my way.

I owe my sincere gratitude towards Daniel Schulte, for discussions on beam-beam processes and support with Guinea-Pig, Marton Ady and Roberto Kersevan for their support and fruitful discussions about photon reflections and Synrad+, and Jani Paavo Komppula for discussions and help with running PyHEADTAIL.

I would like to express my great appreciation to Morag Williams, for her constant support and discussions on the intricacies of the English language.

Last, but not least, I would like to thank both the CLIC detector and physics group, and CLIC beam physics group for the great opportunity and pleasure of working with them.

This work has been done in the framework of the CERN Doctoral Student programme. This research was done using resources provided by the Open Science Grid, which is supported by the National Science Foundation and the U.S. Department of Energy's Office of Science. This work benefited from services provided by the ILC Virtual Organisation, supported by the national resource providers of the EGI Federation.